Stabilization of Bosonic Codes in Superconducting Circuits

A Dissertation
Presented to the Faculty of the Graduate School
of
Yale University
in Candidacy for the Degree of
Doctor of Philosophy

Steven Touzard

Dissertation director: Michel H. Devoret

June 2019

Contents

List of Figures

Chapter 5: Stabilization of a manifold of grid states   92

Appendix B: Wigner functions of GKP states   157

List of Tables

List of Symbols

Constants

h	Planck's constant
$\hbar$	Reduced Planck's constant $\left(= \frac{h}{2\pi} \right)$
e	Charge of an electron
k_B	Boltzmann constant
ϕ_0	Reduced flux quantum $\left(= \frac{\hbar}{2e} \right)$
R_Q	Reduced resistance quantum $\left(= \frac{\hbar}{(2e)^2} \right)$

Qubits

$\boldsymbol{\sigma}_x, \boldsymbol{\sigma}_y, \boldsymbol{\sigma}_z$	Pauli operators for a physical qubit
$\boldsymbol{\sigma}_\pm$	Ladder operators for a physical qubit $\left(= \frac{\boldsymbol{\sigma}_x \pm i\boldsymbol{\sigma}_y}{2} \right)$
$\boldsymbol{X}_L, \boldsymbol{Y}_L, \boldsymbol{Z}_L$	Pauli operators for a logical qubit

Harmonic oscillator

$\boldsymbol{a}^\dagger, \boldsymbol{a}$	Creation and annihilation operators
$\boldsymbol{Q}$	Dimensionless position $\left(= \frac{\boldsymbol{a} + \boldsymbol{a}^\dagger}{2} \right)$
$\boldsymbol{P}$	Dimensionless momentum $\left(= \frac{\boldsymbol{a} - \boldsymbol{a}^\dagger}{2i} \right)$
$\boldsymbol{D}(\alpha)$	Displacement operator by α $\left(= e^{\alpha \boldsymbol{a}^\dagger - \alpha^* \boldsymbol{a}} \right)$
$\boldsymbol{S}(r)$	Squeezing operator by r $\left(= e^{\frac{1}{2}(r^* \boldsymbol{a}^2 - r\boldsymbol{a}^{\dagger 2})} \right)$
$|n\rangle$	Fock state with n excitations
$|\alpha\rangle$	Coherent state with amplitude α
$|Q\rangle, |P\rangle$	Eigenstates of the dimensionless position/momentum
$W(\alpha)$	Wigner function at point α
$C_s(\tilde{\alpha})$	Characteristic function at point $\tilde{\alpha}$

Open quantum systems

ρ	Density matrix
$\boldsymbol{E}_i$	Dissipation operators
$\mathcal{D}\left[\boldsymbol{E}\right]\rho$	Lindbladian $\left(= 2\boldsymbol{E}\rho\boldsymbol{E}^\dagger - \boldsymbol{E}^\dagger\boldsymbol{E}\rho - \rho\boldsymbol{E}^\dagger\boldsymbol{E}\right)$
$\boldsymbol{a}_{\text{in/out}}$	Input/output fields
T_1	Energy relaxation characteristic time
T_φ	Dephasing characteristic time
T_2	Coherence characteristic time $\left(\frac{1}{T_2} = \frac{1}{2T_1} + \frac{1}{T_\varphi}\right)$
κ	Energy decay rate of a harmonic oscillator

Circuit QED

$\boldsymbol{\varphi}$	Dimensionless number of reduced magnetic fluxes
$\boldsymbol{n}$	Dimensionless difference in number of Cooper pairs
E_C	Capacitive energy $\left(= \frac{e^2}{2C}\right)$
E_L	Inductive energy $\left(= \frac{\phi_0^2}{L}\right)$
Z_0	Characteristic impedance of a circuit
ϕ^{ZPF}	Zero-point fluctuations of the reduced magnetic flux $\left(= \sqrt{\frac{Z_0}{2R_Q}}\phi_0\right)$
n_Q^{ZPF}	Zero-point fluctuations of the charge $\left(= \sqrt{\frac{R_Q}{2Z_0}}2e\right)$
φ^{ZPF}	Zero-point fluctuations of the dimensionless flux $= \phi^{\text{ZPF}}/\phi_0$
φ_i	Zero-point fluctuations of the dimensionless flux for a dressed mode i
n^{ZPF}	Zero-point fluctuations of the dimensionless charge $\left(= n_Q^{\text{ZPF}}/(2e)\right)$
E_J	Josephson energy
$\boldsymbol{H}_J$	Josephson Hamiltonian $\left(= -E_J\cos(\boldsymbol{\varphi})\right)$
$\boldsymbol{H}_{\geq 4}$	Non-linear part of the Josephson Hamiltonian $\left(= -E_J\left(\cos(\boldsymbol{\varphi}) + \frac{\boldsymbol{\varphi}^2}{2}\right)\right)$
g	Generic capacitive coupling
Δ	Detuning between two modes
α	Anharmonicity of a qubit in units of frequency $(= E_C/\hbar$ for a transmon$)$

χ	Dispersive coupling in units of frequency $\left(\approx \frac{E_C}{\hbar} \left(\frac{g}{\Delta} \right)^2 \right)$
K	Kerr of a cavity in units of frequency $\left(\approx \frac{E_C}{2} \left(\frac{g}{\Delta} \right)^4 \right)$

Driven circuits

ϵ	Drive amplitude in units of frequency in the stiff-pump approximation
ξ	Dimensionless amplitude of the tracking frame

Readout of superconducting circuits

$\alpha_{g,e}$	Average value of the field of the cavity when the qubit is in g or e
ζ	Amplitude of a longitudinal coupling in units of frequency
Γ_φ	Dephasing rate induced by the measurement
γ_φ	Total dephasing due to the measurement
$\boldsymbol{M}$	Measurement operator
$\boldsymbol{M}_N$	Noise on the measurement operator $\left(= \boldsymbol{M} - \langle \boldsymbol{M} \rangle \right)$
η	Efficiency
$\mathcal{F}$	Total fidelity
$\mathcal{Q}$	QND-ness

Stabilization of a manifold of coherent states

$\lvert \mathcal{C}_\alpha^\pm \rangle$	Schrödinger cat state of amplitude α $\left(\propto \lvert \alpha \rangle \pm \lvert -\alpha \rangle \right)$
$\boldsymbol{\Pi}_\pm$	Projectors onto the stabilized manifold $\left(= \lvert \mathcal{C}_\alpha^\pm \rangle \langle \mathcal{C}_\alpha^\pm \rvert \right)$
χ_{sr}	Dispersive coupling between the storage and the reservoir
κ_r	Single-photon dissipation rate of the reservoir
κ_1	Single-photon dissipation rate of the storage
ϵ_P	Amplitude of the pump in units of frequency
ω_P	Frequency of the pump
ϵ_D	Amplitude of the drive in units of frequency
g_2	Two-photon coupling between the storage and the reservoir $\left(= \frac{\chi_{sr}}{2} \frac{\epsilon_P}{\Delta} \right)$

α_∞	Amplitude of the stabilized coherent states $\left(\pm\sqrt{\frac{2\epsilon_D}{\chi_{sr}}\frac{\Delta}{\epsilon_P}}\right)$
κ_2	Two-photon dissipation rate $\left(=\frac{4|g_2|^2}{\kappa_r}\right)$
$\mathcal{C}_2$	Two-photon cooperativity $\left(=\frac{\kappa_2}{\kappa_1}\right)$
ϵ_s	Amplitude of the Zeno drive in units of frequency

Stabilization of a manifold of grid states

$\Delta_{Q,P}$	Separation between position/momentum peaks
$\boldsymbol{S}_{a,b,c}$	Stabilizers of the GKP manifold
ϕ	Oriented phase enclosed by two displacements $\boldsymbol{D}(\alpha_a)$ and $\boldsymbol{D}(\alpha_b)$ $(= \operatorname{Im}(\alpha_b \alpha_a^*))$
ϕ_ϵ	Oriented phase enclosed by a stabilizer and a shift ϵ
P(Q/P)	Position/momentum probability distribution

Acronyms

QEC	Quantum Error Correction
CQED	Cavity Quantum Electrodynamics
cQED	Circuit Quantum Electrodynamics
RWA	Rotating Wave Approximation
JJ	Josephson Junction
QND	Quantum-non-demolition
SNR	Signal-to-Noise Ratio
resp.	Respectively
OCP	Optimal Control Pulse
QZD	Quantum Zeno Dynamics
CW	Continuous Wave
GKP	D. Gottesman, A. Kitaev and J. Preskill
SNAIL	Superconducting Nonlinear Asymmetric Inductive Element

Acknowledgement

1

Introduction

In the original formulation of quantum mechanics as "matrix mechanics" by Werner Heisenberg, the classical observables of a physical system, such as its position and momentum, are operators represented mathematically by matrices [1]. This formulation of quantum mechanics gives us some insight into the reason why the dynamics of a quantum mechanical system is hard to simulate, even with modern computers, and thus motivates the need for quantum computers. For this, consider a system whose observables are given by $n \times n$ matrices. The observables of a joint system comprising two such subsystems are given by the tensor product of the observables of the subsystems or, mathematically, by the Kroenecker product of their matrices, which results in matrices of dimensions $n^2 \times n^2$. Therefore, the complexity of a simulation of many interacting quantum systems grows exponentially with the number of systems.

Famously, the idea of creating quantum machines to simulate quantum systems was spearheaded by Richard Feynman who, in 1982, proposed to create quantum computers with ensembles of spins [2]. In 1985, David Deutsch showed that *any* quantum system can be efficiently simulated with an ensemble of "two-state observables" with at most a polynomial overhead [3], similarly to how a Turing machine is a universal computer. These "two-state observables" would then be termed quantum bits, or qubits, in analogy with the bits of a classical computer.

The interest for quantum computing increased further when it was demonstrated that their utility reaches beyond the simulation of quantum systems. In 1992, David Deutsch and Richard Josza demonstrated the first quantum algorithm that shows an exponential advantage over the best classical equivalent [4]. This algorithm does not have any practical interest in itself, but it demonstrates that some problems that are intractable for a classical computer can have a structure that makes them tractable for a quantum computer. This "quantum complexity" was further demonstrated with useful algorithms such as Shor's factoring algorithm [5], which has an exponential speed-up over the best known classical algorithm, and Grover's

search algorithm, which has a square-root advantage over the best known classical algorithm [6]. Nowadays, the number of quantum algorithms is much larger and an exhaustive list can be found at *http://quantumalgorithmzoo.org/*.

In these algorithms, a register of bits is encoded onto the state of an ensemble of qubits comprising the quantum computer. By using superpositions of such states, quantum computers can act simultaneously on all the possible registers of bits. This effect is usually referred to as "quantum parallelism". However, when the superposition of all these register states is measured, the ensemble of qubits is projected onto a given state. In a quantum algorithm, only one of these registers encodes the correct output. If the quantum computer is in an equal superposition of all the possible registers of bits, the probability to measure a given register diminishes exponentially with the number of qubits. The crux of such algorithms is to have the undesired outputs interfere destructively, such that the final measurement of the state of the quantum computer reveals the desired outputs with a high probability. For example, in Shor's algorithm, the output is a large superposition of states that are harmonics of one frequency. This key interference effect can be thought of as equivalent to the optical interference fringes in Young's double slit experiment: two possible paths for light rays interfere and create a darker pattern at some locations of the screen, while it creates a brighter pattern at other locations.

In Young's experiment, the contrast between the dark fringes and the bright fringes decreases when the phase of the light wave is lost before creating the interference pattern. Therefore, this contrast is much larger if one uses a highly coherent laser than if one uses the sunlight. Similarly, in quantum computing, the contrast between the probability of measuring the desired output and the probability of measuring the undesired output depends on the coherence of the qubits. The noisier the state of the qubits is, the more random the output of a quantum computer will be.

As of today, qubits that are coherent enough to be assembled into a universal quantum computer able to perform Shor's algorithm at a useful level do not exist (i.e. able to factorize a larger number into its prime factors faster than a classical computer). The idea of quantum error correction (QEC) consists in assembling several noisy qubits into one less noisy *logical* qubit [7, 8]. Although tremendous progress in that direction have been realized in the recent years, making a logical qubit with sufficiently low noise for practical applications remains to be done.

An emerging strategy to build a logical qubit consists in encoding the state of a qubit into the collective excitations of bosonic mode, which is equivalent to a harmonic oscillator [9–12]. Because the Hilbert space of harmonic oscillator is infinite, it could potentially be

used to replace an ensemble of qubits to encode a logical qubit. Moreoever, the structure of the errors of a harmonic oscillator is simple and can be taken advantage of for *hardware efficient* QEC. The main challenge of this strategy is to implement a nonlinear control of the state of the harmonic oscillator. Fortunately, this can be realized using the Kerr effect of slightly anharmonic oscillators [13, 14], photodetectors [15], nonlinear couplings to ancilla harmonic oscillators [11, 12] or a coupling to a nonlinear ancilla two-level system [14, 16–18].

Experimentally, the nonlinear manipulation of harmonic oscillators was pioneered by coupling the internal degree of freedom of trapped ions to their motional degree of freedom [19–21], and by coupling single atoms to the field of superconducting microwave cavities in cavity quantum electrodynamics (CQED) [22, 23]. Recently, in circuit quantum electrodynamics (cQED), these techniques were adapted and refined to manipulate the state of superconducting microwave cavities using superconducting circuits [24]. The idea of encoding quantum information in superconducting microwave cavities gained momentum just before the beginning of my PhD when several teams in the groups of Michel Devoret and Robert Schoelkopf at Yale realized the creation of Yurke-Stoler cat states using the Kerr effect [25] and the deterministic creation of arbitrary photonic Schrödinger cat states [26].

Finally, the development of these control techniques led to the possibility to create logical qubits encoded in the state of a superconducting microwave cavity. These encodings could overcome the control overhead and rival with other physical qubits. This was made possible by developing new bosonic QEC codes [27, 28], experimentally measuring their error syndromes [29] and implementing these QEC protocols experimentally [30, 31]. The logical qubits encoded this way are in fact fully controllable using a two-level ancilla that assists the creation of single-qubit gates [32] or two-qubit gates [33–35].

The work developed in this thesis is in the continuation of this strategy while extending the possible nonlinear couplings available to control the state of a harmonic oscillator. In a first series of experiment, we replace the need of an ancilla two-level system by an engineered dissipation that stabilizes Schrödinger cat states [12, 36, 37]. We also engineered a driven coupling between a two-level ancilla and a harmonic oscillator that displaces the state of the harmonic oscillator conditioned on the state of the ancilla. Importantly, this coupling is strong even when the residual dispersive coupling is weak. We use this interaction to stabilize another type of codes called GKP codes [11].

This work could be important to mitigate the propagation of errors from the ancillary system to the harmonic oscillator that encodes a logical qubit. In our experimental stabilization of Schrödinger cat states, the state of the encoded qubit can be manipulated without the

use of an ancilla. In the stabilization of GKP codes, the errors of the ancilla can be mitigated, such that they only propagate as correctable errors. A complete discussion of this topic is presented in our conclusion.

The rest of this introduction will present the bases of quantum information that are necessary to the understanding of the thesis. In order to understand standard quantum information, we will introduce the notions of qubits, errors and quantum error correction. Then, we will focus on harmonic oscillators and the representations of their states.

1.1 Qubits

In the context of QEC, a qubit is generally not a two-level system, where two states are eigenstates of the Hamiltonian and transitions between the two states can easily be driven. For example, it can be an ensemble of two-level systems or, in this thesis, some states of a harmonic oscillator. We define a qubit as the orthonormal eigenstates $|0\rangle$ and $|1\rangle$ of an observable that has two possible outcomes. These two outcomes are always dimensionless and we take their values to be ± 1. In this basis, the observable is written as a traceless Hermitian matrix

$$\boldsymbol{\sigma}_z = \begin{pmatrix} 1 & 0 \\ 0 & -1 \end{pmatrix} \tag{1.1}$$

All the transformations in the Hilbert space spanned by $|0\rangle$ and $|1\rangle$ are generated by the identity $\boldsymbol{I}$ and the Pauli matrices, which include $\boldsymbol{\sigma}_z$, but also

$$\boldsymbol{\sigma}_x = \begin{pmatrix} 0 & 1 \\ 1 & 0 \end{pmatrix}, \quad \boldsymbol{\sigma}_y = \begin{pmatrix} 0 & -i \\ i & 0 \end{pmatrix}. \tag{1.2}$$

The Pauli matrices anti-commute, are their own inverse and we have $\boldsymbol{\sigma}_x \boldsymbol{\sigma}_y \boldsymbol{\sigma}_z = i\boldsymbol{I}$. Note that the states $|\pm\rangle = \frac{1}{2} \left(|0\rangle \pm |1\rangle \right)$ are eigenstates of $\boldsymbol{\sigma}_x$ with eigenvalues ± 1 and $|\pm i\rangle = \frac{1}{2} \left(|0\rangle \pm i |1\rangle \right)$ are eigenstates of $\boldsymbol{\sigma}_y$ with eigenvalues ± 1. These states correspond to a change of basis for the qubit.

An arbitrary state $|\psi\rangle$ of a qubit can be parametrized using two real numbers θ and φ, such that

$$|\psi\rangle = \cos\left(\frac{\theta}{2}\right) |0\rangle + \sin\left(\frac{\theta}{2}\right) e^{i\varphi} |1\rangle. \tag{1.3}$$

With this parametrization, the expectation values of the Pauli operators are given by

$$\langle \boldsymbol{\sigma}_x \rangle = \sin\theta \cos\varphi \tag{1.4}$$

$$\langle \boldsymbol{\sigma}_y \rangle = \sin\theta \sin\varphi \tag{1.5}$$

$$\langle \boldsymbol{\sigma}_z \rangle = \cos\theta. \tag{1.6}$$

These values correspond to the projections along three axes in spherical coordinates. The state of a qubit can thus be represented as a vector $\vec{b}$ on a sphere, called the Bloch sphere, represented in Fig. 1.1.
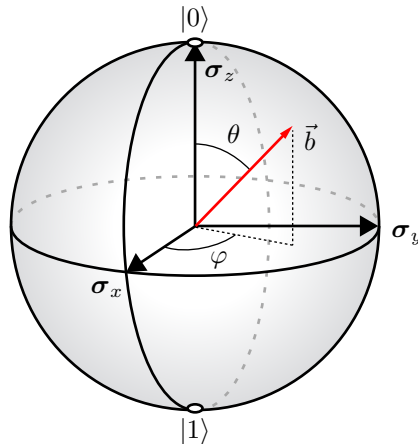
Figure 1.1: Representation of the state of qubit using the Bloch sphere. The poles correspond to the states $|0\rangle$ and $|1\rangle$. The vector $\vec{b}$ represents the state of a qubit and is parametrized by θ and φ (see text).

The transformations of a state that lives in a two-dimension Hilbert space can be represented as rotations on the Bloch sphere. This way, a continuous rotation $\boldsymbol{R}$ parametrized with an angle α around an oriented axis $\vec{n}$ of the Bloch sphere can be written using the Pauli matrices, such that

$$\boldsymbol{R}_{\vec{n}}(\alpha) = \exp\left(-i\frac{\alpha}{2}\vec{n} \cdot \vec{\boldsymbol{\sigma}}\right)$$

$$= \cos\left(\frac{\alpha}{2}\right)\boldsymbol{I} - i\sin\left(\frac{\alpha}{2}\right)\vec{n} \cdot \vec{\boldsymbol{\sigma}}, \tag{1.7}$$

where $\vec{\sigma} = (\sigma_x, \sigma_y, \sigma_z)$.

1.2 Interaction with the environment

A quantum system is, in general, not completely isolated. Everything that is external to the system is defined as its environment. Part of this environment is controlled by the experimentalist and is used to perform unitary transformations on the system under test. However, quantum systems are also coupled to spurious degrees of freedom whose state is not controlled. When the state of the environment is noisy, its coupling to a qubit results in uncontrolled transformations of this qubit that are statistically random. The density matrix ρ is a generalization of the wave function, designed to characterize the best estimate of the state of the system that is subject to random uncontrolled transformations. If a qubit is known to be in a given state $|\psi\rangle$, its density matrix is

$$\rho = |\psi\rangle \langle\psi| . \tag{1.8}$$

In this case, the system is said to be in a *pure state*. After interacting with uncontrolled degrees of freedom, part of the information about the state is transferred to the state of its environment and cannot be accessed. The new density matrix of the system is obtained by dismissing all this information. This way, the state of the qubit is given by probabilities λ_k to be in a state $|\psi_k\rangle$, such that

$$\rho = \sum_k \lambda_k |\psi_k\rangle \langle\psi_k| . \tag{1.9}$$

Usually, the density matrix is written such that $|\psi_k\rangle \langle\psi_k|$ are projectors onto orthonormal states. This way, we have $\text{Tr}(\rho) = \sum_k \lambda_k = 1$. We define the purity of a system as $\text{Tr}(\rho^2) = \sum_k \lambda_k^2 \leq 1$, where the equality is reached only for a pure state. Using the density matrix, the expectation value of an observable $\mathcal{O}$ is given by

$$\langle\mathcal{O}\rangle = \text{Tr}(\mathcal{O}\rho). \tag{1.10}$$

In the particular case of a qubit, the density matrix can be written in term of the Pauli

projectors, such that

$$\rho = \frac{1}{2}\left(\mathbf{I} + \langle\boldsymbol{\sigma}_x\rangle\boldsymbol{\sigma}_x + \langle\boldsymbol{\sigma}_y\rangle\boldsymbol{\sigma}_y + \langle\boldsymbol{\sigma}_z\rangle\boldsymbol{\sigma}_z\right) \tag{1.11}$$

$$= \frac{1}{2}\left(\mathbf{I} + \vec{b}\cdot\vec{\boldsymbol{\sigma}}\right), \tag{1.12}$$

where $\vec{b}$ is a Bloch vector whose norm is now given by the purity, with $|\vec{b}|^2 = 2\mathrm{Tr}(\rho^2) - 1$, which can be inside the Bloch sphere, and is exactly on the Bloch sphere when $\mathrm{Tr}(\rho^2) = 1$.

In order to describe how the environment affects a quantum system, we want an equation that gives the dynamics of ρ taking into account spurious transformations due to the environment. For this, we make a list of spurious transformations $\{\mathbf{L}_k\}$ that the environment is able to perform at each interval of time dt. We assign to each of these operators a probability p_k that it occurs within an interval dt. We also need to assume that these probabilities are the same for all intervals dt, meaning that the environment acts the same way at all times. We can define a rate Γ_k at which operator $\mathbf{L}_k$ occurs, such that $p_k = \Gamma_k dt$. This way, the environment has no memory and is said to be Markovian. We usually redefine a set of evolution operators $\{\mathbf{E}_k\}$ that includes the probabilities p_k, such that $\mathbf{E}_k = \sqrt{p_k}\mathbf{L}_k$. The density matrix at a time $t + dt$ is given by a sum of all these transformations, weighted by their respective probabilities, such that

$$\rho(t + dt) = \sum_k p_k \mathbf{L}_k \rho(t)\mathbf{L}_k^\dagger \tag{1.13}$$

$$= \sum_k \mathbf{E}_k \rho(t)\mathbf{E}_k^\dagger. \tag{1.14}$$

This evolution must conserve the trace of the density matrix, which is 1 at all time. Therefore, we get a condition on the set of evolution operators

$$\sum_k \mathbf{E}_k^\dagger \mathbf{E}_k = \mathbf{I}. \tag{1.15}$$

The form of the evolution of $\rho(t)$ given by equation 1.14 is called the *operator sum representation* [38]. Before developing this description more, we consider two examples that are relevant to qubit errors and that illustrate the dynamics of the density matrix.

1.2.1 Phase-flips

The local environment of a qubit is composed of a large number of quantum degrees of freedom that can couple to the observable $\boldsymbol{\sigma}_z$ of the qubit. If the properties of the uncontrolled degrees of freedom are noisy, they will induce uncontrolled rotations of the qubit around its z-axis. In superconducting circuits, this noise can be due, for example, to local variations of the electric field, causing charge noise [39], to local variations of magnetic field, causing flux noise [40], or to the finite temperature of the local environment [41]. We regroup all these sources of errors under the term phase-flips.

We write the probability that a phase-flip $\boldsymbol{\sigma}_z$ happens in a time interval dt as $\frac{\Gamma_\varphi dt}{2}$. Thus, the first evolution operator $\boldsymbol{E}_1$ is given by

$$E_1 = \sqrt{\frac{\Gamma_\varphi dt}{2}}\,\boldsymbol{\sigma}_z. \tag{1.16}$$

In order to get a set of evolution operators that preserves the trace of ρ, we need to add an operator $\boldsymbol{E}_0$ that fulfills the condition given by equation 1.15. We have

$$E_0^\dagger E_0 = I - E_1^\dagger E_1 \tag{1.17}$$

$$= \left(1 - \frac{\Gamma_\varphi dt}{2}\right) I, \tag{1.18}$$

such that $\boldsymbol{E}_0 = \sqrt{1 - \frac{\Gamma_\varphi dt}{2}}\,\boldsymbol{I}$. The evolution of the density matrix is given by

$$\rho(t + dt) = \left(1 - \frac{\Gamma_\varphi dt}{2}\right)\rho(t) + \frac{\Gamma_\varphi dt}{2}\boldsymbol{\sigma}_z\rho(t)\boldsymbol{\sigma}_z, \tag{1.19}$$

which gives a differential equation on $\rho(t)$

$$\partial_t\rho(t) = \frac{\Gamma_\phi}{2}\left(\boldsymbol{\sigma}_z\rho(t)\boldsymbol{\sigma}_z - \rho(t)\right). \tag{1.20}$$

Using this, we can calculate the evolution of the expectation values of the Pauli operators, given by $\mathrm{Tr}(\sigma_i\rho(t))$, and we get the Bloch equations

$$\partial_t\langle\boldsymbol{\sigma}_z\rangle = 0 \tag{1.21}$$

$$\partial_t\langle\boldsymbol{\sigma}_y\rangle = -\Gamma_\varphi\langle\boldsymbol{\sigma}_y\rangle \tag{1.22}$$

$$\partial_t\langle\boldsymbol{\sigma}_x\rangle = -\Gamma_\varphi\langle\boldsymbol{\sigma}_x\rangle. \tag{1.23}$$

This set of equations indicates that, even in presence phase-flips, the value θ of a qubit in an arbitrary state $\cos\left(\frac{\theta}{2}\right)|0\rangle + \sin\left(\frac{\theta}{2}\right)e^{i\varphi}|1\rangle$ can always be retrieved. However, the phase of the superposition φ is lost with a timescale $1/\Gamma_\varphi$. Here, it becomes apparent that we set the probability that a flip happens as $\Gamma_\varphi/2$, such that the phase is lost at a rate Γ_φ. We illustrate the evolution of possible Bloch vectors subject to phase-flips on Fig. 1.2.
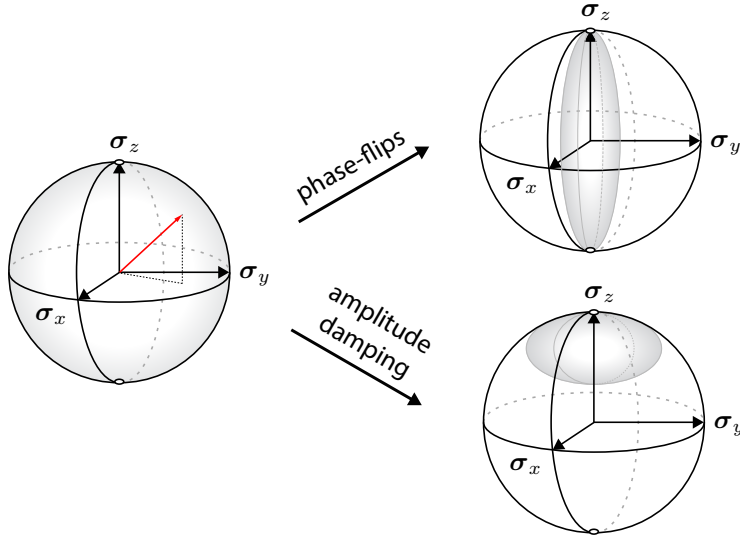
Figure 1.2: Evolution of the Bloch sphere with errors. On the left, we represent a Bloch sphere for pure states: all the Bloch vectors lie on the surface of the sphere. With dissipation, the possible Bloch vectors evolve according to the Bloch equations. The original sphere that represented all the possible pure states is shrunken with a shape that depends on the dissipation. Phase-flips decrease its amplitude on the equator and preserves the poles, while amplitude damping preserves only the north pole.

1.2.2   Amplitude damping

When a two-level system, is in free space, it is coupled to an infinite number of electromagnetic modes that are in their vacuum states. When the two-level system is in its excited state, this coupling leads to the spontaneous emission of a photon in one of these modes, which is accompanied by a transition of the two-level system from its excited state to its ground state. More generally, this type of error on a qubit is called amplitude damping. We denote the amplitude damping rate $\Gamma_\downarrow$. To define an evolution operator that destroys an

excitation in the qubit, we construct the ladder operators

$$\boldsymbol{\sigma}_{\pm} = \frac{\boldsymbol{\sigma}_x \pm i\boldsymbol{\sigma}_y}{2}, \tag{1.24}$$

where $\boldsymbol{\sigma}_+$ is a creation operator, $\boldsymbol{\sigma}_-$ is an annihilation operator, and $\boldsymbol{\sigma}_+^{\dagger} = \boldsymbol{\sigma}_-$. The first evolution operator is thus given by

$$\boldsymbol{E}_1 = \sqrt{\Gamma_{\downarrow}dt}\,\boldsymbol{\sigma}_- = \begin{pmatrix} 0 & \sqrt{\Gamma_{\downarrow}dt} \\ 0 & 0 \end{pmatrix}. \tag{1.25}$$

The other evolution operator must therefore be given by $\boldsymbol{E}_0^{\dagger}\boldsymbol{E}_0 = \boldsymbol{I} - \Gamma_{\downarrow}dt\boldsymbol{\sigma}_+\boldsymbol{\sigma}-$. We get

$$\boldsymbol{E}_0 = \begin{pmatrix} 1 & 0 \\ 0 & \sqrt{1 - \Gamma_{\downarrow}dt} \end{pmatrix} = \boldsymbol{I} - \left(1 - \sqrt{1 - \Gamma_{\downarrow}dt}\right)\boldsymbol{\sigma}_+\boldsymbol{\sigma}_-. \tag{1.26}$$

The evolution operator $\boldsymbol{E}_1$ is easy to interpret: there is a probability Γdt that the two-level system spontaneously emits a photon into the environment during a time interval dt. However, when no photon is emitted, the system is not left in its original state. Instead, because the environment has not observed that there was an excitation in the two-level system, the probability that the two-level system was actually in its excited state diminishes while the probability that it was in its ground state increases.

The operator-sum representation gives the time evolution as

$$\rho(t + dt) = \left(\boldsymbol{I} - \left(1 - \sqrt{1 - \Gamma_{\downarrow}dt}\right)\boldsymbol{\sigma}_+\boldsymbol{\sigma}_-\right)\rho(t)\left(\boldsymbol{I} - \left(1 - \sqrt{1 - \Gamma_{\downarrow}dt}\right)\boldsymbol{\sigma}_+\boldsymbol{\sigma}_-\right)$$
$$+ \Gamma_{\downarrow}dt\boldsymbol{\sigma}_-\rho(t)\boldsymbol{\sigma}_+. \tag{1.27}$$

In order to deduce a differential equation on $\rho(t)$, we need to expand this evolution to first order in dt, such that $1 - \sqrt{1 - \Gamma_{\downarrow}dt} = \frac{\Gamma_{\downarrow}dt}{2} + O\left((\Gamma_{\downarrow}dt)^2\right)$. This way, we obtain the differential equation

$$\partial_t\rho(t) = \frac{\Gamma_{\downarrow}}{2}\left(2\boldsymbol{\sigma}_-\rho(t)\boldsymbol{\sigma}_+ - \boldsymbol{\sigma}_+\boldsymbol{\sigma}_-\rho(t) - \rho(t)\boldsymbol{\sigma}_+\boldsymbol{\sigma}_-\right). \tag{1.28}$$

We can use this equation to obtain the evolution of the expectation values of the Pauli

operators. We get the Bloch equations

$$\partial_t \langle \boldsymbol{\sigma}_z \rangle = \Gamma_\downarrow \left(1 - \langle \boldsymbol{\sigma}_z \rangle \right) \tag{1.29}$$

$$\partial_t \langle \boldsymbol{\sigma}_y \rangle = -\frac{\Gamma_\downarrow}{2} \langle \boldsymbol{\sigma}_y \rangle \tag{1.30}$$

$$\partial_t \langle \boldsymbol{\sigma}_x \rangle = -\frac{\Gamma_\downarrow}{2} \langle \boldsymbol{\sigma}_x \rangle. \tag{1.31}$$

These equations show that the phase of the superposition φ is lost at a rate $\Gamma_\downarrow/2$ and that the amplitude given by θ is lost at a rate $\Gamma_\downarrow$. Any state of the qubit converges to the north pole of the Bloch sphere $|0\rangle$ in steady state. These Bloch equations are illustrated in Fig. 1.2.

In general, superconducting qubits suffer from both phase-flips and amplitude damping. To a lesser extent, they also suffer from heating from $|0\rangle$ to $|1\rangle$ at a rate $\Gamma_\uparrow$. We usually use the notations T_φ as the dephasing characteristic time, and T_1 as the energy relaxation characteristic time, with

$$\frac{1}{T_1} = \Gamma_\uparrow + \Gamma_\downarrow. \tag{1.32}$$

Finally, we define a coherence time T_2, defined as

$$\frac{1}{T_2} = \frac{1}{2T_1} + \frac{1}{T_\varphi}, \tag{1.33}$$

where the factor $2T_1$ comes from the fact that amplitude damping and heating decrease $\langle \boldsymbol{\sigma}_{x,y} \rangle$ at half the rate it decreases $\langle \boldsymbol{\sigma}_z \rangle$.

1.2.3 Lindblad master equation

The operator-sum representation is enough to understand the rest of the introduction. However, in the rest of the thesis, we will sometimes use a differential equation on $\rho(t)$ similar to the ones we found in the previous subsection. For a given set of evolution operators, can we find a general differential equation for ρ? Such an equation is called a master equation. The proper derivation of such an equation is presented in *Exploring the quantum* by J.M. Raimond and S. Haroche [23]. We reproduce part of this derivation to go from the operator-sum representation to the master equation in the Lindblad form.

First, we know that when dt goes to 0, we have $\rho(t + dt) = \rho(t)$. Hence, one of the evolution operators must be close to $\boldsymbol{I}$. In the previous examples, we have always taken $\boldsymbol{E}_0$ as being this operator. To find a differential equation, we expand $\boldsymbol{E}_0$ to first order in dt, such

that

$$E_0 = I - iK\,dt + O(dt^2).\tag{1.34}$$

We now split K into an Hermitian part H (akin to a Hamiltonian) and an anti-Hermitian part J, given by

$$H = \hbar\frac{K + K^\dagger}{2}\tag{1.35}$$

$$J = i\frac{K - K^\dagger}{2}.\tag{1.36}$$

The evolution due to E_0 in the operator-sum representation is now, to first order in dt,

$$E_0\rho E_0^\dagger = \rho - i\frac{dt}{\hbar}[H, \rho] - dt\{J, \rho\},\tag{1.37}$$

where $\{\}$ is the anti-commutator. The normalization condition given by equation 1.15 is now

$$\sum_k E_k^\dagger E_k = I - 2J\,dt + \sum_{k\neq 0} E_k^\dagger E_k\tag{1.38}$$

$$= I - 2J\,dt + dt\sum_{k\neq 0}\Gamma_k L_k^\dagger L_k.\tag{1.39}$$

We deduce the condition

$$J = \frac{1}{2}\sum_{k\neq 0}\Gamma_k L_k^\dagger L_k.\tag{1.40}$$

We now replace the expression for J into equation 1.37, and we rewrite the operator-sum representation with equation 1.14. This way, we obtain the master equation for ρ with the Lindblad form

$$\partial_t\rho(t) = -\frac{i}{\hbar}[H, \rho(t)] + \sum_{k\neq 0}\frac{\Gamma_k}{2}\left(2L_k\rho(t)L_k^\dagger - \{L_k^\dagger L_k, \rho(t)\}\right).\tag{1.41}$$

The dissipative term is usually written in the form of a superoperator as

$$\mathcal{D}[L_k]\rho = 2L_k\rho L_k^\dagger - \{L_k^\dagger L_k, \rho\}.\tag{1.42}$$

1.3 Non-locality as a resource for quantum error correction

The noise due to the environment of each individual qubit limits the performances of a quantum computer by destroying the coherence of the large entangled states that are necessary to run a quantum computation. The goal of quantum error correction is to create logical qubits that are less noisy than the physical qubits that are available. For this, the information of a quantum bit needs to be encoded such that it is hidden from the environment and can be decoded later without errors. To this end, we first need to understand the limitations that are imposed on the environment, and then find a way to exploit these limitations.

Quantum error correcting codes are constructed assuming that the environment only acts locally on each individual qubit. This simply means that the environment can only couple to observables of a single qubit and thus cannot change *simultaneously* the state of two qubits. This assumption seems invalid in experimental situations where qubits are close to each other. In these cases, the same environment can be coupled to several qubits. For example, with trapped ions, the noise of the electromagnetic field of the trap induces a frequency jitter on all the trapped ions. Similarly, in superconducting qubits, several qubits can be coupled to the same resonator, whose thermal noise will also induce a frequency jitter on all the qubits. However, in both cases, the frequency shift of one qubit does not depend on the state of the other qubit. In these examples, the environment is coupled to $\boldsymbol{\sigma}_{z,1} + \boldsymbol{\sigma}_{z,2}$. In order to induce simultaneous phase-flips, the environment would have to be coupled to $\boldsymbol{\sigma}_{z,1} \boldsymbol{\sigma}_{z,2}$, which is not observed and which justifies our locality assumption. With this, it is easy to make a list of the evolution operators of n qubits. If a single qubit has k evolution operators $\boldsymbol{E}_i$, where i takes any value between 0 and $k-1$, then we denote $\boldsymbol{E}_{i_1,\dots,i_n} = \boldsymbol{E}_{i_1} \otimes \dots \otimes \boldsymbol{E}_{i_n}$. This set of operators has a size k^n, however only the subset of single-qubit errors are of order $\sqrt{\Gamma dt}$ or lower.

In QEC codes, the quantum information is distributed among different physical qubits such that a local measurement of one physical qubit cannot reveal the state of the encoded logical qubit. To do this, these codes use the fact that the state of multiple physical qubits can be entangled. Such states can be created using local interactions between two qubits for a given duration. After this duration, even if the two qubits do not interact, the properties of their joint state are different from the properties of each individual qubits.

For example, two qubits 1 and 2 can temporarily interact locally to implement a rotation $\boldsymbol{\sigma}_{x,2}$, conditioned on qubit 1 being in $|1\rangle$. This gate is called a controlled-NOT (CNOT)

and its truth table is

initial state	final state
$|00\rangle$	$|00\rangle$
$|01\rangle$	$|01\rangle$
$|10\rangle$	$|11\rangle$
$|11\rangle$	$|10\rangle$

This gate can be written as the two-qubit matrix

$$\text{CNOT} = \begin{pmatrix} 1 & 0 & 0 & 0 \\ 0 & 1 & 0 & 0 \\ 0 & 0 & 0 & 1 \\ 0 & 0 & 1 & 0 \end{pmatrix} \tag{1.43}$$

This interaction was implemented in cQED for example with the cross-resonance technique [41]. Using this gate, we can create a so-called Bell pair with

$$\text{CNOT} \frac{1}{\sqrt{2}}(|0\rangle + |1\rangle) = \frac{1}{\sqrt{2}}(|00\rangle + |11\rangle). \tag{1.44}$$

After the entangling gate, even if the two qubits stop interacting, the two qubit state is non-local: a local measurement of qubit 1 will *instantly* affect the properties of qubit 2. This non-locality has always been successfully tested, using the violation of Bell's inequality [42–44]. While this seems to make entangled state more fragile, QEC actually utilizes the non-locality of quantum mechanics to protect quantum information against decoherence induced by a local environment.

We will see this through two examples where non-local encodings protect against the phase-flips and amplitude damping errors we introduced earlier. We will use these two examples to introduce the main concepts of QEC that are used to build other codes.

1.3.1 Phase-flips

In order to correct against spurious rotations of a qubit around one axis, it is possible to adapt the strategies of classical error correction. In classical computing, a bit has two possible

evolutions: either it remains in its initial state, or the bit is flipped, which results in an error. In order to correct this error, three bits are assembled together and set to the same value. When one bit flips, the majority of the bits still have the correct value. By using a majority vote, the register can be reset to its correct value. In order to adapt such a code to a qubit and to detect a single phase-flip unambiguously, we encode a single logical qubit in three physical qubits, such that

$$|0\rangle_L = |+++\rangle \tag{1.45}$$

$$|1\rangle_L = |---\rangle\,, \tag{1.46}$$

where $|0/1\rangle_L$ are the basis states of the logical qubit, and $|\pm\rangle = \frac{1}{\sqrt{2}}(|0\rangle \pm |1\rangle)$. An arbitrary state of the logical qubit is

$$|\psi\rangle = \cos\left(\frac{\theta}{2}\right)|+++\rangle + \sin\left(\frac{\theta}{2}\right)e^{i\varphi}|---\rangle\,. \tag{1.47}$$

As we assumed that the phase-flips of each qubits are independent, there are only four evolutions operators that participate to the first order dynamics of the density matrix ρ. After a time interval dt, the initial state $\rho = |\psi\rangle\langle\psi|$ is then transformed into a statistical mixture $\sum_{k_1,k_2,k_3} \boldsymbol{E}_{k_1,k_2,k_3}|\psi\rangle\langle\psi|\boldsymbol{E}^\dagger_{k_1,k_2,k_3}$, with

$$\boldsymbol{E}_{000}|\psi\rangle = \sqrt{1 - \frac{1}{2}(\Gamma_{\varphi,1} + \Gamma_{\varphi,2} + \Gamma_{\varphi,3})dt}\,|\psi\rangle\,, \tag{1.48}$$

$$\boldsymbol{E}_{100}|\psi\rangle = \sqrt{\frac{\Gamma_{\varphi,1}dt}{2}}\left(\cos\left(\frac{\theta}{2}\right)|-++\rangle + \sin\left(\frac{\theta}{2}\right)e^{i\varphi}|+--\rangle\right)\,, \tag{1.49}$$

$$\boldsymbol{E}_{010}|\psi\rangle = \sqrt{\frac{\Gamma_{\varphi,2}dt}{2}}\left(\cos\left(\frac{\theta}{2}\right)|+-+\rangle + \sin\left(\frac{\theta}{2}\right)e^{i\varphi}|-+-\rangle\right)\,, \tag{1.50}$$

$$\boldsymbol{E}_{001}|\psi\rangle = \sqrt{\frac{\Gamma_{\varphi,3}dt}{2}}\left(\cos\left(\frac{\theta}{2}\right)|++-\rangle + \sin\left(\frac{\theta}{2}\right)e^{i\varphi}|--+\rangle\right)\,. \tag{1.51}$$

Importantly, these four states are orthogonal to one another. Therefore, it is possible to construct a measurement that will unambiguously discriminate between these three errors.

From here, one strategy to correct the error consists in crafting a decoding unitary oper-

ation $\boldsymbol{U}_d$ such that

$$\boldsymbol{U}_d\boldsymbol{E}_0\left|\psi\right\rangle \propto \left(\cos\left(\frac{\theta}{2}\right)\left|0\right\rangle + \sin\left(\frac{\theta}{2}\right)e^{i\varphi}\left|1\right\rangle\right)\left|00\right\rangle \qquad (1.52)$$

$$\boldsymbol{U}_d\boldsymbol{E}_1\left|\psi\right\rangle \propto \left(\cos\left(\frac{\theta}{2}\right)\left|0\right\rangle + \sin\left(\frac{\theta}{2}\right)e^{i\varphi}\left|1\right\rangle\right)\left|10\right\rangle \qquad (1.53)$$

$$\boldsymbol{U}_d\boldsymbol{E}_2\left|\psi\right\rangle \propto \left(\cos\left(\frac{\theta}{2}\right)\left|0\right\rangle + \sin\left(\frac{\theta}{2}\right)e^{i\varphi}\left|1\right\rangle\right)\left|01\right\rangle \qquad (1.54)$$

$$\boldsymbol{U}_d\boldsymbol{E}_3\left|\psi\right\rangle \propto \left(\cos\left(\frac{\theta}{2}\right)\left|0\right\rangle + \sin\left(\frac{\theta}{2}\right)e^{i\varphi}\left|1\right\rangle\right)\left|11\right\rangle. \qquad (1.55)$$

Such a unitary transformation is possible because it maps orthogonal states to orthogonal states. The final step consists in performing a quantum-non-destruction (QND) measurement of $\boldsymbol{\sigma}_z$ of qubits 2 and 3. This final measurement will transform ρ, which is the statistical mixture of all possible errors, into a pure state given by the result of the measurement. Once the state of the qubit is purified, it can be re-encoded. Note that here, the purification is the only important part about the correction, the qubit can be re-encoded into an "error state" using the inverse of the decoding operation $\boldsymbol{U}_d^\dagger$ without affecting the future performances of the code. The experimentalist simply needs to redefine the logical basis states taking into account that one qubit has flipped. Hence, this error-correction scheme does not require any fast feedback. The signature of this first order protection has been seen multiple times in NMR [45], superconducting qubits [46] and NV centers [47].

The combination of the decoding $\boldsymbol{U}_d$, the QND measurement of qubits 2 and 3 and the re-encoding effectively implements two error syndrome measurements that can be rewritten as $\boldsymbol{S}_a = \boldsymbol{\sigma}_{x,1}\boldsymbol{\sigma}_{x,2}\boldsymbol{I}_3$ and $\boldsymbol{S}_b = \boldsymbol{I}_1\boldsymbol{\sigma}_{x,2}\boldsymbol{\sigma}_{x,3}$. These two error syndrome compare the values of $\boldsymbol{\sigma}_x$ on two qubits and return +1 if they are the same and -1 if they are different, thus revealing unambiguously what error happened. These two operators are called the *stabilizers* of the code [48]. They are constructed such that they commute with each other and such that each error state is an eigenstate of the stabilizers with a different set of eigenvalues. The stabilizers of a three-qubit code can be measured using ancillary qubits and, therefore, without having to decode the state at any moment. The direct measurement of the stabilizers of three-qubit codes has been realized in superconducting qubits [49] and NV centers [50]. The measurement of these stabilizers play a major part in our stabilization of GKP codes in chapter 5.

Using this example, can we find a general way to construct QEC codes? We see that the

main idea behind the construction of this three-qubit code was that two orthogonal states remain orthogonal after an error. This condition enables QEC and is known as the *Knill-Laflamme criterion* [51]. Formally, it can be written by using the code projector $\mathbf{\Pi}_C$. For a code that implements a single logical qubit, it is given by

$$\mathbf{\Pi}_C = |0\rangle_L \langle 0|_L + |1\rangle_L \langle 1|_L . \tag{1.56}$$

A set of evolution operators creates errors that can be exactly recovered if we have

$$\mathbf{\Pi}_C \mathbf{E}_i^\dagger \mathbf{E}_j \mathbf{\Pi}_C = c_{ij} \mathbf{\Pi}_C, \tag{1.57}$$

where c_{ij} is a Hermitian matrix. This criterion is represented in Fig. 1.3. We will illustrate this property further by considering the more complex case of amplitude damping.

1.3.2 Amplitude damping

The action of amplitude damping is more complicated that a rotation of the Bloch vector along one axis and, therefore, it highlights interesting features of quantum mechanics and QEC. On a single-qubit, amplitude damping has two possible consequences. The first consists simply in the transfer of an excitation from a qubit to its environment, which annihilates the excitation in the qubit. The second one is the result of not observing the transfer of one excitation from the qubit to the environment. In this latter situation, the qubit does not remain in its initial state. Instead, the probability that the qubit was excited in the first place decreases and the probability that it was not excited increases. This backaction has non-trivial consequences on QEC.

Let us first try to build a code that respects the Knill-Laflamme criterion for the loss of an excitation in one qubit. We use a compact notation where the excitation of a qubit is represented by a box that contains a particle ($|\blacksquare\rangle$) or that is empty ($|\square\rangle$). D. Leung *et al.* [52] found a simple four qubit code that respect our condition, with logical states

$$|0\rangle_L = \frac{|\blacksquare\blacksquare\rangle + |\boxplus\rangle}{\sqrt{2}}, \qquad |1\rangle_L = \frac{|\blacksquare\blacksquare\rangle + |\blacksquare\blacksquare\rangle}{\sqrt{2}}. \tag{1.58}$$

Let us first verify that these states remain orthogonal when an excitation leaves one box. In the following table, we indicate in the left column in what box an excitation has been annihilated.
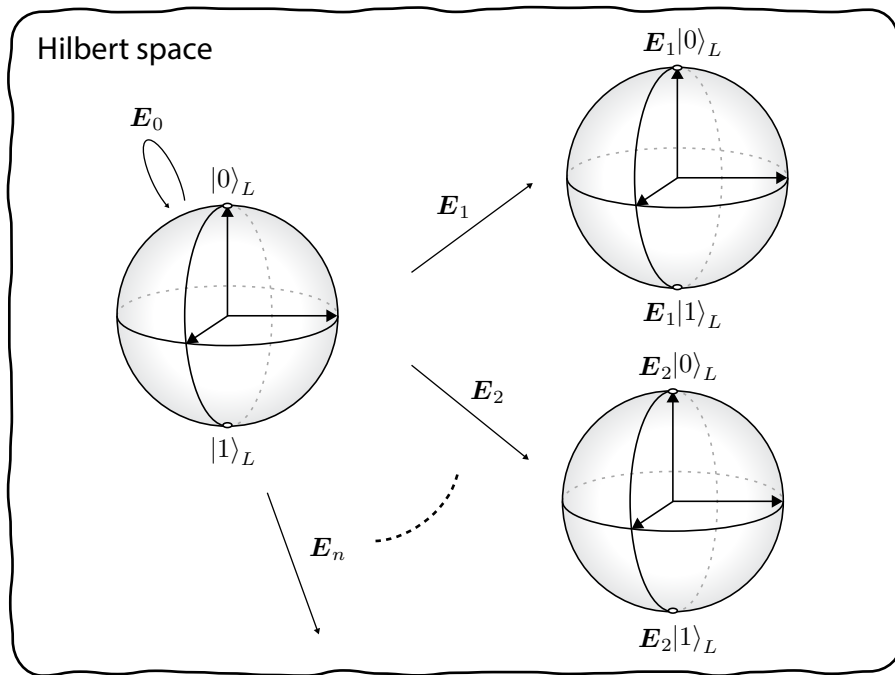
Figure 1.3: Schematic representation of the Knill-Laflamme criterion. One logical qubit is encoded in a manifold of a larger Hilbert space. For an error to be recoverable, the operators E_i must necessary bring the manifold of logical states either to itself or to an orthogonal one within the available Hilbert space. Two different errors must bring the logical states to two different manifolds of this Hilbert space.

emptied box	resulting $|0\rangle_L$	resulting $|1\rangle_L$
▨	$|�ध\rangle$	$|▨\rangle$
▨	$|▨\rangle$	$|▨\rangle$
▨	$|▨\rangle$	$|▨\rangle$
▨	$|▨\rangle$	$|▨\rangle$

This analysis seems to indicate that two orthogonal states are indeed transformed into two orthogonal states. However, one needs to consider that when no excitation is detected, the weights between the two states that compose $|0\rangle_L$ become unbalanced, and that the relative weights of $|0\rangle_L$ and $|1\rangle_L$ are also changed. Even worse, when one excitation is detected, it

means that three excitations were not detected, which also changes the relative weights of the resulting $|0\rangle_L$ and $|1\rangle_L$ of the previous table. It seems as if amplitude damping errors always affect all the qubits. However, we carefully chose $|0\rangle_L$ and $|1\rangle_L$ such that they both have, on average, two excitations. This way, a careful analysis using the set of evolution operators $\boldsymbol{E}_i$ shows that we have

$$\boldsymbol{\Pi}_C \boldsymbol{E}_i^\dagger \boldsymbol{E}_j \boldsymbol{\Pi}_C = c_{ij} \boldsymbol{\Pi}_C + O(\Gamma_\downarrow dt), \tag{1.59}$$

where $\Gamma_\downarrow$ is the order of magnitude of the amplitude damping rate of any qubit. It has been shown that, in this case, the fidelity of the state can be restored to order $1 - O\left((\Gamma_\downarrow dt)^2\right)$. This *approximate QEC condition* has then been generalized and is the basis of the bosonic binomial code [28].

1.3.3 Fault-tolerance

Our analysis of QEC considers that quantum information is already encoded non-locally in the state of several qubits and that, once encoded, various qubits do not interact anymore. This way, when an error occurs on a single qubit, it does not propagate to the rest of the quantum computer. This situation is obviously idealized. In reality, there are multiple occasions for errors to propagate. The first one is when the qubits interact to create entangling gates. The second one is when the qubits are supposingly idle, but have finite interactions among themselves.

In the first case, the propagation of errors happens on a similar timescale as the gate itself. To see this, let us imagine that we want to apply a CNOT gate but that a spurious rotation $\sigma_{x,1}$ happened. Our unitary is now $\text{CNOT}\boldsymbol{\sigma}_{x,1} = \text{CNOT}\boldsymbol{\sigma}_{x,1}(\text{CNOT})^\dagger\text{CNOT}$. By writing the CNOT gate as $\text{CNOT} = \frac{1}{2}\left(\boldsymbol{I}_1 + \boldsymbol{\sigma}_{z,1}\right)\boldsymbol{I}_2 + \frac{1}{2}\left(\boldsymbol{I}_1 - \boldsymbol{\sigma}_{z,1}\right)\boldsymbol{\sigma}_{x,2}$, we have

$$\text{CNOT}\boldsymbol{\sigma}_{x,1}(\text{CNOT})^\dagger\text{CNOT} = \boldsymbol{\sigma}_{x,1}\boldsymbol{\sigma}_{x,2}\text{CNOT}. \tag{1.60}$$

Instead of applying the gate correctly, we applied it and induced a second error.

In the second case, two qubits can have residual interactions from the fact that the interactions to create the gates cannot be turned off completely. This issue is addressed as much as possible by using parametric interactions, meaning that the strength of the interaction can be tuned with a parameter that the experimentalist controls. This principle is applied to two-qubit gates in trapped ions where the gates are controlled with lasers that can be turned on and off [53, 54], but also in superconducting circuits where interactions can be tuned

using a voltage [55] or microwave drives [33, 34]. In this thesis, we describe new parametric interactions that are useful for QEC with superconducting microwave cavities.

Amazingly, quantum computing can be *fault-tolerant* despite the propagation of errors. For this, the QEC code must take into account this possible propagation. As long as the errors induced by the manipulation of qubits are not created faster than the code can correct, it is possible to concatenate more layers of QEC and get an arbitrary fidelity for the quantum computation. For this, it requires that all possible gates and measurements have an accuracy that is below a *threshold* that depends on the code used to perform the quantum computation [56].

In one of such codes, called the surface code [57], the qubits are arranged on an array and can interact only with their nearest neighbour, while the logical states are fully delocalized over the full grid. This way, when an error occurs, it only propagates to the nearest qubits and does not contaminate the entire array. If these errors propagate slowly enough, they can be detected and their progression can be stopped. However, with current technologies, it would take of order 1000 physical qubits to obtain one logical qubit that would be good enough to perform a useful quantum computation such as Shor's algorithm.

1.4   Quantum harmonic oscillator and its representations

Creating a logical qubit out of many physical qubits is challenging because it requires a good control of many moving parts that can interact. This difficulty mainly stems from the fact that we are trying to encode quantum information in a global state of many distinguishable quantum systems by controlling them individually. In order to reduce this overhead, this approach can be replaced by trying to control the collective excitations of an ensemble of undistinguishable non-interacting particles such as bosons. The main drawback of this approach is that creating non-trivial states of non-interacting bosons is difficult, yet necessary to process quantum information. As we mentioned previously, this challenge was investigated for photons and phonons in the fields of quantum optics, CQED, cQED, trapped ions and nano-mechanics. This thesis will present some novel ways to control the state of superconducting microwave cavities. Here, we would like to introduce general concepts about the quantum harmonic oscillator, which describe well the physics of photons trapped in a superconducting microwave cavity. We will introduce phase-space representations, which help visualizing the states of a harmonic oscillator.

A quantum harmonic oscillator (QHO) is built as an analogue of the classical harmonic oscillator, where the classical variables q, the position, and p, the momentum, are replaced

by observables $\boldsymbol{q}$ and $\boldsymbol{p}$, whose commutation relation is given by the canonical

$$[\boldsymbol{q}, \boldsymbol{p}] = i\hbar. \tag{1.61}$$

The evolution of a QHO is given by a Hamiltonian that has two parameters: the angular frequency at which the energy oscillates ω and a mass m, such that

$$\boldsymbol{H} = \frac{1}{m}\frac{\boldsymbol{p}^2}{2} + m\omega^2\frac{\boldsymbol{q}^2}{2}. \tag{1.62}$$

To diagonalize this Hamiltonian, we construct two ladder operators $\boldsymbol{a}$ and $\boldsymbol{a}^\dagger$ that are linear combinations of $\boldsymbol{q}$ and $\boldsymbol{p}$ and such that their commutation relation is $[\boldsymbol{a}, \boldsymbol{a}^\dagger] = \boldsymbol{I}$. With these constraints, we have

$$\boldsymbol{a} = \sqrt{\frac{m\omega}{2\hbar}}\left(\boldsymbol{q} + \frac{i}{m\omega}\boldsymbol{p}\right), \tag{1.63}$$

such that

$$\boldsymbol{H} = \hbar\omega\left(\boldsymbol{a}^\dagger\boldsymbol{a} + \frac{1}{2}\right). \tag{1.64}$$

The eigenstates of this Hamiltonian are Fock states, which have a definite number of excitations n and are noted $|n\rangle$. By inverting the definition of $\boldsymbol{a}$, we find the characteristic value of the position and the momentum when there is one excitation in the QHO, and we get

$$\boldsymbol{q} = \sqrt{\frac{\hbar}{2m\omega}}\left(\boldsymbol{a}^\dagger + \boldsymbol{a}\right), \qquad \boldsymbol{p} = i\sqrt{\frac{\hbar m\omega}{2}}\left(\boldsymbol{a}^\dagger - \boldsymbol{a}\right). \tag{1.65}$$

In order to describe the state of a QHO in phase-space, we define two dimensionless observables that are a "position" $\boldsymbol{Q}$ and a "momentum" $\boldsymbol{P}$, defined as

$$\boldsymbol{Q} = \frac{\boldsymbol{a} + \boldsymbol{a}^\dagger}{2}, \qquad \boldsymbol{P} = \frac{\boldsymbol{a} - \boldsymbol{a}^\dagger}{2i}. \tag{1.66}$$

These two operators are sometimes referred to as the quadrature operators, and we have chosen the convention of quantum optics (other conventions vary by a factor $\sqrt{2}$). From now on, position and momentum will only refer to these dimensionless observables. The com-

mutation relation of these operators is

$$[\boldsymbol{Q}, \boldsymbol{P}] = \frac{i}{2}. \tag{1.67}$$

The eigenstates of the position (resp. momentum) with a definite position Q (resp. momentum P) are noted $|Q\rangle$ (resp. $|P\rangle$). The two continuous variables Q and P are Fourier transform of one another and therefore respect the uncertainty principle

$$\Delta Q \Delta P \geq \frac{1}{4} \tag{1.68}$$

With this convention, the Hamiltonian of a QHO is

$$\boldsymbol{H} = \hbar\omega \left(\boldsymbol{Q}^2 + \boldsymbol{P}^2\right). \tag{1.69}$$

So far, we have found three bases to represent an arbitrary state of a harmonic oscillator: its position, its momentum or its excitation number. However, finding the complex coefficients that make the density matrix in these bases is not easy experimentally. Instead, we use phase-space representations that we can directly measure. These representations require the implementations of the displacement operator, defined as

$$\boldsymbol{D}(\alpha) = e^{\alpha \boldsymbol{a}^\dagger - \alpha^* \boldsymbol{a}}. \tag{1.70}$$

In fact, in superconducting circuits, this operator is simply the unitary evolution of a superconducting cavity subject to a microwave drive. The phase and the amplitude of the parameter α are set by the amplitude and the phase of this drive. This operator allows the creation of coherent states $|\alpha\rangle$, that are equivalently defined as

$$\boldsymbol{D}(\alpha)|0\rangle = |\alpha\rangle, \qquad \boldsymbol{a}|\alpha\rangle = \alpha|\alpha\rangle. \tag{1.71}$$

In the convention we have chosen for the position and momentum, if α is real then its average position is $\langle\alpha|\boldsymbol{Q}|\alpha\rangle = \alpha$ and its average momentum is 0, while if α is purely imaginary, its average momentum is α and its average position is 0. More generally, we have

$$\langle\boldsymbol{Q}\rangle = \mathrm{Re}(\alpha), \qquad \langle\boldsymbol{P}\rangle = \mathrm{Im}(\alpha). \tag{1.72}$$

From this, we can deduce that its average photon number is

$$\langle \boldsymbol{a}^\dagger \boldsymbol{a} \rangle = \langle (\boldsymbol{Q}^2 + \boldsymbol{P}^2) \rangle = |\alpha|^2 \,. \tag{1.73}$$

Moreover, a coherent state is Gaussian in Q and P with a standard deviation $\sigma = \frac{1}{2}$, which maximizes the uncertainty relation given by equation 1.68. Using the properties of the displacement operator, we build two phase-space representation that can be measured experimentally.

1.4.1 Phase-space representations

In classical mechanics, the coordinates of phase-space are position and momentum. The value of a point in phase-space is a direct measurement of the position and the momentum of a state. A large ensemble of particles will have a phase-space distribution which represents the statistical features of the distribution of the particles. In quantum mechanics, the state of a single particle cannot have a precise position and momentum. Therefore, a point in phase-space must use another property of the state, while retaining the essential features of the classical phase-space. As we will see, a special representation, called the Wigner function, gives an intuitive picture of the properties of the states of a harmonic oscillator. In order to build this function, we must first construct a function called the characteristic function. As we will see, these two representations are Fourier tranform of one another and carry the same information. These two functions are usually measured using an ancilla two-level system. We will see that, depending on the coupling between this ancilla and the QHO, it is sometimes more convenient to measure the characteristic function and to deduce the Wigner function from it.

Characteristic function

For a pure state, the characteristic function $C_s(\tilde{\alpha})$ is defined as the overlap between a state $|\psi\rangle$ and a copy of this state displaced by $\tilde{\alpha}$, such that

$$C_s(\tilde{\alpha}) = \langle \psi | \boldsymbol{D}(\tilde{\alpha}) | \psi \rangle \,. \tag{1.74}$$

The subscript s of the characteristic function comes from the fact that it is defined for the "symmetric" ordering of $\boldsymbol{D}(\tilde{\alpha})$, compared to the "normal" or "anti-normal" ordering (for a discussion on ordering, see J.M. Raimond and S. Haroche [23]). Note that this function is the expectation value of a displacement. More generally, for a density matrix ρ, the characteristic

function is the sum of the characteristic functions of the states that statistically compose ρ, such that

$$C_s(\tilde{\alpha}) = \langle \boldsymbol{D}(\tilde{\alpha}) \rangle = \mathrm{Tr}(\boldsymbol{D}(\tilde{\alpha})\rho). \tag{1.75}$$

In general, $C_s(\tilde{\alpha})$ is a complex number with $C_s(-\tilde{\alpha}) = \langle \boldsymbol{D}(-\tilde{\alpha}) \rangle = \langle \boldsymbol{D}^\dagger(\tilde{\alpha}) \rangle = C_s(\tilde{\alpha})^*$. Therefore, if ρ has symmetric wavefunctions in P and Q, then $\mathrm{Im}(C_s) = 0$.

The advantage of measuring the characteristic function is that it can be measured with a conditional displacement between an ancilla two-level system and the cavity. In superconducting circuits, one can create strong conditional displacements even if the two-level system is only weakly coupled to the cavity, as is discussed in chapter 3 and 5. We denote a conditional displacement

$$\boldsymbol{D}(\tilde{\alpha}\boldsymbol{\sigma}_z) = e^{(\tilde{\alpha}\boldsymbol{a}^\dagger - \tilde{\alpha}^*\boldsymbol{a})\boldsymbol{\sigma}_z} \tag{1.76}$$

$$= \frac{1}{2}((\boldsymbol{D}(\tilde{\alpha}) + \boldsymbol{D}(-\tilde{\alpha}))\boldsymbol{I} + (\boldsymbol{D}(\tilde{\alpha}) - \boldsymbol{D}(-\tilde{\alpha}))\boldsymbol{\sigma}_z). \tag{1.77}$$

In order to measure the characteristic function using an ancilla two-level system, we initialize the ancilla in $|+\rangle$ and use a conditional displacement. A simple calculation done in appendix A shows that

$$\mathrm{Tr}_c\left(\boldsymbol{D}\left(\frac{\tilde{\alpha}}{2}\boldsymbol{\sigma}_z\right)\rho_c \otimes |+\rangle\langle +| \boldsymbol{D}\left(-\frac{\tilde{\alpha}}{2}\boldsymbol{\sigma}_z\right)\right) = \frac{\boldsymbol{I} + \mathrm{Re}(C_s(\tilde{\alpha}))\boldsymbol{\sigma}_x + \mathrm{Im}(C_s(\tilde{\alpha}))\boldsymbol{\sigma}_y}{2},$$

$$\tag{1.78}$$

where Tr_c is the partial trace over the cavity. This way, measuring the ancilla along $\boldsymbol{\sigma}_x$ gives the real part of the characteristic function, while measuring it along $\boldsymbol{\sigma}_y$ gives its imaginary part.

The characteristic function represents only the correlations between a state and its displaced copy and it is not easy to interpret for an arbitrary state. We give some basic examples of characteristic functions that are relevant experimentally.

First, a displaced vacuum overlaps with the vacuum for small displacements and does not overlap for large displacements. Thus, the characteristic function of the vacuum state is

$$C_s^{|0\rangle}(\tilde{\alpha}) = \langle 0| \boldsymbol{D}(\tilde{\alpha}) |0\rangle = \langle 0|\tilde{\alpha}\rangle = e^{-\frac{|\tilde{\alpha}|^2}{2}}. \tag{1.79}$$

This is a 2D Gaussian with a standard deviation $\sigma = 1$. As vacuum is the steady-state

of a dissipative cavity, such a state can be used to calibrate the strength of a conditional displacement.

Second, we show that the characteristic function of a displaced state $D(\beta)\,|\psi\rangle$ can be deduced from the characteristic function of its corresponding undisplaced state $|\psi\rangle$. To see this, we write

$$C_s^{D(\beta)|\psi\rangle}(\tilde{\alpha}) = \langle\psi|\,D(-\beta)D(\tilde{\alpha})D(\beta)\,|\psi\rangle \tag{1.80}$$

$$= \langle\psi|\,D(-\beta)D(\beta)D(\tilde{\alpha})\,|\psi\rangle\,e^{2i\mathrm{Im}(\tilde{\alpha}\beta^*)} \tag{1.81}$$

$$= C_s^{|\psi\rangle}e^{2i\mathrm{Im}(\tilde{\alpha}\beta^*)}, \tag{1.82}$$

where we have used the commutation relation of two displacements $D(\tilde{\alpha})D(\beta) = e^{2i\mathrm{Im}(\alpha\beta^*)}D(\beta)D(\tilde{\alpha})$. In particular, the characteristic function of a coherent state is related to the characteristic function of the vacuum state: its real part is a 2D Gaussian modulated with a cosine and its imaginary part is a 2D Gaussian modulated with a sine. The angular frequency of the modulation is always $\omega = 2|\beta|$. We represent the real part of their characteristic functions in Fig. 1.4.
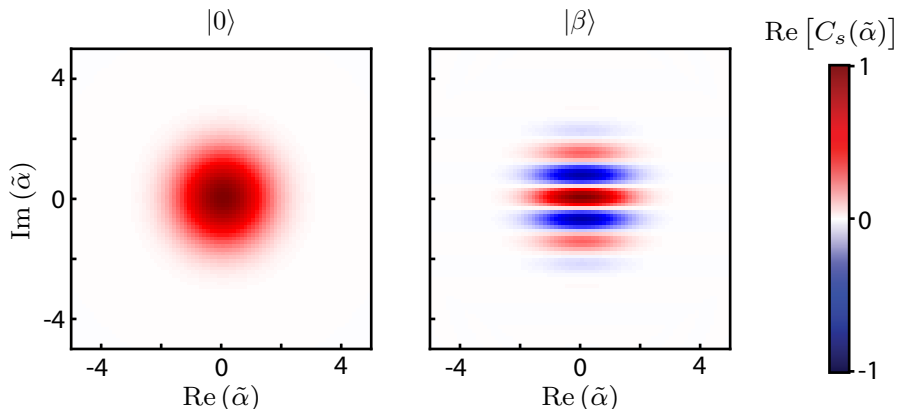
Figure 1.4: Real part of the characteristic functions $C_s(\tilde{\alpha})$ of the vacuum state (left) and a displaced vacuum state (right). For the vacuum, $C_s(\tilde{\alpha})$ is real and is a 2D Gaussian with $\sigma = 1$. For a coherent state with real amplitude $\beta = 2$, which is a displaced vacuum, the real part of C_s is similar to the one of the vacuum state with a cosine modulation along $\mathrm{Im}(\tilde{\alpha})$, with an angular frequency 2β. The imaginary part (not represented) is similar with a sine modulation instead.

As we will see in chapter 5, the main advantage of the characteristic function is that it can characterize the state of a cavity with a weakly coupled ancilla two-level system. Moreover, it is useful to characterize states that display correlations in phase-space, such as grid-states, also called GKP states.

Wigner function

The Wigner function is the most widely used phase-space representation of the state of an harmonic oscillator because some of its features are reminiscent of the classical phase-space. The Wigner function can be defined as the 2D Fourier transform of the characteristic function

$$W(\alpha) = \frac{1}{\pi^2} \int d^2\tilde{\alpha} \, C_s(\tilde{\alpha}) e^{\alpha\tilde{\alpha}^* - \alpha^*\tilde{\alpha}}. \tag{1.83}$$

We now want to highlight the similarities between the Wigner function and the classical phase-space distribution. First, because we have $C_s(-\tilde{\alpha}) = C_s^*(\tilde{\alpha})$, the Wigner function is always real. Then, this function is normalized:

$$\int d^2\alpha \, W(\alpha) = C_s(0) = 1. \tag{1.84}$$

In order to fully relate the Wigner function to its classical analogue, we rewrite it by introducing the position $Q = \mathrm{Re}(\alpha)$ and the momentum $P = \mathrm{Im}(\alpha)$. By expressing the characteristic function $C_s(\tilde{\alpha})$ in the position basis, a derivation done in the appendix of *Exploring the quantum* [23] leads to the familiar expression of the Wigner function

$$W(Q, P) = \frac{1}{\pi} \int du \, e^{-2iPu} \langle Q + u/2 | \, \rho \, | Q - u/2 \rangle. \tag{1.85}$$

Importantly, this expression can be inverted to get any coefficient of ρ, expressed here in the position basis $|Q\rangle$, such that

$$\langle Q + u/2 | \, \rho \, | Q - u/2 \rangle = \int dP \, e^{2iPu} W(Q, P). \tag{1.86}$$

This expression of ρ indicates that all the information on the state of a QHO can be extracted from the Wigner function. The Wigner function is a complete tomography of the state of the QHO, and because the characteristic function is its Fourier transform, it is an equivalently

complete tomography of the QHO.

Finally, with this expression of the Wigner function, we are able to see that its marginal distributions, i.e. the integrals of the Wigner along one variable, are probability distributions (they are positive and normalized to 1 because of the normalization of the Wigner function). In particular, for the position, we see that by setting $u = 0$ in equation 1.86, we have the probability $P(Q)$ for the oscillator to be have a position Q with

$$P(Q) = \langle Q| \rho |Q\rangle = \int dP\, W(Q, P). \qquad (1.87)$$

Similarly, by doing a similar analysis with the characteristic function expressed in the momentum basis, we have

$$P(P) = \langle P| \rho |P\rangle = \int dQ\, W(Q, P). \qquad (1.88)$$

In fact, the integral of the Wigner function along any axis is a positive probability distribution in a basis that is a rotation of the position basis. The momentum basis P corresponds to a special case when this rotation is $\pi/2$.

In Fig. 1.5, we represent the Wigner functions of a few states that are relevant to this thesis, together with their marginal distributions. First, we represent the Wigner function for a classical state: a statistical mixture of two coherent states

$$\rho = \mathcal{N}(|\beta\rangle \langle\beta| + |-\beta\rangle \langle-\beta|), \qquad (1.89)$$

with $\beta = 2$, and $\mathcal{N}$ is a normalization factor close to 0.5. The probability distributions of the position and momentum of these states are Gaussians and their width illustrates the Heisenberg uncertainty principle. The fact that the Wigner function of such a state is always positive shows that this state is entirely classical. The situation is different in Fig. 1.5(b), where we represent the Wigner function of a so-called *Schrödinger cat state*, given by

$$|\psi\rangle = \mathcal{N}(|\beta\rangle + |-\beta\rangle). \qquad (1.90)$$

For this state, the Wigner functions displays "fringes" with a Gaussian envelope around 0. This interference pattern results in a momentum distribution that is not Gaussian. Finally, we introduce squeezed states, which have a larger uncertainty than a coherent state along one quadrature (here the momentum) and a smaller one along the oorthogonal quadrature (here

the position). A squeezed vacuum can be generated using the unitary

$$\boldsymbol{S}(r) = e^{\frac{1}{2}\left(r^*\boldsymbol{a}^2 - r\boldsymbol{a}^{\dagger 2}\right)}. \tag{1.91}$$

In particular, a position state $|Q\rangle$ is a coherent state that has been infinitely squeezed along its position. On Fig. 1.5(c), we plot a superposition of two squeezed states

$$|\psi\rangle = \mathcal{N}(\boldsymbol{D}(-\beta) + \boldsymbol{D}(\beta))\boldsymbol{S}(r)|0\rangle. \tag{1.92}$$

This superposition has similar features as the Schrödinger cat state where the envelope of the fringes is replaced by the envelope of a squeezed state.
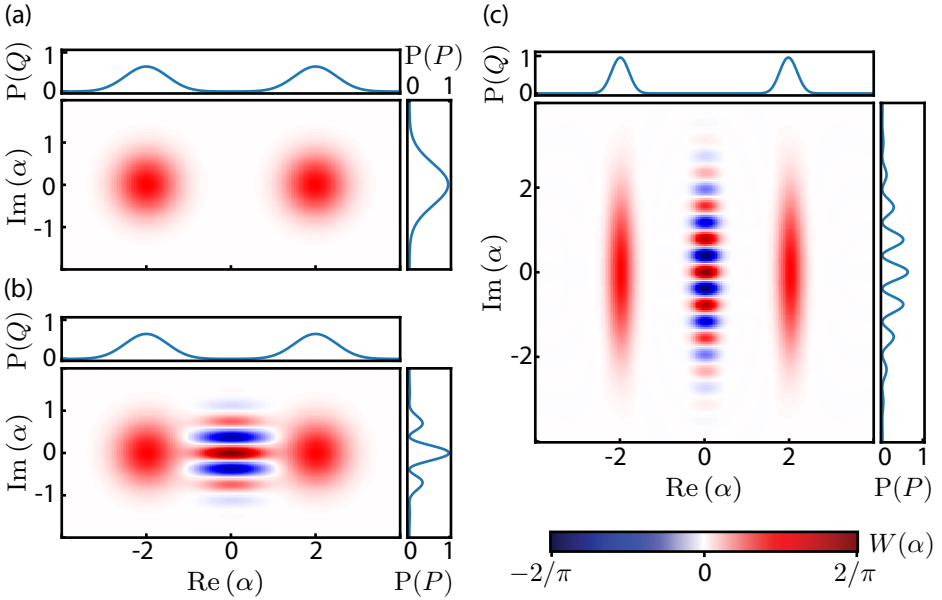
Figure 1.5: Examples of Wigner functions and their marginal distributions. Wigner functions of a statistical mixture of two coherent states $|\pm\beta\rangle\langle\pm\beta|$ (a), a superposition of two coherent states $|\pm\beta\rangle$(b), and a superposition of two squeezed states $\boldsymbol{D}(\pm\beta)\boldsymbol{S}(r)|0\rangle$(c), with $r = 0.9$, and $\beta = 2$. See text for more description.

Lastly, we give a last expression of the Wigner function that shows how it can be experimentally measured using an ancilla two-level system [29, 58, 59]. From equation 1.85, we

rewrite

$$e^{-iPu}\left|Q - u/2\right\rangle = e^{-iQP}\boldsymbol{D}(Q + iP)\left|-u/2\right\rangle \tag{1.93}$$

$$\left\langle Q + u/2\right|e^{-iPu} = \left\langle u/2\right|\boldsymbol{D}(-Q - iP)e^{iQP}, \tag{1.94}$$

such that, by writing $\alpha = Q + iP$, we get

$$W(\alpha) = \frac{1}{\pi}\int du\,\left\langle u/2\right|\boldsymbol{D}(-\alpha)\rho\boldsymbol{D}(\alpha)\left|-u/2\right\rangle \tag{1.95}$$

$$= \frac{1}{\pi}\int du\,\left\langle u/2\right|\boldsymbol{D}(-\alpha)\rho\boldsymbol{D}(\alpha)\boldsymbol{\mathcal{P}}\left|u/2\right\rangle \tag{1.96}$$

$$= \frac{2}{\pi}\langle\boldsymbol{D}(\alpha)\boldsymbol{\mathcal{P}}\boldsymbol{D}(-\alpha)\rangle, \tag{1.97}$$

where we have introduced the parity operator $\boldsymbol{\mathcal{P}}$, which takes $|Q\rangle$ to $|-Q\rangle$ and $|P\rangle$ to $|-P\rangle$. Equivalently, we have $\boldsymbol{\mathcal{P}} = e^{i\pi\boldsymbol{a}^\dagger\boldsymbol{a}}$. The Wigner function can be defined as the expectation value of the displaced parity operator. In appendix A, we show that this expectation value can be measured using an ancilla two-level system coupled to the QHO with a rotation of the two-level system, conditioned on the excitation number of the QHO. We first initialize the ancilla in a state $|+\rangle\langle+|$, and after the interaction, the state of the qubit is given by

$$\mathrm{Tr}_c(e^{-i\pi\boldsymbol{a}^\dagger\boldsymbol{a}\sigma_z/2}(\boldsymbol{D}(\alpha)\rho_c\boldsymbol{D}(-\alpha))\left|+\right\rangle\left\langle+\right|e^{i\pi\boldsymbol{a}^\dagger\boldsymbol{a}\sigma_z/2})$$
$$= \frac{\boldsymbol{I} + \langle\boldsymbol{D}(\boldsymbol{\alpha})\boldsymbol{\mathcal{P}}\boldsymbol{D}(-\boldsymbol{\alpha})\rangle\boldsymbol{\sigma}_x}{2}. \tag{1.98}$$

The value of the Wigner function can be read directly from the expectation value of $\boldsymbol{\sigma}_x$ of the qubit, up to the normalization factor. When we do not calculate the probability distributions when we display a Wigner function, we omit this factor. Notice here that the Wigner function can take negative values, which indicates that it deviates from its classical analogue. Nevertheless, the marginal distributions of the Wigner function are always positive and are true probability distributions. This measurement of the Wigner function relies on an interaction between the number of excitations of the QHO and $\boldsymbol{\sigma}_z$ of the ancilla two-level system. This type of interaction is ubiquitous across various quantum systems and is called a dispersive coupling. It arises naturally when a two-level system and a QHO are coupled through a Jaynes-Cummings interaction and that they are

1.4.2 Dissipation of a quantum harmonic oscillator

One advantage to use the excitations of a bosonic mode to encode quantum information is that their dissipation is simpler than the dissipation of distinguishable qubits, while still providing a Hilbert space that is large enough to perform QEC. When the QHO is maintained at low temperature ($k_b T \ll \hbar\omega$), the dissipation is dominated by the absorption of one excitation by the environment. This dissipation is similar to the amplitude damping, where the operator $\boldsymbol{\sigma}_-$ is replaced by the bosonic annihilation operator $\boldsymbol{a}$. The dynamics of the density matrix of a QHO is thus well described by the master equation

$$\partial_t \rho = \frac{\kappa}{2} \left(2\boldsymbol{a}\rho\boldsymbol{a}^\dagger - \boldsymbol{a}^\dagger\boldsymbol{a}\rho - \rho\boldsymbol{a}^\dagger\boldsymbol{a} \right), \tag{1.99}$$

where κ is the rate at which a single excitation is absorbed by the environment. Equivalently, we get the operator-sum representation to first order in dt

$$\rho(t + dt) = \left(\boldsymbol{I} - \frac{\kappa dt}{2}\boldsymbol{a}^\dagger\boldsymbol{a} \right) \rho(t) \left(\boldsymbol{I} - \frac{\kappa dt}{2}\boldsymbol{a}^\dagger\boldsymbol{a} \right) + \kappa dt \, \boldsymbol{a}\rho(t)\boldsymbol{a}^\dagger. \tag{1.100}$$

The effect of this dissipation is particularly interesting to study on a coherent state $|\alpha\rangle = \boldsymbol{D}(\alpha)|0\rangle$. First, when the environment does not absorb an excitation, the probability that the QHO is in a lower number state increases, while the probability that it is in a higher number state decreases. However, the coherent state is not deformed, its amplitude simply gets renormalized, such that

$$|\alpha(t)\rangle = \left| \alpha e^{-\frac{\kappa t}{2}} \right\rangle. \tag{1.101}$$

When the environment absorbs an excitation, the annihilation operator $\boldsymbol{a}$ is applied. However, as we have seen, a coherent state is an eigenvector of $\boldsymbol{a}$, such that $\boldsymbol{a}|\alpha\rangle = \alpha|\alpha\rangle$. Paradoxically, when the environment measures an excitation, the coherent state is "frozen" for an infinitesimal amount of time. Thus, it is only when no energy is absorbed by the environment that the amplitude of the coherent state diminishes. While this seems to violate the conservation of energy, it is important to remember that a coherent state is not an eigenstate of the Hamiltonian, and thus does not have a definite energy. The effect of the environment is simply to update the statistical properties of the energy until its average is 0.

There are multiple QEC codes that use bosonic modes in order to correct against amplitude damping. We can categorize them in two groups: codes that use Fock-states and codes that use coherent states. The first type of codes was proposed the same year as the four-qubit

code we previously presented, by the same group, and proposes to use several bosonic modes in finite superpositions of Fock-states [9]. This work was adapted 20 years later into the binomial code that uses a single-bosonic mode and has the possibility to correct other types of errors [28].

The second type of codes is based on superpositions of coherent states, which corresponds to the codes that are investigated in this thesis. The original idea comes from the group of G. Milburn in 1998 where they proposed to use photonic Schrödinger cat states as a logical qubit, with

$$|0\rangle_L = \mathcal{N}(|\alpha\rangle + |-\alpha\rangle), \qquad |1\rangle_L = \mathcal{N}'(|\alpha\rangle - |-\alpha\rangle). \tag{1.102}$$

Notice that such states are also non-local: if a measurement localizes the state of the harmonic oscillator, the superposition is destroyed. These states are almost left unchanged under the deterministic part of amplitude damping, while the "jumps", which correspond to applying $\boldsymbol{a}$, are now bit-flips that can be corrected. The original paper proposed to correct for the deterministic part using the Kerr nonlinearity of a harmonic oscillator, together with a squeezing Hamiltonian, which stabilizes the two cat states without distinguishing between them (this idea was rediscovered recently and applied to superconducting circuits [60]).

More recently, it was realized that, by encoding quantum information in cat states that are orthogonal in phase-space, the action of $\boldsymbol{a}$ would lead to a jump to an orthogonal manifold, thus approximately satisfying the Knill-Laflamme criterion. By choosing the logical states to have the same excitation number parity, an error could then be detected with a change of parity [27]. The logical states are then

$$|0\rangle_L = \mathcal{N}(|\alpha\rangle + |-\alpha\rangle), \qquad |1\rangle_L = \mathcal{N}(|i\alpha\rangle + |-i\alpha\rangle). \tag{1.103}$$

Within a few years, it became possible to encode such states in superconducting microwave cavities using an ancilla two-level system [17, 26] and to correct errors [30].

Lastly, another QEC code using bosonic excitation is based on arrays of coherent states or, equivalently, superposition of squeezed states: the Gottesman-Kitaev-Preskill (GKP) codes [11]. Importantly, these codes take advantage of the structure of any possible errors at short times. To see this, we first notice that $\boldsymbol{a}$ can be decomposed, at short times, into a sum of

displacements

$$\sqrt{\kappa dt}\boldsymbol{a} \approx -\frac{i}{2}\left(e^{i\sqrt{\kappa dt/2}\boldsymbol{Q}} - e^{-i\sqrt{\kappa dt/2}\boldsymbol{Q}}\right) + \frac{1}{2}\left(e^{i\sqrt{\kappa dt/2}\boldsymbol{P}} - e^{-i\sqrt{\kappa dt/2}\boldsymbol{P}}\right)$$
$$= -\frac{i}{2}\left(\boldsymbol{D}(i\sqrt{\kappa dt/2}) + \boldsymbol{D}(-i\sqrt{\kappa dt/2})\right) + \frac{1}{2}\left(\boldsymbol{D}(\sqrt{\kappa dt/2}) + \boldsymbol{D}(-\sqrt{\kappa dt/2})\right).$$
$$(1.104)$$

In fact, it is possible to expand any evolution that is a finite polynomial in $\boldsymbol{a}$ and $\boldsymbol{a}^\dagger$ in term of a superposition of displacements. Thus, the GKP codes, which protect against shifts in phase-space to achieve QEC, protect against most errors. On top of providing a protected logical qubit, these codes easily implement the set of logical Clifford gates in a fault-tolerant manner.

1.5 Overview of this thesis

The main challenge facing bosonic codes is to find ways to control the bosonic modes. In this thesis, we experimentally investigate novel controls of superconducting microwave cavities using the nonlinearity of superconducting qubits, which is provided by the Josephson effect.

Chapter 2 describes the circuit quantum electrodynamics (cQED) architecture used experimentally. In particular, it provides a framework to treat driven and dissipative quantum circuits. For this, we describe the building blocks of our field, namely superconducting cavities and nonlinear superconducting circuits. Then, we consider how these building blocks interact between themselves, and how they interact with a transmission line. This description introduces the quantum Langevin equation and input-output theory. We will then describe how to treat external drives in order to create the novel controls used in this thesis.

Chapter 3 presents how to use such a driven-dissipative cQED architecture to read the state of superconducting qubits. We use data from our recent paper on the readout of superconducting qubits to illustrate the relevant notions of the measurement of a qubit. As we have seen in this introduction, the state of a QHO, and in particular of a superconducting cavity, can be measured using an ancilla qubit. By adding the possibility to read the state of a superconducting qubit, we are able to fully characterize the state of a superconducting microwave cavity.

Chapter 4 contains our first application of driven-dissipative dynamics to stabilize a bosonic code. In that experiment, we engineer a two-photon dissipation and combine it

with a two-photon drive to stabilize a manifold of the Schrödinger cat states presented in this introduction. The stabilization can protect this encoding against any error that conserves the excitation number parity, such as the deterministic part of the amplitude decay, but also dephasing or spurious Kerr effect. The projection of errors that do not conserve parity onto the stabilized manifold of cat states results in simple bit-flips within this encoding, which can be corrected with a three-qubit code, as presented in this introduction. Finally, we show that such a qubit can be controlled within the stabilized subspace using an effect called quantum Zeno dynamics.

Chapter 5 discusses our experimental work to stabilize codes that are grids of coherent states, also called GKP codes. For this, we introduce these codes and describe them in terms of stabilizers. In order to measure these stabilizers, we introduce a new driven interaction that results in a conditional displacement of a cavity, conditioned on the state of an ancilla qubit. This interaction can be strong while the residual dispersive interaction is very weak. We introduce a new Markovian protocol that we designed to stabilize these GKP codes in steady-states and show that we can perform the first deterministic creation of GKP states. Finally, we show that our protocol protects GKP codes against errors and slows the decoherence of these codes.

Chapter 6 concludes this thesis and discusses the fault-tolerance of the QEC codes presented. We discuss recent theoretical proposals that could lead to future experiments demonstrating fault-tolerant quantum computing. In particular, we characterize the stabilized Schrödinger cat states as half-stabilized qubits, or qubits with a noise bias (susceptible to only one error), while the errors that propagate during the stabilization of GKP codes can be mitigated by using such qubits with a noise bias.

2

Driven-dissipative circuit QED

Studying the properties of quantum mechanics and utilizing them to manipulate quantum information has been achieved with various physical systems that share similarities. In general, such experiments associate a non-linear quantum system with a well controlled environment. For example, in atomic physics the non-linearity stems from the spherical potential of the nucleus and the spin of the electron, and in quantum optics it stems from non-linear light-matter interactions, which enable photon counting, single-photon creation and the Kerr effect. Such systems have a characteristic energy $\hbar\omega$ and their environment is maintained at a temperature such that $k_b T \ll \hbar\omega$. Finally, to manipulate the state of such systems, their characteristic control time needs to be much smaller than their coherence time.

Superconductivity reduces the complex dynamics of the macroscopic number of particles that constitute a metal to the dynamics of a few quantum degrees of freedom that can be coherently manipulated. Such superconductors can be assembled into bespoken LC circuits with large quality factors. Moreover, the Josephson effect, which arises when Cooper pairs tunnel through an insulating barrier, provides a source of non-linearity that enables the manipulation of interesting quantum states. The development of some technologies have allowed superconducting circuits to become a possible platform to build a quantum computer. First, the use of lithographic techniques leads to the possibility to print circuits with a wide range of parameters. Second, dilution refrigerators are crucial to maintain the temperature of such systems below their superconducting critical temperature and well below the characteristic temperature of their resonance frequency. Lastly, superconducting circuits are controllable using commercially available low-noise microwave techniques.

In this chapter, we will develop a framework to describe the dynamics of superconducting circuits. For this, we will admit the circuit quantization, which can be found in other references [61, 62]. Instead, we will focus on the interaction of such circuits with their environment through the quantum Langevin equation and the input-output theory. From this, we will discuss how to treat drives acting on superconducting circuits.

2.1 Driven-dissipative superconducting LC oscillator

A simple example of superconducting circuit is the superconducting LC oscillator represented in Fig. 2.1(a). In this section, we describe individual LC oscillators then we describe the coupling of LC oscillators to transmission lines and the input-output formalism.

2.1.1 Single superconducting LC oscillator

An LC oscillator is composed of an inductance (L part) and a capacitance (C part). Similarly to the quantum harmonic oscillator, the Hamiltonian of such systems is characterized by two parameters: the inductance L and the capacitance C. The inductive energy stems from the fact that charges moving in a conductor create a magnetic field which tends to oppose changes in current. The capacitive energy comes from the electrostatic energy between two distant pieces of superconductors that have a different number of charges.

The dynamics of this system is described with two dimensionless observables. The first one, φ, can be thought of as the number of reduced flux quanta threaded through the loops that make the inductance, such that the total magnetic flux observable is $\phi = \phi_0 \, \varphi$, where $\phi_0 = \hbar/2e$ is the reduced magnetic flux quantum. The second one, $\boldsymbol{n}$, is the difference of number of charges on the two plates of the capacitor, where the charge is given in units $2e$, which is the charge of a Cooper pair. These two observables obey the canonical commutation relation

$$[\boldsymbol{\varphi}, \boldsymbol{n}] = i. \tag{2.1}$$

Note here that the nature of these two observables is more intricate than the simplistic presentation done here and their origin is rooted in the theory of superconductivity. With this choice of observables, the Hamiltonian of the superconducting LC oscillator is

$$\boldsymbol{H} = \frac{E_L}{2}\boldsymbol{\varphi}^2 + 4E_C\boldsymbol{n}^2, \tag{2.2}$$

where $E_L = \frac{\phi_0^2}{L} = \frac{\hbar^2}{4e^2 L}$ and $E_C = \frac{e^2}{2C}$. The capacitive energy was derived for the case where the number of charges is expressed in units of e, therefore a factor 4 appears in the Hamiltonian where the number of charges is expressed in units of $2e$. The convention for E_L comes from the equivalence between a superinductor and an array of Josephson junctions [62, 63].

This Hamiltonian can be rewritten using two standard circuit parameters: the angular
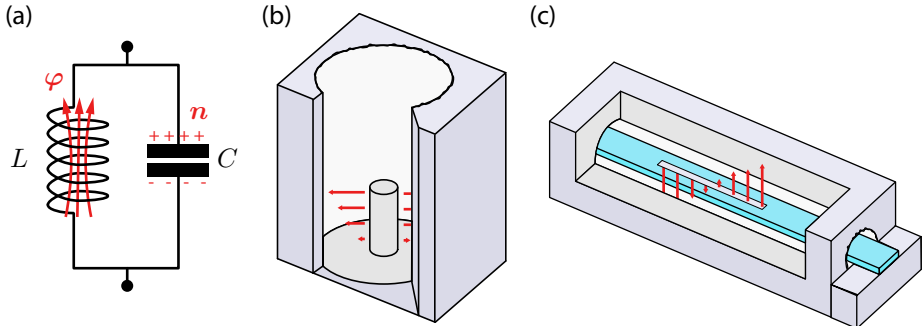
Figure 2.1: Schematic representation of LC circuits. (a) Lumped element representation of an LC circuit. The observable φ represents the number of magnetic flux quanta threaded through the loops forming the inductor (red arrows), while the observable n represents the difference in number of charges on the two superconducting islands (red + and -). (b) Schematic of a post-cavity. A reentrant aluminum post is at the bottom of an aluminum cylindrical cavity and implements a $\lambda/4$ resonator whose electric field is represented with red arrows. The hollow section on top of the post acts as a waveguide, such that the field is concentrated below the post. This way, the lossy seam at the top of the cylinder does not affect the quality factor of the resonator. Our schematic contains an open face for clarity. (c) Schematic of a coaxline resonator. A strip of aluminum is printed on a sapphire wafer (blue) and forms a $\lambda/2$ resonator within an aluminum tunnel. This tunnel acts as a waveguide for the field represented with red arrows, such that it does not propagate to the seams where the sapphire is held. The actual devices corresponding to these two schematics have a characteristic size of a few centimeters.

frequency ω and the impedance Z, defined as

$$\omega = \frac{\sqrt{8E_J E_C}}{\hbar} = \frac{1}{\sqrt{LC}}, \qquad Z_0 = \sqrt{\frac{L}{C}}, \tag{2.3}$$

such that the Hamiltonian has the form

$$\boldsymbol{H} = \hbar\omega \left(\left(\frac{R_Q}{Z_0} \right) \frac{\boldsymbol{\varphi}^2}{2} + \left(\frac{Z_0}{R_Q} \right) \frac{\boldsymbol{n}^2}{2} \right), \tag{2.4}$$

where we have introduced the reduced quantum of resistance for superconductors $R_Q = \frac{\hbar}{(2e)^2} \approx 1\,\text{k}\Omega$, and we have $R_Q/Z_0 = \sqrt{E_L/8E_C}$

We want to find ladders operators $\boldsymbol{a}$ and $\boldsymbol{a}^\dagger$ that are linear combinations of $\boldsymbol{\varphi}$ and $\boldsymbol{n}$ such that $[\boldsymbol{a}, \boldsymbol{a}^\dagger] = 1$ and such that its Hamiltonian is diagonal as described in the introduction

with equation 1.64. We find

$$\boldsymbol{a} = \sqrt{\frac{R_Q}{2Z_0}}\boldsymbol{\varphi} + i\sqrt{\frac{Z_0}{2R_Q}}\boldsymbol{n} \tag{2.5}$$

From this, we can make the dimensioned flux $\boldsymbol{\phi} = \phi_0\boldsymbol{\varphi}$ and charge $\boldsymbol{n}_Q = 2e\boldsymbol{n}$ observables appear explicitly. Thus, we can get the a physical sense of the zero point fluctuations of the magnetic flux and of the charge by writing $\boldsymbol{\phi} = \phi^{\mathrm{ZPF}}(\boldsymbol{a} + \boldsymbol{a}^\dagger)$ and $\boldsymbol{n}_Q = n_Q^{\mathrm{ZPF}}\frac{\boldsymbol{a}-\boldsymbol{a}^\dagger}{i}$, we get

$$\phi^{\mathrm{ZPF}} = \sqrt{\frac{\hbar Z_0}{2}} = \sqrt{\frac{Z_0}{2R_Q}}\,\phi_0, \tag{2.6}$$

$$n_Q^{\mathrm{ZPF}} = \sqrt{\frac{\hbar}{2Z_0}} = \sqrt{\frac{R_Q}{2Z_0}}\,2e. \tag{2.7}$$

We deduce that when the impedance of the resonator is large ($Z_0 \gg R_Q$), the zero point fluctuations of the magnetic flux are large compared to ϕ_0, while the fluctuations of the charge are small compared to $2e$, and the situation is reversed when the impedance is small compared to the flux quantum. The former situation is favored when a noisy environment couples to the flux of the circuit while the latter situation is favored when a noisy environment couples to the charge of the circuit.

In this thesis, we use exclusively the coupling to the charge degree of freedom of our circuits and thus we use only low impedance circuits. Such resonators are easy to engineer by using superconducting aluminum as a conductor and the vacuum or sapphire as a dielectric for the capacitors. The two types of LC resonators we use are "$\lambda/4$" post-cavities [64] and "$\lambda/2$" stripline resonators on sapphire within an aluminum tunnel, also called "coaxline" [65]. We represent schematically such devices in Fig. 2.1(b) and (c).

2.1.2 Coupling to the environment: input-output theory

The formalism of the operator-sum representation and of the Lindblad master equation are appropriate to describe uncontrolled interactions with the environment and QEC. However, part of the environment is controlled by the experimentalist with drives and by looking at the response of the system. Thus, in order to model an experiment, it is important to develop another formalism, called input-output theory. In this thesis, we highlight the parts of this formalism that are important for the experiments carried in the following chapters. More detailed derivations are available in the references [62, 66, 67].

The input-output formalism extends the Heisenberg equations to take into account interactions between the system and its environment. The environment of the circuit itself is modeled by an impedance that can depend on the frequency. Within the Caldeira-Leggett model, this impedance can be represented by an infinite amount of LC circuits with all possible resonance frequencies and whose impedance depends possibly on the frequency. The Hamiltonian of the environment is thus described with

$$\boldsymbol{H}_{\text{env}} = \hbar \int_0^\infty d\omega' \, \omega \boldsymbol{b}^\dagger(\omega) \boldsymbol{b}(\omega), \tag{2.8}$$

where $\boldsymbol{b}(\omega)$ is the annihilation operator for a bath mode at frequency ω, whose commutation relations are

$$[\boldsymbol{b}(\omega), \boldsymbol{b}^\dagger(\omega')] = \delta(\omega - \omega'). \tag{2.9}$$

Notice that the delta function is dimensioned, such that $\boldsymbol{H}_{\text{env}}$ has the dimension of an energy.

In this thesis, the systems we consider are always coupled to their environment through a capacitance: the inner conductor of a coaxial cable ends close to the LC circuit we study but is not galvanically coupled to it. This way, the charges on each of these resonators influence each other, such that the coupling Hamiltonian is given by

$$\boldsymbol{H}_{\text{int}} = \frac{\hbar}{\sqrt{2\pi}} \int_0^\infty d\omega' \, \sqrt{\kappa(\omega')} \boldsymbol{n} \frac{\boldsymbol{b}(\omega') - \boldsymbol{b}^\dagger(\omega')}{i} \tag{2.10}$$

$$= -\frac{\hbar}{\sqrt{2\pi}} \int_0^\infty d\omega' \, \sqrt{\kappa(\omega')} (\boldsymbol{a} - \boldsymbol{a}^\dagger)(\boldsymbol{b}(\omega') - \boldsymbol{b}^\dagger(\omega')). \tag{2.11}$$

Here, we perform the rotating wave approximation (RWA), which consists in neglecting the terms that oscillate rapidly. We will justify this approximation later. Note that a treatment of the coupling to the environment without using the RWA is possible [68]. With this approximation, the interaction Hamiltonian is simply

$$\boldsymbol{H}_{\text{int}} = \frac{\hbar}{\sqrt{2\pi}} \int_0^\infty d\omega' \, \sqrt{\kappa(\omega')} (\boldsymbol{a}^\dagger \boldsymbol{b}(\omega') + \boldsymbol{a} \boldsymbol{b}^\dagger(\omega')). \tag{2.12}$$

We write the Heisenberg equation for operator $\boldsymbol{a}$ with the total Hamiltonian

$\boldsymbol{H}_{\text{tot}} = \boldsymbol{H}_{\text{sys}} + \boldsymbol{H}_{\text{int}} + \boldsymbol{H}_{\text{env}}$, where $\boldsymbol{H}_{\text{sys}}$ is the Hamiltonian of the LC circuit, and we get

$$\partial_t \boldsymbol{a} = -\frac{i}{\hbar}[\boldsymbol{a}, \boldsymbol{H}_{\text{tot}}] \tag{2.13}$$

$$= -i\omega\boldsymbol{a} - \frac{i}{\sqrt{2\pi}} \int_0^\infty d\omega' \sqrt{\kappa(\omega')}\boldsymbol{b}(\omega'). \tag{2.14}$$

In order to solve this equation, we need to write the Heisenberg equations for $\boldsymbol{b}(\omega)$. To solve them, we split the evolution of $\boldsymbol{b}(\omega')$ into its free evolution under $\boldsymbol{H}_{\text{env}}$ and its evolution driven by the coupling with $\boldsymbol{a}$, such that the integrated solutions from a previous time t_0 to t are

$$\boldsymbol{b}(\omega') = \boldsymbol{b}_0(\omega')e^{-i\omega'(t-t_0)} - i\sqrt{\frac{\kappa(\omega')}{2\pi}} \int_{t_0}^t dt' \boldsymbol{a}(t')e^{i\omega't'}, \tag{2.15}$$

where $\boldsymbol{b}_0(\omega')$ is the state of the mode at t_0. When this solution is included in the equation of motion of $\boldsymbol{a}$, the resulting dynamics of $\boldsymbol{a}$ is analytical only for a known function $\kappa(\omega')$. Here, we perform the Markov approximation, which consists in taking $\kappa(\omega) = \kappa$, where κ is constant. For this approximation to describe our system correctly, it only needs to be valid around the resonance frequency of our circuit. With this, the dynamics of $\boldsymbol{a}$ is

$$\partial_t \boldsymbol{a} = -i\omega\boldsymbol{a} - \frac{\kappa}{2}\boldsymbol{a} - \sqrt{\kappa}\boldsymbol{a}_{\text{in}}, \tag{2.16}$$

which is the *quantum Langevin equation*. This equation brings two new terms to the dynamics of $\boldsymbol{a}$. The first one is in $-\frac{\kappa}{2}\boldsymbol{a}$ and corresponds to the "spontaneous emission" of the resonator. We see that this term comes from the resonator driving the bath modes. The second one corresponds to the incoming field onto the cavity. This term can be obtained explicitly with

$$\boldsymbol{a}_{\text{in}}(t) = \frac{i}{\sqrt{2\pi}} \int_0^\infty d\omega' \boldsymbol{b}_0(\omega')e^{-i\omega'(t-t_0)}. \tag{2.17}$$

We see that the free evolution of the bath modes, initially given by $\boldsymbol{b}_0(\omega')$, can drive the state of the circuit. Notice that this term is crucial for the operator $\boldsymbol{a}$ to keep the same commutation relation at all times even in presence of damping.

We have seen that by separating the bath modes before interacting with the cavity and their interaction with the cavity we could obtain the quantum Langevin equation. Now we would like to get the state of the environment once it has interacted with the cavity. For

this, we can integrate the dynamics of the bath modes from a time t_1 to t, where $t_1 > t$. Again, we input such a solution for $\boldsymbol{b}(\omega')$ into the Heisenberg equation for $\boldsymbol{a}$ and we get the *reversed-time quantum Langevin equation*

$$\partial_t \boldsymbol{a} = -i\omega \boldsymbol{a} + \frac{\kappa}{2}\boldsymbol{a} - \sqrt{\kappa}\boldsymbol{a}_{\text{out}}, \tag{2.18}$$

where

$$\boldsymbol{a}_{\text{out}} = \frac{i}{\sqrt{2\pi}} \int_0^\infty d\omega' \, \boldsymbol{b}_1(\omega') e^{-i\omega'(t-t_1)}, \tag{2.19}$$

with $\boldsymbol{b}_1(\omega')$ the bath modes at time t_1.

Finally, by combining these two quantum Langevin equations together, we obtain the *input-output relation*

$$\boldsymbol{a}_{\text{out}}(t) - \boldsymbol{a}_{\text{in}}(t) = \sqrt{\kappa}\boldsymbol{a}(t). \tag{2.20}$$

This equation shows that the output field is the sum of the incoming drive and the current field inside the circuit.

In practice, only a part of the bath modes is controlled by the experimentalist and another part corresponds to uncontrolled intrinsic loss. The κ we have derived contains only the controlled part, that we usually called κ_c for "kappa coupling". The intrinsic losses are noted κ_i for "kappa internal". The total losses are thus represented with $\kappa_{\text{tot}} = \kappa_c + \kappa_i$. When the LC circuit is used to read the state of a qubit, it is important to extract as much information as possible on a timescale that is small compared to the intrinsic lifetime of the qubit. Hence, in that situation, we choose $\kappa_c \gg \kappa_i$ and we neglect the internal losses. On the other hand, when the LC circuit is used to store quantum information for as long as possible, we choose $\kappa_c \ll \kappa_i$.

To conclude this chapter, we discuss a crucial approximation called the *stiff pump approximation*. When a drive is applied to a circuit, the fluctuations of the drive should not be transmitted to the cavity. Thus, we split the driving field into two part, such that it is given by $\boldsymbol{a}_{\text{in}} = \boldsymbol{a}_{\text{in}}^0 + \bar{\boldsymbol{a}}_{\text{in}}(t)$, with $\langle \boldsymbol{a}_{\text{in}}^0 \rangle = 0$. For the fluctuations of this field to not be transmitted to the field of the circuit, we need to have a small κ, while keeping $\sqrt{\kappa}\bar{a}_{\text{in}}(t)$ constant (and strong enough to do something interesting with the state of the circuit). The stiff-pump approximation consists in driving as hard as possible through a port that is as weakly coupled as possible. In this case, the energy transferred to the circuit from the drive is negligible com-

pared to the total amount of energy in the drive. Therefore, the drive is never depleted. The resulting Langevin equation is

$$\partial_t \boldsymbol{a} = -i\omega\boldsymbol{a} - \frac{\kappa}{2}\boldsymbol{a} - \sqrt{\kappa}\bar{a}_{\text{in}} - \sqrt{\kappa}\boldsymbol{a}_{\text{in}}^0. \tag{2.21}$$

The average part of the input field can be put into a drive Hamiltonian. We define the drive amplitude as $\epsilon(t) = i\sqrt{\kappa}\bar{a}_{\text{in}}$, such that the drive Hamiltonian is

$$\boldsymbol{H}_{\text{d}} = \hbar\left(\epsilon(t)\boldsymbol{a}^\dagger + \epsilon^*(t)\boldsymbol{a}\right). \tag{2.22}$$

We will use this type of Hamiltonian to treat the drives and we will usually not write explicitly the fluctuation part $\boldsymbol{a}_{\text{in}}^0$.

2.2 Transmon superconducting qubits

The non-linear element that enables the quantum control of superconducting circuits is called the Josephson junction (JJ). This element is made of two superconducting electrodes separated by an insulating tunnel barrier, represented in Fig. 2.2(a). In all the devices used in this thesis, the JJ are made using the bridge-free technique [69] and resemble the schematic in Fig. 2.2(b).

The states of the two superconducting islands can be different, and in particular, they might be described with a different number of Cooper pairs. The joint state of the system can be described using the difference in number of Cooper pairs $\boldsymbol{n}$ as an observable. Notice that $\boldsymbol{n}$ is the same observable used to describe an LC circuit. The tunnel barrier between the two electrodes can increase or decrease the difference in number of Cooper pairs. Thus, in the basis of eigenstates of $\boldsymbol{n}$, we can write the tunneling Hamiltonian, called the Josephson Hamiltonian for superconductors, as

$$\boldsymbol{H}_J = -\frac{E_J}{2}\sum_{n=-\infty}^{+\infty}\left(|n\rangle\langle n+1| + |n+1\rangle\langle n|\right), \tag{2.23}$$

where E_J is called the Josephson energy. We now change basis to write this Hamiltonian by introducing the conjugate observable of $\boldsymbol{n}$ that we call $\boldsymbol{\varphi}$. Because $\boldsymbol{n}$ is defined the same way as for the LC circuit, we can identify $\boldsymbol{\varphi}$ with the same operator for the LC circuit. Using this
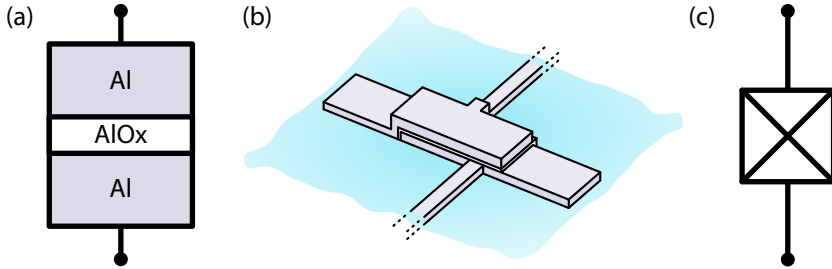
Figure 2.2: Schematic representation of a Josephson junction. (a) In this thesis, Josephson junctions are composed of two aluminum electrodes (gray) separated by an aluminum oxide tunnel barrier (white). (b) Our Josephson junctions are made using the bridge-free technique on a sapphire wafer (blue). The two aluminum electrodes overlap with a certain area that controls the Josephson energy. Each electrode is connected to a lead that connects the Josephson junction to the rest of the circuit. In reality, the layer of oxide covers the entire device, but we only represent the part forming the tunnel barrier for clarity. The characteristic length on this drawing is 100 nm (c) The symbol that represents a Josephson junction in a circuit is a boxed cross.

operator, we can rewrite

$$\boldsymbol{H}_J(\varphi) = -E_J \cos(\varphi). \tag{2.24}$$

Up to a constant term, which is not relevant for the dynamics of the system, this Hamiltonian can be broken down into a quadratic part in φ and a non-linear part that is of order 4 or more in φ, such that $\boldsymbol{H}_J(\varphi) = \frac{E_J}{2}\varphi^2 - E_J\left(\cos(\varphi) + \frac{\varphi^2}{2}\right)$. With this decomposition, the JJ can be thought of as a non-linear inductor and we can rewrite $E_J = \frac{\phi_0^2}{L_J}$, where L_J is the Josephson inductance. We denote the non-linear part of this Hamiltonian

$$\boldsymbol{H}_{\geq 4}(\varphi) = -E_J\left(\cos(\varphi) + \frac{\varphi^2}{2}\right). \tag{2.25}$$

This non-linear inductor can be used together with a capacitance to form an anharmonic oscillator whose Hamiltonian is

$$\boldsymbol{H} = \frac{E_J}{2}\varphi^2 + 4E_C\boldsymbol{n}^2 + \boldsymbol{H}_{\geq 4}(\varphi). \tag{2.26}$$

The Transmon qubit is a special case of this Hamiltonian where the linear part of the

circuit has a low impedance $Z_0 \ll R_Q$ [39]. In practice, this regime is usually expressed as choosing $E_J/E_C > 50$. As we have previously seen, in the low-impedance regime, the zero-point fluctuations of the phase are small compared to the flux quantum. Hence, as long as the number of excitations in this circuit is close to unity (which is the case to make a two-level system), the anharmonicity can be treated as a perturbation. In the spirit of perturbation theory, we diagonalize the linear part of the Hamiltonian, such that

$$\boldsymbol{H} = \hbar\omega \left(\boldsymbol{a}^\dagger \boldsymbol{a} + \frac{1}{2} \right) + \boldsymbol{H}_{\geq 4} \left(\varphi^{\text{ZPF}}(\boldsymbol{a} + \boldsymbol{a}^\dagger) \right), \tag{2.27}$$

with $\varphi^{\text{ZPF}} = \sqrt{\frac{Z_0}{2R_Q}} = \left(\frac{2E_C}{E_J} \right)^{\frac{1}{4}} \lesssim 0.5$ and $\omega = \sqrt{8E_J E_C}/\hbar$.

In order to study the effect of the anharmonicity on the system, we will expand $\boldsymbol{H}_{\geq 4}$ to its lowest order and keep only the non-rotating terms, i.e. the ones that have as many $\boldsymbol{a}^\dagger$'s as $\boldsymbol{a}$'s. These terms will be all possible combinations of order four and we need to reorder them to get a single term. Each reordering will create a term of lower order that will contribute to a small change of ω, called the *Lamb shift*, which we will not explicitly calculate. Therefore, up to the Lamb shift, all the fourth order terms commute. We now want to count the combinations that lead to a fourth order term with two $\boldsymbol{a}$'s and two $\boldsymbol{a}^\dagger$'s. In normal ordering, this term is usually noted $-\hbar\frac{\alpha}{2}\boldsymbol{a}^{\dagger 2}\boldsymbol{a}^2$, with

$$\begin{aligned} \hbar\alpha &= 2\frac{E_J}{24} \binom{4}{2}\binom{2}{2} \left(\varphi^{\text{ZPF}} \right)^4 \\ &= \frac{E_J}{2} \left(\varphi^{\text{ZPF}} \right)^4 \\ &= E_C. \end{aligned} \tag{2.28}$$

We see that the transition frequency $\omega_{01} = \omega$ from $|0\rangle$ to $|1\rangle$ is now different than the transition frequency $\omega_{12} = \omega_{01} - \alpha$ from $|1\rangle$ to $|2\rangle$. Thus, one can address the 0 and 1 levels without exciting the transmons to its second excited state, thus forming a qubit. We usually note these three states $|g\rangle$, $|e\rangle$ and $|f\rangle$.

In practice, in order to manipulate this qubit as fast as possible considering the speed of the control electronics, we choose $E_C/h = 100\text{-}250\,\text{MHz}$. In the transmon limit of $E_J/E_C = 50 - 100$, this allows a range of $E_J/h = 5\text{-}25\,\text{GHz}$. Therefore, the frequency of a transmon is usually in a range 2-7 GHz.

2.3 Coupling a transmon to a cavity

As we have seen when we treated the environment of a cavity, the Hamiltonian of a transmon capacitively coupled to a cavity can be written after using the RWA as

$$\boldsymbol{H}/\hbar = \omega_a \boldsymbol{a}^\dagger \boldsymbol{a} + \omega_b \boldsymbol{b}^\dagger \boldsymbol{b} + g(\boldsymbol{a}\boldsymbol{b}^\dagger + \boldsymbol{a}^\dagger \boldsymbol{b}) + \boldsymbol{H}_{\geq 4}\left(\varphi^{\text{ZPF}}(\boldsymbol{b} + \boldsymbol{b}^\dagger)\right)/\hbar, \qquad (2.29)$$

where we have dropped the constant terms. $\boldsymbol{b}$ is the annihilation operator of the transmon, and g is the coupling strength, which can be designed by changing the capacitive coupling of the two modes.

We usually consider that the transmon is not directly coupled to the transmission line. For now, we also neglect the internal losses of both the transmon and the cavity. Thus, we get two coupled Langevin equations

$$\partial_t \boldsymbol{a} = -i\left(\left(\omega_a - i\frac{\kappa}{2}\right)\boldsymbol{a} + g\boldsymbol{b}\right) \qquad (2.30)$$

$$\partial_t \boldsymbol{b} = -i\left(\omega_b \boldsymbol{b} + g\boldsymbol{a}\right) - \frac{i}{\hbar}\left[\boldsymbol{b}, \boldsymbol{H}_{\geq 4}\left(\varphi^{\text{ZPF}}(\boldsymbol{b} + \boldsymbol{b}^\dagger)\right)\right]. \qquad (2.31)$$

We now diagonalize the linear part of this equation, which corresponds to a matrix

$$M = \begin{pmatrix} (\omega_a - i\kappa/2) & g \\ g & \omega_b \end{pmatrix}. \qquad (2.32)$$

The eigenvalues of this matrix are two complex frequencies of two independent modes. In our experiments, we are always in the regime $\kappa \ll g \ll \Delta$, with $\Delta = \omega_b - \omega_a$. Up to the second order in g/Δ, we have

$$\omega_+ = \left(\omega_a + \frac{g^2}{\Delta}\right) - i\frac{\kappa}{2} + i\left(\frac{g}{\Delta}\right)^2 \kappa \qquad (2.33)$$

$$\omega_- = \left(\omega_b - \frac{g^2}{\Delta}\right) - i\left(\frac{g}{\Delta}\right)^2 \kappa. \qquad (2.34)$$

$$(2.35)$$

We see that the frequency of each mode is slightly shifted by a negligible amount g^2/Δ.

We also see that the transmon inherits losses from the fact that the cavity is coupled to a transmission line. The rate

$$\Gamma_P = \left(\frac{g}{\Delta}\right)^2 \kappa \tag{2.36}$$

is called the Purcell limit on the energy lifetime of the transmon [70]. In practice, we design our systems such that the energy lifetime of the transmon is limited by its internal losses instead of the Purcell limit, either by having the Purcell rate to be much lower than the internal loss rate or by engineering a Purcell filter [71].

We define two new ladder operators c (for the cavity) and q (for the qubit) that corresponds to the *dressed modes* that are resonant at $\omega_c = \omega_+$ and $\omega_q = \omega_-$ and such that $\left[c, c^\dagger\right] = \left[q, q^\dagger\right] = 1$ and $\left[c, q^\dagger\right] = 0$. We define the mixing angle θ, such that

$$\tan(\theta) = \frac{g}{\Delta}, \tag{2.37}$$

and we get the relations

$$c = \cos(\theta)a + \sin(\theta)b \approx a + \frac{g}{\Delta}b \tag{2.38}$$

$$q = -\sin(\theta)a + \cos(\theta)b \approx -\frac{g}{\Delta}a + b. \tag{2.39}$$

With these relations, the linear part of the Hamiltonian is now proportional to $\omega_c c^\dagger c + \omega_q q^\dagger q$. We now want to treat the non-linear Hamiltonian $H_{\geq 4}$. For this, we invert the last two equations to find b as a function of c and q. We find

$$H_{\geq 4}\left(\varphi^{\mathrm{ZPF}}(b + b^\dagger)\right) = H_{\geq 4}\left(\varphi^{\mathrm{ZPF}}(\cos(\theta)(q + q^\dagger) + \sin(\theta)(c + c^\dagger))\right)$$

$$\approx H_{\geq 4}\left(\varphi^{\mathrm{ZPF}}(q + q^\dagger) + \varphi^{\mathrm{ZPF}}\frac{g}{\Delta}(c + c^\dagger)\right). \tag{2.40}$$

Here, we usually redefine the the zero-point fluctuations of these modes as $\varphi_q = \varphi^{\mathrm{ZPF}}$ and $\varphi_c = \varphi^{\mathrm{ZPF}}\frac{g}{\Delta}$.

The non-linear Hamiltonian creates new terms that couple the dressed modes. Once again, we ignore the Lamb shift due to the commutation relations and we look for the fourth

order resonant terms. These two terms are

$$-\hbar\chi(\boldsymbol{c}^\dagger\boldsymbol{c})(\boldsymbol{q}^\dagger\boldsymbol{q}) = -E_J\varphi_c^2\varphi_q^2 = -E_C\left(\frac{g}{\Delta}\right)^2 \tag{2.41}$$

$$-\hbar\frac{K}{2}\boldsymbol{c}^{\dagger 2}\boldsymbol{c}^2 = -E_J\varphi_c^4 = -E_C\left(\frac{g}{\Delta}\right)^4. \tag{2.42}$$

The term in χ is called the dispersive shift or the cross-Kerr, while the term in K is called the Kerr. With these parameters, the Purcell rate can be rewritten as $\Gamma_P = \frac{\chi}{2E_C}\kappa$.

In most experiments, the orders of magnitude are $g/2\pi = 10\text{-}300\,\text{MHz}$ and $\Delta/2\pi = 1\text{-}5\,\text{GHz}$, such that $\chi/2\pi$ is usually of order 0.1-5 MHz. When the cavity is used to read the state of a qubit, we usually use $\kappa/2\pi = 1\text{-}5\,\text{MHz}$.

In summary, the coupling Hamiltonian of a transmon qubit and a superconducting cavity is well described, using the rotating wave approximation, with the dispersive Hamiltonian

$$\frac{\boldsymbol{H}}{\hbar} = \omega_c\boldsymbol{c}^\dagger\boldsymbol{c} + \omega_q\boldsymbol{q}^\dagger\boldsymbol{q} - \frac{\alpha}{2}\boldsymbol{q}^{\dagger 2}\boldsymbol{q}^2 - \chi(\boldsymbol{c}^\dagger\boldsymbol{c})(\boldsymbol{q}^\dagger\boldsymbol{q}) - \frac{K}{2}\boldsymbol{c}^{\dagger 2}\boldsymbol{c}^2 \tag{2.43}$$

$$= \left(\omega_c - \frac{\chi}{2}\right)\boldsymbol{c}^\dagger\boldsymbol{c} + \omega_q\boldsymbol{\sigma}_z + \frac{\chi}{2}\boldsymbol{c}^\dagger\boldsymbol{c}\boldsymbol{\sigma}_z - \frac{K}{2}\boldsymbol{c}^{\dagger 2}\boldsymbol{c}^2, \tag{2.44}$$

where we have kept only the first two excited states of the transmon and used the Pauli operator $\boldsymbol{\sigma}_z$.

2.4 Tracking frame of a drive

Finally, we arrive at one of the main point of this thesis, which consists in performing careful changes of frame in order to obtain new non-linear terms for a driven system. These terms are not described by simply using the last step of the previous derivation that led to the dispersive Hamiltonian and adding the drive term afterwards. Instead, it requires to keep the non-linear Hamiltonian $\boldsymbol{H}_{\geq 4}$ as long as possible without performing the RWA, while performing changes of frame that account for the drive terms. The goal of changing frame is to zoom on the interesting physics by highlighting the role of the non-linear term. These changes of frame amount to using the *interaction picture*. In order to keep this derivation clear, we consider here a single driven-dissipative non-linear mode with a generic annihilation operator $\boldsymbol{a}$. In the laboratory frame, we denote the annihilation operator $\boldsymbol{a}_0$, such that we can increment the index after each change of frame. When this mode is driven, it is subject

to the Hamiltonian

$$\boldsymbol{H}/\hbar = \omega_a \boldsymbol{a}_0^\dagger \boldsymbol{a}_0 + \epsilon(t)\boldsymbol{a}_0^\dagger + \epsilon^*(t)\boldsymbol{a}_0 + \frac{1}{\hbar}\boldsymbol{H}_{\geq 4}\left(\phi_a(\boldsymbol{a}_0 + \boldsymbol{a}_0^\dagger)\right), \tag{2.45}$$

where $\epsilon(t)$ is an arbitrary time dependent amplitude of a drive. The quantum Langevin equation of this system is

$$\partial_t \boldsymbol{a}_0 = -i\omega_a \boldsymbol{a}_0 - \frac{\kappa}{2}\boldsymbol{a}_0 - i\epsilon(t) - \frac{i}{\hbar}\left[\boldsymbol{a}_0, \boldsymbol{H}_{\geq 4}\left(\phi_a(\boldsymbol{a}_0 + \boldsymbol{a}_0^\dagger)\right)\right], \tag{2.46}$$

where we have omitted the fluctuations of the incoming field.

We start by going into the rotating frame at frequency ω_a by considering the dynamics of the operator $\boldsymbol{a}_1 = e^{i\omega_a t}\boldsymbol{a}_0$. This way, we have $\partial_t \boldsymbol{a}_1 = i\omega_a \boldsymbol{a}_1 + e^{i\omega_a t}\partial_t \boldsymbol{a}_0$, thus

$$\partial_t \boldsymbol{a}_1 = -\frac{\kappa}{2}\boldsymbol{a}_1 - i\epsilon(t)e^{i\omega_a t} - \frac{i}{\hbar}\left[\boldsymbol{a}_1, \boldsymbol{H}_{\geq 4}\left(\phi_a(\boldsymbol{a}_1 e^{-i\omega_a t} + \boldsymbol{a}_1^\dagger e^{i\omega_a t})\right)\right], \tag{2.47}$$

where we have substituted $\boldsymbol{a}_0 = \boldsymbol{a}_1 e^{-i\omega_a t}$ inside $\boldsymbol{H}_{\geq 4}$. Notice that the non-linear Hamiltonian could be any function of $\boldsymbol{a}$ and $\boldsymbol{a}^\dagger$ such that this derivation remains general for other circuits. The main idea of this step was to remove the part of the Hamiltonian that depends explicitly on ω_a and to displace it inside the non-linear part.

We now use another change of frame to remove the explicit dependence of the Langevin equation with the drive term. For this, we consider an arbitrary time-dependent displaced frame, such that

$$\boldsymbol{a}_2 = \boldsymbol{a}_1 + \xi(t), \tag{2.48}$$

where $\xi(t)$ is an arbitrary scalar operator. The quantum Langevin equation for $\boldsymbol{a}_2$ is now $\partial_t \boldsymbol{a}_2 = \partial_t \boldsymbol{a}_1 + \partial_t \xi$, which leads to

$$\partial_t \boldsymbol{a}_2 = -\frac{\kappa}{2}\left(\boldsymbol{a}_2 - \xi(t)\right) - i\epsilon(t)e^{i\omega_a t} + \partial_t \xi(t)$$
$$- \frac{i}{\hbar}\left[\boldsymbol{a}_2, \boldsymbol{H}_{\geq 4}\left(\varphi_a\left((\boldsymbol{a}_2 - \xi(t))e^{-i\omega_a t} + (\boldsymbol{a}_2^\dagger - \xi^*(t))e^{i\omega_a t}\right)\right)\right]. \tag{2.49}$$

In order to remove the explicit dependence in $\epsilon(t)$, we now choose $\xi(t)$ such that it solves

the differential equation

$$\partial_t \xi(t) = i\epsilon(t)e^{i\omega_a t} - \frac{\kappa}{2}\xi(t). \tag{2.50}$$

Now, the dynamics of a_2 is only given by the non-linear part $H_{\geq 4}$ and by the usual losses. A general solution to this equation is given by

$$\xi(t) = i\int_0^t \epsilon(t')e^{\left(i\omega_a \frac{\kappa}{2}\right)t'}dt'e^{-\frac{\kappa}{2}t}. \tag{2.51}$$

We start by analyzing the case where the drive has a square envelope and turns instantly on at $t = 0$ with a frequency ω, such that $\epsilon(t) = \epsilon_0 e^{-i\omega t}$. Here, we only treat the cases where $\Delta = \omega_a - \omega$ is large compared to the amplitude of any other term in $H_{\geq 4}/\hbar$, such that the RWA is valid. In this particular case we have

$$\xi(t) = \frac{i\epsilon_0}{i\Delta + \frac{\kappa}{2}}e^{i\Delta t} - \frac{i\epsilon_0}{i\Delta + \frac{\kappa}{2}}e^{-\frac{\kappa}{2}t}. \tag{2.52}$$

The first term of this solution corresponds to the desired effect: it modulates the non-linear terms of $H_{\geq 4}$ such that some non-linear terms can be made resonant. The second term is a spurious effect which temporary populates the driven mode despite the fact that the drive is non-resonant. This part is damped at rate κ, which is only a problem if the driven mode has a long lifetime. We will first treat the permanent regime $\kappa t \gg 1$, and later we will see how to mitigate this spurious effect.

In order to illustrate the interesting properties of this driven Hamiltonian, we reintroduce a second mode b that is already in its rotating frame. In this tracking frame, the Hamiltonian of the system is now approximately

$$H_{\geq 4}\left(\varphi_a\left(ae^{-i\omega_a t} + a^\dagger e^{i\omega_a t}\right) + \varphi_a\left(\xi_0 e^{i\omega t} + \xi_0^* e^{-i\omega t}\right) + \varphi_b\left(be^{-i\omega_b t} + b^\dagger e^{i\omega_b t}\right)\right), \tag{2.53}$$

where, we reuse the notation a as there is no more possible confusion, and where we denote $\xi_0 = \epsilon_0/\Delta$. We see that, after expanding this Hamiltonian to the fourth order, the drive creates many new terms that can be resonant, depending on the choice of ω.

Some of these terms shift the frequency of the modes and are always present when a fourth-order non-linear system is driven. They are called *AC Stark shifts*, and they regroup all

terms that lead to $\hbar\Delta_a \boldsymbol{a}^\dagger\boldsymbol{a}$ and $\hbar\Delta_b \boldsymbol{b}^\dagger\boldsymbol{b}$. To fourth order, their expressions are

$$\Delta_a = -\frac{E_J}{\hbar}\phi_a^4|\xi_0|^2 = 2K|\xi_0|^2 \tag{2.54}$$

$$\Delta_b = -\frac{E_J}{\hbar}\phi_a^2\phi_b^2|\xi_0|^2 = \chi|\xi_0|^2. \tag{2.55}$$

Note that we have used the Kerr K, however if the driven mode is a transmon and not a cavity we would have used α. These terms are mostly useless but need to be accounted for to know the precise detuning Δ between the drive and the driven mode.

Some terms in this expansion can create new interactions between modes that were not available without drives. As an example, we take the case where $\omega = (\omega_a + \omega_b)/2$, such that the engineered Hamiltonian is

$$\boldsymbol{H}_{\text{int}} = -\frac{E_J}{4!}\binom{4}{2}\binom{2}{1}\varphi_a^3\varphi_b\left(\xi_0^2\boldsymbol{a}\boldsymbol{b} + \xi_0^{*2}\boldsymbol{a}^\dagger\boldsymbol{b}^\dagger\right), \tag{2.56}$$

which creates two-mode squeezing and can be used to create amplifiers. In the following chapters, we will describe several ways to use this driven Hamiltonian to engineer new controls of superconducting qubits and cavities.

In some cases, it might be interesting to drive a mode with a long lifetime, as we will see in the conditional displacement readout of a transmon. In such situations, the transient term of $\xi(t)$ given by equation 2.52 is detrimental. However, such a term can easily be mitigated by adding a slowly rising envelope to the drive term. As we will see, the rise time of such an envelope can be fast compared to $1/\kappa$, as long as it is slow compared to $1/\Delta$. As an example, we take a drive such that

$$\epsilon(t) = \epsilon_0\left(1 - e^{-\gamma t}\right)e^{-i\omega t}, \tag{2.57}$$

with $\kappa \ll \gamma \ll \Delta$. For this particular case, the solution $\xi(t)$ is simply

$$\xi(t) = i\epsilon_0\left(\frac{e^{i\Delta t}}{i\Delta + \frac{\kappa}{2}} - \frac{e^{-\frac{\kappa}{2}t}}{i\Delta + \frac{\kappa}{2}} - \frac{e^{i\Delta t - \gamma t}}{i\Delta + \frac{\kappa}{2} - \gamma} + \frac{e^{-\frac{\kappa}{2}t}}{i\Delta + \frac{\kappa}{2} - \gamma}\right). \tag{2.58}$$

In this expression, the fourth term cancels the second term as long as $\gamma \ll \Delta$. At short times $t \ll \gamma$, the third term also cancels the first one. However, when the steady state set by γ is reached, the drive acts as intended. Usually, we have Δ of order several GHz. This way, the driven terms can be activated in a time $1/\gamma$ of a few nanoseconds.

2.5 Rotating wave approximation

In this chapter, we have always neglected the action of Hamiltonian terms that oscillate in time. To understand the reasoning behind this approximation, we consider a Hamiltonian that acts for a duration $T/2$, such that its unitary evolution is $\boldsymbol{U}(0, T/2) = e^{-i\boldsymbol{H}T/2}$. Then, reversing the sign of this Hamiltonian for the same duration results in $\boldsymbol{U}(T/2, T) = e^{+i\boldsymbol{H}T/2}$, which cancels the first evolution. If the Hamiltonian commutes with itself at all times and changes sign periodically, it has no effect. However, this is only approximately true when the Hamiltonian is a sum of terms that do not commute, which is the case for our driven dynamics. In this case, the evolution is approximately given by the time average of the Hamiltonian.

To see this, we write the time dependent Hamiltonian as

$$\frac{\boldsymbol{H}(t)}{\hbar} = a(t)\boldsymbol{h}_1 + b(t)\boldsymbol{h}_2, \tag{2.59}$$

where $a(t)$ and $b(t)$ have the dimensions of a frequency and such that $\boldsymbol{h}_{1,2}$ are dimensionless, of order 1 and time independent. In such a situation, we cannot write the Schrödinger equation and we have to divide the time evolution into N infinitesimal steps of duration dt, with $N \to \infty$. We define $t_k = T - kdt$, and we have

$$\boldsymbol{U}(0, T) = \prod_{k=1}^{N} e^{-i(a(t_k)\boldsymbol{h}_1 + b(t_k)\boldsymbol{h}_2)dt}. \tag{2.60}$$

We now use the Baker-Campbell-Hausdorff formula to break the exponential. To second order in dt, we have

$$\boldsymbol{U}(0, T) = \prod_{k=1}^{N} e^{-ia(t_k)\boldsymbol{h}_1 dt} e^{-ib(t_k)\boldsymbol{h}_2 dt} e^{-\frac{dt^2}{2}a(t_k)b(t_k)[\boldsymbol{h}_1, \boldsymbol{h}_2]}. \tag{2.61}$$

When we commute the term in dt^2 with a term in dt, it creates a new term in dt^3. We use this commutation to stack all the second order terms at the end of this expression. Doing so creates of order N^2 terms in dt^3, and the stacked term has N terms in dt^2. These two terms will thus disappear when $N \to \infty$.

We now want to regroup together all the term in $\boldsymbol{h}_1$ and all the terms in $\boldsymbol{h}_2$ by commuting their infinitesimal evolution. Again, doing so creates of order N^2 terms that will be of order

dt^2, and thus relevant to the dynamics of the system. We have

$$\boldsymbol{U}(0,T) = \left(\prod_{k=1}^{N} \prod_{l=1}^{k-1} e^{-\frac{dt^2}{2} a(t_k) b(t_k) [\boldsymbol{h_1}, \boldsymbol{h_2}]} \right) \left(\prod_{k=1}^{N} e^{-ia(t_k)\boldsymbol{h_1} dt} \right) \left(\prod_{k=1}^{N} e^{-ib(t_k)\boldsymbol{h_2} dt} \right) \tag{2.62}$$

Taking the continuous limit, we have

$$\boldsymbol{U}(0,T) = e^{-\frac{1}{2}[\boldsymbol{h_1},\boldsymbol{h_2}] \int_0^T \int_0^t a(t')b(t) dt dt'} e^{-i\boldsymbol{h_1} \int_0^T a(t) dt} e^{-i\boldsymbol{h_2} \int_0^T b(t) dt}. \tag{2.63}$$

This equation shows that, up to the first term, the evolution is given by the time average of the Hamiltonian. Hence, if the time average of $b(t)$ is 0, then the evolution of the system is approximately due only to $a(t)\boldsymbol{h_1}$. The first order term given by the double integral will be negligible if the frequency of $b(t)$ is large compared to its amplitude.

As an example, we take $a(t) = a_0$ constant and $b(t) = b_0 e^{i\omega t}$, and for convenience we take T to be an integer number of periods. The integral over b goes to 0 and the dynamics of $\boldsymbol{h_2}$ is indeed cancelled. The total evolution is then given by

$$\boldsymbol{U}(0,T) = e^{-\frac{a_0 b_0 T}{\omega} [\boldsymbol{h_1},\boldsymbol{h_2}]} e^{-i\boldsymbol{h_1} a_0 T}. \tag{2.64}$$

From this example, we deduce that the rotating approximation is valid when the amplitude of the rotating term (here b_0) is small compared to the rotation frequency (here ω).

The RWA is well illustrated in chapter 5, when we engineer a conditional displacement. In that particular case, the rotation we engineer is slow and we have a spurious evolution due to the non-commutation of $\boldsymbol{\sigma}_z(\boldsymbol{a} + \boldsymbol{a}^\dagger)$ and $\boldsymbol{\sigma}_z \boldsymbol{a}^\dagger \boldsymbol{a}$. This dynamics results in a spurious displacement that is taken into account in our stabilization.

3

Readout of superconducting qubits

Reading the state of superconducting qubits is an essential task for quantum information processing [72]. In the context of this thesis, the readout is mostly used to extract information on the state of an harmonic oscillator, whose properties have been mapped onto the state of a two-level system that we usually refer to as an ancilla qubit. For the dissipative stabilization of manifolds of coherent states (chapter 4), the readout is used only as a characterizing tool. For the stabilization of manifolds of GKP states, the readout actually removes entropy from the cavity hosting the GKP states. In this latter case, we also apply feedback to the system, based on the result of a readout process.

In this chapter, there is not ambiguity between a logical qubit and an ancilla qubit. Thus, we will refer to two-level transmons as qubits. In order to read the state of a qubit, we usually use an interaction Hamiltonian that entangles the relevant degree of freedom of the target qubit and a coherent state of a readout cavity. After amplifying the wave leaking from the readout cavity through an output port, an experimenter can easily measure its properties, such as its phase and amplitude, with commercial electronic components.

Thus, the main challenge is to engineer such an interaction Hamiltonian. Most cQED experiments rely on a frequency shift of the readout cavity that depends on the state of the qubit [73–75]. This readout scheme is referred to as the dispersive readout because the state of the qubit changes the dispersion relation of the readout cavity. After describing the ubiquitous dispersive readout, we will discuss how we engineered a new readout scheme based on a displacement of the readout cavity, conditioned on the state of the measured two-level system.

We also present relevant quantities for a readout process that is useful in the context of quantum computing, such as its fidelity and its quantum-non-demolition nature. These quantities are directly relevant for the stabilization of GKP qubits (chapter 5) where feedback

is necessary.

3.1 Dispersive readout

As we previously discussed, a simple capacitive coupling between an anharmonic oscillator and an harmonic oscillator gives rise to the dispersive interaction Hamiltonian $\boldsymbol{H}_{int} = -\frac{\chi}{2}\boldsymbol{a}^\dagger \boldsymbol{a}\boldsymbol{\sigma}_z$ (see chapter 2). The detuning $\pm\frac{\chi}{2}$, caused by the qubit, is probed with a drive on resonance with the bare frequency of the cavity and by looking at the reflected signal. In this situation, the field inside of the readout cavity follows the Langevin equation $\partial_t \boldsymbol{a} = \left(\pm i\frac{\chi}{2} - \frac{\kappa}{2}\right)\boldsymbol{a} - \sqrt{\kappa}\bar{a}_{in}$, where we have performed the stiff pump approximation on the incoming field. If the readout cavity is initially in the vacuum state, the solutions to these equations are coherent states with amplitude

$$\alpha_{g,e}(t) = \frac{2\sqrt{\kappa}\bar{a}_{in}}{\pm i\chi - \kappa}\left(1 - \exp\left(\left(-\frac{\kappa}{2} \pm \frac{\chi}{2}\right)t\right)\right). \tag{3.1}$$

We represent the average time-dependant trajectory in phase space in Fig. 3.1(a). We observe that the two trajectories have a similar imaginary part and an opposite real part. Thus, by measuring the real part of the field leaving the readout cavity using a phase-sensitive amplifier, one can infer the state of the qubit. This output field follows the input-output relation $\boldsymbol{a}_{out} = \sqrt{\kappa}\boldsymbol{a} + \boldsymbol{a}_{in}$. We plot the real part of the averaged outgoing field α_{out} as a function of time in Fig. 3.1(b). When the input field is turned on, it is first completely reflected off the cavity and the output fields sharply rises to the value of the input field. Then, the field inside of the cavity increases with a timescale $\frac{2}{\kappa}$ and interferes constructively (resp. destructively) when the qubit is in $|e\rangle$ (resp. $|g\rangle$), with the input signal. Finally, when the input field is switched off, the output field is composed solely of the field leaking out of the readout cavity with a timescale $\frac{2}{\kappa}$. Overall, the two trajectories first separate on a timescale given by the readout lifetime, then their separation is constant and they recombine when the input field is turned off, as shown in Fig. 3.1(c).

Although this scheme enabled many experiments requiring a fast and high fidelity readout, it has flaws that can be deduced from this description. Its first flaw stems from the fact that the dispersive interaction is obtained from the diagonalization of the transverse interaction (see chapter 2). The original interaction couples the bare $\boldsymbol{\sigma}_x$, which does not commute with the bare $\boldsymbol{\sigma}_z$, to the readout cavity. The fact that the interaction and the measured quantity do not commute results in the Purcell limit on the lifetime of the qubit [70]. This limit is
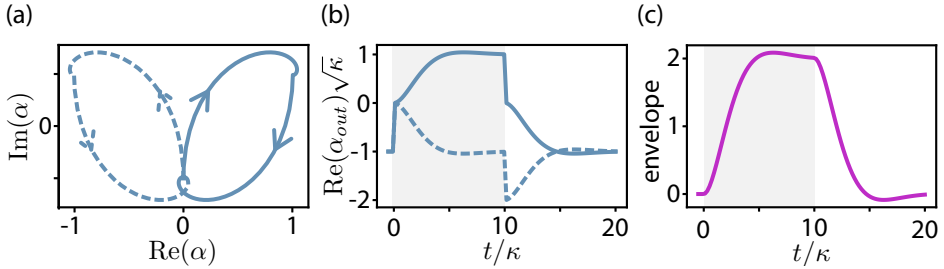
Figure 3.1: Simulation of the trajectories of the readout cavity for the dispersive readout, measured in reflection. On each curve, the trajectory corresponding to the qubit being in $|g\rangle$ is a blue dashed line and the one corresponding to the qubit being in $|e\rangle$ is a blue solid line. (a) Average internal state of the readout cavity represented in phase-space. The arrows indicate how the state evolves in time. (b) Average reflected signal as a function of time. The light-gray area represents the time during which the input field is on. (c) Average distance between the reflected signal corresponding to the qubit being in $|g\rangle$ and $|e\rangle$. Similarly, the light-gray area represents when the input field is on.

usually mitigated using a Purcell filter [71], but this contraption results in added complexity. Its second flaw comes from the fact that, in the dispersive limit, $\boldsymbol{\sigma_z}$ is coupled to the number of photons $\boldsymbol{a}^\dagger\boldsymbol{a}$, whereas what is measured is the real part of the outgoing field. In order to distinguish between the two states of the qubit, the cavity must first be loaded with photons and only then, the two states are separated by the dispersive coupling. This fact is seen in Fig. 3.1, where the trajectories have the same tangent at short times. We finally identify a third flaw due to the fact that the strong coupling between the qubit and the readout cavity is always present, even when we choose not to send any input field. Because of this, spurious photons inside of the readout cavity can also read the state of the qubit and cause decoherence [41]. We tried to address these flaws by implementing a different type of qubit readout that we describe in the following sections.

3.2 Conditional displacement readout

3.2.1 Ideal readout via a gated longitudinal coupling

After considering the various flaws of the dispersive readout, we can wonder what would be the best interaction Hamiltonian to read the state of a superconducting qubit? For this, we want the degree of freedom that we are trying to measure, $\boldsymbol{\sigma_z}$, to be directly coupled

to what we are able to measure using previously developed quantum-limited amplifiers [76–78] and commercial microwave components. At best, a quantum-limited amplifier is phase-sensitive, meaning that it measures a single quadrature of a microwave field and destroys any signal contained in the other quadrature. Thus, our ideal interaction couples the qubit to a quadrature operator. On top of that, in order to address the last flaw of the dispersive readout, this interaction also needs to be turned on and off on-demand. We say that such an interaction is gated. We identified that the desired ideal readout Hamiltonian is

$$\boldsymbol{H}_{int}/\hbar = \zeta(t)\boldsymbol{\sigma_z}\left(\boldsymbol{a} - \boldsymbol{a}^\dagger\right)/(2i), \tag{3.2}$$

where $\zeta(t)$ is the time-dependant strength of the interaction, and where we have chosen the coupled quadrature to be the momentum. Notice that, because the quadrature operator appears, this interaction is not necessarily resonant (this consideration is discussed extensively in the next subsection). Nevertheless, if this interaction is resonant, it causes a displacement of the state of the readout cavity, conditioned on the state of the qubit. As we chose this coupling to be along the momentum, the trajectory of the readout cavity is solely along the position, as represented in Fig. 3.2(a). This coupling is referred to as "longitudinal" in contrast to the capacitive coupling seen before, that is referred to as transverse [79, 80]. This name comes from the fact that, for the bare qubit mode, the longitudinal interaction couples directly $\boldsymbol{\sigma_z}$ to the quadrature of the readout mode, whereas the transverse interaction couples $\boldsymbol{\sigma_x}$. As such, the longitudinal interaction cannot be put on the same level as the dispersive interaction: the former is a bare interaction, while the latter is expressed in a diagonalized basis. The bare longitudinal interaction has been realized experimentally with superconducting circuits [81–83].

Solving the Langevin equation for a constant interaction, with the readout cavity starting in the vacuum state, we obtain the qubit-dependant trajectories

$$\alpha_{g,e}(t) = \mp\frac{\zeta}{\kappa}\left(1 - \exp\left(-\frac{\kappa t}{2}\right)\right). \tag{3.3}$$

We see that, because of our choice of interaction, the separation between the trajectories corresponding to the qubit being in $|g\rangle$ and $|e\rangle$ is more direct. We observe in Fig. 3.2(b) that the derivative of the trajectories is not 0 when the interaction is turned on. This way, we can expect that, using this interaction in a readout scheme, would allow for a better readout at short times. Notice that, beside this difference, the readout timescale is still set by the cavity quadrature lifetime $\frac{2}{\kappa}$.
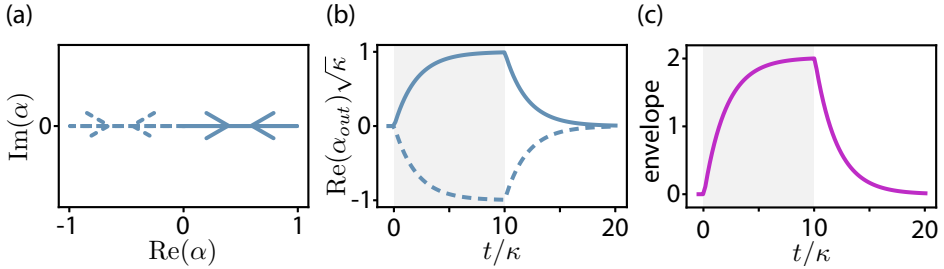
Figure 3.2: Simulation of the trajectories of the readout cavity for the conditional displacement readout. On each curve, the trajectory corresponding to the qubit being in $|g\rangle$ is a blue dashed line and the one corresponding to the qubit being in $|e\rangle$ is a blue solid line. (a) Average internal state of the readout cavity represented in phase-space. The arrows indicate how the state evolves in time. (b) Average output signal as a function of time. The light-gray area represents the time during which the interaction is on. (c) Average distance between the signal corresponding to the qubit being in $|g\rangle$ and $|e\rangle$. Similarly, the light-gray area represents when the interaction is on.

Such a coupling has been theoretically studied previously and offers other advantages than the ones stated above. In particular, if we were to squeeze the initial state of the readout cavity along the position quadrature, the overall quality of the readout would be enhanced [84].

3.2.2 Parametrically induced conditional displacement

Throughout this manuscript, we use 3D cQED architectures for our experiments. Previous experiments using this architecture have shown that the intrinsic lifetime of a transmon qubit can be pushed up to a couple hundreds of microseconds [85] and that quantum information can be stored in superconducting microwave cavities for up to several milliseconds [64]. In such 3D architectures, the different pieces of metal that constitute each mode are not galvanically connected. Unfortunately, all the proposals to engineer a resonant longitudinal readout rely on having a shared loop between a microwave resonator and a superconducting qubit, and on threading a time-dependant magnetic field through this loop [79, 84]. Because of this, it is currently impossible to engineer a longitudinal readout in a 3D architecture. How can we have both the benefits of the 3D cQED architecture and the benefits of the longitudinal interaction at the same time?

The solution to this conundrum is to minimize the transverse coupling and to use stiff microwave drives to induce the interaction needed. As previously mentioned, in the interaction frame, the longitudinal interaction is not resonant because it involves the annihilation
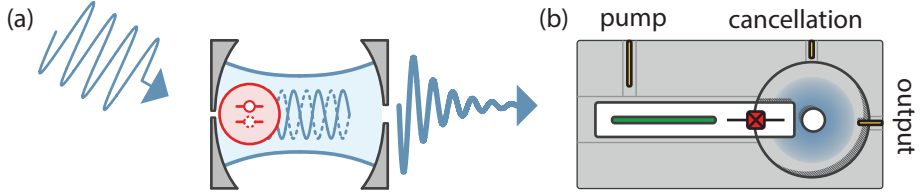
Figure 3.3: Schematic of a parametrically induced conditional displacement.(a) A schematic superconducting two-level artificial atom (red) is placed where the field of a cavity (blue) is weak, for instance close to a partially transmitting mirror, to be in the weak coupling regime. When the atom is driven at the frequency of the cavity, the electromagnetic field of the cavity is spontaneously displaced with a sense which depends on the state of the atom (dotted or solid line) and exits through the main aperture. (b) Schematic of a practical cQED architecture implementing a conditional displacement readout. The artificial atom is a transmon qubit (red) coupled to a readout post-cavity (blue) in aluminum. The transmon is weakly coupled to a pump port through a filter stripline resonator (green). The field inside of the readout cavity is picked-up by a strongly coupled output port. Coherent leakages from the pump port to the readout cavity can be cancelled using the weakly coupled cancellation port [86].

operator an odd number of times. To compensate for this, we use the four-wave mixing capability of the Josephson Hamiltonian and a drive at the frequency of the readout cavity. Because we want to minimize the transverse coupling of the qubit to the cavity (hence, we want to minimize χ), and because we want to not have to load photons into the cavity for the interaction to take place, the drive is directly applied to the qubit, but at the frequency of the cavity, as shown in Fig. 3.3.

In order to develop the theory that leads to the conditional displacement readout, we need to consider the qubit as an anharmonic oscillator with annihilation operator $\boldsymbol{q}$. Neglecting the dissipation of the qubit, the dynamic of the qubit-cavity system is given by the coupled Langevin equations

$$\partial_t \boldsymbol{a} = -i\omega_a \boldsymbol{a} - \frac{i}{\hbar} \left[\boldsymbol{a}, \boldsymbol{H}_4(\boldsymbol{a}, \boldsymbol{a}^\dagger, \boldsymbol{q}, \boldsymbol{q}^\dagger) \right] - \frac{\kappa}{2} \boldsymbol{a} \qquad (3.4)$$

$$\partial_t \boldsymbol{q} = -i\omega_q \boldsymbol{q} - i\frac{i}{\hbar} \left[\boldsymbol{q}, \boldsymbol{H}_4(\boldsymbol{a}, \boldsymbol{a}^\dagger, \boldsymbol{q}, \boldsymbol{q}^\dagger) \right] - i\epsilon(t).$$

The drive on the qubit is given by $\epsilon(t) = \tilde{\epsilon}(t) \exp(-i\omega_a t)$, where $\tilde{\epsilon}(t)$ is an envelope that rises slowly compared with $\Delta = \omega_a - \omega_q$ and saturates to a constant value ϵ_0. We first transform the Langevin equations to their respective rotating frames at frequencies ω_a and

ω_q by writing the dynamic of $\tilde{\boldsymbol{a}} = \boldsymbol{a} e^{i\omega_a t}$ and $\tilde{\boldsymbol{q}} = \boldsymbol{q} e^{i\omega_q t}$. We find

$$\partial_t \tilde{\boldsymbol{a}} = -\frac{i}{\hbar} \left[\tilde{\boldsymbol{a}}, \boldsymbol{H}_4(\tilde{\boldsymbol{a}} e^{-i\omega_a t}, \tilde{\boldsymbol{a}}^\dagger e^{i\omega_a t}, \tilde{\boldsymbol{q}} e^{-i\omega_q t}, \tilde{\boldsymbol{q}}^\dagger e^{i\omega_a t}) \right] - \frac{\kappa}{2} \tilde{\boldsymbol{a}} \tag{3.5}$$

$$\partial_t \tilde{\boldsymbol{q}} = -\frac{i}{\hbar} \left[\tilde{\boldsymbol{q}}, \boldsymbol{H}_4(\tilde{\boldsymbol{a}} e^{-i\omega_a t}, \tilde{\boldsymbol{a}}^\dagger e^{i\omega_a t}, \tilde{\boldsymbol{q}} e^{-i\omega_q t}, \tilde{\boldsymbol{q}}^\dagger e^{i\omega_a t}) \right] - i\tilde{\epsilon}(t) e^{-i\Delta t}.$$

We ignore the transient regime of the envelope $\tilde{\epsilon}(t)$ and we consider the dynamic of the qubit after a time which is large compared with $1/\Delta$ (realistically, $1/\Delta$ is much shorter than the rise time of any microwave component). For this, we go into a displaced frame of the qubit and look at the dynamic of $\bar{\boldsymbol{q}} = \tilde{\boldsymbol{q}} + \frac{\epsilon_0}{\Delta} e^{-i\Delta t}$, which is now only given by the fourth order Hamiltonian $\boldsymbol{H}_4 \left(\tilde{\boldsymbol{a}} e^{-i\omega_a t}, \tilde{\boldsymbol{a}}^\dagger e^{i\omega_a t}, \left(\bar{\boldsymbol{q}} - \frac{\epsilon_0}{\Delta} e^{-i\Delta t} \right) e^{-i\omega_q t}, \left(\bar{\boldsymbol{q}}^\dagger - \frac{\epsilon_0^*}{\Delta} e^{i\Delta t} \right) e^{i\omega_q t} \right)$. To extract the dynamic of the driven system, we develop this Hamiltonian and neglect the non-resonant terms using the RWA. In order to highlight the interesting dynamics, we do not write the Stark-shift terms. We obtain an effective Hamiltonian

$$\frac{\boldsymbol{H}_{eff}}{\hbar} = -\frac{\alpha}{2} \bar{\boldsymbol{q}}^{\dagger 2} \bar{\boldsymbol{q}}^2 - \chi \bar{\boldsymbol{q}}^\dagger \bar{\boldsymbol{q}} \tilde{\boldsymbol{a}}^\dagger \tilde{\boldsymbol{a}} + \sqrt{2\alpha\chi} \bar{\boldsymbol{q}}^\dagger \bar{\boldsymbol{q}} \left(\frac{\epsilon_0^*}{\Delta} \tilde{\boldsymbol{a}} + \frac{\epsilon_0}{\Delta} \tilde{\boldsymbol{a}}^\dagger \right). \tag{3.6}$$

As we have seen before, we can treat the anharmonic mode $\bar{\boldsymbol{q}}$ using the Pauli matrices and we get a similar equation as equation 3.2 with $|\zeta| = \sqrt{2\alpha\chi} \left| \frac{\epsilon_0}{\Delta} \right|$. The first important feature of this expression is the prefactor $\sqrt{2\alpha\chi}$. For an usual transmon, the anharmonicity is of order $\frac{\alpha}{2\pi} = 200$ MHz, and the observed experimental limit for the drive strength is $\left| \frac{\epsilon_0}{\Delta} \right| \approx 1$. With these parameters, the dispersive coupling χ required to displace a readout cavity with dissipation rate $\frac{\kappa}{2\pi} = 1$ MHz by one photon is of order $\frac{\chi}{2\pi} \approx \frac{\kappa^2}{2\pi\alpha} = 5$ kHz, which places us in the weak dispersive regime $\chi \ll \kappa$. This way, even without a bare longitudinal interaction, we can read the state of the qubit without suffering from the flaws of the strong dispersive regime. The second important feature is the tunability of the interaction. By changing the phase of the strong drive, we can change what quadrature is the qubit coupled to, and by changing the strength of the strong drive, we can change the strength of the interaction, and even switch it off when the qubit is not supposed to be measured.

3.3 Cavity induced dephasing

In the previous sections, we focused on how to achieve interactions that entangle the eigenstates of $\boldsymbol{\sigma}_z$, $|g\rangle$ and $|e\rangle$, to coherent states of a readout cavity, $\left| \alpha_g(t) \right\rangle$ and $\left| \alpha_e(t) \right\rangle$. When the readout cavity leaks information about the qubit-cavity system into the environ-

ment, the qubit is projected into one of the eigenstates of $\boldsymbol{\sigma}_z$, which means that the phase of a superposition of $|g\rangle$ and $|e\rangle$ is lost [75]. In this section, we will quantify how the dissipation of the readout cavity destroys the coherence of a superposition of $|g\rangle$ and $|e\rangle$.

The main dissipation channel of a superconducting cavity is through single-photon loss at rate κ, that can be written using the Lindblad superoperator acting on the density matrix ρ as $\frac{\kappa}{2}\mathcal{D}[\boldsymbol{a}]\rho = \frac{\kappa}{2}\left(2\boldsymbol{a}\rho\boldsymbol{a}^\dagger - \boldsymbol{a}^\dagger\boldsymbol{a}\rho - \rho\boldsymbol{a}^\dagger\boldsymbol{a}\right)$. We assume that the state of the system is always a superposition of the joint states $|\alpha_g(t), g\rangle$ and $|\alpha_e(t), e\rangle$ and we perform a unitary transformation that describes the evolution of such states. Notice that we do not assume what Hamiltonian was used to generate this state, which makes our derivation valid for both the dispersive readout and the conditional displacements readout. We study the Lindblad superoperator in a frame where the field of the readout cavity is

$$\boldsymbol{a} \rightarrow \boldsymbol{a} + \frac{\alpha_g(t) + \alpha_e(t)}{2} + \frac{\alpha_g(t) - \alpha_e(t)}{2}\boldsymbol{\sigma}_z. \tag{3.7}$$

In this frame we first have a displacement to the center of mass of the two coherent states, and then a displacement of $\pm\frac{\alpha_g(t) - \alpha_e(t)}{2}$, dependant on the state of the qubit. This frame has a convenient symmetry which makes $\boldsymbol{\sigma}_z$ appear, even if $\alpha_g(t)$ and $\alpha_e(t)$ are not centered around the origin (as it is the case for the dispersive readout). After this unitary transform, the Lindblad superoperator becomes

$$\frac{\kappa}{2}\mathcal{D}[\boldsymbol{a}]\rho \rightarrow \frac{\kappa}{2}\left(\mathcal{D}[\boldsymbol{a}]\rho + \frac{1}{4}\left|\alpha_g(t) - \alpha_e(t)\right|^2\mathcal{D}[\boldsymbol{\sigma}_z]\rho + ...\right), \tag{3.8}$$

where the last part is either unitary or is neglected using the RWA. We identify the dephasing part with the usual dephasing rate of a qubit written $\frac{\Gamma_\varphi}{4}\mathcal{D}[\boldsymbol{\sigma}_z]\rho$, where Γ_φ is here the measurement induced dephasing. It is time dependent and is given by

$$\Gamma_\varphi(t) = \frac{\kappa}{2}\left|\alpha_g(t) - \alpha_e(t)\right|^2. \tag{3.9}$$

Note that, both for the dispersive readout and the conditional displacement readout, the distance between α_g and α_e is constant after a time $\frac{2}{\kappa}$, after which the decay of the coherence is exponential with a constant rate. However, for a pulsed readout with an arbitrary shape, the measurement rate is not a constant and cannot be determined by the usual exponential fit of the Ramsey fringes. Nevertheless, we define the total dephasing due to a pulsed measurement

lasting a time τ as

$$\gamma_\varphi(\tau) = \frac{\kappa}{2} \int_0^\tau \left| \alpha_g(t) - \alpha_e(t) \right|^2 dt. \tag{3.10}$$

This expression of the dephasing is quite practical from an experimental point of view. The total decoherence can be measured using a Ramsey experiment with fixed time. We display the results of such an experiment in Fig. 3.4(a), where we varied the amplitude of the interaction for a conditional displacement readout. According to equation 3.10, the amplitude decay of the fringes is Gaussian with respect to the coherent states separation. As we will see in the following section, the dephasing is directly linked to the signal-to-noise ratio of a measurement and to the efficiency of the transmission of the signal.

3.4 Signal-to-noise ratio and efficiency

The signal-to-noise ratio is a quantity designed to represent the quantity of information that is received from the system. If the measurement scheme used is efficient, one should be able to extract as much information about the system as it is destroyed by the dephasing. However, some information is lost between the system and the measurement apparatus, either because the signal is reduced due to the dissipation, or because it is corrupted by added noise. From the point of view of the observer, these two processes are not distinguishable and are grouped under a single parameter η, the efficiency [67]. The value of η goes between 0, when no information reaches the observer while the qubit is entirely dephased, and 1, when as much information reaches the observer as it is destroyed. In the spirit of the previous section, we will construct the SNR and the efficiency as quantities that are agnostic to the interaction Hamiltonian and to the temporal shape of the field. However, we will develop the theory only for the cases where the qubit states are entangled with coherent states, and where the travelling coherent states are measured using a phase-sensitive amplifier.

As we have seen, our ability to distinguish the two states of the qubit comes from the difference of the averages of the output field. Even if the readout was ideal, noise is added to the signal because the field operators of the output field do not commute. Therefore, our definition of the SNR must be based on the operators that we measure. For a phase-sensitive
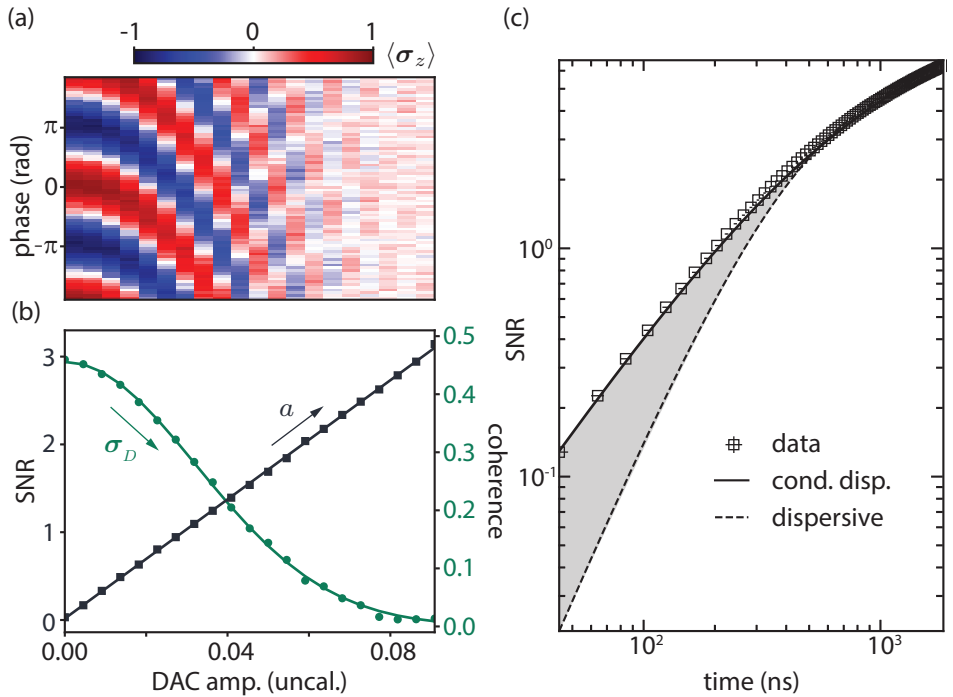
Figure 3.4: Efficiency calibrations and SNR. (a) Ramsey fringes of a measured qubit. The qubit is initially prepared on the equator of the Bloch sphere and a readout pulse, whose amplitude is varied (x-axis), is played. Once the readout cavity is empty, we play a $\pi/2$-pulse with a varying phase (y-axis), on the qubit. When the readout pulse amplitude is larger, the amplitude of the fringes decay because of the cavity-induced dephasing, and the phase of the fringes is shifted because of the Stark-shift.(b) Coherence of the qubit (green) and SNR (gray) as a function of the uncalibrated readout amplitude. The coherence is extracted by fitting the Ramsey fringes in (a). The green solid line is a Gaussian fit of the coherence with standard deviation σ_D, and the gray solid line is a linear fit of the SNR with a slope a. (c) SNR for a time varying square readout pulse. The square markers are data for the conditional displacement readout and the solid black curve is a theory plot with one fit parameter (the photon number). The dashed line is a theory plot of the dispersive readout with the same efficiency η, number of photons and readout lifetime. The gray area emphasizes the different time dependences at small times (see text).

measurement along the real axis, we define the dimensionless measurement operator

$$\boldsymbol{M}(\tau) = \int_0^\tau \left(\frac{\boldsymbol{a}_{out}(t) + \boldsymbol{a}_{out}^\dagger(t)}{2} \right) K(t)dt, \qquad (3.11)$$

where $K(t)$ is a demodulation envelope, chosen by the observer (sometimes called the kernel [87, 88]). For convenience, we will use the quadrature operator, analogous to the position of a harmonic oscillator, $\boldsymbol{Q}_{out}(t) = \frac{\boldsymbol{a}_{out}(t) + \boldsymbol{a}_{out}^\dagger(t)}{2}$. It has been shown that the optimal demodulation envelope is $K(t) = \langle \boldsymbol{Q}_{out}(t) \rangle_g - \langle \boldsymbol{Q}_{out}(t) \rangle_e$, where $\langle . \rangle_i$ indicates that the expectation value of the field operator is taken when the qubit is in a state $|i\rangle$. Notice that, even if we made a choice to have two coherent states that separates along the real axis of phase-space, and to measure along this axis, our situation remains general: one can always choose the measurement axis to follow the separation axis of two such coherent states. We now define the noise operator for the field as the difference between the signal operator and its average value

$$\boldsymbol{M}_N(t) = \boldsymbol{M}(t) - \langle \boldsymbol{M}(t) \rangle. \tag{3.12}$$

The SNR is defined from these operators as

$$\mathrm{SNR}(\tau) = \sqrt{\frac{\left| \langle \boldsymbol{M}(\tau) \rangle_g - \langle \boldsymbol{M}(\tau) \rangle_e \right|^2}{\langle \boldsymbol{M}_N(\tau)^2 \rangle_g + \langle \boldsymbol{M}_N(\tau)^2 \rangle_e}}. \tag{3.13}$$

Note that the noise when the qubit is in $|g\rangle$ or $|e\rangle$ is the same and that we added both contributions. The definition of the SNR differs by a factor $\sqrt{2}$ across the literature, depending on whether the two contributions are added or not. This SNR is also said to be in amplitude. Sometimes the SNR is expressed in energy, which would be the square of the expression used here. The signal part of the SNR is easily calculated and is

$$\left| \langle \boldsymbol{M}(\tau) \rangle_g - \langle \boldsymbol{M}(\tau) \rangle_e \right| = \int_0^\tau \left| \alpha_{out,g}(t) - \alpha_{out,e}(t) \right|^2 dt \tag{3.14}$$

We now evaluate the noise part.

$$\langle \boldsymbol{M}_N(\tau)^2 \rangle = \int_0^\tau \int_0^\tau \left(\langle \boldsymbol{Q}_{out}(t) \boldsymbol{Q}_{out}(t') \rangle - \langle \boldsymbol{Q}_{out}(t) \rangle \langle \boldsymbol{Q}_{out}(t') \rangle \right) K(t) K(t') dt dt' \tag{3.15}$$

$$= \int_0^\tau \int_0^\tau \frac{\delta(t - t')}{4} K(t) K(t') dt dt'$$

$$= \frac{1}{4} \int_0^\tau \left| \alpha_{out,g}(t) - \alpha_{out,e}(t) \right|^2 dt.$$

Finally, the SNR as a function of time is

$$\text{SNR}(\tau) = \sqrt{2 \int_0^\tau \left| \alpha_{out,g}(t) - \alpha_{out,e}(t) \right|^2 dt}. \tag{3.16}$$

From this derivation, we see that the effect of amplitude loss on the coherent states, because of dissipation, and the effect of added noise on their variance both intervene as a factor reducing the SNR. As we cannot distinguish those two phenomena, we simply consider that there is a factor η, called the efficiency, to go from the field inside of the cavity, to the signal received. This way, the SNR is written

$$\text{SNR}(\tau) = \sqrt{2\kappa\eta \int_0^\tau \left| \alpha_g(t) - \alpha_e(t) \right|^2 dt}. \tag{3.17}$$

Similarly to the total dephasing, in steady-state, the $\text{SNR}^2(\tau)$ increases linearly in time. From the equations 3.10 and 3.17, we get an operational way to measure the efficiency, as shown in [89], with

$$\eta = \frac{\text{SNR}^2}{4\gamma_\varphi}. \tag{3.18}$$

Experimentally, the fact that we can determine η with an arbitrary readout pulse shape is convenient. It allows us to fix a pulse duration, such that the readout cavity is in the vacuum state both at the beginning and at the end of the readout pulse, similarly to the cases represented in Fig. 3.1 and 3.2. This way, the qubit can be manipulated without having any photons in the readout cavity and so its coherence can be measured using the contrast of Ramsey fringes, as shown in Fig. 3.4(a). We observe that the coherence decrease of the qubit has a Gaussian shape, as predicted by our theory. For each pulse amplitude we extract the SNR and observe that it increases linearly, as shown in Fig. 3.4(b). Equation 3.18 shows that calibrating the efficiency does not rely on an independent calibration of the number of photons in the readout cavity. The efficiency is simply calculated by fitting the coherence decay with a Gaussian with standard deviation σ_D and the SNR with a line with slope a, which gives, for this particular experiment

$$\eta = \frac{\sigma_D^2 a^2}{2} = 0.6. \tag{3.19}$$

The number of photons in the readout cavity can also be deduced by using a known pulse shape and by looking at the SNR as a function of time. We use a square readout pulse, such that the shape of the readout response is analytic, as in equations 3.1 and 3.3. The calculation of the SNR as a function of time for the dispersive readout and the conditional displacement readout are straight forward [84, 86] and we do not reproduce them here. We use the expression to fit the SNR of the conditional displacement, represented in Fig. 3.4(c), and we use compare it to the expression for the dispersive readout, using the optimal $\chi = \kappa$, the same efficiency and the same number of photons. These two readout schemes are equivalent in steady-state, however, the conditional displacement extracts more information at short times than the dispersive readout. This feature could already be seen by looking at the slope of the trajectories at the origin in Fig. 3.1 and 3.2. The analytic expressions of the SNR tell us that, at short times, the SNR for the dispersive readout goes as $(\kappa\tau)^{5/2}$, whereas for the conditional displacement readout it goes as $(\kappa\tau)^{3/2}$, as can be seen on the log-log plot of the SNR in Fig. 3.4(c).

3.5 Quantum-non-demolition measurement

The theory of the readout of superconducting qubits suggests that a readout protocol gets better when one increases the number of photons and measures for longer. However, this remains true only if the value that we are trying to measure, $\boldsymbol{\sigma}_z$, does not vary while we are measuring it. Previous results showed that increasing the number of photons involved in the measurement results in more transitions between $|g\rangle$ and $|e\rangle$ [90–93]. The measured qubit also has natural energy decays happening during the readout at rate $1/T_1$, which sets a limit on the duration of the measurement. When the state of the qubit after a measurement is the same as the measured state, the measurement is said to be quantum-non-demolition (QND). In this section, we will see how to optimize a readout to be QND and how to quantify how QND it is.

3.5.1 Fast unconditional reset of the readout cavity

In a readout protocol that is modulated with a square shape, the end of the protocol consists in waiting that the readout cavity is empty before being able to reuse the qubit (as shown in the time traces in Fig. 3.1 and 3.2). During this decay, the observer receives less information about the qubit than when the signal is at its maximum. The readout protocol is more optimal if the time when the signal is maximum lasts longer and if, then, the cavity is

reset unconditionally as fast as possible. The unconditional reset maps the joint states $\left|\alpha_g, g\right\rangle$ and $|\alpha_e, e\rangle$ onto $|0, g\rangle$ and $|0, e\rangle$ respectively. Notice that the initial states are orthogonal, and so are the target states. Hence, there is no need for dissipation: a unitary unconditional reset is possible. In practice, it simply requires to reverse the unitary that led to the separation of the two coherent states.
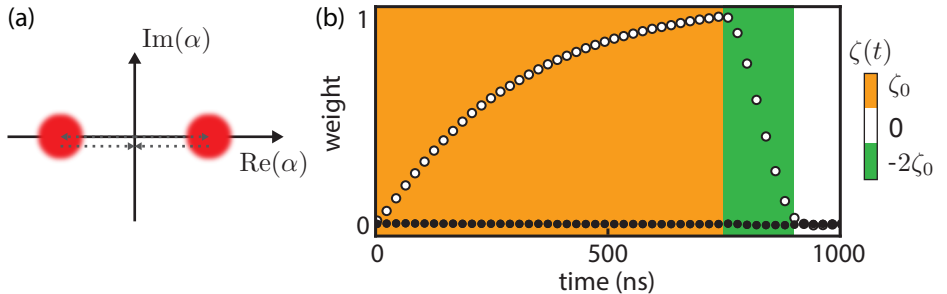
Figure 3.5: (a) Schematic of the dynamics of the internal state of the readout cavity. (b) Optimal demodulation envelope for the conditional displacement readout including a fast reset of the readout cavity. The interaction is turned on to ζ_0, using a square pulse lasting 750 ns (orange area), and the fast reset is implemented by reversing the interaction to $-2\zeta_0$ for 120 ns (green area). The white markers represent the real part of the envelope and the black markers represent its imaginary part. The y-axis is written as a weight applied to each point of an individual trajectory.

Reversing this unitary evolution is easy for the conditional displacement readout. In this case, as we control the phase of the interaction, simply changing the phase of the strong microwave drive will implement the unconditional reset, as shown in Fig. 3.5(a). We show the effect of this reset experimentally in Fig. 3.5(b), where we display the optimal demodulation envelope for the conditional displacement comprising a fast reset of the readout cavity. As we saw in the previous section, this envelope represents, up to a factor in the y-axis, the difference between the average trajectories when the qubit is in $|g\rangle$ and when it is in $|e\rangle$. This experiment was realized using a cavity with a natural energy lifetime of 100 ns and we observed that the readout cavity was entirely empty after using a fast reset protocol lasting 120 ns.

A similar protocol exists for the dispersive readout [88]. It can be understood using similar ideas as the ones developed to create stroboscopic interactions (used in Berkeley to measure a qubit with squeezed light [94] and in our experiment on grid states stabilization). We schematically represent this protocol in Fig. 3.6(a). This protocol starts the same way as a normal dispersive readout with a drive with amplitude ϵ_1 that loads the cavity with a coherent
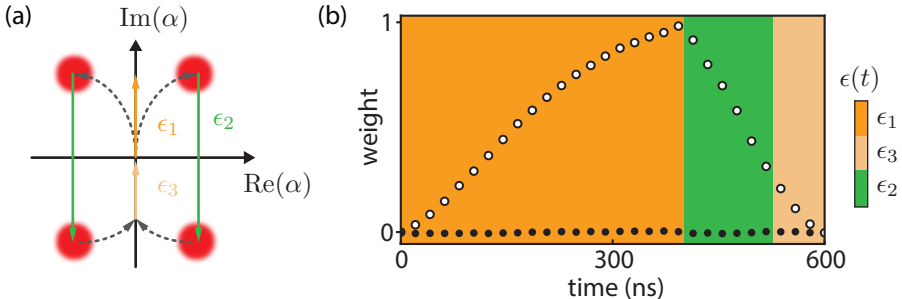
Figure 3.6: (a) Schematic phase-space representation of the fast unconditional reset of the readout cavity using the dispersive interaction (see text for a description of the protocol). (b) Optimal demodulation envelope for the dispersive readout, implementing the fast reset protocol. A square input pulse is initially turned on for 400 ns with amplitude ϵ_1 (orange area). The amplitude of this drive is then changed to an amplitude $\epsilon_2 = -1.58\epsilon_1$ for 110 ns (green area). Finally, the drive is reversed back to an amplitude $\epsilon_3 = 0.7\epsilon_1$ (beige area) for 100 ns. The white markers represent the real part of the envelope and the black markers represent its imaginary part. The y-axis is written as a weight applied to each point of an individual trajectory.

state, which separates along an angle given by the state of the qubit. Here, we propose a second interpretation of this step that will help understanding our stroboscopic conditional displacement in chapter 5. We place ourselves in a frame of the cavity that follows the center of mass of the two coherent states, $\alpha_{CM}(t) = \frac{\alpha_g(t)+\alpha_e(t)}{2}$, and we look at how the dispersive Hamiltonian is transformed in this frame:

$$-\frac{\chi}{2}\boldsymbol{a}^\dagger \boldsymbol{a}\boldsymbol{\sigma}_z \rightarrow -\frac{\chi}{2}\boldsymbol{a}^\dagger \boldsymbol{a}\boldsymbol{\sigma}_z - \frac{\chi}{2}\left|\alpha_{CM}(t)\right|^2 \boldsymbol{\sigma}_z - \frac{\chi}{2}\left(\alpha_{CM}(t)^*\boldsymbol{a} + \alpha_{CM}(t)\boldsymbol{a}^\dagger\right)\boldsymbol{\sigma}_z.$$
(3.20)

After the transformation, we get three terms. The first one is a rotation of each "blob", which is invisible for coherent states (however, this rotation makes it impossible to use squeezed states instead of coherent states in the dispersive readout). The second term is the qubit Stark-shift. Finally, the third term is a conditional displacement. Notice that we performed a similar transformation previously to obtain the conditional displacement readout but, because we were not driving the readout cavity directly, we had $\alpha_{CM}(t) = 0$. For our fast reset protocol, we want to cancel the unitary evolution due to this last conditional displacement term. From our transformation, there is an easy way to perform this: we reverse the sign of α_{CM} by

reversing the amplitude of the drive to a value ϵ_2, as seen with the green arrow in Fig. 3.6(a). Finally, the recombined coherent states are brought back to the origin using a third drive with amplitude ϵ_3.

We used this protocol in practice for the readout of our experiment stabilizing grid states, with a readout cavity whose lifetime was 60 ns. We optimized the exact amplitudes and phases of $\epsilon_{1,2,3}$ using a Python algorithm that minimizes the number of photons in the readout cavity after 600 ns. The resulting optimal envelope, displayed in Fig. 3.6(b), shows that we manage to reset the readout cavity in 200 ns.

3.5.2 Figures of merit of a QND measurement

With all the tools developed in the previous sections, we now know how to optimize a readout protocol. First, we pick the maximum readout amplitude that does not degrade the energy lifetime of the target qubit significantly. Second, we choose the readout time such that, for a given efficiency and number of photons, the two states can be distinguished. Finally, we optimize the shape of the pulse such that the measurements stops as soon as possible once enough information about the state of the qubit is acquired. By choosing a longer readout time, one could get more information about the state of the qubit. This information is only relevant if the state of the qubit has not changed during this acquisition. Thus, there is a trade-off between the SNR of a measurement and how QND it is.

In order to balance this trade-off, we must define figures of merit to quantify how QND a readout protocol is. The two figures of merit we will use are the total fidelity $\mathcal{F}$ and the QND-ness $\mathcal{Q}$. These two quantities are defined using the correlations between two successive measurements. If the state of the target qubit is always left unchanged after a measurement, the correlations in a train of such measurements should always be unity. We measured such correlations in the context of our experiment on a conditional displacement readout. We performed a train of measurements that included a fast reset of the readout cavity, and we plot the demodulated signal as a function of time in Fig. 3.7(a). On this figure, we denote I the classical signal received for each instance of a measurement done with the measurement operator $\boldsymbol{M}(t_{int})$, where t_{int} is the integration time. The specific value of the classical signal I is not a relevant part of a readout scheme and, therefore, it is always normalized by σ, the standard deviation of this classical signal. When the classical signal corresponds to a measurement along the perpendicular quadrature, we name it Q. Because we use a phase-sensitive measurement, this latter quadrature is not measured. We observe that the signal is mostly constant with some discrete jumps between two values. The jumps from the lowest
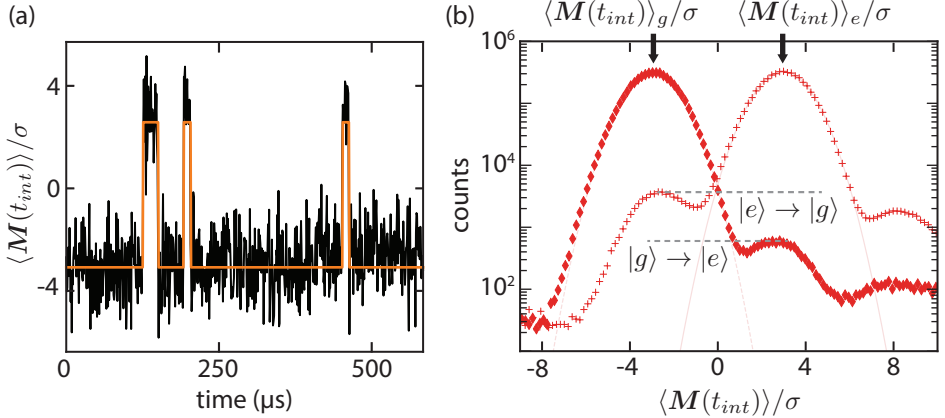
Figure 3.7: Correlations between successive measurements. (a) Results of successive single-shot measurements displaying 6 discrete jumps (black). The orange trace is a guide for the eye and is obtained with a latching filter applied to the data. The correlation between successive measurements indicates that the readout is non-destructive. (b) Histogram of the demodulated signal along the I quadrature with post-selecting the qubit in $|g\rangle$ (diamonds) and in $|e\rangle$ (crosses). The two distributions are fitted with Gaussians (light red, dashed and solid lines). When the qubit starts in $|g\rangle$ (resp. $|e\rangle$) it mostly persists in $|g\rangle$ (resp. $|e\rangle$). The gray dashed lines emphasize the number of jumps from $|g\rangle$ (resp. $|e\rangle$) to $|e\rangle$ (resp. $|g\rangle$).

value, which corresponds to the qubit being in $|g\rangle$, to the highest value, which corresponds to the qubit being in $|e\rangle$, are due to the finite temperature of the qubit mode. The reverse jumps are due to the finite energy lifetime of the qubit.

To estimate the fidelity, we plot in Fig. 3.7(b) a histogram of the measurement distribution after a first stringent post-selection measurement: if the first measurement yields a value $\langle \boldsymbol{M}(t_{int})\rangle < \langle \boldsymbol{M}(t_{int})\rangle_g$ (resp. $\langle \boldsymbol{M}(t_{int})\rangle > \langle \boldsymbol{M}(t_{int})\rangle_e$), where the bar indicates the average of the distribution, we count the second measurement as being post-selected on $|g\rangle$ (resp. $|e\rangle$). This selection does not eliminate the spurious thermal population in the excited $|f\rangle$ state. We fit each distribution with a Gaussian and adjust a threshold to minimize the readout errors. We define the fidelities for the state $|g\rangle$ (resp. $|e\rangle$) as $\mathcal{F}_g = 1 - p(g|e)$ (resp. $\mathcal{F}_e = 1 - p(e|g)$), where $p(i|j)$ is the probability to measure the state i if the qubit was initialized in j. In this particular experiment, we found $\mathcal{F}_g = 99.3\%$ and $\mathcal{F}_e = 98.5\%$. From this, we define the total fidelity $\mathcal{F} = 1 - p(e|g) - p(g|e) = 97.8\%$.

On the other hand, the QND-ness is defined as $\mathcal{Q} = (p_{e,e} + p_{g,g})/2$, where $p_{i,i}$ is the probability to measure the state i twice in two successive measurements. We find $\mathcal{Q} = 98.4\%$.

These numbers are typical in cQED, whether the readout is realized using the dispersive interaction or our conditional displacement readout. In practice, in both cases, $\mathcal{F}$ and $\mathcal{Q}$ are mainly limited by the energy relaxation of the qubit.

4

Stabilization of a manifold of coherent states

The design of quantum computers that are robust against errors is often inspired by the design of classical technologies. For example, the repetition code of classical communications can be adapted to correct quantum bit-flips. In the repetition code, three bits encode the value of one logical bit redundantly, such that one bit-flip can be detected with a majority vote. More subtly, the quantum bit-flip code needs to measure the pairwise parity of the qubits. The work we present in this chapter is analogous to the bit stabilization in a static random access memory of a classical computer (SRAM). For a classical computer, a bit is stabilized using a latching mechanism: in this configuration, a classical voltage has two possible average values, forming the stabilized bit. Small fluctuations around one of these average values are not sufficient to drive the bit to the other value. In order to change the value of such a stabilized bit, a large enough amount of energy is provided to the system to make it latch to the desired value. In a closed system, this energy would remain and could cause oscillations between the two stable states. In order to prevent this, the system needs enough dissipation to stabilize the classical bit around its desired value. Adapting such a scheme for a quantum bit is challenging because all possible quantum superpositions of the two stable states need to be stable too, similarly to how the quantum bit-flip code is more complicated than the classical repetition code. Here, the mechanism that produces the bistability needs to be agnostic to whether the system latches to one state or the other. When the project of engineering such a stabilization started, dissipation was already known to be a valuable resource to stabilize *single quantum states* [95–98], which is different from stabilizing *quantum manifolds of states* [12]. Recently, dissipation engineering has also been used to perform highly non-trivial tasks such as detecting single microwave photons with a low dark count rate [99] and engineering a chemical potential for many-body simulations using superconducting circuits [100].

Dissipation engineering could also be valuable to make new non-reciprocal devices such as isolators or even directional quantum-limited amplifiers [101]. In the following sections, we will show how we engineered a dissipation that stabilizes a manifold of states using strong microwave drive. We will also show that such stable manifolds display a purely quantum effect called Quantum Zeno Dynamics (QZD).

4.1 Dissipative stabilization of a manifold of two coherent states

In this first section, we formalize the idea of a dissipation that stabilizes two coherent states. Our main tool for this is the Lindblad master equation. We consider a system whose dynamic, in some well chosen frame, is entirely given by a dissipation $\partial_t \rho = \frac{\kappa_{\text{stab}}}{2} \mathcal{D}[\boldsymbol{L}_{\text{stab}}]\rho$, where $\boldsymbol{L}_{\text{stab}}$ is, for now, an arbitrary dissipation operator, and κ_{stab} is the rate of this dissipation. If the density matrix ρ is an eigenstate of $\boldsymbol{L}_{\text{stab}}$ with eigenvalue 0, we get $\partial_t \rho = 0$, which means that ρ is a steady state of the system. Moreover, this dissipation can lead all states of quantum system to systematically converge to a unique stable manifold [102]. Our goal here is to find $\boldsymbol{L}_{\text{stab}}$ such that any superposition of two coherent states with opposite phases and a given amplitude α_∞ ($|\pm\alpha_\infty\rangle$) are steady states. For the sake of simplicity, we will always consider that $|\alpha_\infty|$ is large enough that $|\alpha_\infty\rangle$ and $|-\alpha_\infty\rangle$ are orthogonal states to a good approximation. For this, we choose the dissipation operator $\boldsymbol{L}_{\text{stab}} = \boldsymbol{a}^2 - \alpha_\infty^2$. In this particular case, we denote the dissipation rate κ_2. The Lindblad master equation we want to engineer is thus

$$\partial_t \rho = \frac{\kappa_2}{2} \mathcal{D}\left[\boldsymbol{a}^2 - \alpha_\infty^2\right] \rho. \tag{4.1}$$

When an oscillator is subject to this dissipation, the stabilized manifold contains two states and thus encodes a qubit. We define $\left|0/1_L\right\rangle = \left|\mathcal{C}_{\alpha_\infty}^{\pm}\right\rangle \propto |\alpha_\infty\rangle \pm |-\alpha_\infty\rangle$. The dissipation we would like to engineer can be visualized in Fig. 4.1. In the next section, we will explore how to go from this very abstract description of the dissipation to a system that is experimentally feasible.
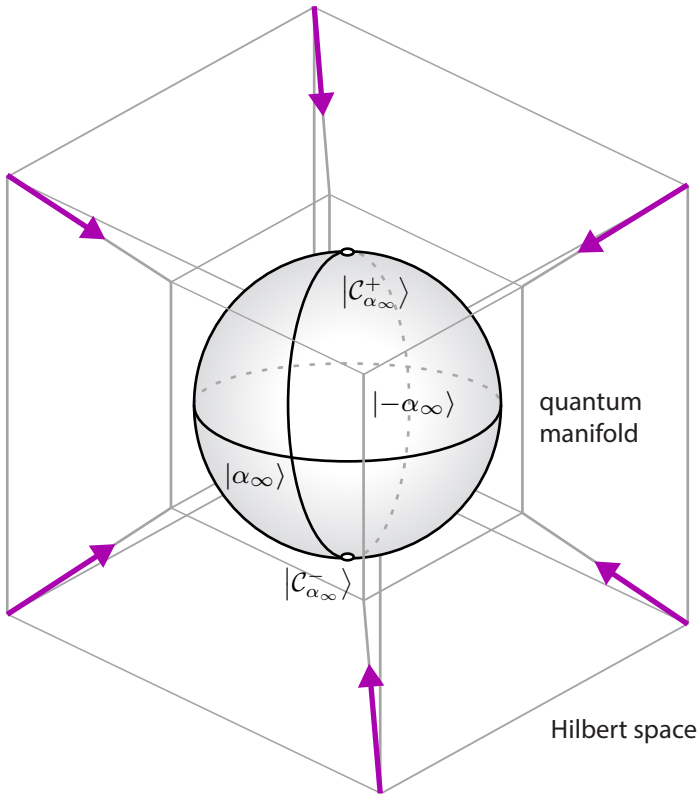
Figure 4.1: Confinement of a quantum state belonging to a large Hilbert space into a 2D quantum manifold. The outer and inner cubes form a hypercube representing a multidimensional Hilbert space. The inner blue sphere represents the manifold of states spanned by the two coherent states $|\pm\alpha_\infty\rangle$. Quantum states such as the even and odd Schrödinger cat states $|\mathcal{C}^{\pm}_{\alpha_\infty}\rangle$ also belong to this manifold. Stabilizing forces direct all states toward the inner sphere without inducing any rotation in this subspace, as indicated by the purple arrows.

4.2 Reservoir engineering of a two-photon dissipation

4.2.1 Adiabatic elimination of the reservoir

In a closed system, any time evolution is unitary, which makes dissipation engineering impossible. With the Lindblad master equation formalism and with the Langevin equations, we take into account the coupling of the system with many external degrees of freedom,

called the environment. We then deduce the dissipation acting on the system by discarding the information contained in the environment, as it is not accessible. We usually refer to the system of interest as the storage, because it stores the quantum information. In this section, we will see that, by inserting an intermediary lossy reservoir between the storage and the environment, we can engineer any type of dissipation on the storage using only unitary operators, as shown in Fig. 4.2. For this, we need that each action of the dissipation operator $\boldsymbol{L}_{\text{stab}}$ is accompanied by the creation of an excitation in the reservoir (whose annihilation operator is $\boldsymbol{r}$), through a Hamiltonian

$$\boldsymbol{H}_{sr} = g\boldsymbol{L}_{\text{stab}}\boldsymbol{r}^{\dagger} + g^{*}\boldsymbol{L}_{\text{stab}}^{\dagger}\boldsymbol{r}. \tag{4.2}$$

Then, as this excitation is quickly lost to the environment at rate κ_r, the reverse process is inhibited. We will now prove that, in the regime $|g|/\kappa_r \ll 1$, the dynamic of the reservoir mode is too fast to be relevant and can be adiabatically eliminated in order to get the dynamic of the system alone.
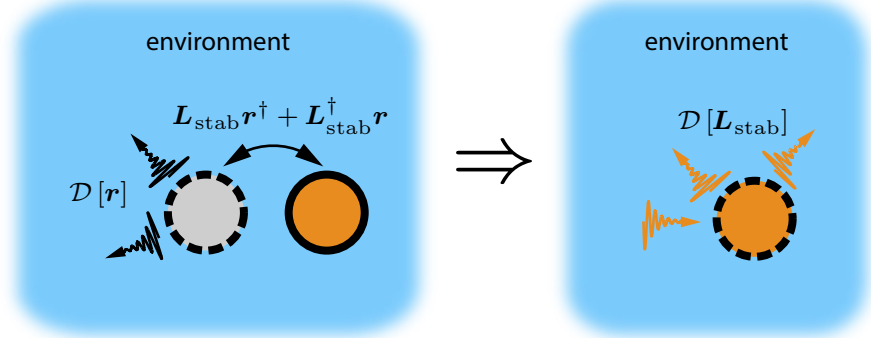
Figure 4.2: Schematic of the engineering of an arbitrary dissipation $\boldsymbol{L}_{\text{stab}}$. The system of interest is in orange, the environment is in blue and the intermediary reservoir is in gray. If the edge of the system or the reservoir is a solid line, it cannot exchange energy with the environment, while if it is a dashed line, it can. On the left, the system is coupled to the reservoir with a Hamiltonian $\propto \boldsymbol{L}_{\text{stab}}\boldsymbol{r}^{\dagger} + \boldsymbol{L}_{\text{stab}}^{\dagger}\boldsymbol{r}$ and the reservoir loses photons one by one. As explained in the text, this dynamic can be reduced to an exotic dissipation $\boldsymbol{L}_{\text{stab}}$ acting on the system (represented by orange arrows).

For this, we assume that, because the reservoir emits photons very quickly, the density matrix of the system comprising the storage and the reservoir, ρ_{sr}, can be written, up to the

second order, as

$$\rho_{sr} = \rho_{00} \otimes |0\rangle \langle 0| + \delta\rho_{01} \otimes |0\rangle \langle 1| + \delta\rho_{10} \otimes |1\rangle \langle 0| + \delta^2 \rho_{11} \otimes |1\rangle \langle 1|, \qquad (4.3)$$

where δ is a small dimensionless parameter and where ρ_{mn} describes the Hilbert space of the storage while $|m\rangle \langle n|$ describes the Hilbert space of the reservoir. The goal is to deduce the dynamic of the density matrix of the storage $\rho_s = \text{Tr}_r(\rho_{sr}) = \rho_{00} + \delta^2 \rho_{11}$ (up to the second order), where Tr_r is the partial trace over the reservoir. We can get the dynamic of ρ_{mn} by projecting the Lindblad equation over $\langle m|$ and $|n\rangle$. The dynamic of ρ_{00} is thus given by

$$\frac{1}{\kappa_r} \partial_t \rho_{00} = -\frac{i}{\kappa_r} \langle 0| [\boldsymbol{H}_{sr}, \rho_{sr}] |0\rangle + \delta^2 \rho_{11} \qquad (4.4)$$

$$= -i\delta \left(\frac{g^*}{\kappa_r} \boldsymbol{L}_{\text{stab}}^\dagger \rho_{10} - \frac{g}{\kappa_r} \rho_{01} \boldsymbol{L}_{\text{stab}} \right) + \delta^2 \rho_{11}. \qquad (4.5)$$

This equation shows that the dynamic of all the parts of the density matrix will be coupled. We now find the dynamic for $\rho_{01,10,11}$:

$$\delta \frac{1}{\kappa_r} \partial_t \rho_{01} = -i \frac{g}{\kappa_r} \boldsymbol{L}_{\text{stab}} \rho_{00} - \delta \frac{1}{2} \rho_{10} \qquad (4.6)$$

$$\delta \frac{1}{\kappa_r} \partial_t \rho_{11} = -i \left(\frac{g}{\kappa_r} \boldsymbol{L}_{\text{stab}} \rho_{01} - \frac{g^*}{\kappa_r} \boldsymbol{L}_{\text{stab}}^\dagger \rho_{10} \right) - \delta \rho_{11}. \qquad (4.7)$$

The adiabatic approximation comes into play at this moment. For this, we assume $\frac{|g|}{\kappa_r} \sim \delta \ll 1$. In this case, notice that, in the dynamics of $\rho_{01,10,11}$, the δ simplifies and that $\rho_{01,10,11}$ relax very quickly to a steady-state. We thus perform the approximation $\partial_t \rho_{01,10,11} = 0$, and thus

$$\delta\rho_{10} = -2i \frac{g}{\kappa_r} \boldsymbol{L}_{\text{stab}} \rho_{00} \qquad (4.8)$$

$$\delta^2 \rho_{11} = 4 \frac{|g|^2}{\kappa_r^2} \boldsymbol{L}_{\text{stab}} \rho_{00} \boldsymbol{L}_{\text{stab}}^\dagger. \qquad (4.9)$$

We replace these into eq. 4.4 and we get

$$\partial_t \rho_{00} = \frac{2|g|^2}{\kappa_r} \left(2\boldsymbol{L}_{\text{stab}} \rho_{00} \boldsymbol{L}_{\text{stab}}^\dagger - \boldsymbol{L}_{\text{stab}}^\dagger \boldsymbol{L}_{\text{stab}} \rho_{00} - \rho_{00} \boldsymbol{L}_{\text{stab}}^\dagger \boldsymbol{L}_{\text{stab}} \right) \qquad (4.10)$$

$$= \frac{2|g|^2}{\kappa_r} \mathcal{D}\left[\boldsymbol{L}_{\text{stab}}\right] \rho_{00}. \qquad (4.11)$$

The same derivation is done in the supplementary materials of [36], where we actually carry all spurious terms such as the Kerr effect and the dissipation of the storage. As long as these spurious effects are much smaller than all the other terms in the dynamic, the result is unchanged.

We started this section by having to engineer an exotic dissipation and we changed this problem to having to engineer an exotic interaction Hamiltonian. In the next section we will see how to engineer this interaction in the case of the dissipation $\boldsymbol{L}_{\text{stab}} = \boldsymbol{a}^2 - \alpha_\infty^2$.

4.2.2 Parametric pumping of the two-photon interaction

Let us develop the type of interaction Hamiltonian that corresponds to the stabilization of two coherent states:

$$\boldsymbol{H}_{sr} = g_2 \left(\boldsymbol{a}^2 - \alpha_\infty^2 \right) \boldsymbol{r}^\dagger + g_2^* \left(\boldsymbol{a}^2 - \alpha_\infty^2 \right)^\dagger \boldsymbol{r} \qquad (4.12)$$

$$= g_2 \boldsymbol{a}^2 \boldsymbol{r}^\dagger + g_2^* \boldsymbol{a}^{2\dagger} \boldsymbol{r} + g_2 \alpha_\infty^2 \boldsymbol{r}^\dagger + \left(g_2 \alpha_\infty^2 \right)^* \boldsymbol{r}, \qquad (4.13)$$

where g_2 is the strength of the two-photon coupling. This Hamiltonian has been extensively studied in optics and is known as the Degenerate Parametric Oscillator (DPO) [103]. Experimentally, this Hamiltonian has been used first in the regime where the "pump" strength on the reservoir, here noted $g_2 \alpha_\infty^2$ was much larger than the linewidth of the reservoir κ_r. This way, the fluctuations of $\boldsymbol{r}$ could be neglected and the operator could be replaced by a large number. In this regime, the DPO could be used to generate a large amount of squeezed light [104]. The same Hamiltonian has been studied in the opposite regime $(g_2 \alpha_\infty^2) \ll \kappa_r$ in 1988 and was known to stabilize superpositions of coherent states [105]. This Hamiltonian is naturally realized in some crystals, where a three-wave mixing term (referred to as $\chi^{(2)}$) converts two photons into a single one at higher frequency. How can a similar Hamiltonian be obtained in cQED?

The answer to this is the same as throughout this thesis: we use the four-wave mixing capability of the Josephson junction and we use a strong microwave drive in the stiff pump ap-
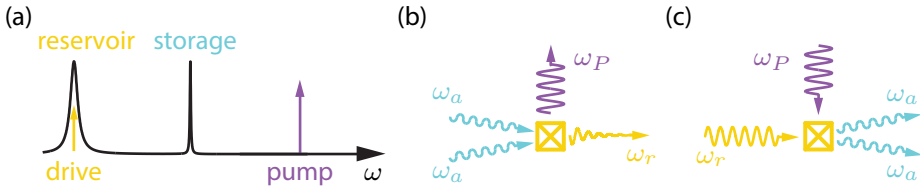
Figure 4.3: (a) Schematic spectrum of different modes involved in the experiment. The pump and drive tones are shown as vertical arrows. (b and c) Four-wave processes involved in the nonlinear damping and nonlinear drive, respectively, experienced by the storage. In (b), two photons of the storage combine and convert, stimulated by the pump tone, into a reservoir photon that is irreversibly radiated away by the transmission line. This process is balanced by the conversion of the drive tone, which, in the presence of the pump, creates two photons in the storage (c).

proximation. Because this development is already done, in general, in chapter 2 and because it is already used for the conditional displacement readout in chapter 3, we will not mention all the details (they are available in [36, 37]), but we will summarize the main ingredients of this system. The main part of this system comprises two modes: the storage (a) and the reservoir (r) coupled through the fourth order Josephson Hamiltonian $H_4\left(a, a^\dagger, r, r^\dagger\right)$. The second part comprises the microwave drives on the reservoir. One of them is strong and detuned, and thus is in the stiff pump approximation, we call it the "pump", while the other one is weak and on resonance with the reservoir, and thus is in the opposite regime and can be adiabatically eliminated as seen in the previous subsection, we call it the "drive". The pump has an amplitude ϵ_P and an angular frequency

$$\omega_P = 2\omega_a - \omega_r, \tag{4.14}$$

where ω_a and ω_r are the angular frequencies of the storage and of the reservoir (taking into account frequency Stark-shifts induced by the drives). The drive has an amplitude ϵ_D and an angular frequency $\omega_D = \omega_r$. At this point of the development, we usually go into the doubly rotating frame of the storage and of the reservoir and into the tracking frame of the drives. Here, only one microwave drive is in the stiff pump approximation and should be tracked with this change of frame. The rise time of the envelope of this pump drive should be small compared to the detuning to the reservoir, which is $\Delta = 2\left(\omega_a - \omega_r\right)$. Once again, this is not a concern for our detuning of several GHz. The last step of this development is to neglect the terms that oscillate quickly in time using the RWA. Overall, we get the same

Hamiltonian as in equation 4.12, with

$$g_2 = \frac{\chi_{sr}}{2} \frac{\epsilon_P}{\Delta} \tag{4.15}$$

$$\alpha_\infty = \pm\sqrt{\frac{2\epsilon_D}{\chi_{sr}} \frac{\Delta}{\epsilon_P}}, \tag{4.16}$$

where χ_{sr} is the dispersive shift between the storage and the reservoir. The normalized amplitude of the pump is usually referred to as $\xi \equiv \frac{\epsilon_P}{\Delta}$ and, experimentally, is at best of order 1. The way we use the four-wave mixing capability of the Josephson junction to engineer the stabilization is summarized in Fig. 4.3. We will now see how to implement this in a 3D cQED architecture.

4.3 Experimental implementation

In order to reach the regime described by Wolinsky and Carmichael [105], the stabilization rate needs to be larger than the intrinsic dissipation rate of the storage. For this particular case, we denote the stabilization rate $\kappa_2 = \frac{4|g_2|^2}{\kappa_r}$ and we denote the single photon dissipation of the storage κ_1. We define the figure of merit

$$\mathcal{C}_2 = \frac{\kappa_2}{\kappa_1} \tag{4.17}$$

$$= \frac{4|g_2|^2}{\kappa_r \kappa_1}, \tag{4.18}$$

which is larger than 1 if the quantum features of this stabilization are visible. This figure of merit is very similar to the cooperativity that is usually defined in frequency conversion experiments.

Our first experimental platform reached the regime $\mathcal{C}_2 = 1$ and showed the quantum features of this regime [36]. We then refined the design of the experiment and reached $\mathcal{C}_2 = 100$, which allowed us to show the coherent manipulation of quantum information within this stabilized manifold, using the effect known as quantum Zeno dynamic. Here, we describe the latter optimized experimental architecture, represented in Fig. 4.4.

In this architecture, the storage is the fundamental mode of an aluminum post-cavity [64, 65] and the reservoir is a transmon anharmonic oscillator that evacuates its energy quickly through a strong coupling with a transmission line. The storage mode is coupled to another transmon whose role is to perform the Wigner tomography of the storage (it is referred to
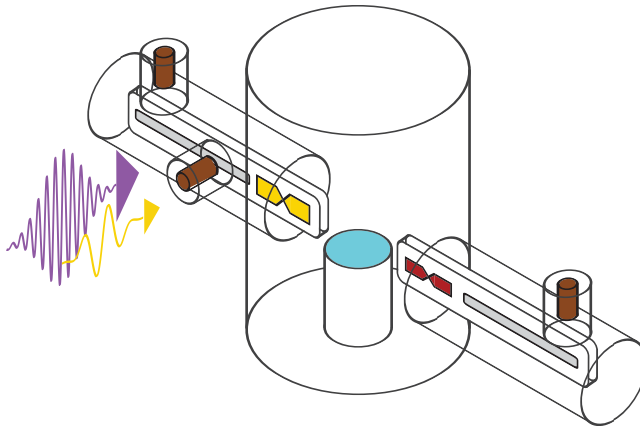
Figure 4.4: Schematical representation of the experimental device. The quantum manifold is stabilized within the Hilbert space of the fundamental mode of an aluminum post cavity (cyan, storage in the text). This resonator is coupled to two Josephson junctions on sapphire (yellow for the reservoir and crimson for the Wigner transmon, see text), which are read out by stripline resonators (gray). Three couplers (brown) bring microwave drives into the system and carry signals out of it.

as Wigner transmon). When the system is not driven, its dynamic is well described by the usual dispersive Hamiltonian. We summarize the parameters of the experimental device in tables 4.1 and 4.2. Let us first look at the coupling between the reservoir and the storage. We see that, on the one hand, the lifetime of the storage is 92 μs which corresponds to $\kappa_1/2\pi = 1.7\,\text{kHz}$. On the other hand, $\chi_{sr}/2\pi = 471\,\text{kHz}$, which means that, for the experimental limit $\xi = 1$, we get a figure of merit $\mathcal{C}_2 > 100$. We now look at the coupling between the storage and the Wigner transmon. The dispersive coupling of 2.29 MHz makes the speed of a parity measurement large compared to the coherence times of the Wigner transmon. This way, we get a good contrast for the Wigner function. More details about how we measured each parameter are available in the supplementary materials of our paper [37].

4.4 Steady-state of the two-photon stabilization

The first experiments we carried on this system were made to prove that, in steady-state, we could convert photons from a drive at the frequency of the reservoir into photons in the storage, and also to prove that the resulting state of the storage was confined in two wells.

Table 4.1: Frequencies, coherence times and thermal populations of each mode of the experimental design.

Mode	Frequency (GHz)	T_1 (µs)	T_2 (µs)	Thermal population
W. Transmon	5.89064	70	30	5%
Storage	8.10451	92	40	$\leq 1\%$
Reservoir	6.6373	0.317	-	0.7-2%

Table 4.2: Parameters of the Hamiltonian of the experimental device.

$\chi_{ij}/2\pi$ (MHz)	W. transmon	Storage	Reservoir
W. transmon	268	-	-
Storage	2.29	~ 0.003	-
Reservoir	-	0.471	86

This means that, at this point of the chapter, the physics we describe is entirely classical. As we will explain in this section, these classical experiments were mostly used to calibrate the parameters of the driven system, such as the resonance condition, the stabilization rate and the size of the stabilized coherent states.

4.4.1 Finding the frequency matching condition

In order for this experiment to work, it requires all the frequencies of the drives to be aligned according to the frequency matching condition given by equation 4.14. This task would be easy if the relevant frequencies were fixed, however, in a driven system, all the frequencies change with the power of the drives because of the Stark-shift. In order to tune the frequencies of the drive, we want to observe the conversion of reservoir photons into storage photons.

We first perform an experiment where the reservoir is weakly probed in transmission and where the strong pump tone is played with various frequencies around the resonance condition. The result of this experiment is displayed in Fig. 4.5(a). We see that, when the probe drive does not meet the resonance condition, it is transmitted with the usual Lorentzian response, and when it does meet the resonance condition, its transmission is strongly sup-
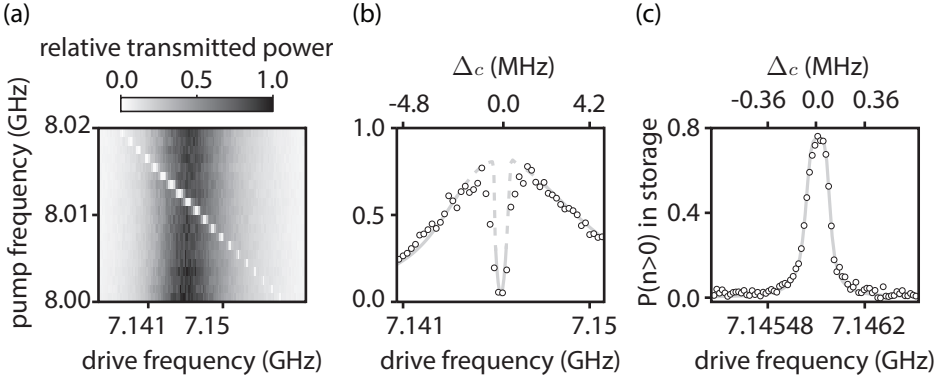
Figure 4.5: Spectroscopy of the two-photon conversion process. (a and b) CW spectroscopy of the reservoir in presence of the pump tone. The grayscale represents transmitted power of the probe tone through the readout as a function of probe frequency (horizontal axis) and pump frequency (vertical axis). In (a), the usual Lorentzian response develops a sharp and deep dip, signaling conversion of probe photons into storage photons. The dip frequency decreases as the pump frequency increases. (b) Cut of the gray-scale map (a) at $\omega_P/2\pi$ giving a centered dip. The top axis represents the detuning from the conversion matching condition $\Delta_c = (2\omega_s - \omega_P)/2\pi$ (c) Conversion seen from the storage, represented as the probability of not being in the vacuum state, as a function of drive frequency. The dashed and full lines in (b) and (c) are the result of a numerical computation of the steady-state density matrix of the system, sweeping the drive frequency and keeping the pump frequency fixed.

pressed. in Fig. 4.5(b), we show a cut of this experiment where the frequency of the transmission suppression matches the resonance frequency of the reservoir mode.

On this latter plot, the gray line demonstrates our ability to model this transmission suppression. The end of this subsection will develop our method to model this transmission. Let us first summarize the results of this model and we will then explicit it mathematically. It is important at this point to remember that this experiment reveals the steady-state of the reservoir. We expect that, in such a steady-state, the number of photons in the storage saturates to $|\alpha_\infty|^2$, and thus, the transmission dip cannot be due to the photons being continuously converted from the reservoir drive to the storage. If the energy of the drive does not go to the storage and is not stored in the reservoir, where does it go? In fact, the drive is almost fully reflected from the reservoir. We also observe that this dip does not reach exactly 0. The reservoir mode has a residual small coherent state that feeds energy into the storage cavity to compensate for its internal loss. In order to understand this interpretation, let us look at the

Langevin equation of the driven system:

$$\partial_t r = -i\Delta_D r - ig_2^* a^2 - i\epsilon_D - \frac{\kappa_r}{2} r + \sqrt{\kappa_r} r^{in} \tag{4.19}$$

$$\partial_t a = -i\frac{\Delta_P + \Delta_D}{2} a - 2ig_2 a^\dagger r - \frac{\kappa_1}{2} a + \sqrt{\kappa_1} a^{in}, \tag{4.20}$$

where Δ_D is the detuning of the drive frequency from the reservoir mode frequency and Δ_P is the detuning of the pump frequency from the resonance matching condition. We treat these equations classically by replacing the operators by complex numbers representing their average. Now, in steady-state, we have

$$0 = -i\Delta_D r - ig_2^* a^2 - i\epsilon_D - \frac{\kappa_r}{2} r \tag{4.21}$$

$$0 = -i\frac{\Delta_D + \Delta_P}{2} a - 2ig_2 a^* r - \frac{\kappa_1}{2} a. \tag{4.22}$$

One solution is

$$a = 0, \qquad r = -\frac{i\epsilon_D}{i\Delta_D + \kappa_r/2}. \tag{4.23}$$

This is the usual Lorentzian response of a driven-damped oscillator. Now assuming $a \neq 0$, we obtain a second solution for r:

$$r = \frac{-(\Delta_D + \Delta_P) + i\kappa_1}{4g_2} e^{i\theta_s}, \tag{4.24}$$

where θ_s is the phase of the storage (hence, the phase of α_∞). When the frequency matching condition is fulfilled, $|r| = \frac{\kappa_1}{g_2} \ll 1$, which corresponds to a small coherent state feeding energy to the storage to compensate for its internal loss. The modulus square of this field describes a parabola in Δ_D, which corresponds to the dip we observe in Fig. 4.5(b).

The fact that we have two sets of solutions is typical of a bistable state with a bifurcation. From equation 4.16, we know the amplitude of the stabilized coherent states $|\pm\alpha_\infty\rangle$ when the frequency matching condition is met. What is this amplitude when the drives are detuned from this condition and with damping of the storage? We solve the classical equations of motions with our previous solution for r and find

$$\alpha_\infty^2 = \frac{1}{4|g_2|^2} \left(-\Delta_D + i\frac{\kappa_r}{2}\right)(\Delta_P + \Delta_D - i\kappa_1) - \frac{\epsilon_D}{g_2^*}. \tag{4.25}$$

Using this expression, we can calculate the probability of not being in the vacuum state $(1 -$

$\left|\langle 0|\alpha_\infty\rangle\right|^2$) as a function of the parameters of the system. When this probability is not 0, we have converted photons from the microwave drives into photon in the storage mode. This theory matches the experimental results displayed in Fig. 4.5(c).

4.4.2 Classical bi-stability of the nonlinearly driven damped oscillator

So far, we have only shown experimental evidence that there was an energy input into the storage without driving it at its own frequency, meaning that frequency conversion takes place. However, to prove that our theory describes our system, we need to show that the field of the storage has two possible phases. In order to show this, the pump and the drive need to keep their phase over the duration of the experiment. For this, we engineered a phase-locking mechanism between these drives that is detailed in the paper [36]. We show this bistability behavior by initializing the storage in various coherent states with constant amplitude and whose phase takes 8 values regularly spaced over a span of 2π. We then measure the Wigner function of the storage and display the results in Fig. 4.6. We observe that the final state of the storage is a classical mixed state of the two possible stable steady states $|\pm\alpha_\infty\rangle$. The weight of each possible stable steady state (SSS) is determined by how close the initial state is to each well. At this point, the dynamic of the driven system resembles that of a classical double well. In the next sections we will show that our stabilization also has properties that are fundamentally quantum in nature.

4.5 Falling into two indistinguishable potential wells

The main innovation of this experiment over previous implementations of bistable driven systems and over the classical SRAM is the ability of the steady states to be in a superposition without being disturbed by the manifold stabilization. This feature is purely quantum in nature and gives rise to an interesting effect when the state of the storage can fall into one well or the other with equal probabilities. In this situation, the state does not choose a well and falls into a superposition state of two coherent states. One could argue that this effect was already observed in Fig. 4.6, however, for an initial coherent state with a large number of photons located on the separatrix of these wells, the resulting state is not pure [12]. Because of this, we have, so far, only observed statistical mixtures of the two steady states. If the storage cavity is initially in a vacuum state, then its state remains pure while falling into the two indistinguishable potential wells and it forms a Schrödinger cat state. Eventually, the single-
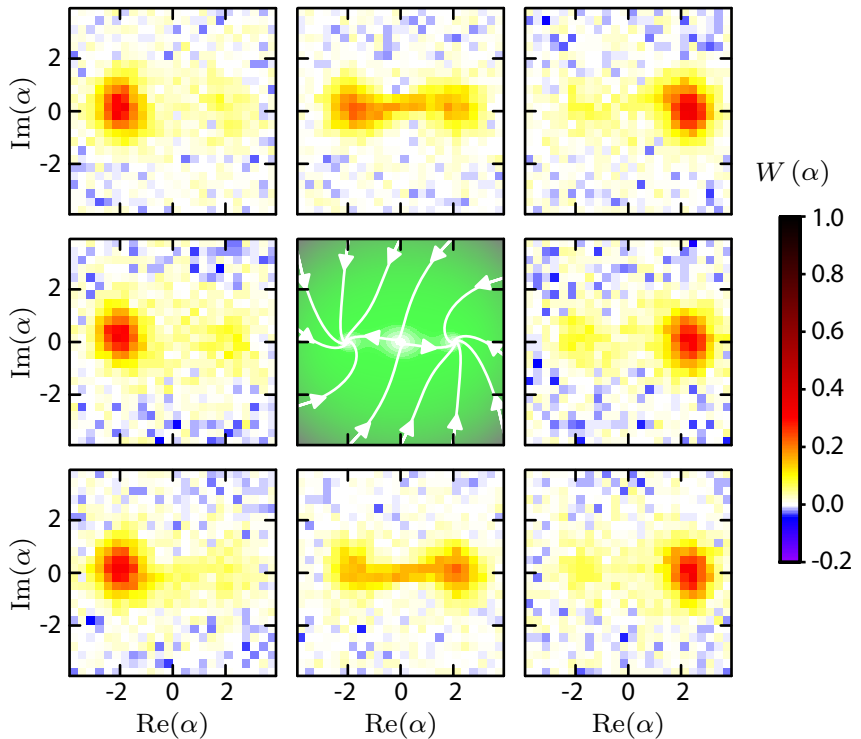
Figure 4.6: Bistable behavior of the steady-state manifold of the nonlinearly driven damped storage oscillator. The central panel shows the theoretical classical equivalent of a potential of the storage nonlinear dynamics. The modulus of the velocity (color) has three zeroes corresponding to two steady states $|\pm\alpha_\infty\rangle$ and the saddle point $|0\rangle$. Trajectories initialized on the panel border converge to one of these two steady states. These trajectories are curved due to the Kerr effect. The outside panels show the measured Wigner function $W(\alpha)$ of the storage after 10 μs of pumping for different initial states. For each panel, we initialize the storage in a coherent state of amplitude αk, where $|\alpha k| = 2.6$ and various $\arg(\alpha k)$. The storage converges to a combination of $|\pm\alpha_\infty\rangle$. The weight of each of these two states and the coherence of their superposition is set by the initial state. For the initial phases $\arg(\alpha k) = 0, \pm\pi/4$, the storage mainly evolves to $|\alpha_\infty\rangle$, with only a small weight on $|-\alpha_\infty\rangle$. On the other hand, for initial phases $\arg(\alpha k) = \pm 3\pi/4, \pi$, the state mainly evolves to $|-\alpha_\infty\rangle$, with a small weight on $|\alpha_\infty\rangle$. For the initial phases $\arg(\alpha k) = \pm\pi/2$, the initial state is almost symmetrically positioned with respect to the two states $|\pm\alpha_\infty\rangle$ and has no definite parity (even and odd photon number states are almost equally populated). Hence, the state evolves to a mixture of $|\pm\alpha_\infty\rangle$.

photon dissipation of the storage cavity dephases the obtained Schödinger cat state and it also becomes a statistical mixture of coherent states. We observed the transient coherent regime in our first experiment on the manifold stabilization [36] and we demonstrated it using the Wigner representation of the state of the storage mode at different times, as shown in Fig. 4.7. Our data also agrees with numerical simulations that use the parameters measured from our system.
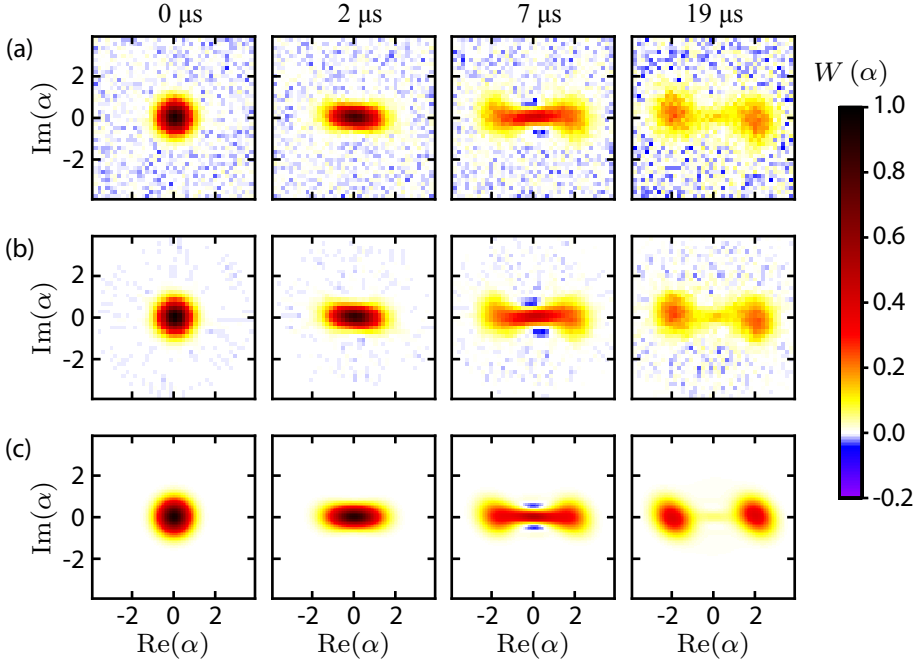
Figure 4.7:   Time evolution of the storage state in the presence of the nonlinear drive and dissipation processes. The panels correspond to measured data (a), reconstructed density matrices [26] (b), and numerical simulations (c). They display the Wigner function after a pumping duration indicated at the top of each column. The storage is initialized in the quantum vacuum state at time $t = 0\,\mu s$. First, the state squeezes in the Q quadrature ($t = 2\,\mu s$). Small but visible negativities appearing at $t = 7\,\mu s$ indicate that the superposition of the steady states shown in Fig. 4.6 is now coherent and that a continuous evolution from a squeezed state to a quantum state approximating a Schrödinger cat state is taking place. Finally, these negativities disappear as a consequence of the unavoidable storage single-photon loss, and the state decays into a statistical mixture of the two steady states ($t = 19\,\mu s$).

We could also check that our stabilization does not dephase superpositions of the two

steady states by preparing a known Schrödinger cat state and then stabilize it. If its coherence decays at the expected rate for a given cat state, then its decoherence is not due to the engineered stabilization, but by the residual single-photon dissipation. We tested this in our improved experimental implementation described previously [37]. We describe that experiment in the next section, where we also experimented on the so-called Quantum Zeno Dynamic.

4.6 Quantum Zeno Dynamics in a manifold of coherent states

We previously described the dissipation that acted on Schrödinger cat states and, in particular, we saw that there were no continuous errors that could cause a jump between the two distant coherent states. However, by considering the simple single-photon dissipation, we saw that there is a continuous error that links two Schrödinger cat states $|\mathcal{C}_\alpha^\pm\rangle$. We usually summarize this property using the language of a logical qubit encoded using these cat states and say that, within this manifold, phase-flips are suppressed exponentially while bit-flips are enhanced polynomially (with respect to the size of the encoding cat states). Similarly, we interpret this fact by saying that the states $|\pm\alpha_\infty\rangle$ are analogous to two positions of an oscillator that are very distinct from each other (compared to their fluctuations). Because these two positions are easy to distinguish for the environment, the dissipation has a large back-action onto the phase of their coherent superpositions. The noise from the environment is converted onto a continuous noisy drive that changes the phase of the coherent superposition of two coherent states. The result of this continuous noisy drive on the Wigner function of a Schrödinger cat state is a continuous loss of contrast of its fringes. As we have seen previously, this decay is exponential in time and given by the rate $\kappa_{\text{eff}} = 2\bar{n}\kappa_1$, where $\bar{n}$ is the average photon number.

This continuous exponential decay is due to the fact that the stabilization is agnostic to the phase of the superposition. When an external drive changes the phase of the superposition, the stabilization does not act to correct this change. It stabilizes only the position of the center of the coherent states $|\pm\alpha_\infty\rangle$. If the environment can induce continuous noisy transitions between different superpositions of coherent states, it means that we can use a known coherent drive to induce them too. However, because we have a constant phase on this drive, we can track this evolution in time.

It is important to notice here that this evolution is not possible if the engineered dissi-

pation stabilizes a single state. In this latter case, all dynamic is frozen by the stabilization as predicted by the effect called the Quantum Zeno Effect (QZE) [106, 107], which has been experimentally tested [108]. However, when the dissipation stabilizes a manifold of states, movement is allowed within this manifold, as predicted by the effect called Quantum Zeno Dynamics (QZD) [109]. QZD offers a path towards quantum computation while the encoded qubit stays in a "decoherence free subspace" [102, 110–113]. In the context of this thesis, QZD allows to perform quantum computation on qubits encoded in Schrödinger cat states [12], which have a very strong noise bias (both single and two-qubit gates).

Let us first formalize these statements. We want to see what is the action of a resonant drive on the storage within the stable manifold. A standard way to formalize this problem is to apply the manifold projector $\mathbf{\Pi} = \mathbf{\Pi}_+ + \mathbf{\Pi}_-$ (with $\mathbf{\Pi}_\pm = \left| \mathcal{C}_{\alpha_\infty}^\pm \right\rangle \left\langle \mathcal{C}_{\alpha_\infty}^\pm \right|$) to the storage drive $\epsilon_s(t)\boldsymbol{a}^\dagger + \epsilon_s^*(t)\boldsymbol{a}$. This projection is only valid when $\epsilon_s \ll \kappa_2$, meaning that the storage drive strength needs to be much smaller than the stabilization strength to respect the adiabaticity condition [112–115]. We get

$$
\begin{aligned}
& (\mathbf{\Pi}_+ + \mathbf{\Pi}_-) \left(\epsilon_s(t)\boldsymbol{a}^\dagger + \epsilon_s^*(t)\boldsymbol{a} \right) (\mathbf{\Pi}_+ + \mathbf{\Pi}_-) \\
& = \left(\epsilon_s(t)\alpha_\infty^* + \epsilon_s^*(t)\alpha_\infty \right) \left(\left| \mathcal{C}_{\alpha_\infty}^+ \right\rangle \left\langle \mathcal{C}_{\alpha_\infty}^- \right| + \left| \mathcal{C}_{\alpha_\infty}^- \right\rangle \left\langle \mathcal{C}_{\alpha_\infty}^+ \right| \right) \\
& = 2\mathrm{Re} \left(\epsilon_s(t)\alpha_\infty^* \right) \boldsymbol{X}_L,
\end{aligned}
\tag{4.26}
$$

where $\boldsymbol{X}_L$ is the logical Pauli operator in the manifold of cat states depicted in Fig. 4.1. Equation 4.26 tells us that, for this continuous rotation to happen, the drive needs to couple to the same variable that encodes $|\pm\alpha_\infty\rangle$. For example, if α_∞ is real, the drive must create a displacement along the momentum axis.

In order to demonstrate that the QZD takes place in the stable manifold of coherent states, we use the pulse sequence depicted in Fig. 4.8. The main innovation of this pulse sequence is that the initial state is not prepared by letting a vacuum state evolve into a Schrödinger cat state. Instead, we use optimal control pulses to prepare such cat states [32] or a simple displacement to create a coherent state. These control methods yield better initial states that are then stabilized. During this stabililization we add a constant weak storage drive with amplitude ϵ_s for a duration Δt. The phase of the drive is locked to create a displacement that is orthogonal to the phase of the stabilization, as described in the supplementary materials of our paper [37]. At the end of the sequence, we measure the effect of the QZD on the initial state by taking a Wigner tomography.

When the phase of the storage drive is chosen correctly, we observe that the fringes of
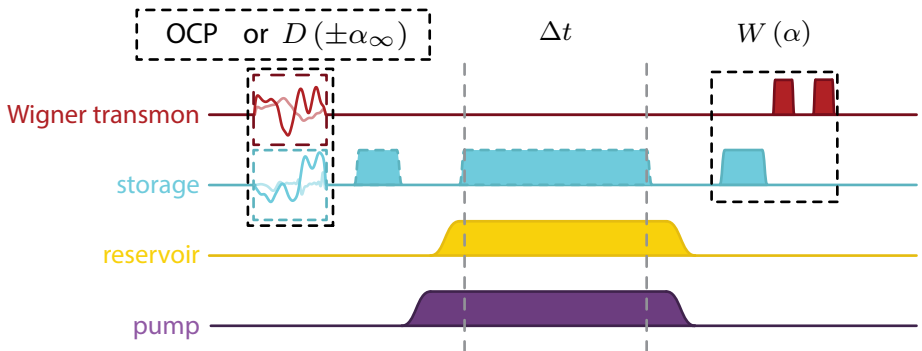
Figure 4.8: Pulse sequence to test the Quantum Zeno Dynamics. The storage is initialized either in a Schrödinger cat state $\propto |\alpha_\infty\rangle \pm |-\alpha_\infty\rangle$ with optimal control pulses (OCP) or in a coherent state $|\pm\alpha_\infty\rangle$ with a displacement $\boldsymbol{D}\,(\pm\alpha_\infty)$. The drives stabilizing the manifold are turned on in 24 ns (purple and yellow). They are on for a duration Δt during which the storage drive (cyan) can be turned on to induce the parity oscillations. The drives are left on for another 500 ns and then turned off in 24 ns, after which the Wigner function is measured.

a cat state roll continuously while the center of the coherent states $|\pm\alpha_\infty\rangle$ are stabilized, as shown on the Wigner functions in fig. 4.9. It is remarkable here that the coherence of the cat state remains while it is being stabilized.

We now look at the time dependence of this effect. For this, we consider the center point of the Wigner function ($W\,(0)$) as a function of time, instead of the entire state tomography. This point is the parity of the state, which we expect to oscillate in time. We perform such experiments for various state sizes ($\bar{n} = 2, 3, 5$) and for various drive strength and we report our results in Fig. 4.10(a). On this figure, the free decay of the cat states reveal a coherence time which is in agreement with the calculated coherence decay for a non-stabilized cat state. This demonstrates one more time that our stabilization does not distinguish between the two potential wells and allow quantum superpositions of the two steady states. We denote $\epsilon_{s,0}$ the storage drive amplitude which induces, roughly, one parity oscillation before the coherence of the superposition is lost (critically damped oscillations). This experiment is then repeated for drive amplitudes that are multiples of $\epsilon_{s,0}$. We observe that the oscillation frequency increases with ϵ_s and with $\bar{n}$, however we also observe that when the drive is too strong, the oscillations lose their coherence on a smaller timescale. Notice that these features are expected, as shown by our numerical simulations (solid lines).

We quantify these observations by fitting the experimental data with a sine function mod-
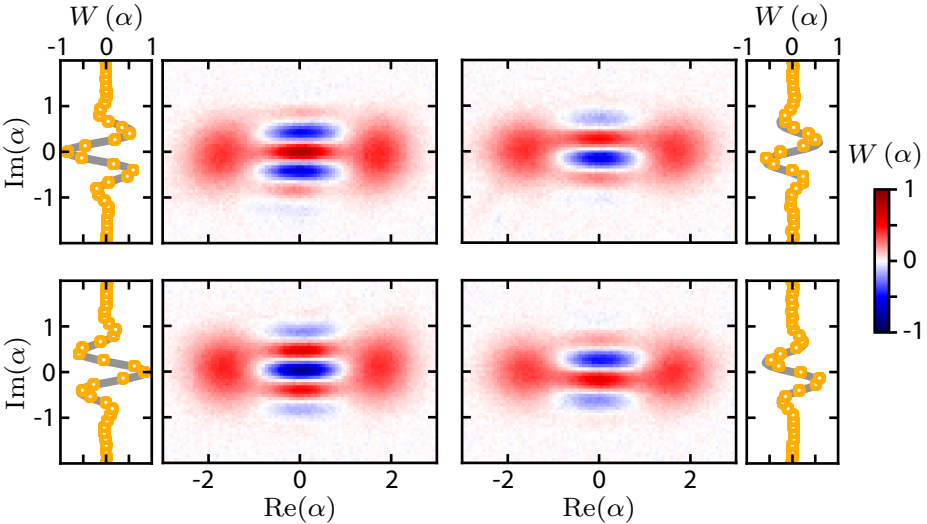
Figure 4.9: Wigner tomography result of the Quantum Zeno Dynamic time evolution. In the left-hand column is the Wigner functions of the storage cavity after initialization in an even or odd cat state $\propto |\alpha_\infty\rangle \pm |-\alpha_\infty\rangle$. The right-hand column shows the corresponding Wigner functions after a quarter of an oscillation. The color maps are averaged raw data of the Wigner function measurement and the orange circles are cuts along $\text{Re}\,(\alpha) = 0$. The gray solid lines are theoretical curves corresponding to even or odd cats (left-hand column, lines 1 and 2, respectively) and parityless cats (right-hand column, lines 1 and 2). The only fit parameter in the theory is the renormalization of the amplitude by a factor 0.87 on the left, and 0.65 on the right. These factors account for the fidelity of the parity measurement and the decay of the fringes of the cat states during the stabilization.

ulated with an envelope that decays exponentially. The results of this analysis are displayed in Fig. 4.10(b). On the top panel, we plot the effective Rabi frequency of these oscillations Ω as a function of the normalized drive strength ϵ_s. According to eq. 4.26 we have $\Omega = 2\text{Re}\,(\epsilon_s \alpha_\infty^*)$. By fitting Ω as a function of ϵ_s in the case $\bar{n} = 2$, we deduce that $\epsilon_{s,0}/2\pi = 7\,\text{kHz}$, which is well into the adiabatic regime, where the storage drive strength is much weaker than the stabilization strength $(|\epsilon_s| \ll |\alpha_\infty|^2 \kappa_2)$. This value allows us to model the evolution of Ω as a function of ϵ_s, for $\bar{n} = 3, 5$, which agrees well with the data. The second panel of Fig. 4.10(b) shows the evolution of the normalized decay time constant τ/τ_0 as a function of the drive strength, (where τ_0 is the time constant for the non-driven cat state) for different cat state amplitudes. If the storage drive was infinitely slow (adiabatic limit), the decay constant would be the same as in the non-driven case. However, when

$\epsilon_s/\epsilon_{s,0}$ increases, the oscillations decay faster. This is explained by the fact that the gate does not perfectly respect the adiabaticity condition $|\epsilon_s| \ll |\alpha_\infty|^2 \kappa_2$. Nevertheless, when the number of photons in the initial state is larger, the decay constant of the oscillations gets closer to the ideal limit: the adiabaticity condition is easier to fulfill for higher number of photons. Although encoding with a Schrödinger cat state of larger amplitude increases the bit-flip rate, given by $2\bar{n}\kappa_1$, it also increases the quality of our manipulation.
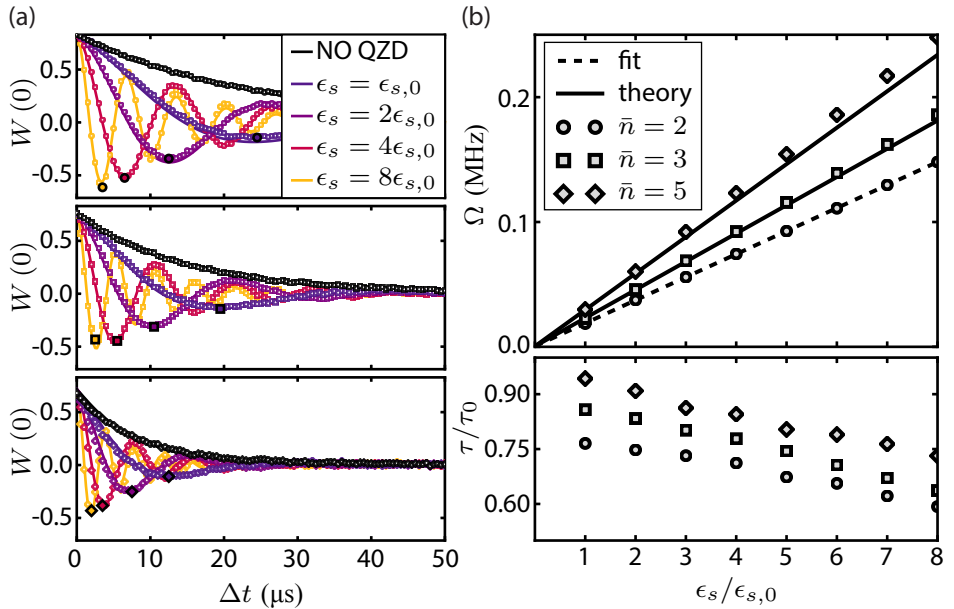
Figure 4.10: Characterization of the oscillations. (a) Evolution of the measured parity as a function of time. The initial cat states are even, with $\bar{n} = |\alpha_\infty|^2 = 2, 3, 5$ (circles, squares, diamonds). The storage drive is either off (black markers) or on (colored markers) with various strengths given in units of a chosen base strength $\epsilon_{s,0}$. Simulations are shown as solid lines. The minimum of each experimental curve is emphasized for each drive strength (full marker with black contour). (b) A fit of the data gives the frequency Ω and the time constant τ of the decaying oscillations. The former is plotted as a function of the relative drive strength $\epsilon_s/\epsilon_{s,0}$ (top panel). The case $\bar{n} = 2$ is fitted with a linear function (dashed line). Based on this, we make predictions for $\bar{n} = 3, 5$ (solid lines). The bottom panel shows the characteristic decay time of the oscillations τ, normalized by the decay time of the non-driven case τ_0.

4.7   Outlook on stabilized manifolds of coherent states

When our research on the stabilization of manifolds of coherent states started, stabilizing superpositions of *two* coherent states (so-called two-legged cats) was viewed as a stepping stone towards the stabilization of superpositions of *four* coherent states (so-called four-legged cats). The first one creates a qubit with a biased noise whereas the second one allows for full quantum error correction. As of today, it has been realized that stabilizing a manifold of states that allow for full quantum error correction is hard to do with dissipation engineering, but also that biased-noise qubits might be more powerful than originally envisioned.

The recent excitement in the field of biased-noise qubits has been introduced at Yale mostly by Mazyar Mirrahimi and Shruti Puri, whose work on cat stabilization has inspired new experiments. First of all, Shruti introduced an alternative way to think about manifold stabilization. In her paradigm, the stabilization of a cat manifold can also be done by creating a Hamiltonian that has degenerate ground states and that are protected from their excited states by a gap [60]. This protection does not guaranty that a state that is not in the degenerate manifold can be brought to it deterministically but, nevertheless, this scheme could eventually have some advantages over the dissipative stabilization described in this chapter. These advantages stem from the fact that the Hamiltonian protection relies on a strong Kerr non-linearity to be effective. When this non-linearity is large, it is easier to couple such systems together or to couple them to other superconducting microwave cavities. Also, they do not require to be well coupled to lossy modes, on the contrary of our dissipative stabilization. This way, the stabilization is potentially less susceptible to noise induced by the environment. This stabilization has been realized [116] and is being more investigated at Yale by Nicholas Frattini and Alexander Grimm.

All the work done after what is presented in this chapter made this type of stabilization enter in a new phase, beyond the proof of concept that we performed. In particular, in our two experiments [36, 37], the noise from the reservoir disturbed the stabilization and kept us from observing an exponential suppression of phase-flips. At the time of this thesis, Zaki Leghtas, now at Ecole Normale Superieure de Paris, managed to obtain a phase-flip timescale of 600 μs in a storage mode with a single-photon lifetime of 3 μs using the dissipative stabilization.

In the future, these stabilized qubits with highly biased-noise could enable fault-tolerant quantum computation with a much higher threshold than for usual qubits [117], on the condition that the two-qubit gates of such codes preserve the noise bias. For example, it has been shown that, for a surface code comprising highly biased-noise qubits, the error threshold could be as high as 43%, which could potentially reduce the number of physical

qubits needed [118]. Shruti Puri and Mazyar Mirrahimi recently showed that such noise-preserving two-qubit gates were possible using stabilized cat states and other four-wave mixing terms previously demonstrated, including the two-photon conversion of this chapter and conditional displacements [119, 120].

Finally, such biased-noise qubits are useful to check errors in codes that correct for all types of errors. One of these codes is the previously mentioned surface code, which allows fault-tolerant quantum computing, but they also allow checks on single quantum-error-corrected qubits [121] such as the Gottesman-Kitaev-Preskill (GKP) qubits [11] that are also developed in the following chapter.

5

Stabilization of a manifold of grid states

The emergence of universal quantum computers that are able to perform complex algorithm depends on the resilience of such devices against any type of errors. This property is now well defined and is referred to as fault-tolerance [8]. In theory, fault-tolerance can be achieved with an ensemble of two-level systems in various architectures, such as the surface codes [57]. When operations on individual qubits and between neighboring qubits are done with enough precision, adding more qubits will only amount to a better quantum computer [56]. This so-called "threshold" has been attained and thus, fault-tolerant quantum computing seems within reach [122]. However, to create a full blown universal quantum computer, millions of such qubits need to be assembled. While this task is currently being tackled by companies such as Google, a lot of work is underway at Yale to make the requirements for fault-tolerance more *hardware efficient*. Our current approach to hardware efficiency consists in encoding a logical qubit into the large Hilbert space of harmonic oscillators, hosted in the electromagnetic field of superconducting microwave cavities.

The errors inside of a superconducting cavity consist mostly of spurious linear couplings with its environment, which results in single-photon losses. Such simple errors can be dealt with using the four-legged cat codes [30] or the binomial codes [28, 31]. However, there is a large zoo of errors and spurious effects that take place in a superconducting cavity, such as the Kerr effect, dephasing, amplitude damping and more. In order to address all of these errors in a single encoding, we need to find what they have in common. In their seminal paper of 2001, Daniel Gottesman, Alexei Kitaev and John Preskill (GKP) emphasized the fact that all of these errors are continuous in phase-space [11]. This means that, at small times, any point in a phase-space representation will remain close to where it started (the smaller the time, the closer it will be). Thus, in order for a code to correct any error at small time, it only needs to

correct for small shifts in phase-space.

In this chapter, we will first theoretically describe such shift-resistant codes, called GKP codes, and see that they are in fact, grids in phase-space. We will describe how quantum error correction was envisioned using these codes and the stabilizer formalism. Finally, we will describe how we were able to stabilize such codes by using the measurement of an ancilla qubit and a simple feedback law.

5.1 Construction of shift-resistant codes

The difficulty in building a logical qubit that is resistant to shifts in phase-space stems from the fact that these shifts can be both in position (denoted Q), and in momentum (denoted P), which are two conjugate variables. We illustrate this subtlety by considering two-legged cat states that are superpositions of two coherent states $|\pm\alpha\rangle$, where α is real and large. These two coherent states cannot be mistaken when their position is slightly shifted. However, there superpositions $|\alpha\rangle \pm |-\alpha\rangle$ have very similar momentum distributions. This can be seen by looking at their Wigner function and observing that, for large Schrödinger cat states, the fringes are densely packed. Because of this, a small shift in momentum will completely scramble the information contained in these states. As we have seen before, this type of encoding does not encode a fully protected qubit. How can we build states that are distant from each other, and whose superpositions are also distant from each other?

The solution found by GKP was to construct the logical states using a distribution that looks similar in position and in momentum. These two quadratures are Fourier transforms of one another, and only a few distributions have the property to be similar under Fourier transform. For example, the Fourier transform of a Dirac comb is also a Dirac comb. Therefore, an infinite superposition of perfect position states $|Q\rangle$ would have the properties we are looking for. Using the Dirac notation, a generic wavefunction of this kind of state is given by

$$|\Psi\rangle = \sum_{n=-\infty}^{+\infty} |Q = n\Delta_Q + Q_0\rangle, \tag{5.1}$$

where Δ_Q is the period of this state and Q_0 is an offset. Note that, for clarity, this state is not normalized. These wavefunctions encode a logical qubit when we choose two states that have the same period Δ_Q and that are offset by half a period $\Delta_Q/2$. We represent the wavefunctions of such logical states in Fig. 5.1, where the wavefunctions are expressed both in
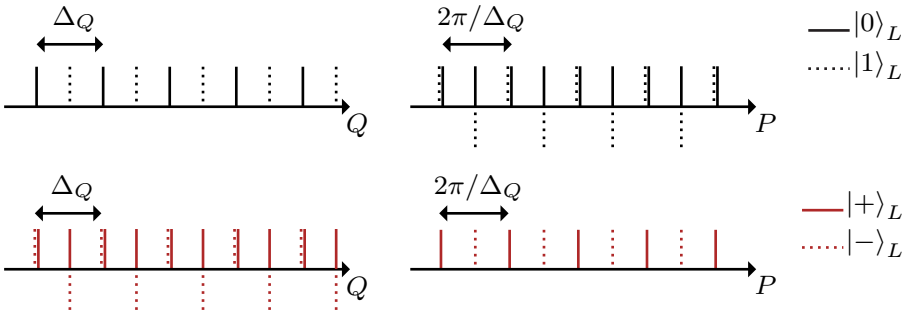
Figure 5.1: Wavefunctions of an ideal GKP code. These wavefunctions are expressed, on the left, in the position basis $|Q\rangle$ and, on the right, in the momentum basis $|P\rangle$. The solid and dashed vertical bars represent Dirac delta functions. The basis states are represented in black and are Dirac combs with a period Δ_Q in Q, offset by $\Delta_Q/2$ from one another. In P, these combs have twice as many "teeth" and their common period is $2\pi/\Delta_Q$. In this representation, the sign of the teeth of $|1\rangle_L$ alternates while it is constant for $|0\rangle_L$. This way, their symmetric and antisymmetric superpositions $|\pm\rangle_L$, represented in red, are also Dirac combs with a period $2\pi/\Delta_Q$, offset by π/Δ_Q from one another. For completeness, we also represent these superposed states in the Q representation. Note that, for clarity, two overlapping delta functions are represented slightly offset.

the position basis $|Q\rangle$ and in the momentum basis $|P\rangle$. The periodicity of these states in the P quadrature is, by virtue of the Fourier transform, $2\pi/\Delta_Q$. This way, the spacing between their symmetric and antisymmetric superpositions $|\pm\rangle_L$ is π/Δ_Q. We choose $\Delta_Q = \sqrt{2\pi}$, such that the encoded qubit is equally protected against bit-flips and phase-flips.

Unfortunately, perfect position states and infinite superpositions are not physical because they contain an infinite number of photons. This approach can nevertheless be made physically doable by choosing an approximate Dirac comb, where the overall wavefunction is modulated by a large Gaussian. In this case, the "teeth" of the comb are position squeezed states instead of ideal Dirac distributions, as shown in Fig. 5.2. These two states are exponentially close to being orthogonal for large squeezing parameter of the quasi-position states. This property is reminiscent of the quasi-orthogonality of coherent states for the cat codes.

The wavefunctions of these states illustrate the protection of this encoding against small shifts. When one of the states of the logical qubit is slightly shifted, in position or in momentum, it remains orthogonal to the other states of the logical qubit. For example, if the state $|0\rangle_L$ is shifted in position by less that a quarter of a period, it remains closer to its original position than from $|1\rangle_L$. If these shifts are detected quickly enough (i.e. before they become
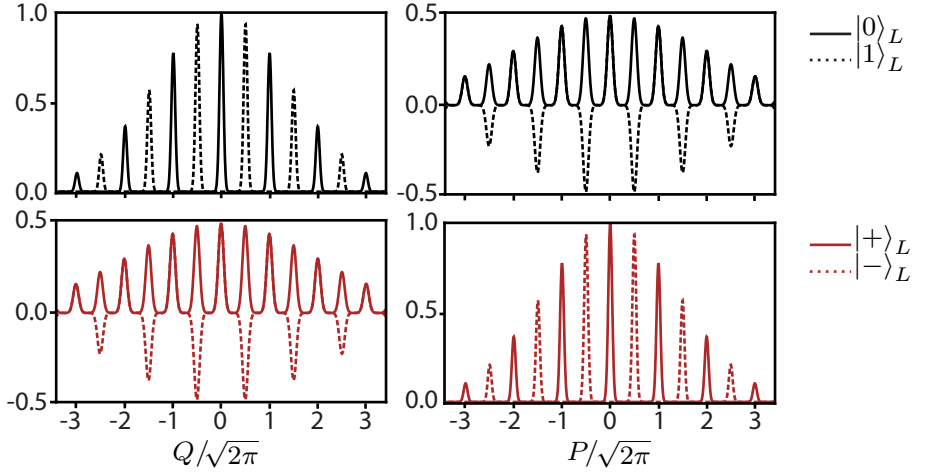
Figure 5.2: Wavefunctions of an approximate GKP code. The real parts of the wavefunctions of the basis states $|0\rangle_L$ and $|1\rangle_L$ are plotted in the top frames, with a solid black line for $|0\rangle_L$ and a dashed black line for $|1\rangle_L$. The real part of their superpositions $|\pm\rangle_L$ are plotted in the bottom frames, with a solid red line for $|+\rangle_L$ and a dashed red line $|-\rangle_L$. In the left column, the wavefunctions are expressed in the position basis $|Q\rangle$ whereas in the right column they are expressed in the momentum basis $|P\rangle$. The position and momentum axes are renormalized by $\sqrt{2\pi}$ to emphasize their quasi-period of $\sqrt{2\pi}$.

large), they can be corrected before the information of the qubit is completely scrambled. In the next section we will construct a way to detect such shifts.

5.2 GKP qubit stabilizers

From the description of the GKP states, we deduced that they are well suited to implement quantum error correction, as the two logical basis states remain orthogonal when they suffer small errors. To detect these errors, we need to find operators that are able to detect unambiguously if an error has occurred, while preserving the information of the logical qubit. Such operators are called the stabilizers of the code [48]. In order to not destroy the information of the logical qubit, we want these operators to have the same outcome for the two logical states $|0\rangle_L$ and $|1\rangle_L$, therefore, this operator should have the same periodicity as the code. Both $|0\rangle_L$ and $|1\rangle_L$ have a period $\sqrt{2\pi}$ in position and in momentum, but they are offset by $\sqrt{\pi/2}$, therefore the period of the code is $\sqrt{\pi/2}$, and the frequency of the code

is $\frac{2\pi}{\sqrt{\pi/2}} = 2\sqrt{2\pi}$. Moreoever, these two operators must commute such that they can be simultaneously measured. Two operators that fulfill these properties are

$$\boldsymbol{S}_a = e^{2i\sqrt{2\pi}\boldsymbol{Q}} = \boldsymbol{D}\left(i\sqrt{2\pi}\right) \tag{5.2}$$

$$\boldsymbol{S}_b = e^{-2i\sqrt{2\pi}\boldsymbol{P}} = \boldsymbol{D}\left(\sqrt{2\pi}\right), \tag{5.3}$$

where we have rewritten these unitary operators using the displacement operator $\boldsymbol{D}(\alpha) = e^{\alpha \boldsymbol{a}^\dagger - \alpha^* \boldsymbol{a}}$. We will check that these stabilizers commute in the next section. We represent the stabilizers in phase-space in Fig. 5.3. The descriptions using the matrix exponential or the displacement operators are more or less convenient depending on what basis is being used. As an example, let us see how they act on a position state $|Q_0\rangle$:

$$\boldsymbol{S}_a |Q_0\rangle = e^{2i\sqrt{2\pi}\boldsymbol{Q}} |Q_0\rangle = e^{2i\sqrt{2\pi}Q_0} |Q_0\rangle \tag{5.4}$$

$$\boldsymbol{S}_b |Q_0\rangle = \boldsymbol{D}\left(\sqrt{2\pi}\right) |Q_0\rangle = \left|Q_0 + \sqrt{2\pi}\right\rangle. \tag{5.5}$$

The matrix exponential is more practical when a displacement in momentum acts on a position state, whereas the position displacement operator is easy to write when it acts on a position state. This situation is reversed when the operators are written in the momentum basis.

Using these tools, we now look at how the stabilizers act on the basis states $\left|0/1\right\rangle_L$ on which a small shift has occurred. Let us first write the wavefunctions of the basis states after a small shift has happened. A small shift in position is represented by a displacement $\boldsymbol{D}\left(\epsilon_Q\right)$ while a small shift in momentum is represented by a displacement $\boldsymbol{D}\left(i\epsilon_P\right)$ ($\epsilon_{Q,P}$ are real). If we write the basis states as $|l\rangle_L$, where $l = 0, 1$, we get

$$\boldsymbol{D}\left(\epsilon_Q\right) |l\rangle_L = \sum_{n=-\infty}^{+\infty} \boldsymbol{D}\left(\epsilon_Q\right) \left|n\sqrt{2\pi} + l\sqrt{\pi/2}\right\rangle$$

$$= \sum_{n=-\infty}^{+\infty} \left|n\sqrt{2\pi} + l\sqrt{\pi/2} + \epsilon_Q\right\rangle, \tag{5.6}$$

and

$$D\left(i\epsilon_P\right)\left|l\right\rangle_L = \sum_{n=-\infty}^{+\infty} e^{2i\epsilon_P Q} \left|n\sqrt{2\pi} + l\sqrt{\pi}/2\right\rangle$$

$$= \sum_{n=-\infty}^{+\infty} e^{2i(n\sqrt{2\pi} + l\sqrt{\pi/2})} \left|n\sqrt{2\pi} + l\sqrt{\pi}/2\right\rangle. \tag{5.7}$$

We now apply the stabilizers to these shifted states. The stabilizer S_b is designed to catch a position shift while the stabilizer S_1 is designed to catch a momentum shift. We get

$$S_a\left(D\left(\epsilon_Q\right)\left|0/1\right\rangle_L\right) = e^{2i\sqrt{2\pi}\epsilon_Q} D\left(\epsilon_Q\right)\left|0/1\right\rangle_L \tag{5.8}$$

$$S_b\left(D\left(i\epsilon_P\right)\left|0/1\right\rangle_L\right) = e^{2i\sqrt{2\pi}\epsilon_P} D\left(i\epsilon_P\right)\left|0/1\right\rangle_L. \tag{5.9}$$

The stabilizers detect a small shift by imprinting it in the phase of the state. This phase is the same whether the shift happens on $\left|0\right\rangle_L$ or $\left|1\right\rangle_L$, thus the stabilizers do not change the state of the qubit. To achieve the quantum error correction of a GKP qubit, this global phase needs to be mapped onto the relative phase of an ancilla system. This type of protocol is called "phase-estimation" [123] and was envisioned as a way to create GKP states [124]. Our stabilization protocol is directly derived from this idea.

Before describing our stabilization protocol, let us first generalize the stabilizers of GKP codes and show that they allow for the stabilization of grids that are not square, such as the hexagonal code.

5.3 Generalization of the stabilizers of GKP codes

In the previous sections of this chapter, we looked for a logical qubit encoded in a harmonic oscillator that would be protected against small shifts. From there, we deduced the stabilizers of such a logical qubit. We could also have defined GKP states as being the eigenstates of two displacement operators, which form a periodic lattice in phase-space. In this section, we will do this reasoning and see that it leads to the creation of a whole family of GKP codes that are not necessarily square grids.

5.3.1 GKP states as eigenstates of two displacements

We start this reasoning by looking for quantum states that are periodic along two axes that are not collinear (and not necessarily perpendicular). The basis vectors that generate such a grid are parametrized by two complex numbers α_a and α_b (their norms are the periods along these axes and their arguments are the angles of the axes). Such periodic states are simultaneously eigenstates of two displacements $\boldsymbol{D}(\alpha_1)$ and $\boldsymbol{D}(\alpha_2)$. However, for two operators to have simultaneous eigenstates, they must commute. For displacements operators we have

$$\boldsymbol{D}\left(\alpha_b\right)\boldsymbol{D}\left(\alpha_a\right) = e^{i\phi}\boldsymbol{D}\left(\alpha_a + \alpha_b\right) \tag{5.10}$$

$$= e^{2i\phi}\boldsymbol{D}\left(\alpha_a\right)\boldsymbol{D}\left(\alpha_b\right) \tag{5.11}$$

where $\phi = \mathrm{Im}(\alpha_b\alpha_a^*)$, is the oriented area of the parallelogram formed with two vectors whose coordinates are given by the complex numbers α_a and α_b (this area is also the norm of the cross-product of these vectors)[1]. These two operators commute if $\phi = n\pi$ (n is an integer). In analogy with the square code we described before, we pick the same $n = 2$. Notice that, although we will not develop it here, an arbitrary n encodes a qu$n$it. In addition, because we want the same protection against both bit-flips and phase-flips, we pick $|\alpha_a| = |\alpha_b|$. From this, we define the generalized stabilizers

$$\boldsymbol{S}_a = \boldsymbol{D}(\alpha_a) \tag{5.12}$$

$$\boldsymbol{S}_b = \boldsymbol{D}(\alpha_b) \tag{5.13}$$

$$\phi = \mathrm{Im}(\alpha_b\alpha_a^*) = 2\pi \tag{5.14}$$

We define a new GKP code that is hexagonal in phase-space by choosing a phase $2\pi/3$ between the vectors generating the states. This code is depicted in Fig. 5.3(b). Because the commutation relation needs to be conserved, the periodicity along these two axes is changed to $|\alpha_a| = |\alpha_b| = \sqrt{2\pi/\sin(2\pi/3)}$, which is only 7% larger than the periodicity of the square GKP code. However, we will see that the hexagonal codes possess nice symmetry properties. In particular, it is the optimal code to protect against the dominant error in superconducting cavities: single-photon losses [125].

---

[1] The factor 2 comes from the definition of the displacement operator and the choice of quadrature operators $\boldsymbol{Q} = \frac{a+a^\dagger}{2}$ and $\boldsymbol{P} = \frac{a-a^\dagger}{2}$. Alternatively, one can define the quadrature operators as $\boldsymbol{q} = \frac{a+a^\dagger}{\sqrt{2}}$ and $\boldsymbol{p} = \frac{a-a^\dagger}{\sqrt{2}i}$, together with a translation operator $\boldsymbol{T}(\alpha) = e^{\frac{1}{\sqrt{2}}\left(\alpha a^\dagger - \alpha^* a^\dagger\right)}$, such that $\boldsymbol{T}(\alpha_b)\boldsymbol{T}(\alpha_a) = e^{i\phi}\boldsymbol{T}(\alpha_a)\boldsymbol{T}(\alpha_b)$.
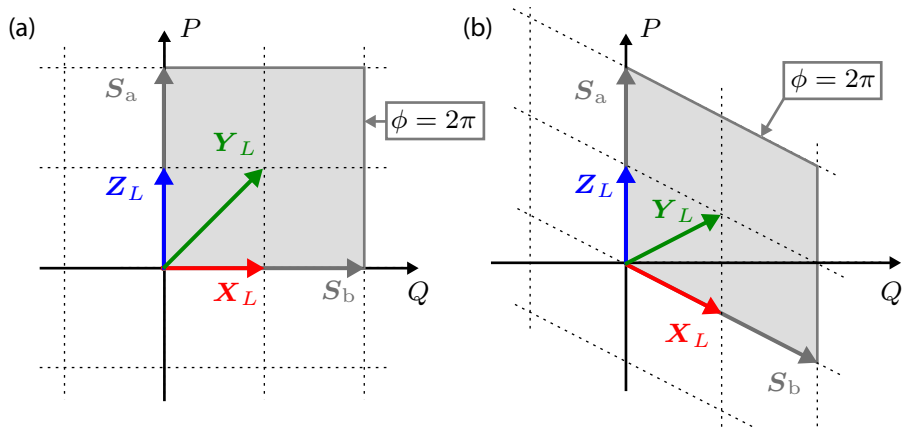
Figure 5.3: Schematic representation of the stabilizers and Pauli operators of GKP codes. We represent the square code in (a) and the hexagonal (b). Each arrow represents a displacement. The stabilizers S_a and S_b are represented by gray arrows, while the Pauli operators X_L, Y_L and Z_L are represented by green, red and blue arrows respectively. The area enclosed by the stabilizers vectors is colored in gray. It corresponds to the case $\phi = 2\pi$, which ensures that the stabilizers commute and that they commute with each Pauli operator.

5.3.2 Pauli algebra

The commutation relation given by equation 5.10 has another interesting case when $\phi = (2k + 1)\pi/2$. In this case, the two displacements anti-commute, which resembles the usual Pauli algebra. To fully define the Pauli matrices of this code we write

$$X_L = D(\alpha_b/2) \tag{5.15}$$

$$Z_L = D(\alpha_a/2) \tag{5.16}$$

$$Y_L = D\left(\frac{\alpha_a + \alpha_b}{2}\right). \tag{5.17}$$

From these, we get

$$X_L Z_L = -Z_L X_L, \quad Y_L Z_L = -Z_L Y_L, \quad Y_L X_L = -X_L Y_L \tag{5.18}$$

$$X_L^2 = Y_L^2 = Z_L^2 = -i X_L Y_L Z_L = I_L, \tag{5.19}$$

where the identity within the code is a displacement by one period. These Pauli matrices are easy to understand in the case of the square GKP code. One can check in Fig. 5.1 and 5.2

that the displacements corresponding to $\boldsymbol{X}_L$ and $\boldsymbol{Z}_L$ take, respectively, $|0\rangle_L$ to $|1\rangle_L$ and $|+\rangle_L$ to $|-\rangle_L$ (and vice versa).

The Pauli operators for the square code and for the hexagonal code are represented in Fig. 5.3. In this figure, we see that, for the square code, the logical Pauli $\boldsymbol{Y}_L$ is a larger displacement than $\boldsymbol{X}_L$ and $\boldsymbol{Z}_L$. In this case, an eigenstate of $\boldsymbol{Y}_L$ is encoded in larger range correlations than eigenstates of $\boldsymbol{X}_L$ and $\boldsymbol{Z}_L$, which makes these states more fragile against dissipation. This fact was observed in our experiment as we will see later. On the other hand, for the hexagonal code, the norm of the displacements corresponding to the three logical Pauli operators are equal, which makes the corresponding logical qubit more resistant to single-photon loss.

The commutation relation of displacements also shows that the stabilizers commute with the Pauli operators, because their cross product has a norm of π. This property emphasizes that the stabilizers are agnostic to the state of the logical qubit within the stabilized manifold.

5.3.3 Error detection in the generalized GKP codes

When the GKP code is square, it is easy to write all the states into a chosen basis. This task is harder for a generalized GKP code such as the hexagonal code. Thus, we write them in terms of abstract states that are eigenstates of the operators we just defined. This description actually corresponds to the way we prepare these states experimentally. For example, we define $|0\rangle_L$ as the only state such that

$$\boldsymbol{S}_a |0\rangle_L = \boldsymbol{S}_b |0\rangle_L = \boldsymbol{Z}_L |0\rangle_L = |0\rangle_L . \tag{5.20}$$

This state is in fact unique. Similarly, we define $|1\rangle_L = \boldsymbol{X}_L |0\rangle_L$, which verifies

$$\boldsymbol{S}_a |1\rangle_L = \boldsymbol{S}_b |1\rangle_L = |1\rangle_L \tag{5.21}$$

$$\boldsymbol{Z}_L |1\rangle_L = \boldsymbol{Z}_L \boldsymbol{X}_L |0\rangle_L = -\boldsymbol{X}_L \boldsymbol{Z}_L |0\rangle_L = -|1\rangle_L . \tag{5.22}$$

At short enough time, an error acting on these states is a combination of small displacements. After one of these small displacements, the logical state is changed to $\boldsymbol{D}(\epsilon) |0/1\rangle_L$, where ϵ is a complex number whose modulus is much smaller than the periodicity of the array $(|\epsilon| \ll |\alpha_a|, |\alpha_b|)$. By using the commutation relation given by equation 5.10, we get

$$\boldsymbol{S}_{a,b} \boldsymbol{D}(\epsilon) = e^{2i\phi_\epsilon} \boldsymbol{D}(\epsilon) \boldsymbol{S}_{a,b} \tag{5.23}$$
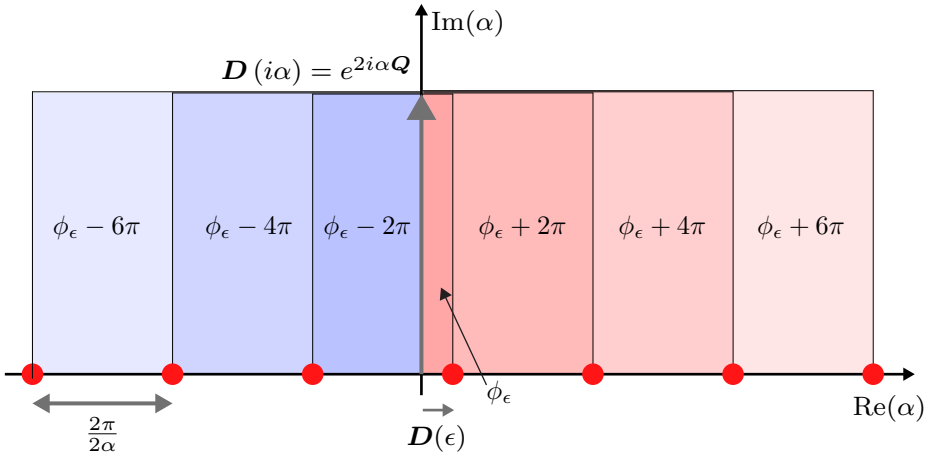
Figure 5.4: Schematic representation of the action of a stabilizer on the Wigner function of a mixed GKP state. One line of the Wigner function of a GKP mixed state is represented. The Wigner function of the mixed state would extend to infinity and be periodic along the imaginary axis too. One stabilizer of this code is chosen as $D(i\alpha)$, which means that the position probability distribution of this mixed state has peaks spaced by $\frac{2\pi}{2\alpha}$. The state is offset by a position displacement $D(\epsilon)$. Each point of the Wigner function adds the same phase onto the state $e^{i(2\phi_\epsilon + 2k\pi)} = e^{2i\phi_\epsilon}$, with k an integer.

where ϕ_ϵ is the oriented area between the error displacement and the displacement corresponding to one of the stabilizers, as shown in Fig. 5.4. Note that this area is most likely different for S_a and S_b, which results in different phases. This error displacement ϵ cannot be collinear with both stabilizers, thus this area cannot be 0 for both stabilizers. This way we get

$$S_{a,b}\left(D(\epsilon)\left|0/1\right\rangle_L\right) = e^{2i\phi_\epsilon}\left(D(\epsilon)\left|0/1\right\rangle_L\right). \tag{5.24}$$

In conclusion, at least one of the stabilizers necessarily imprints a phase on both states $\left|0/1\right\rangle_L$ without discriminating between the two states. As we will see now, this phase can be imprinted on an ancillary system and detected. This mapping of the phase of the stabilizers is at the heart of our stabilization of GKP codes.

5.4 Measuring the stabilizers using a stroboscopic conditional displacement in cQED

In the original GKP paper, the quantum error correction of GKP codes was supposed to be realized using GKP state ancillas [11]. The state encoding the logical qubit would be susceptible to errors, and these errors would be mapped onto an ancillary GKP state. Finally, the error could be detected using a high-efficiency homodyne detection of the ancilla GKP state. This approach is directly tailored for quantum optics, where the entanglement of two GKP states is simply realized with a beam-splitter and where homodyne detection is common. The original GKP paper predates the development of many platforms that could reliably process quantum information, such as superconducting circuits. However, in superconducting circuits, coupling two superconducting microwave cavities on-demand is a very recent feat [33–35]. Instead, here, we describe a way to use the coupling of an ancilla transmon to a storage microwave cavity in order to detect an error that acted onto a GKP logical qubit, without destroying the encoded qubit.

When the stabilizers act on GKP states of the storage, a displacement error is revealed by a global phase. This global phase can only be measured by comparing it to a phase reference. We use the phase of an ancilla qubit, just after being initialized on the equator of the Bloch sphere, as the phase reference. In order to map the global phase of the stabilizers onto the relative phase of a superposition state of a two-level ancilla, we use the circuit represented in Fig. 5.5. The key element of this circuit is the possibility to apply one of the stabilizers $S_{a,b}$ only if the ancilla is in its excited state $|e\rangle$. This element is realized with a displacement conditioned on the state of the qubit and whose phase can be changed. The remainder of this section will describe how we engineered this conditional displacement in a cQED architecture.

5.4.1 Engineering a stroboscopic conditional displacement using only the dispersive interaction

In our previous chapter on the readout of superconducting qubits, we already mentioned that we managed to engineer a conditional displacement [86]. In theory, the same technique could be used to measure the phase of the stabilizers of GKP codes. In the conditional displacement readout, we engineered the conditional displacement using strong off-resonance drives. This scheme had some technical overheads such as the need for a cancellation tone and the need for good filtering. The conditional displacement we engineered to stabilize GKP codes is simpler as it relies solely on the dispersive Hamiltonian. For this, we simply noticed
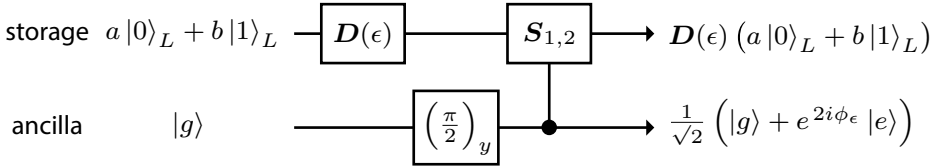
Figure 5.5: Circuit mapping the phase of the stabilizers onto an ancilla two-level system. The sequence acting on the storage is depicted in the top line, while the sequence acting on the ancilla is depicted in the bottom line. The storage is initially in an arbitrary code state $a \left|0\right\rangle_L + b \left|1\right\rangle_L$, with $|a|^2 + |b|^2 = 1$ (a and b are not related to the subscripts of the stabilizers). The ancilla is initially in $\left|g\right\rangle$. First, the storage suffers from an uncontrolled small shift $\boldsymbol{D}(\epsilon)$. In order to detect this error, the ancilla is set on the equator in $\frac{1}{\sqrt{2}} \left(\left|g\right\rangle + \left|e\right\rangle\right)$. Then, one of the stabilizers, $\boldsymbol{S}_{a,b}$, acts on the storage, conditioned on the ancilla being in $\left|e\right\rangle$. At the end of this sequence, the state of the storage is simply shifted, while the state of the ancilla is in a superposition whose phase depends on the error shift ϵ.

that, in a displaced frame of the storage $\alpha_s(t)$, the dispersive Hamiltonian already creates a conditional displacement. As we will see, this conditional displacement of the storage cavity is always accompanied by a conditional phase, which is not compatible with the stabilization of grid states whose axes have to be preserved. We used a dynamical decoupling technique to cancel this conditional phase while keeping the conditional displacement [126]. The resulting conditional displacement is a variation of a readout scheme used in Berkeley to enhance the readout of superconducting circuits using squeezed states [94]. It is important to notice that this dynamical decoupling technique is also compatible with the conditional displacement we engineered for the conditional displacement readout. In fact, in future implementations of the GKP codes, using our previous conditional displacement could lead to faster interactions.

We begin the description of the conditional displacement we used in this experiment by considering a storage cavity with dissipation given by the Lindblad superoperator $\frac{\kappa_s}{2} \mathcal{D}[\boldsymbol{a}]$. This cavity is subjected to a drive $\boldsymbol{H}_{\text{drive}}/\hbar = \epsilon_s \boldsymbol{a}^\dagger + \epsilon_s^* \boldsymbol{a}$, which displaces the storage state by $\alpha_s(t)$ given by

$$\alpha_s(t) = \frac{2i\epsilon_s}{\kappa_s} \left(1 - e^{-\frac{\kappa_s t}{2}}\right) \tag{5.25}$$

$$\approx i\epsilon_s t, \tag{5.26}$$

where we have considered $\kappa_s \ll \epsilon_s$, meaning that the losses of the storage cavity are negligible. This change of frame is thus linear in time with a slope that depends only on the drive
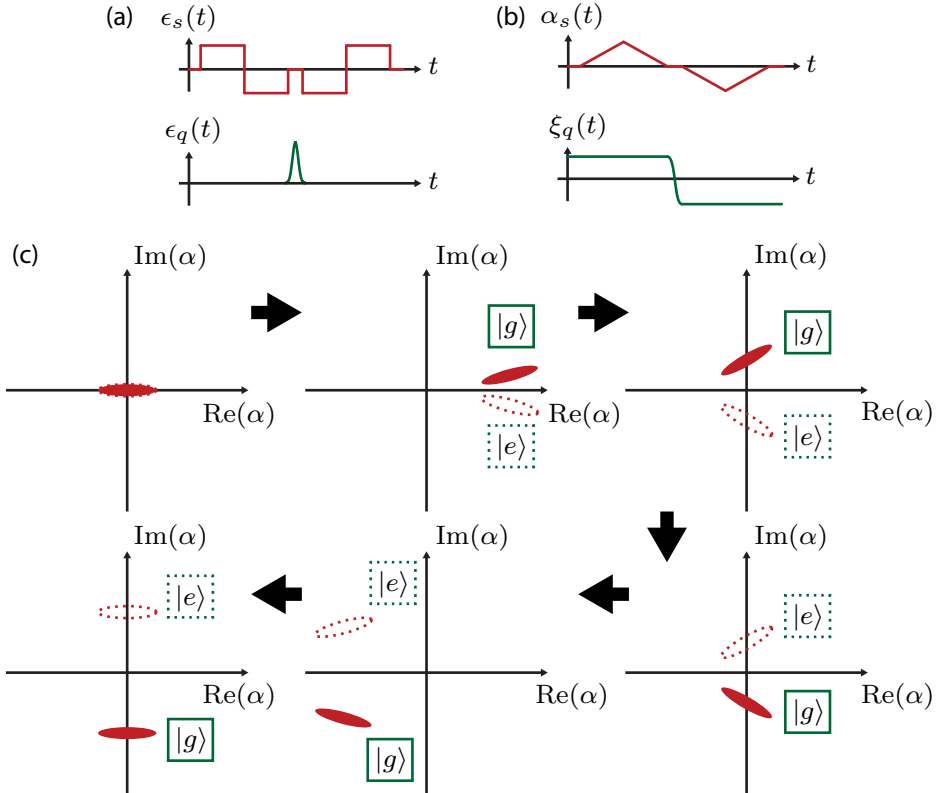
Figure 5.6: Representation of a stroboscopic conditional displacement. (a) Pulse sequence played to control the state of the storage mode (red) and the ancilla transmon (green). (b) Reponse of the storage and ancilla transmon. $\alpha_s(t)$ represents the center of mass of a state in the storage while $\xi_q(t)$ represents the sign of $\boldsymbol{\sigma}_z$, which changes from 1 to -1 when the transmon is pulsed. (c) Evolution of the Wigner function of the storage. The initial state of the storage is a squeezed vacuum, such that a change of phase of that state is visible through a change of squeezing axis. The evolution of the state of the storage is conditioned on the state of the ancilla transmon: when the ancilla is in $|g\rangle$, the storage is in the state represented by a full ellipse, whereas when the ancilla is in $|e\rangle$, the storage is in the state represented by the dashed ellipse. This evolution is a Trotterized version of the three-wave mixing effective Hamiltonian $\boldsymbol{\sigma}_z(\boldsymbol{a} + \boldsymbol{a}^\dagger)$.

strength ϵ_s. This linear evolution is represented in Fig. 5.6(b), where we observe that the response of the storage is a combination of linear evolutions.

The storage cavity is coupled to an ancilla transmon whose state can be manipulated with fast pulses. For our conditional displacement, we use the possibility to exchange the role of $|g\rangle$ and $|e\rangle$ using a π-pulse, which corresponds to a change of frame for the qubit where $\boldsymbol{\sigma}_z$ is transformed into $-\boldsymbol{\sigma}_z$. We denote $\xi_q(t)$ the sign in front of $\boldsymbol{\sigma}_z$ at time t.

The sequence of pulses played to create a Trotterized conditional displacement is represented in Fig. 5.6(a), and the corresponding response of the system is represented in Fig. 5.6(b). This conditional displacement is called *stroboscopic*, as defined by L. Viola *et al.* [126]. We also represent a schematic of the Wigner function of the state of the storage to help understanding the conditional displacement. In this representation, the initial state of the storage is chosen to be a squeezed vacuum to visualize the spurious conditional rotation of the axes.

We look at the dispersive Hamiltonian after the transformations we previously described, namely a displacement and possibly flipping the Bloch sphere:

$$-\frac{\chi}{2}\boldsymbol{a}^\dagger\boldsymbol{a}\boldsymbol{\sigma}_z \rightarrow -\xi_q(t)\frac{\chi}{2}\boldsymbol{a}^\dagger\boldsymbol{a}\boldsymbol{\sigma}_z - \xi_q(t)\left|\alpha_s(t)\right|^2\frac{\chi}{2}\boldsymbol{\sigma}_z + \xi_q(t)\frac{\chi}{2}\left(\alpha_s(t)^*\boldsymbol{a} + \alpha_s(t)\boldsymbol{a}^\dagger\right)\boldsymbol{\sigma}_z.$$
$$(5.27)$$

The first terms of this transformation are spurious effects, namely a rotation of the axes of the storage conditioned on the state of the ancilla, and a frequency Stark-shift of the ancilla. The conditional phase-shift is visible in Fig. 5.6(c). The third term is the conditional displacement we wish to engineer. In order to keep the action of the conditional displacement and cancel the action of the spurious terms, we repeat this transformation with opposite signs for both $\xi_q(t)$ and $\alpha_s(t)$. As equation 5.27 shows, the spurious terms depend only on the sign of $\xi_q(t)$, which is now opposite, while the sign of the conditional displacement depends on the product $\xi_q(t)\alpha_s(t)$, which remains unchanged. After this second change of frame, the action of the spurious terms is unitarily cancelled while the action of the conditional displacement continues. At the end of this protocol, we obtain a conditional displacement that does not change the axes of the state of the storage mode, as shown in the last frame of Fig. 5.6(c).

As presented in the introduction, we can use this conditional displacement $\boldsymbol{D}\left(\frac{\tilde{\alpha}}{2}\boldsymbol{\sigma}_z\right) = e^{\frac{1}{2}(\tilde{\alpha}\boldsymbol{a}^\dagger - \tilde{\alpha}^*\boldsymbol{a})\boldsymbol{\sigma}_z}$ to measure directly the characteristic function of the storage cavity. In particular, we know that the steady-state of the storage is a vacuum state. Hence, we use a 1D cut of the characteristic function of the vacuum state to calibrate the strength of the conditional displacement, as shown in Fig. 5.7(a). Here, we assume that the state of the storage cavity is not thermal, such that the expression of the characteristic function is simply a Gaussian with standard deviation 1. Using this calibrated conditional displacement, we can calibrate the strength of an unconditional displacement, as represented in Fig. 5.7(b) and (c). For this, we
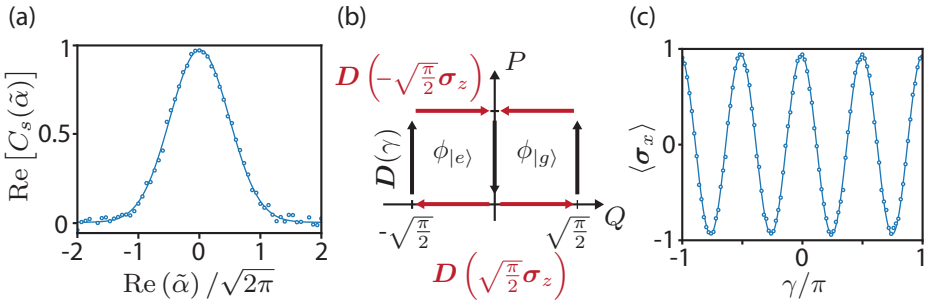
Figure 5.7: Experimental calibration of conditional and unconditional displacements. (a) 1D cut of the real part of the characteristic function of the vacuum state. The blue circles are data points and the blue solid line is a Gaussian fit. The scale of the x-axis is scaled such that the Gaussian has a standard deviation of 1. (b) Schematic of the experimental calibration of a displacement. The ancilla qubit starts in $|+\rangle$ and, using a calibrated conditional displacement $D\left(\sqrt{\frac{\pi}{2}}\sigma_z\right)$ (red arrows) and an uncalibrated displacement by an amount $\sqrt{2\pi}\gamma$ (black arrow), the qubit gains a phase $\phi = \phi_+ - \phi_-$. (c) Expectation value of σ_x as a function of γ. The blue circles are data points and the blue solid line is a sine fit. The x-axis is scaled such that the sine has a frequency 0.5.

first initialize the ancilla qubit in $|+\rangle$. Then, we use a series of conditional and unconditional displacements to enclose an area ϕ_- is the qubit is in $|e\rangle$ and ϕ_+ if the qubit is in $|g\rangle$. By fixing the amplitude of the conditional displacement, we know that the expectation value of σ_x should be opposite when the difference of the area enclosed is $(2k+1)\pi/2$, and it should be unchanged when the difference of area enclosed is $k\pi$. We use this dependence to extract the calibrated value of the displacement.

With this implementation of a conditional displacement, the speed of the error-mapping operation is limited by the fact that the separation of the two states occurs only if the state of the cavity is already displaced. As we have seen, this displacement happens linearly in time. Once the cavity mode is displaced, the conditional displacement starts and splits the state of the cavity with a separation that is also linear in time, meaning that the overall conditional displacement is quadratic in time. This scaling is not favorable to reduce the total interaction time. One could replace this scheme with the one described in the conditional displacement readout [86], which would lead to a conditional displacement that depends only linearly in time.

5.4.2 cQED architecture compatible with GKP code stabilization

We would like to implement the quantum error correction of GKP codes using a 3D cQED architecture such as the one depicted in Fig. 5.8. Performing quantum error correction on GKP codes using a cQED architecture is only possible if the error syndrome check is much faster than the errors themselves. Let us start by comparing these two durations and see if they are compatible with the desired architecture.
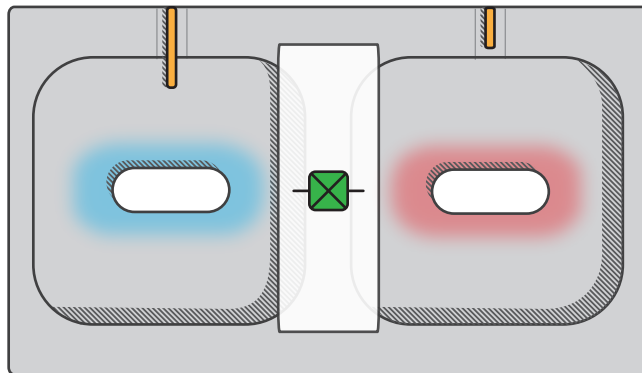

Figure 5.8: cQED architecture implementing quantum error correction of GKP codes. Two rectangular aluminum post cavities (blue and red) are coupled together through a transmon qubit (green) on a sapphire chip (white). The two cavities are coupled to transmission lines through coupling pins (orange). The fundamental mode of the blue cavity is used to readout the state of the transmon. This mode is well coupled to its pin in order for the readout to be fast. The fundamental mode of the red cavity is used as a storage mode for the GKP codes. Its coupling to the pin is sufficient to engineer a fast conditional displacement while not limiting its single-photon lifetime.

We anticipate several types of errors to be the most relevant in this experiment. The first one is the main source of decoherence in superconducting cavity: the single-photon dissipation (we denote its rate κ_s). In the first iteration of our experiment presented here, we used a post cavity [64] made of 6061 aluminum, which had a single-photon dissipation time of $1/\kappa_s = 250\,\mu s$. In order to calibrate this lifetime, we initialized the storage cavity in a coherent state and measured cuts of its characteristic function as a function of time. As presented in the introduction, the cuts of the characteristic function of a coherent state are Gaussians modulated by a sine. This measures the quadrature lifetime, which we know is twice as long as the energy lifetime in absence of pure dephasing. We neglected pure dephasing and deduced

the energy relaxation time by dividing the quadrature lifetime by two. This characteristic time can be improved by using etched high-purity aluminum, however, as we will see, it would not help by itself because the logical lifetimes of our GKP qubits are limited by error propagation from the ancilla to the cavity. The second source of error we considered is the unitary self-Kerr evolution of the cavity given by a Hamiltonian $\boldsymbol{H}_{\mathrm{Kerr}} = -\frac{K}{2}\boldsymbol{a}^{\dagger 2}\boldsymbol{a}^2$. This unitary evolution does not preserve the squeezing required for GKP codes and is thus not desirable. Its spurious effect is actually amplified for large squeezing. However, at small enough times, this unwanted unitary evolution is corrected by measuring the stabilizers of the code. Given the squeezing parameter and the error-checking time we anticipated, we designed our system such that $\frac{K}{2\pi} < \frac{\kappa_s}{2\pi}\frac{1}{50} \approx 10\,\mathrm{Hz}$. This value of K forces us to be in an unusual regime for recent cQED experiments where the dispersive coupling χ is weak, as we will see later. Last but not least, the errors of the ancilla transmon themselves are relevant to our experiment. In particular, the amplitude damping of the transmon propagates into a logical error of the qubit encoded using the GKP code. We used a transmon with decoherence times $T_1 \approx T_2 \approx 50\,\mu\mathrm{s}$.

As long as the error detection is fast enough, quantum error correction can be demonstrated with this architecture. In particular, the time during which the ancilla is entangled with the storage mode has to be small compared to the T_1 of the ancilla. We will see in the conclusion of this chapter that a T_1 error during this interaction completely scrambles the information of the GKP code, whereas a T_2 error simply results in a measurement error. In the first case, the system will never recover from the error, whereas in the second case, the error can be detected on the next stage of quantum error correction. This interaction time is directly proportional to the dispersive shift $\chi/2\pi = 28\,\mathrm{kHz}$, but also to the displacement α_s. In practice, we managed to implement a conditional displacement corresponding to the stabilizers of the GKP code in 1 μs, which is much smaller than T_1.

A full round of quantum error correction also includes the detection of the phase of the ancilla transmon. In practice, we perform this tomography using the dispersive readout described previously in the chapter about the readout of superconducting qubits. As we showed, this readout is performed in around 600 ns using a phase-sensitive parametric amplifier [78]. The error detection sequence is further lengthened by the fact that we use a feedback loop to act on the system after each readout, as will become apparent when we describe our chosen quantum error correction protocol. Overall, the total duration of a round of quantum error correction is approximately 2.5 μs, which is much faster than the error rate of our system. We summarize the parameters of our system in tables 5.1 and 5.2.

Table 5.1: Frequencies and coherence times coherence times of each mode of the experimental design. *Only the quadrature coherence time was measured and we made the reasonable assumption, for a superconducting cavity, $T_2 = 2\,T_1$.

Mode	Frequency (GHz)	T_1 (μs)	T_2 (μs)
Storage	5.260625	245*	490
Transmon	6.715001	49	57
Readout	6.6373	0.064*	0.128

Table 5.2: Parameters of the Hamiltonian of the experimental device. **Calculated using black-box quantization [127], not measured directly.

$\chi_{ij}/2\pi$ (MHz)	Storage	Transmon	Readout
Storage	(10^{-6})**	-	-
Transmon	0.028	191	1.0

5.5 Protocol to stabilize GKP codes

5.5.1 Introduction to the stabilization of GKP codes

In the previous section, we have demonstrated that we could map the phase of the stabilizers of the GKP codes onto an ancilla two-level system. We also showed that, by doing so, we could detect a small shift of a GKP code. In fact, in stabilizer codes, the measurement of a stabilizer does more than simply detecting errors: it projects the state of the system into a state that is compatible with the value obtained for the stabilizers. For example, after one round of measurement of the stabilizers of the surface code, the state of the array of physical qubits is projected into the so-called *quiescent state* [57]. Similarly, if one measures the stabilizers $\boldsymbol{S}_a$ and $\boldsymbol{S}_b$ of a GKP code, then any state of the storage mode is projected into the closest state of the ideal GKP code that is compatible with the values measured for the stabilizers. Thus, preparing a GKP logical qubit requires only a good measurement of its stabilizers. Moreover, the protection of a GKP logical qubit against any type of error also stems from this projection. All possible errors acting on a superconducting cavity are continuous, which means that at small times, an error transforms a GKP state into a state that is close to

the same GKP state. When this transformed state is projected, after a measurement of the stabilizers, it is projected into the same GKP state with, at worst, a small (known) shift.

The stabilization, and thus quantum error correction, of GKP codes, relies only on our ability to measure efficiently the stabilizers. Once the phase of the stabilizer is mapped onto the phase of a superposition of an ancilla two-level system, this task is shifted to the measurement of the phase of the ancilla. Unfortunately, there is no direct measurement of this phase. In fact, all the measurements we can perform on a two-level system are projections of the two-level system along one axis, which yield only binary results, whereas the phase of a superposition is a real number. Thus, the measurement of the phase of the stabilizers can only be done approximately by repeating the mapping of this phase onto the ancilla and measuring this ancilla along different axes. The choice of the axes of these measurements is what constitutes the stabilization protocol.

In this section, we will first show how the state of the storage is projected after each measurement of the ancilla. We will then use this formalism to review the previous protocols that have been proposed to create/stabilize GKP states. Finally, we will introduce the protocol that we implemented experimentally, that we named the short memory protocol.

5.5.2 Projection of the state of the storage after a measurement of the ancilla

Let us see with an example how each measurement of the ancilla projects the state of the storage. We write the density matrix of the state of the storage ρ_s in the position basis $|q\rangle$, such that

$$\rho_s = \int dQ_1 \, dQ_2 \, c(Q_1, Q_2) \, |Q_1\rangle \langle Q_2| , \tag{5.28}$$

with the normalization condition $\int dQ \, c(Q, Q) = 1$. The position probability distribution of ρ_s is given by

$$\begin{aligned} \mathrm{P}(Q) &= \langle Q| \, \rho_s \, |Q\rangle \\ &= c(Q, Q). \end{aligned} \tag{5.29}$$

Our goal is to find the evolution of the position probability distribution after an interaction with the ancilla and the measurement of this ancilla. We know from the section on the stabilizers that the stabilizer that impacts the position the most is a displacement along the momentum axis, which we denote $\boldsymbol{S}_a = \boldsymbol{D}(i\alpha)$ (with α real) for the square and the

hexagonal codes (see Fig. 5.3). We write the corresponding interaction between the ancilla and the storage mode $\boldsymbol{D}\left(i\frac{\alpha}{2}\boldsymbol{\sigma}_z\right) = e^{i\alpha\boldsymbol{Q}\boldsymbol{\sigma}_z}$, which is a displacement by $\alpha/2$, upward when the ancilla is in $|e\rangle$ and downward when the ancilla is in $|g\rangle$. When the ancilla is initialized in the state $|+\rangle = (|g\rangle + |e\rangle)/\sqrt{2}$, the total density matrix of the system is

$$\rho_{\text{tot}} = \int dQ_1 \, dQ_2 \, c(Q_1, Q_2) \, |Q_1\rangle \langle Q_2| \otimes |+\rangle \langle +|. \tag{5.30}$$

When the conditional displacement acts on the density matrix, we get

$$\boldsymbol{D}\left(i\frac{\alpha}{2}\boldsymbol{\sigma}_z\right)\rho_{\text{tot}}\boldsymbol{D}\left(i\frac{\alpha}{2}\boldsymbol{\sigma}_z\right)^\dagger = \int dQ_1 \, dQ_2 \, c(Q_1, Q_2)e^{i\alpha\boldsymbol{Q}\boldsymbol{\sigma}_z} |Q_1\rangle \langle Q_2| \otimes$$

$$|+\rangle \langle +| e^{-i\alpha\boldsymbol{Q}\boldsymbol{\sigma}_z}$$

$$= \frac{1}{2} \int dQ_1 \, dQ_2 \, c(Q_1, Q_2) \, |Q_1\rangle \langle Q_2| \otimes$$

$$(e^{i\alpha(Q_2-Q_1)} |g\rangle \langle g| + e^{-i\alpha(Q_2-Q_1)} |e\rangle \langle e| + e^{i\alpha(Q_1+Q_2)} |e\rangle \langle g| + e^{-i\alpha(Q_1+Q_2)} |g\rangle \langle e|)$$

$$= \int dQ_1 \, dQ_2 \, c(Q_1, Q_2) \, |Q_1\rangle \langle Q_2| \otimes$$

$$(\cos(\alpha(Q_2 - Q_1))\boldsymbol{I}_L + i\sin(\alpha(Q_2 - Q_1))\boldsymbol{\Pi}_z + \cos(\alpha(Q_1 + Q_2))\boldsymbol{\Pi}_x$$

$$+ \sin(\alpha(Q_1 + Q_2))\boldsymbol{\Pi}_y), \tag{5.31}$$

where $\boldsymbol{\Pi}$'s are the projectors in the Pauli basis, for example $\boldsymbol{\Pi}_x = |+\rangle \langle +| - |-\rangle \langle -|$ (these matrices are equal to the Pauli matrices but they live in the space of density matrices). From this complicated expression, we can deduce the position probability distribution after a measurement of the ancilla along any axis. We summarize in a table the cases where the ancilla is measured along x, y or any axis $\cos(\varphi)x + \sin(\varphi)y$.

axis	result	$P(Q) = \langle Q| \rho_s |Q\rangle$
x	+1	$c(Q,Q)(1 + \cos(2\alpha Q)) = c(Q,Q)\cos^2(\alpha Q)$
	-1	$c(Q,Q)\sin^2(\alpha Q)$
y	+1	$c(Q,Q)\sin^2(\alpha Q - \frac{\pi}{4})$
	-1	$c(Q,Q)\sin^2(\alpha Q + \frac{\pi}{4})$
φ	+1	$c(Q,Q)\cos^2\left(\alpha Q + \frac{\varphi}{2}\right)$
	-1	$c(Q,Q)\sin^2\left(\alpha Q + \frac{\varphi}{2}\right)$

This projection is at the center of all the protocols that realize the stabilization of GKP states using an ancilla two-level system. For example, the first creation of GKP states was done using the motional degree of freedom of a trapped ion as the harmonic oscillator storing the GKP state [21]. In that architecture, the readout of the ancilla, which is the internal degree of freedom of the ion, is half-QND: it destroys the state of the oscillator if the ancilla is found in $|g\rangle$ and preserves it only if it is found in $|e\rangle$. Because of this, their protocol is based on post-selection and is not deterministic. In that paper, the storage mode is initially in a squeezed state of the position Q (which is anti-squeezed in the momentum P). The initial momentum distribution $\mathrm{P}(P)$ of such a state is a large Gaussian. Their group then realized an effective conditional displacement $\boldsymbol{D}(\sqrt{\frac{\pi}{2}}\boldsymbol{\sigma}_z)$, measured the ancilla along the x axis and kept only the events where the measurements all yielded +1. According to our table, after n such measurements, the momentum probability distribution is changed into $\mathrm{P}(P)\cos^{2n}(\sqrt{2\pi}P)$, which "carves" sharp peaks at the values of momentum that correspond to a GKP state $|0\rangle_L$.

By using a QND readout, this protocol can be refined in order to obtain a deterministic creation and stabilization of GKP states. For this, one needs to repeat each QND measurement of the ancilla multiple times and along various axes, which effectively realizes a phase estimation. A "naive" approach to phase estimation would be to only measure the ancilla along two orthogonal axes such as x and y. Actually, a more optimal protocol consists in adapting the ancilla measurement angle φ by considering all the previous measurements [124]. Such a protocol is called adaptative phase estimation. In both cases, the phase of the ancilla, or equivalently the offset of the stabilized GKP code, is deduced by analyzing the outcome of n measurements, and for each string of n binary outcomes corresponds one phase. In practice, such protocols are not well suited for the steady state stabilization of GKP codes because they require a look-up table with 2^n entries. To avoid this, we created a Markovian protocol that requires only a simple feedback law, which uses only the latest measurement outcome.

5.5.3 Markovian protocol to stabilize GKP codes

A stabilization protocol that remains tractable for an arbitrary amount of time can only consider the results of a finite number of measurements. Taken to the extreme, the protocol with the shortest memory takes into account only the outcome of the last measurement and takes a decision based on it. In such a protocol, what is the optimal measurement angle, and what feedback law should we implement based on the binary outcome of this measurement?

In order to find the optimal measurement angle of this measurement, we need to analyze the steady state we would like to get with our protocol. After enough time, a finite amount
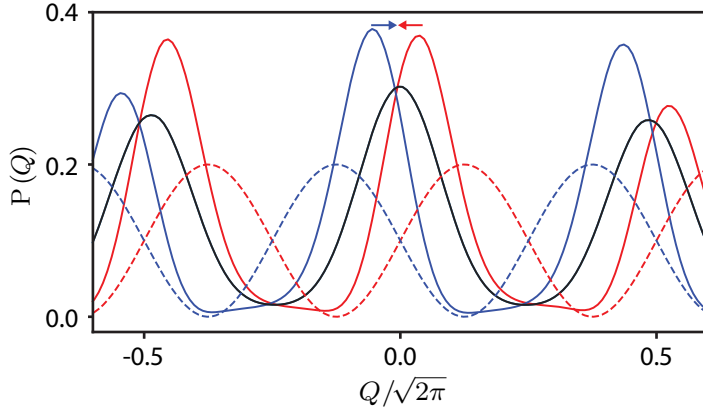
Figure 5.9:   Projection of a mixed square GKP state after a stabilizer measurement. We represent, with a black line, the position probability distribution of the state just before a stabilization measurement. The stabilization measurement multiplies this probability distribution by $\sin^2\left(\sqrt{2\pi}Q \pm \frac{\pi}{4}\right)$, depending on the result of the measurement. These two functions are represented in blue and red dashed lines. Finally, the new, outcome-dependent, probability distribution of this state after the measurement is represented in blue and red solid lines. After the measurement, we apply a corrective displacement represented with blue and red arrows.

of dissipation will lead to mixed state of $|0\rangle_L$ and $|1\rangle_L$, even in presence of the stabilizing protocol. Here, we choose a GKP code with finite squeezing, where the wavefunctions of $|0\rangle_L$ and $|1\rangle_L$ resemble the ones from Fig. 5.2. During the finite amount of time between two stabilization steps, this mixed state will get distorted. For example, dephasing and Kerr would twist the outer peaks of this state, while single-photon dissipation will contract such peaks towards the center and enlarge them. We represent the position probability distribution of such a state, which suffered from realistic dissipation expected for our superconducting cavity in Fig. 5.9. Ideally, the measurement protocol needs to purify this state and undo, as much as possible, the effect of the dissipation. As we mentioned previously, at short time, the dissipation is a superposition of small shifts $\boldsymbol{D}(\epsilon)$ which leads to a continuous diffusion in phase-space. As we saw in Fig. 5.5, this displacement is mapped onto the ancilla, which is then in $1/\sqrt{2}\left(|g\rangle + e^{2i\phi_\epsilon}|e\rangle\right)$. In this state, the expectation value of $\boldsymbol{\sigma}_x$ is proportional to $\cos(2\phi_\epsilon)$ while the expectation value of $\boldsymbol{\sigma}_y$ is proportional to $\sin(2\phi_\epsilon)$. We thus see that, to first order in ϕ_ϵ, all the information about ϵ is in the expectation value of $\boldsymbol{\sigma}_y$. If the measurement of $\boldsymbol{\sigma}_y$ contains the most information, this measurement also has the strongest

backaction. As we saw previously, and as represented in Fig. 5.9, this measurement multiplies the position probability distribution by $\sin^2\left(\alpha Q \pm \frac{\pi}{4}\right)$, which has a maximum slope where the peaks of the distribution are. Thus, this chosen projection can be viewed as the one that sharpens the peaks of the distribution the most, by "trimming" their edges.

After the projection, the peaks of the position distribution are sharper and thus are more distinguishable, which realizes our desired correction. However, the distribution is now off-set, and thus we will not start the next round of correction in the same state as we started. In steady-state, this offset is always the same and depends only on the binary outcome of the measurement. We complete our protocol by adding a simple feedback which centers the distribution by using a corrective displacement $\boldsymbol{D}(\pm\epsilon_c)$, where the direction of this dis-placement is decided on the outcome of the measurement. In practice, the value of ϵ_c is first optimized numerically to get the highest steady-state value for the stabilizer, taking into account all the parameters of the system that we experimentally measured. This first guess is finally refined to get the maximum stabilizer value possible experimentally. In our experi-ment, the conditional displacement that we previously described has a non-RWA term that results in a small unconditional displacement. We use two values of corrective displacements that are $\epsilon_{c,g} = +0.10$ and $\epsilon_{c,e} = -0.18$ (this unconditional displacement is thus +0.04).

In theory, this protocol would converge to a large GKP code, whose extent would be limited only by the dissipation acting between each stabilization step. However, we will now see that it is preferable to artificially limit the extent of the envelope of the GKP codes.

5.5.4   Limiting the number of photons in the GKP codes by trimming their envelope

Numerical simulations of the stabilization steps previously described led us to the sur-prising conclusion that this protocol does not obtain a stable steady state that is a GKP state. We analyzed the possible spurious effects of these steps and reached the conclusion that, in order to reach a stable steady state, we need to artificially limit the size of the envelope of the stabilized GKP state, and we need to guarantee that it remains centered. Let us first describe the spurious effects we identified and we will then describe how we mitigate them.

First, notice that each stabilization step for the position Q is realized with a condi-tional displacement in momentum P, which spreads the momentum probability distribu-tion. More generally, each stabilization step along one direction spreads the envelope of the state in the orthogonal direction. Intuitively, the more a GKP state is spread, the more its peaks are squeezed, which diminishes the overlap between two neighboring peaks and should

lead to a better protection. However, this link between the squeezing of a peak and the spread of the envelope is only guaranteed for pure states. In fact, a GKP state whose envelope is very extended might be more susceptible to dissipation instead of being more protected. For example, pure dephasing and the Kerr effect are more detrimental to the outer peaks of a GKP state than to the center peaks. Similarly, single-photon dissipation contracts each peak towards center, but this contraction rate is larger for the peaks that are the furthest from the center.

A second spurious effect can be observed in Fig. 5.9. In the previous paragraph, we have stated that single-photon dissipation leads to the contraction of outer peaks of the distribution towards the center. Said in another way, the peaks on the left of the distribution are statistically more shifted towards the right, whereas the peaks on the right are more shifted towards the left. The stabilization steps we described cut the distribution by multiplying it by a sine squared function that is either offset to the left or to the right. Therefore, after this projection, one side has a larger weight than the other. This effect can be observed in Fig. 5.9, where the red peak on the left is higher than the one on the right and, inversely, the blue peak on the right is higher than the blue peak on the left. This shift of the center of mass of the distribution does not appear as an error: it is only a shift of the weight of the envelope. Thus, this shift is never detected by an error correction protocol. Nevertheless, because it unbalances the distribution it makes it more susceptible to dissipation.

Our goal is analogous to the goal of the previously described stabilization steps. In the previous section, we engineered a measurement that sharpens the peaks and keeps them centered. Here, we would like to sharpen the envelope and keep it centered. This can be realized by engineering a weak version of the previous measurement. For example, to limit the spread of the envelope in the q quadrature, we will use a small conditional displacement $D\left(i\frac{\delta}{2}\boldsymbol{\sigma}_z\right)$, where δ is a small real number. The effect of such a measurement is represented in Fig. 5.10, where we show that the probability distribution is multiplied by $\sin^2\left(\delta Q \pm \frac{\pi}{4}\right)$. Once the state is projected, its center of mass is still offset. We conclude the weak measurement step by displacing the storage mode towards the center by half a stabilizer. This displacement preserves the code while minimizing the offset of the center of mass of the envelope. Notice that such a small conditional displacement displacement does not commute with the measurement of the stabilizers of the ideal GKP code. Because such a measurement is aimed at limiting the extent of the envelope, it also limits the squeezing of the peaks to a finite value. Thus, the value of δ has to be chosen experimentally in order to get the best steady state GKP code possible. This δ is a function of the duration of each measurement step and of the dissipation that acts on the system. In practice, similarly to the previous corrective displacement
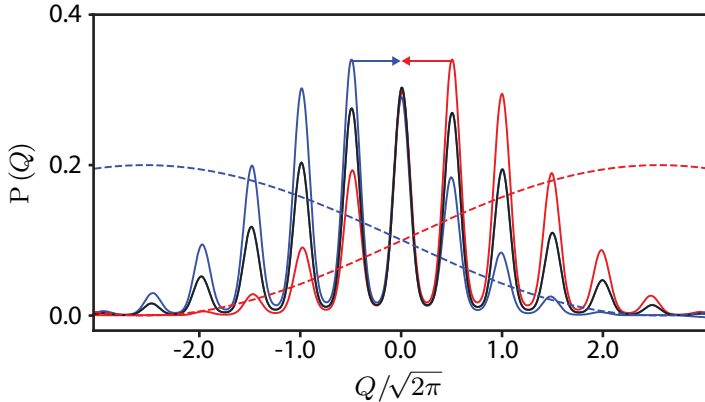
Figure 5.10: Projection of a mixed square GKP state using a weak measurement of a displacement. We plot the position probability distribution of a mixed GKP state with finite envelope. Before the interaction, the state of the storage mode is represented with a black line. We use a small conditional displacement $\boldsymbol{D}(i\delta\boldsymbol{\sigma}_z)$ to limit the size of the envelope. The probability distribution is thus multiplied by $\sin^2\left(\delta Q \pm \frac{\pi}{4}\right)$, represented with blue and red dashed lines. The probability distributions after the projection are represented with blue and red dashed lines. We then apply a corrective displacement of half a stabilizer with a direction which depends on the result of the measurement. These displacements are represented using blue and red arrows.

ϵ_c, we first numerically optimize δ and then adjust it experimentally to get the maximum value for the stabilizers in steady state. We found the optimal value for our system to be $\delta = 0.28$ (which corresponds to 11% of the stabilizer value $\sqrt{2\pi}$ for a square grid).

5.5.5 Experimental implementation of the Markovian protocol

We now have a recipe that allows to implement this protocol on any system. In this subsection, we give the details of the implementation of this protocol for our particular system, whose parameters are summarized in tables 5.1 and 5.2. These details will be useful to understand how we obtain the data that will be shown in the rest of this chapter.

We represent the circuit of a complete stabilization step including the weak measurement in Fig. 5.11(a). In this circuit, we take the particular case of the stabilization of the q quadrature of a square code. The measurement of the ancilla along its y axis is done by combining a rotation of $\pi/2$ around the x axis and a measurement of $\boldsymbol{\sigma}_z$.

In Fig. 5.11(b), we represent the pulses that implement half of this circuit. The first thing
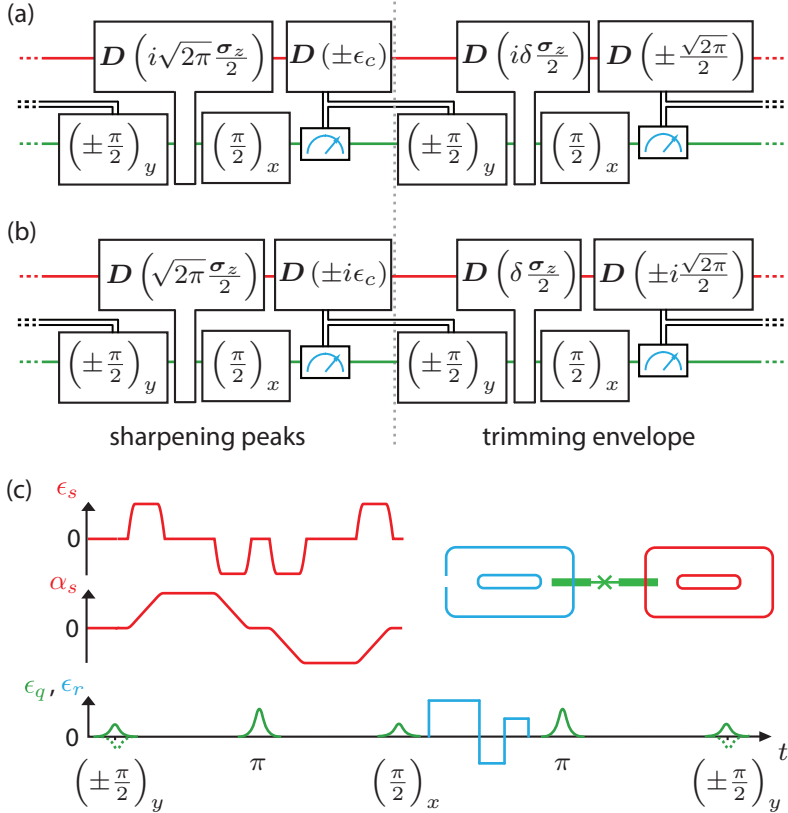
Figure 5.11: Description of the experimental implementation of a measurement step. (a-b) Circuit representation of a full stabilization step for Q (a) and for P (b). The red line represents the actions on the storage while the green line represents those on the ancilla. The blue measurement apparatus represents a measurement of σ_z of the ancilla using the readout mode. Finally, the double black line represents feedback using classical communication. The first half of this circuit is used to sharpen the peaks of the distribution while the second half is used to trim its envelope. (c) We represent the shape of the pulses acting on the storage (in red), the ancilla transmon (in green) and the readout (in blue), with amplitudes ϵ_s, ϵ_q and ϵ_r respectively. The response of the storage α_s is also represented. The pulses before the readout implement a conditional displacement in a similar way as described in Fig. 5.6. The blue readout pulse corresponds to the depleted readout described in Fig. 3.6. After the readout, the transmon is flipped and we added a delay of the same length as the readout. Based on the result of the measurement, the transmon is then re-initialized in $|+\rangle$ with a $(\pi/2)$-pulse around the y axis. This last pulse corresponds to the first pulse of the next measurement step. The total duration of such a step is 2.5 µs, which means that the total duration of circuits (a) or (b) is 5.0 µs.

to notice is that the implementation of the conditional displacement is slightly different than previously described. We limited the maximum number of photons in the storage cavity by using successive fast square pulses that displace the state of the storage mode by 320 photons, instead of using continuous square pulses as described previously. We know that, the larger the maximum photon number in the cavity is during the conditional displacement, the more the conditional displacement is susceptible to very small pure dephasing (even of the order of 100 Hz). However, we do not have conclusive evidence that it was the main limitation on the conditional displacement speed. Nevertheless, because the duration of our sequence is actually limited by the incompressible readout time, we did not try to shorten the duration of the conditional displacement. The total duration of the conditional displacement is 1.2 µs.

After each interaction, the state of the ancilla transmon is measured and a decision is made based on the result of this measurement. The readout duration itself is 660 ns, but the treatment of this measurement takes an additional 300 ns approximately. During this readout process, the dispersive interaction remains, which rotates the state of the storage conditioned on the state of the ancilla. We cancel this interaction by adding a π-pulse on the ancilla right after the readout pulse. The state of the storage refocuses after waiting an additional 660 ns, during which the measurement of the ancilla is analyzed.

Finally, once the result of this measurement is recorded, we apply the corrective displacement on the storage mode and we re-initialize the ancilla transmon in $|+\rangle$. Notice that this re-initialization requires a $\pi/2$-pulse in a direction which depends on the result of the previous measurement.

The total duration of a single stabilization step is 2.5 µs, thus the duration of a stabilization step including the weak measurement is 5 µs, which remains small compared to the dominating single-photon dissipation time of 245 µs.

5.6   Steady state stabilization of GKP codes

We first verify that, when this protocol is applied to a storage mode initially in the vacuum state, the state of the storage mode reaches a steady state that corresponds to the desired GKP code. As the stabilization is realized by measuring the stabilizers of the storage cavity, we can plot their average expectation value as a function of stabilization round number (and thus time). Because the feedback is always centering and symmetrizing the state of the storage, the expectation value of the stabilizer is always real. For the ideal GKP code, this value should converge to 1. However, for our approximate GKP code, the expectation value of the stabilizer is bounded by a value lower than 1, both because of the dissipation and because of

the artificial limit set on the width of the envelope. Finally, to characterize fully the steady state reached by the storage mode, we give a complete phase-space representation of this state. Our system is designed to have a low dispersive coupling, and thus, the Wigner function of the state cannot be measured. However, because we have engineered a tunable conditional displacement, we can measure the characteristic function of this state. Our results are shown in Fig. 5.12.

For the square GKP code, the stabilization protocol is exactly the one given in Fig. 5.11(a), where we alternate the stabilization of the Q quadrature and the stabilization of the P quadrature. As we can see, the value of both stabilizers increases and saturates at approximately 0.6. We also notice that, when one quadrature is stabilized, the other one decays. This decay is purely due to the dissipation and not to the backaction of the measurement, because the two stabilizers commute. The features of this evolution of the stabilizers are well captured by numerical simulations of our system, which use only the parameters we have measured. The steady state that we reach is represented by its characteristic function, whose real part is plotted in Fig. 5.12(c). As expected, the characteristic function resembles a square grid. Because the protocol is such that the state is symmetric around the origin, the imaginary part of the characteristic function is 0. The expectation value of the stabilizers is emphasized with black dots located at $\sqrt{2\pi}$ in position and momentum. Finally, when we introduced the Pauli algebra of the GKP codes we saw that the Pauli matrices are displacements of half a stabilizer. Thus, the characteristic function, which measures the expectation values of displacements, also contains information on the Pauli matrices of the GKP qubit: they are points that are halfway between the origin and the stabilizers. Notice that, for approximate GKP states, these points will never reach the maximum value of ± 1, even if the overlap between $|0\rangle_L$ and $|1\rangle_L$ is negligible. As we expect, the expectation values of all the Pauli matrices are 0 because, in steady state, the logical qubit has fully decohered *within* the stabilized manifold.

The protocol is slightly different for the hexagonal code, mostly for technical reasons. First, the axes of the weak measurements are slightly changed. For example, if we measure the stabilizer $\boldsymbol{S}_a = \boldsymbol{D}(i\alpha)$ (blue in Fig. 5.12(d), then the following weak measurement uses a conditional displacement perpendicular to $\boldsymbol{S}_a$. This way, the corrective displacement for the weak measurement is $\boldsymbol{D}(\pm i\alpha/2)$, which remains in the stabilized code. Notice that if we had kept the weak measurement in the same direction as the previous stabilization, then the corrective displacement to apply would not have been within the code. As a consequence, if we keep only the stabilizers $\boldsymbol{S}_{a,b}$ of the hexagonal code, the envelope is better defined along the momentum P than along the position Q. This is due to the fact that the two necessary stabilizers of the hexagonal code are not orthogonal to one another. In order to get the
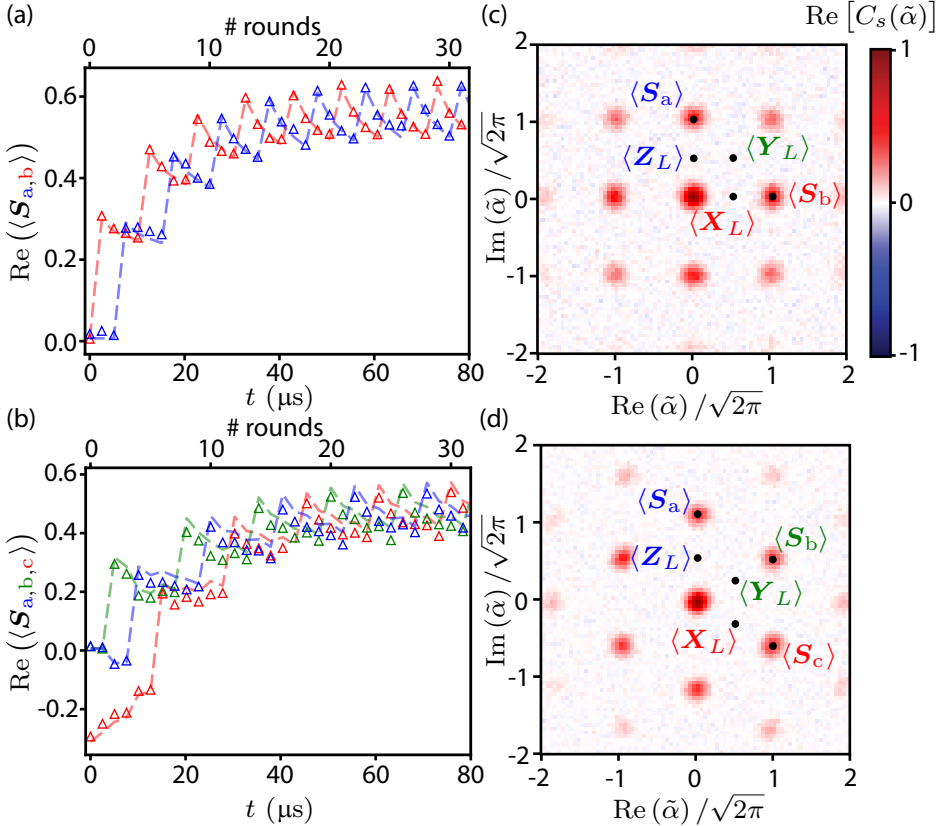
Figure 5.12: Steady state stabilization of the square and hexagonal GKP codes. (a), (b) Real part of the stabilizers of the GKP codes as a function of time (bottom axis) and round number (top axis) for the square GKP code (a) and for the hexagonal GKP code (b). The triangles are data points while the dashed lines are numerical simulations. (c), (d) Real part of the characteristic function of the storage mode after 84 stabilization steps for the square GKP code (c) and for the hexagonal GKP code (d). We indicate with black dots the particular points of the characteristic functions that correspond to the average values of the stabilizers $S_{a,b,c}$ and of the logical Pauli matrices X_L, Y_L and Z_L. These points would reach an absolute value of 1 only for the ideal GKP codes.

confinement of the envelope to be isotropic, we added the measurement of a third stabilizer in the direction of Y_L, as shown in green in Fig. 5.12(d). The three stabilizers of the code are now $S_a = D(i\alpha)$, $S_b = D\left(e^{i\frac{\pi}{6}}\alpha\right)$ and $S_c = D\left(e^{-i\frac{\pi}{6}}\alpha\right)$, with $\alpha = \sqrt{2\pi}\sqrt{\frac{2}{\sqrt{3}}}$. Notice that the length of the stabilizers did not change, the added stabilizer commutes with the

previously described ones. Note that the information measured using this latter stabilizer is redundant with the information measured with the other ones, but in practice it was easier to code a script that measured these three stabilizers. Besides these details, the behavior observed for the hexagonal code is the same as for the square code. You can notice in Fig. 5.12(b) that the sequence for the hexagonal code had an error. The first point of this plot corresponds to the real part of the stabilizers after a strong measurement of S_c. However, the phase of the first $\pi/2$-pulse on the ancilla had the wrong phase, which led to a negative value for the expectation value of S_c. This error is then corrected once the protocol enters the feedback loop.

We now want to estimate how thin are the peaks of the stabilized GKP state. Unfortunately, the window of the characteristic function is too narrow to capture all the details of the stabilized states. In fact, we have noticed that the coherence of our conditional displacement diminishes for large conditional displacements, which lowers the contrast of the outer points of the characteristic function. Crucially, because the characteristic function is the Fourier transform of the Wigner function, the width of the peaks of the distribution is captured in the overall width of the characteristic functions. In order to evaluate the width of these peaks, we use the numerical simulation used to produce the dashed lines in Fig. 5.12(a) and (b). For both the square code and the hexagonal code, we look at the position probability distribution of the steady state. We then fit the peaks of this distribution with a Gaussian distribution and deduce a squeezing parameter, which gives the ratio of the width of these peaks compared to the width of the vacuum state. The squeezing parameter is usually given in dB and is defined as

$$r_{\mathrm{dB}} = 10 \log \left(\frac{\Delta Q_0^2}{\Delta Q^2} \right), \tag{5.32}$$

where ΔQ^2 is the variance of the GKP peak, and ΔQ_0^2 is the variance of the vacuum. The simulations suggest that we reach a squeezing of 8.4 dB for the square code and of 7.8 dB for the hexagonal code. In comparison, the lowest threshold for fault-tolerant quantum computing using GKP states is around 10 dB of squeezing [128]. This number corresponds to a standard deviation of 0.19 for the square code and 0.20 for the hexagonal code, when the standard deviation of the vacuum is 0.5. In order to get an idea of the overlap between the distributions of the approximate GKP states $|0\rangle_L$ and $|1\rangle_L$ that are superpositions of such squeezed states, we use the error function. Let us consider two Gaussian distributions with standard deviation σ and separated by $\sqrt{\frac{\pi}{2}}$. We place a threshold between these two distribu-

tions at $\frac{1}{2}\sqrt{\frac{\pi}{2}}$. The overlap between these two distributions is given by $1 - \mathrm{erf}\left(\frac{1}{2}\sqrt{\frac{\pi}{2}}\frac{1}{\sqrt{2}\sigma}\right)$. For the squeezing parameters we estimated, this overlap is approximately 0.1% for the square code and 0.2% for the hexagonal code, which shows that, even if these GKP codes are approximate, the two logical basis states barely overlap.

5.7 Deterministic preparation of arbitrary GKP states

As we have seen before, the value of the stabilizers can be mapped onto the state of the ancilla transmon. We have also seen that the Pauli operators are simply displacements by half a stabilizer. We can thus map the expectation values of the Pauli operators onto the ancilla by using conditional displacements of half a stabilizer. These points are indicated in Fig. 5.12(c) and (d). However, this measurement of the Pauli operators can only reach -1 or 1 for ideal GKP codes that are infinitely squeezed. Hence, even if the basis states of the approximate GKP code have a negligible overlap, this measurement of the Pauli operator is only approximate. It is, nevertheless, the only experimentally available approximate measurement of the Pauli operators of the stabilized codes. We use such approximate measurements of the Pauli operators to project the steady state mixed state into one of the basis states. For example, we can measure the logical Pauli $\boldsymbol{Z}_L$ and apply the logical Pauli operator $\boldsymbol{X}_L$ when the result of the measurement is +1. This way, we approximately prepare the state $|1\rangle_L$. The characteristic functions of the state we obtain after such a measurement is plotted in Fig. 5.13 for a measurement of $\boldsymbol{Z}_L$ and of $\boldsymbol{Y}_L$.

After the measurement of $\boldsymbol{Z}_L$, how much of the state is projected into $|1\rangle_L$? To answer this, we estimate how much of the position probability distribution of the projected state corresponds to the distribution of $|1\rangle_L$. For example, for the square code, the position probability distribution of $|1\rangle_L$ is entirely contained outside position stripes of width $\sqrt{\frac{\pi}{2}}$ centered at $Q = k\sqrt{2\pi}$, as shown in gray in Fig. 5.14. On that figure, we plot the simulated position probability distribution of the square state after it is projected. By integrating this distribution over the gray stripes, we deduce what part of the distribution is closer to $|0\rangle_L$ than to $|1\rangle_L$. Our simulations suggest that 8.4% of the distribution is within these gray stripes. For the hexagonal code, the same analysis suggests that 11.2% of the distribution is closer to $|0\rangle_L$ after a single measurement.

Note that this result is obtained after only one measurement. If the goal were to prepare an eigenstate of a Pauli operator, this could be done in a better way than with a single measurement on the mixed steady state. For example, the stabilization protocol could be adapted such that it converges to a single state, instead of a manifold of two states, by replac-
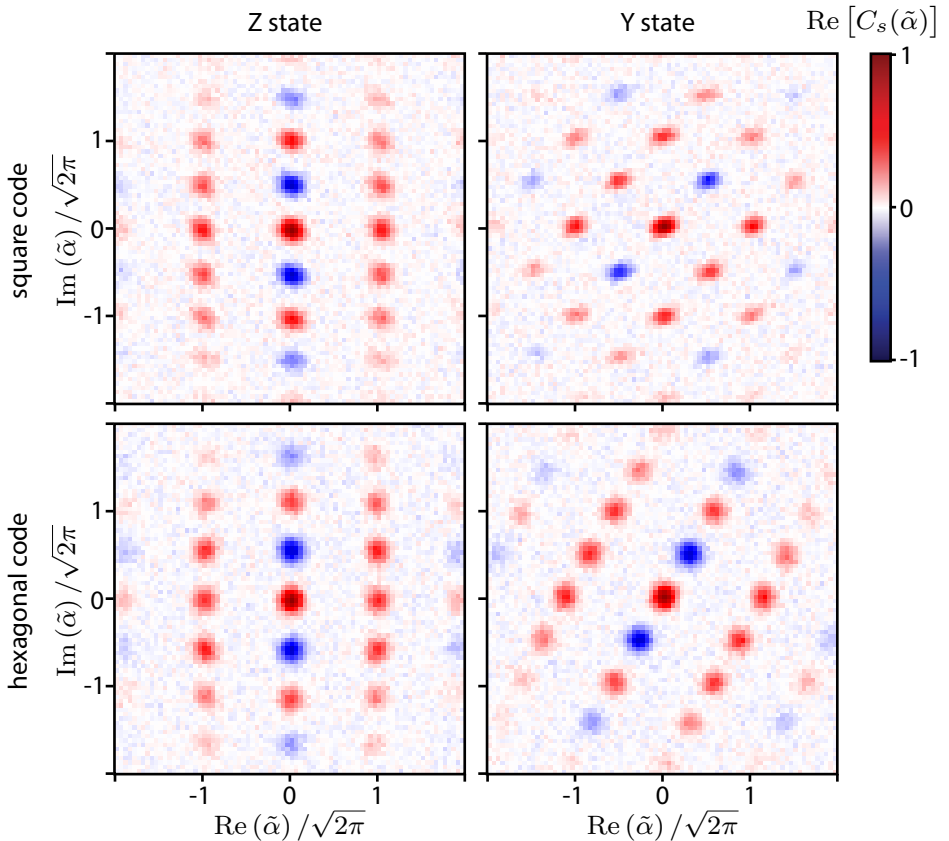
Figure 5.13: Preparation of the GKP basis states. We represent the real part of the characteristic functions of the state of the storage mode after one round of preparation of $|1\rangle_L$ (left column) and $\frac{1}{\sqrt{2}}(|0\rangle_L - i|1\rangle_L)$ (right column), for both the square code (top line) and the hexagonal code (bottom line).

ing the measurement of one of the stabilizer by its corresponding Pauli operator (for example replacing $\boldsymbol{S}_a$ by $\boldsymbol{X}_L$).

Finally, we want to show that we can also prepare states that are not eigenstates of the Pauli operators using gates developed in the group of Jonathan Home [21]. These gates use arbitrary rotations of the ancilla and map them onto arbitrary rotations of the GKP state. The direction of the rotation depends on a final measurement of the ancilla. In our implementation, because the readout of the ancilla is QND, these gates can be done deterministically. Using the method described in this paper, we demonstrate that we can create one of the
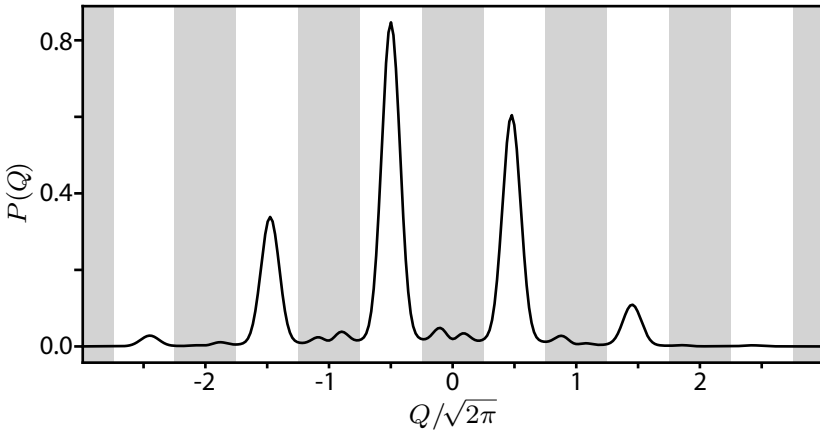
Figure 5.14: Simulated position probability distribution of the state after a Pauli measurement and a feedback preparation of $|1\rangle_L$ of the square code.

so-called "magic states". It has been shown that the preparation of such states, even noisy, added to the ability to do Clifford gates fault-tolerantly, is enough to perform a fault-tolerant quantum computation [129].

To describe our magic state preparation, we first start with a state $|0\rangle_L \otimes (|g\rangle + |e\rangle)$, up to normalization factors. We then perform an X_L gate, conditioned on the state of the qubit (using a conditional displacement of half a stabilizer). We get

$$|0\rangle_L \otimes (|g\rangle + |e\rangle) \rightarrow |0\rangle_L \otimes |g\rangle + |1\rangle_L \otimes |e\rangle. \tag{5.33}$$

Then, we perform a rotation of the ancilla of angle $\pi/4$ around its y axis, leading to a state

$$|0\rangle_L \otimes \left(\cos\left(\frac{\pi}{8}\right) |g\rangle + \sin\left(\frac{\pi}{8}\right) |e\rangle \right) + |1\rangle_L \otimes \left(\cos\left(\frac{\pi}{8}\right) |e\rangle - \sin\left(\frac{\pi}{8}\right) |g\rangle \right)$$

$$= \left(\cos\left(\frac{\pi}{8}\right) |0\rangle_L - \sin\left(\frac{\pi}{8}\right) |1\rangle_L \right) \otimes |g\rangle + \left(\sin\left(\frac{\pi}{8}\right) |0\rangle_L + \cos\left(\frac{\pi}{8}\right) |1\rangle_L \right) \otimes |e\rangle. \tag{5.34}$$

Finally, the ancilla is measured and the state of the storage mode is projected into one of two states. Note that these two states can be mapped onto one another using a Y_L gate, which makes the magic state preparation deterministic. In practice, the initial state of the
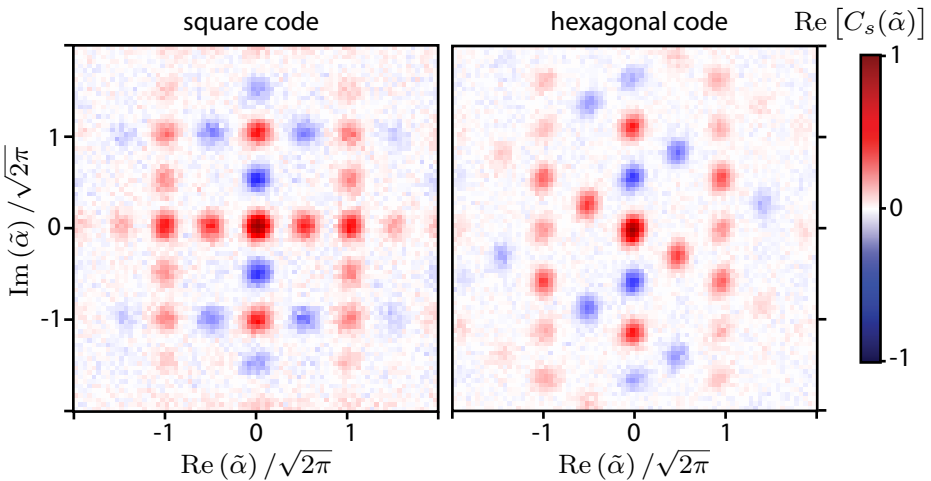
Figure 5.15: Preparation of GKP magic states. We represent the real part of the characteristic functions of the prepared magic states for the square code (left) and the hexagonal code (right). These states correspond approximately to $\sin\left(\frac{\pi}{8}\right)|0\rangle_L + \cos\left(\frac{\pi}{8}\right)|1\rangle_L$ for their respective codes.

storage is approximately $|0\rangle_L$, up to the fact that we prepare it with a single approximate Pauli measurement, and we prepare the state $\sin\left(\frac{\pi}{8}\right)|0\rangle_L + \cos\left(\frac{\pi}{8}\right)|1\rangle_L$, both for the square and hexagonal codes. In such a state, we expect $\langle Z_L\rangle = -\langle X_L\rangle = \sin^2\left(\frac{\pi}{8}\right) - \cos^2\left(\frac{\pi}{8}\right) \approx -0.7$. The characteristic functions of the prepared states are represented in Fig. 5.15. As you can see, the points corresponding to the $\langle Z_L\rangle$ is negative and of same, but opposite, amplitude as the point representing $\langle X_L\rangle$.

5.8 Lifetime of the GKP logical qubits

We have now demonstrated that our protocol stabilizes a manifold of GKP states in steady state and that we can initialize a GKP logical qubit into a given state. How do these purified states evolve into a mixed state? During each stabilization round, the logical qubit suffers from dissipation and spurious unitary evolutions, such as the Kerr effect, which can mix the states within the stabilized manifold. When the stabilization is much faster than the timescale of these errors, a given GKP state should persist in time. However, the errors of the ancilla used for the stabilization will also propagate to the logical qubit. The goal of this section is to observe the dynamics of the logical qubit in time, after the preparation of given states.
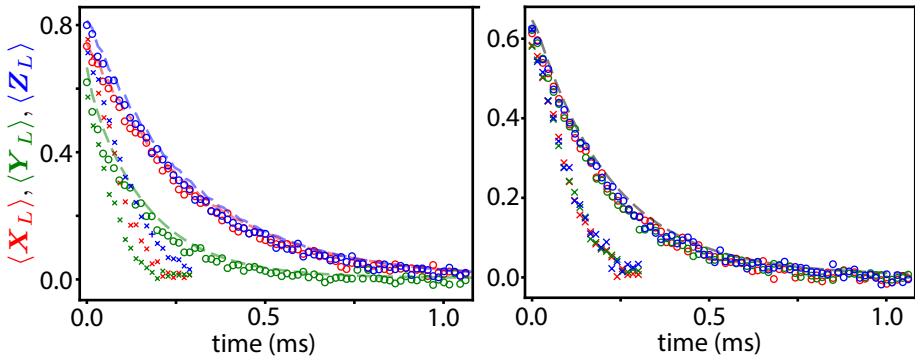
Figure 5.16: Lifetime of the logical GKP qubits. We represent the expectation values of the logical Pauli operators $\boldsymbol{X}_L$ (in red), $\boldsymbol{Y}_L$ (in green) and $\boldsymbol{Z}_L$ (in blue) as a function of time, for the square code (on the left) and the hexagonal code (on the right). The initial state is, in each case, an approximate eigenstate of the corresponding Pauli with eigenvalue +1. The square code is initially prepared using two consecutive measurements of the corresponding Pauli operators, with a feedback preparation on the first measurement, and with a post-selection on the second measurement when it agrees with the first one. The hexagonal code is initially prepared using a single measurement and feedback. The crosses correspond to the free decay of the GKP states, while the circles correpond to the decay while the manifold is being stabilized. The dashed lines represent the numerically simulated decay while the manifold is being stabilized.

For this we, start by initializing the GKP logical qubit in the eigenstates of the Pauli operators with eigenvalue +1. For the square code, we perform a first feedback preparation, as detailed in the previous section, followed by a second measurement. The state is then kept only if the second measurement agrees with the first one. For the hexagonal code, we initialized the logical qubit by using a single measurement and feedback.

We then look at the free decay of such states. For this, we simply follow the average values of the Pauli operators in time, without any stabilization, and we report the results in Fig. 5.16. For each state, we follow only the Pauli operator that is not 0. Notice that, at small times, the GKP states should remain orthogonal, whereas here, we observe a sharp decrease of the Pauli operators. In fact, at each given time there would be a maximum recovery operator for these states that is not accessible experimentally [125]. Our knowledge of the Pauli operators is, at all time, our best estimate of the state of the logical qubit. Our experiment shows that, after 250 μs, the expectation values of these states have decayed to 0.

Instead of looking at the free decay of these states, we can stabilize them. The stabilization

does not distinguish between two states that are within the manifold, therefore, we expect the states to mix over time. However, as long as the squeezing is good enough, there is no way to go from one state to the other while staying in the code. Thus, the stabilization should slow this dissipation within the manifold. Our experiment shows that this decay is indeed slowed when the manifold stabilization is active, compared to when it is not. Moreover, this decay is exponential, which points to the fact that we introduce a fixed percentage of errors at each round.

For the square code, we observe a decay of the eigenstates of X_L and Z_L on a timescale of 275 μs, which is longer than the single-photon dissipation timescale of 250 μs. However, the decay timescale of the eigenstate of Y_L is 150 μs. As can be seen in Fig. 5.16, this feature is expected from our numerical simulations. We explain this with the fact that the Y state corresponds to larger spatial correlations of the wavefunction: the peaks of this state are spaced by a factor $\sqrt{2}$ more than for the X and Z states. These correlations are more easily destroyed by errors.

This feature disappears for the hexagonal code, where we found a common decay timescale of 210 μs. In the hexagonal code, all the Pauli operators are displacements of the same length. Thus, the three components of the logical qubit are affected by errors in the same way.

5.9 Summary and discussion

Because a lot of points are developed in this section, let us first review them. We started by constructing the square GKP code as a logical qubit encoded in the state of a harmonic oscillator. In this type of system, the errors are continuous in phase-space. Thus, at short time, they can be decomposed as a superposition of small shift. Therefore, we constructed a logical qubit whose logical states $|0\rangle_L$ and $|1\rangle_L$, and symmetric and anti-symmetric superpositions $|+\rangle_L$ and $|-\rangle_L$, are protected against small shifts. Such a logical qubit can be constructed by encoding $|0\rangle_L$ into a position Dirac comb with period $\sqrt{2\pi}$, and $|1\rangle_L$ into the same position Dirac comb, offset by $\sqrt{\frac{\pi}{2}}$. This way, $|\pm\rangle_L$ are also Dirac combs but in momentum. Such states are not physical because they require an infinite amount of squeezing in order to get perfect position and momentum states. They can be approximated by superpositions of squeezed states that have a negligible overlap. From these basis states, we construct operators that detect a small shift unambiguously: the stabilizers of the code. For this square code, the stabilizers are two displacements $S_a = D(i\sqrt{2\pi})$ and $S_b = D(\sqrt{2\pi})$. The first stabilizer adds a global phase to the state of the logical qubit when it is shifted in position by ϵ, while the second stabilizer adds a global phase to the state of the logical qubit when it is shifted

momentum. This phase is proportional to the magnitude of the vector product between ϵ and the displacement vector of the stabilizer.

This concept of stabilizers can be extended to any periodic array in phase-space. Such arrays are left invariant under two displacements $\boldsymbol{S}_{a,b} = \boldsymbol{D}(\alpha_{a,b})$. The condition for such an array to encode a logical qubit is that the magnitude of the cross product of α_a and α_b is 2π. In this case, the two stabilizers have two simultaneous eigenstates with the same eigenvalue that constitute the basis states of the logical qubit. A particular case of this generalization is the hexagonal code, where α_a and α_b make an angle $2\pi/3$, and their magnitude is $\sqrt{2\pi \frac{2}{\sqrt{3}}}$. In this case, $\left|0/1\right\rangle_L$ are equivalent to $\left|\pm\right\rangle_L$ by a rotation of $2\pi/3$, instead of $\pi/2$ for the square code. The added feature of this code is that $\left|0/1\right\rangle_L$ are also equivalent to $\frac{1}{2}(\left|0\right\rangle_L \pm i \left|1_L\right\rangle)$ by a rotation of $\pi/3$.

For all of these codes, the Pauli operators are obtained with displacements of half a stabilizer, such that $\boldsymbol{Z}_L = \boldsymbol{D}(\alpha_a/2)$, $\boldsymbol{X}_L = \boldsymbol{D}(\alpha_b/2)$ and $\boldsymbol{Y}_L = \boldsymbol{D}((\alpha_a + \alpha_b)/2)$. The fact that these matrices are discrete displacements, while the errors of a harmonic oscillator are continuous in phase-space, shows that it is possible to perform quantum error correction on such states. These Pauli operators commute with the stabilizers, which shows that the stabilization is agnostic to the state of the logical qubit.

For quantum error correction, the global phase of the stabilizer needs to be transformed into a relative phase of an ancilla system. In our implementation, we choose this ancilla system to be a transmon two-level system. Applying the stabilizer of the GKP code conditioned on the ancilla being in $\left|e\right\rangle$ imprints the phase of the stabilizer onto the relative phase of the superposition $\frac{1}{2}(\left|g\right\rangle + \left|e\right\rangle)$. We showed that we could implemented a fast conditional displacement in a simple cQED architecture.

However, the phase of this ancilla cannot be measured in a single-shot manner. Because of this, we needed to develop a protocol to estimate this phase. The phase-estimation protocols previously studied require to analyze the outcome of all the previous measurements of the ancilla and analyze them in a complex way. We developed a Markovian protocol, which uses a simple feedback law and proportional feedback. This protocol stabilizes the GKP codes with a stabilizers eigenvalue of 1. However, it also increases the extent of the GKP codes until they are too sensitive to errors, compared to the stabilization rate. We thus add simple correction steps that limit the extent of the envelope of the GKP states.

Using the characteristic function, we showed that the steady states of this stabilization are mixed GKP states. We then showed that we could prepare an arbitrary state of the GKP codes deterministically. Finally, we demonstrated that the lifetime of the GKP logical qubits is enhanced by the stabilization protocol. In particular, the hexagonal code has a lifetime that

is homogeneous for the three components of the logical qubit, which is not the case for the square code.

To conclude this chapter, we will argue that our current protocol does not meet the criterion of fault-tolerance. Possible solutions to this problem will be discussed in the conclusion of the thesis. For this protocol to be fault-tolerant, it needs that any error, including measurement errors, can still be corrected in a future round of quantum error correction.

Let us first see what errors our code can correct. As stated before, the errors that are corrected by the GKP codes are small displacements. For the square code, we have two Gaussian distributions that are offset by $\sqrt{\frac{\pi}{2}}$. We can set a threshold in the middle of these distributions, at $\frac{1}{2}\sqrt{\frac{\pi}{2}}$, in a similar way as in Fig. 5.14. For an ideal square GKP code, *any* shift smaller than this threshold can be perfectly detected and corrected. For a GKP code with finite squeezing, the peaks have a standard deviation σ. The overlap of the distributions of $|0\rangle_L$ and $|1\rangle_L$ is given by the error function, as previously described. If the code is shifted by an amount ϵ, the distributions get closer to the threshold we set, which means that part of the Gaussian distribution crosses this threshold and will never be recovered. This part can be calculated with

$$\text{error} = 1 - \text{erf}\left(\left(\frac{1}{2}\sqrt{\frac{\pi}{2}} - \epsilon\right)\frac{1}{\sqrt{2}\sigma}\right). \tag{5.35}$$

Here, we have simply shifted the threshold by an amount ϵ. As an example, we take ϵ of 0.1, which is the order of magnitude of our corrective displacement, and we take $\sigma = 0.19$, which is the estimated width of our experimental square code. In this case, we get an amount of error that will not be recovered of 0.5%. Such errors are responsible for the finite amount of leakage within the manifold that cannot be corrected. However, notice that there is a favorable scaling for these errors: when the width of the peaks of the steady state GKP code decreases, the errors decrease too.

We now do an inventory of the errors that become negligible when σ goes to 0. As discussed in this chapter, all the dissipation and spurious unitary evolutions of the cavity itself contribute to a finite σ. Thus, decreasing σ means that the stabilization rate is much faster than any of these errors, and the faster is the stabilization rate, the smaller σ becomes. We now analyze the errors in the measurement of the ancilla. As we saw in the section on the readout, a transmon can only be read with a fidelity of 98-99%. On top of the pure readout errors, the dephasing of the ancilla during the interaction will also contribute to measurement errors. These errors can happen at two different times: either after a stabilization of the peaks of the

GKP state, or after the trimming of the envelope. In the latter case, the result of this error measurement is a displacement of the center of mass of the distribution by half a stabilizer in the wrong direction, which is not a code error. In the former case, the measurement error results in a corrective displacement ϵ_c in the wrong direction. As we have seen, this error can be corrected for σ and ϵ_c sufficiently small.

Finally, we find one error that cannot be corrected in this version of the stabilization: the amplitude damping of the ancilla transmon during the stabilization of the peaks of the GKP code. Such errors happen at a random time during a conditional displacement by one stabilizer. If the ancilla suffers from a jump from $|e\rangle$ to $|g\rangle$ (or, more rarely, from $|g\rangle$ to $|e\rangle$ because of the finite temperature of the transmon), the conditional displacement is trans-formed into a displacement with a random amplitude between 0 and $\sqrt{2\pi}$. If the duration of the conditional displacement is small compared to T_1 of the ancilla, these jumps can be thought as equally distributed over this duration. Such errors of the ancilla will, thus, result in logical errors of the GKP logical qubit.

To conclude this chapter, the Markovian protocol we developed is not fault-tolerant be-cause of the finite T_1 of the ancilla transmon. However, it is possible to extend this protocol to be fully fault-tolerant, as we will see in the conclusion of this thesis.

6

Conclusion and perspectives

In this thesis, we have presented two ways to mitigate errors in superconducting cavities. The first one uses an encoding where the states of a logical qubit are Schrödinger cat states $\left|\mathcal{C}_\alpha^\pm\right\rangle \approx \frac{1}{2}\left(|\alpha\rangle \pm |-\alpha\rangle\right)$. We engineered a two-photon dissipation which stabilizes the manifold of this logical qubit without distinguishing its precise state. This stabilization projects all the errors that act on the superconducting cavity into either the identity or logical bit-flips. In particular, it suppresses phase-flips between $|\alpha\rangle$ and $|-\alpha\rangle$ exponentially. This suppression was not yet observed in our experiments because the phase-flips were caused by the thermal excitations of the transmons that is strongly coupled to the superconducting cavities. This large dispersive shift resulted in a frequency mismatch of the stabilizing drives when the transmon was in its excited state, leading to dephasing errors of the cat qubit. However, more recent implementations, in the group of Zaki Leghtas, have now shown this distinctive feature of the stabilization of Schrödinger cat states. However, this stabilization cannot meet the quantum error correction criterion [130] because the stabilized manifold still allows for logical bit-flips, which are actually quadratically enhanced with the size of the Schrödinger cat state. Our second approach to correct errors in a superconducting cavity uses the GKP codes to implement the correction of arbitrary errors. Our stabilization of GKP states manifolds is not autonomous, instead, it requires the active measurement of the stabilizers of the code. However, we have simplified the previous analysis of these stabilizers which is now compatible with a simple feedback loop. This way, we were able to demonstrate the first preparation of GKP states in superconducting circuits. Using this method, we were also able to stabilize GKP states manifolds in steady state. We also proved that the lifetime of the GKP states was improved with the stabilization.

The conclusion of this thesis will now focus on future opportunities based on the work presented here, and in particular on how to extend the tools we presented here to construct fault-tolerant architectures for quantum computing.

6.1   Concatenation of stabilized Schrödinger cat states

As we have seen in this thesis, the dissipative stabilization of Schrödinger cat states results in a qubit that has a noise bias, meaning here that its phase-flips are exponentially suppressed but that its bit-flips are not suppressed (in this case, they are actually quadratically enhanced with the size of the stabilized cat). It seems appropriate to imagine that having one type of noise suppressed would lead to a smaller overhead when one tries to scale such qubits into a universal fault-tolerant quantum computer. However, for this, the gates that are available in such a quantum computer would have to preserve the noise bias of the qubits. For example, in this thesis, we have explored the possibility to realize a continuous logical X-gate [37], while we do not have access to a Z-gate. It has been proposed to realize such a gate using the Kerr effect of superconducting cavities previously observed [25], but this gate transforms the single-photon loss of a cavity into dephasing noise which we are trying to reduce. Similarly, in our stabilized cat codes, a natural two-qubit gate is done with a beam-splitter type of interaction $\boldsymbol{a}^{\dagger}\boldsymbol{b} + \boldsymbol{a}\boldsymbol{b}^{\dagger}$, as shown in the original proposal for stabilized cats [12]. In the basis we have chosen, this gate is akin to an interaction $\boldsymbol{X}_a \boldsymbol{X}_b$, which can be seen as a rotation of the fringes of cat b in one direction when cat a is in the +1 eigenstate of $\boldsymbol{X}_a$ and in the other direction if it is in the -1 eigenstate (notice that in the basis that is now mostly used where $\left|0/1\right\rangle_L = \left|\pm\alpha\right\rangle$, this gate is a continuous control phase $CZ(\theta)$). Similarly to how there is no Z-gate for a single cat qubit in our basis, there is no CPHASE for two cat qubits. In fact, it has been noticed that for two-level systems, it was unreasonable to imagine that both CNOT and CPHASE gates could commute with the reduced noise at all times during the gate [117]. Recently, a no go theorem has been proven which shows this property [119].

Despite this restriction on the possible gates, having a biased-noise qubit still leads to an improvement of the overhead to concatenate such codes into a fault-tolerant quantum computer [117]. For this, Aliferis and Preskill showed that one could create a first layer of concatenation where the dominant source of errors of the biased qubit was corrected to the same level as the non-dominant source of errors, for example using a simple repetition code. Such first level codes can then be assembled into a fault-tolerant quantum computer.

Many quantum architectures could benefit from such a result. For example, nuclear spins in diamond have a T_1 typically larger than 1 s, while their T_2 is typically of order 10 μs. Such architectures are already trying to correct their main source of error using repetition codes [47, 50].

However, stabilized cats have an advantage over other biased qubits that stems from the fact that they are not encoded in two-level systems. Instead, they are encoded in a continuous

variable of phase space: the amplitude α of coherent states $|\pm\alpha\rangle$. This difference allows us to bypass the no-go theorem in order to create new gates that preserve the noise bias. For example, experimentally, the phase of α is simply decided by the phase of the stabilizing microwave drive. One can continuously and adiabatically change the phase of this drive between 0 and π until $|\alpha\rangle$ is transformed into $|-\alpha\rangle$ and vice-versa. This transformation amounts to a discrete Z-gate in the manifold of stabilized cats. This idea has been extended by Mazyar Mirrahimi to create a discrete CPHASE gate which preserves the noise bias of the stabilized cats [119]. Simultaneously, such ideas have been developed for the "Kerr cats" we mentioned in the conclusion of chapter 4, which have a Hamiltonian stabilization [120]. Amazingly, this two-qubit gate only requires tools that have already been demonstrated in this thesis. Obviously, it requires the two-photon dissipation we showed, but tt also needs an induced single photon dissipation, similar to how state-transfer between two cavities has been demonstrated [131–133]. Finally, to mitigate the errors of this gate, it requires the interaction we created for the conditional displacement readout [86]. Additionally, this gate can be extended to a Toffoli gate, or control-control-not gate, by using higher order parametric processes. For this, the rotation of a cat qubit needs to be conditioned on the joint state of two other cat qubits. Such a gate decreases the overhead due to the concatenation of quantum error correcting codes because it removes the requirement of creating and distilling magic states. The group of Mazyar Mirrahimi projects that with a ratio between the stabilization rate and the single-photon decay rate κ_2/κ_1 of 1000, we should be well below the threshold of the repetition code by using stabilized cats with $\bar{n} = 10$ photons. In comparison, we went from a ratio κ_2/κ_1 of 10 in 2015 to a ratio of 100 in 2017. Gaining one more order of magnitude seems within reach of current technologies.

6.2   Fault-tolerant quantum error correction of GKP codes

As we have seen in the conclusion of chapter 5, the main source of logical errors at the level of a GKP code is the propagation of errors from the transmon ancilla, which measures the stabilizers, to the storage mode in which the GKP code is. As we designed a conditional displacement type of interaction, meaning a Hamiltonian $\boldsymbol{\sigma}_z \left(\alpha^* \boldsymbol{a} + \alpha \boldsymbol{a}^\dagger \right)$ ($\boldsymbol{\sigma}_z$ acts on the ancilla transmon and $\boldsymbol{a}$ is the annihilation operator of the storage), the T_1 errors of the ancilla propagate into logical errors of the GKP logical qubit, which cannot be corrected. Notice that dephasing errors of the ancilla commute with this Hamiltonian and thus do not propagate to the GKP logical qubit. Thus, if two ancilla systems have no T_1, each one of them can be used to measure a stabilizer without propagating errors. Therefore, GKP codes can be thought

of as a way to transform physical qubits with a biased noise into a GKP logical qubit whose noise is not biased. In particular, a quantum error correction code which corrects only for one type of errors, such as the repetition code for bit-flips, can reach an arbitrarily large bias, where bit-flips are suppressed and phase-flips are enhanced. GKP codes will transform such codes into a code which corrects for any error.

Let us illustrate the fact that dephasing, by itself, does not necessarily lead to logical errors. For this, let us imagine that the storage cavity has no naturally occuring errors. This storage cavity is coupled to n ancilla qubits whose T_1 error rates can be made arbitrarily small, but whose dephasing rate is potentially large (arbitrarily large, as long as it is not 0). The measurement of the stabilizers by the ancilla qubits can be seen as a phase estimation algorithm [124]. The dephasing noise of the ancilla qubits results in an uncertainty on the estimated value of the phase of the stabilizer. However, this uncertainty can be arbitrarily reduced by making the number of ancilla qubits n larger. We can say that each imperfect ancilla qubit extract less information about the stabilizer than a perfect ancilla qubit, however this amount is not 0, therefore by having more ancilla we can estimate the stabilizer with arbitrary precision. Similarly, this means that the squeezing of the GKP code can be made arbitrarily large and thus, that the logical errors can be arbitrarily small. A possible objection to this model can be made when, by increasing the T_1 of the ancilla, one needs to decrease its dephasing time by the same amount or more. In this case, it is possible that extracting the information about the stabilizers of the GKP code requires too many ancilla qubits and that their added T_1 decays result in logical errors of the GKP logical qubit. However, in quantum repetition codes and in bosonic codes, one type of error can be suppressed exponentially in the number of physical qubit (or in number of photons), while the other type of error is enhanced polynomially in number of physical qubit (or in number of photons). This toy model needs to be complemented by evaluating how this situation changes when the storage cavity has a finite amount of dissipation. An important point is that the speed of the gate can increase when the ancilla qubit is encoded. For example, the interaction time between the storage and a GHZ state $|0\rangle^{\otimes n} + |1\rangle^{\otimes n}$ can be reduced by a factor n. Similarly, for a Schrödinger cat state ancilla, we observed that the frequency of the parity oscillations increases with α, the size of the cats [37]. Hence, the speed of the gate could be increased compared to the dissipation of the GKP mode, at the cost of additional dephasing of the ancilla qubit (which does not propagate to the GKP mode). For such realistic situations, one can imagine that there might exist a threshold on the fidelity of the gates between ancilla qubits and on the conditional displacement between the ancilla qubits and the GKP mode, such that increasing the number of ancilla n results only in better GKP codes.

Regardless, the squeezing of GKP codes does not need to be arbitrarily large for fault-tolerant quantum computing. Noisy GKP logical qubits can also be assembled into another layer of concatenation in order to create a fault-tolerant quantum computer, using for example the toric-code [134] or cluster-states [128]. In the latter code, a threshold squeezing as low as 10 dB has been found.

In the remaining of this final section, we will explore two ways to perform fault-tolerant error syndrome measurements on GKP codes that are possible to implement with current technologies.

6.2.1   Using stabilized Schrödinger cat states as ancillary systems of the GKP codes

The stabilization of Schrödinger cat states create a qubit whose phase-flip errors are exponentially suppressed while its bit-flip errors are quadratically enhanced with the size of the stabilized cat, which correspond to our criterion to measure the stabilizers of the GKP codes fault-tolerantly. The analysis of the stabilizer measurement using stabilized cats has been done for the Kerr cats [121] but it can easily be extended to the dissipative stabilization presented in this thesis. This error-syndrome measurement relies on the gate we demonstrated using the quantum Zeno dynamics in the stabilized manifold, but now it needs to be conditioned on the quadrature of the GKP mode. Such an interaction can be realized with a simple bilinear interaction between the GKP mode and the cat mode. If we call $\boldsymbol{a}$ and $\boldsymbol{b}$ their respective annihilation operators, a beam-splitter interaction of the type

$$\frac{\boldsymbol{H}}{\hbar} = g\left(\boldsymbol{a}^\dagger \boldsymbol{b} e^{-i\varphi} + \boldsymbol{a}\boldsymbol{b}^\dagger e^{i\varphi}\right) \tag{6.1}$$

is enough to create this interaction, as long as it is adiabatic (i.e. $g \ll \kappa_2$). To show this, we use the code projector $\boldsymbol{\Pi} = \boldsymbol{\Pi}_+ + \boldsymbol{\Pi}_-$ (with $\boldsymbol{\Pi}_\pm = \left|\mathcal{C}_\alpha^\pm\right\rangle\left\langle\mathcal{C}_\alpha^\pm\right|$). As long as the adiabaticity condition is respected, the dynamic due to our interaction can be reduced to its dynamics within the stable manifold. We get

$$g\boldsymbol{\Pi}\left(\boldsymbol{a}^\dagger \boldsymbol{b} e^{-i\varphi} + \boldsymbol{a}\boldsymbol{b}^\dagger e^{i\varphi}\right)\boldsymbol{\Pi} = g\left(\alpha^* e^{i\varphi}\boldsymbol{a} + \alpha e^{-i\varphi}\boldsymbol{a}^\dagger\right)\left(\left|\mathcal{C}_\alpha^+\right\rangle\left\langle\mathcal{C}_\alpha^-\right| - \left|\mathcal{C}_\alpha^-\right\rangle\left\langle\mathcal{C}_\alpha^+\right|\right)$$
$$= g\left(\alpha^* e^{i\varphi}\boldsymbol{a} + \alpha e^{-i\varphi}\boldsymbol{a}^\dagger\right)\boldsymbol{X}_{\text{cat}}. \tag{6.2}$$

By controlling the phase φ of the interaction, one can choose what stabilizer to measure for the GKP codes. Here, the bit-flips within the cat manifold impact only the decoding and

not the interaction. This way, there is not propagation of errors between the cat manifold and the GKP code. Such a protocol would end with a measurement of the parity of the cat qubit.

Such an interaction can be realized with the four-wave mixing capability of a transmon [34] or with the three-wave mixing capability of a SNAIL [135, 136]. Between these two possibilities, using a SNAIL has the advantage of having a strong three-wave mixing without having a strong fourth order non-linearity, which is advantageous to protect the GKP code. The interaction can then be created using a single microwave drive whose frequency is the difference between the frequencies of the cat mode and that of the GKP mode. The phase φ of the interaction is simply given by the phase of this strong drive.

6.2.2   Using superpositions of squeezed states as ancillary systems of the GKP codes

The setup we described in the previous sub-section adds together several difficulties. We would like to simplify this setup by not relying on the stabilization of Schrödinger cat states. Unfortunately, without the stabilization, the beam-splitter interaction does not result in the stabilization of GKP codes. In fact, as presented in the original GKP paper [11] and more recently in the group of Liang Jiang [137], stabilizing a GKP code with a beam-splitter inter-action requires to use a GKP state ancilla. The emphasis on the beam-splitter interaction was directly tailored for the quantum optics community, however, in cQED, we can engineer more complex bilinear operations. For example, let us consider an interaction

$$\frac{\boldsymbol{H}}{\hbar} = g\left(\frac{\boldsymbol{a} + \boldsymbol{a}^{\dagger}}{2}\right)\left(\frac{\boldsymbol{b} + \boldsymbol{b}^{\dagger}}{2}\right)$$
$$= g\boldsymbol{Q}_a\boldsymbol{Q}_b, \tag{6.3}$$

where a is the GKP mode and b is the ancillary harmonic oscillator. Such an interaction creates a displacement of b conditioned on the position of Q, and the noise in the position of b propagates as a noisy momentum displacement of a. Remarkably, a simple superposition of position states $|Q\rangle + |-Q\rangle$ can be used to perform the phase-estimation protocol without propagating any noise to the GKP mode. More realistically, a superposition of squeezed states will propagate an amount of noise proportional to their squeezing. This type of state can be thought of as half protected GKP states.

In practice, such states should be easy to create using a SNAIL, to get the squeezing,

and a conditional displacement. For this proposal, the architecture would be the same as the previous one but without the stabilization. In order to obtain the interaction given by equation 6.3, the SNAIL would then have to be driven at both the frequency difference and sum of the two modes. Finally, the phase of the drives can be changed to the stabilize a chosen quadrature.

In summary, by choosing the interaction between two harmonic oscillators carefully, we should be able to fully protect a logical qubit encoded in a GKP code of one oscillator with a half protected qubit encoded in a second oscillator. This replaces the requirement of having to stabilize a GKP code using a second GKP code and it emphasizes our point that a GKP code can be though of as the concatenation of half protected codes.

Bibliography

[1] W. Heisenberg, "Über quantentheoretische Umdeutung kinematischer und mechanischer Beziehungen.", Zeitschrift für Physik **33**, 879–893 (1925) (cit. on p. 1).

[2] R. P. Feynman, "Simulating physics with computers", International Journal of Theoretical Physics **21**, 467–488 (1982) (cit. on p. 1).

[3] D. Deutsch, "Quantum Theory, the Church-Turing Principle and the Universal Quantum Computer", Proceedings of the Royal Society A: Mathematical, Physical and Engineering Sciences **400**, 97–117 (1985) (cit. on p. 1).

[4] D. Deutsch and R. Jozsa, "Rapid Solution of Problems by Quantum Computation", Proceedings of the Royal Society A: Mathematical, Physical and Engineering Sciences **439**, 553–558 (1992) (cit. on p. 1).

[5] P. Shor, "Algorithms for quantum computation: discrete logarithms and factoring", in Proceedings 35th annual symposium on foundations of computer science (1994), pp. 124–134 (cit. on p. 1).

[6] L. K. Grover, "A fast quantum mechanical algorithm for database search", in Proceedings of the twenty-eighth annual ACM symposium on Theory of computing (1996), pp. 212–219 (cit. on p. 2).

[7] P. W. Shor, "Scheme for reducing decoherence in quantum computer memory", Phys. Rev. A **52**, R2493–R2496 (1995) (cit. on p. 2).

[8] P. Shor, "Fault-tolerant quantum computation", in Proceedings of 37th conference on foundations of computer science (May 1996), pp. 56–65 (cit. on pp. 2, 92).

[9] I. L. Chuang, D. W. Leung, and Y. Yamamoto, "Bosonic quantum codes for amplitude damping", Phys. Rev. A **56**, 1114–1125 (1997) (cit. on pp. 2, 31).

[10] P. T. Cochrane, G. J. Milburn, and W. J. Munro, "Macroscopically distinct quantum-superposition states as a bosonic code for amplitude damping", Phys. Rev. A **59**, 2631–2634 (1999) (cit. on p. 2).

[11] D. Gottesman, A. Kitaev, and J. Preskill, "Encoding a qubit in an oscillator", Phys. Rev. A **64**, 012310 (2001) (cit. on pp. 2, 3, 31, 91, 92, 102, 136).

[12] M. Mirrahimi, Z. Leghtas, V. V. Albert, S. Touzard, R. J. Schoelkopf, L. Jiang, and M. H. Devoret, "Dynamically protected cat-qubits: A new paradigm for universal quantum computation", New J. Phys. **16**, 1–28 (2014) (cit. on pp. 2, 3, 70, 82, 86, 132).

[13] B. Yurke and D. Stoler, "The dynamic generation of Schrödinger cats and their detection", Physica B **151**, 298–301 (1988) (cit. on p. 3).

[14] S. Lloyd and S. L. Braunstein, "Quantum Computation over Continuous Variables", Phys. Rev. Lett. **82**, 1784–1787 (1999) (cit. on p. 3).

[15] E. Knill, R. Laflamme, and G. J. Milburn, "A scheme for efficient quantum computation with linear optics", Nature **409**, 46–52 (2001) (cit. on p. 3).

[16] B. C. Travaglione and G. J. Milburn, "Preparing encoded states in an oscillator", Phys. Rev. A **66**, 052322 (2002) (cit. on p. 3).

[17] Z. Leghtas, G. Kirchmair, B. Vlastakis, M. H. Devoret, R. J. Schoelkopf, and M. Mirrahimi, "Deterministic protocol for mapping a qubit to coherent state superpositions in a cavity", Phys. Rev. A **87**, 042315 (2013) (cit. on pp. 3, 31).

[18] S. Krastanov, V. V. Albert, C. Shen, C.-L. Zou, R. W. Heeres, B. Vlastakis, R. J. Schoelkopf, and L. Jiang, "Universal control of an oscillator with dispersive coupling to a qubit", Phys. Rev. A **92**, 040303 (2015) (cit. on p. 3).

[19] D. M. Meekhof, C. Monroe, B. E. King, W. M. Itano, and D. J. Wineland, "Generation of Nonclassical Motional States of a Trapped Atom", Phys. Rev. Lett. **76**, 1796–1799 (1996) (cit. on p. 3).

[20] P. C. Haljan, K.-A. Brickman, L. Deslauriers, P. J. Lee, and C. Monroe, "Spin-Dependent Forces on Trapped Ions for Phase-Stable Quantum Gates and Entangled States of Spin and Motion", Phys. Rev. Lett. **94**, 153602 (2005) (cit. on p. 3).

[21] C. Flühmann, T. L. Nguyen, M. Marinelli, V. Negnevitsky, K. Mehta, and J. P. Home, "Encoding a qubit in a trapped-ion mechanical oscillator", Nature **566**, 513–517 (2019) (cit. on pp. 3, 112, 123).

[22] J. M. Raimond, M. Brune, and S. Haroche, "Manipulating quantum entanglement with atoms and photons in a cavity", Rev. Mod. Phys. **73**, 565–582 (2001) (cit. on p. 3).

[23] S. Haroche and J. Raimond, *Exploring the quantum: atoms, cavities and photons.* (Oxford University Press, 2006) (cit. on pp. 3, 11, 23, 26).

[24] M. Hofheinz, H. Wang, M. Ansmann, R. C. Bialczak, E. Lucero, M. Neeley, A. D. O'Connell, D. Sank, J. Wenner, J. M. Martinis, and A. N. Cleland, "Synthesizing arbitrary quantum states in a superconducting resonator", Nature **459**, 546–549 (2009) (cit. on p. 3).

[25] G. Kirchmair, B. Vlastakis, Z. Leghtas, S. E. Nigg, H. Paik, E. Ginossar, M. Mirrahimi, L. Frunzio, S. M. Girvin, and R. J. Schoelkopf, "Observation of quantum state collapse and revival due to the single-photon Kerr effect", Nature **495**, 205–209 (2013) (cit. on pp. 3, 132).

[26] B. Vlastakis, G. Kirchmair, Z. Leghtas, S. E. Nigg, L. Frunzio, S. M. Girvin, M. Mirrahimi, M. H. Devoret, and R. J. Schoelkopf, "Deterministically Encoding Quantum Information Using 100-Photon Schrodinger Cat States", Science **342**, 607–610 (2013) (cit. on pp. 3, 31, 84).

[27] Z. Leghtas, G. Kirchmair, B. Vlastakis, R. J. Schoelkopf, M. H. Devoret, and M. Mirrahimi, "Hardware-Efficient Autonomous Quantum Memory Protection", Physical Review Letters **111**, 120501 (2013) (cit. on pp. 3, 31).

[28] M. H. Michael, M. Silveri, R. T. Brierley, V. V. Albert, J. Salmilehto, L. Jiang, and S. M. Girvin, "New Class of Quantum Error-Correcting Codes for a Bosonic Mode", Phys. Rev. X **6**, 031006 (2016) (cit. on pp. 3, 19, 31, 92).

[29] L. Sun, A. Petrenko, Z. Leghtas, B. Vlastakis, G. Kirchmair, K. M. Sliwa, A. Narla, M. Hatridge, S. Shankar, J. Blumoff, L. Frunzio, M. Mirrahimi, M. H. Devoret, and R. J. Schoelkopf, "Tracking photon jumps with repeated quantum non-demolition parity measurements", Nature **511**, 444–448 (2014) (cit. on pp. 3, 28).

[30] N. Ofek, A. Petrenko, R. Heeres, P. Reinhold, Z. Leghtas, B. Vlastakis, Y. Liu, L. Frunzio, S. M. Girvin, L. Jiang, M. Mirrahimi, M. H. Devoret, and R. J. Schoelkopf, "Extending the lifetime of a quantum bit with error correction in superconducting circuits", Nature **536**, 441–445 (2016) (cit. on pp. 3, 31, 92).

[31] L. Hu, Y. Ma, W. Cai, X. Mu, Y. Xu, W. Wang, Y. Wu, H. Wang, Y. P. Song, C.-L. Zou, S. M. Girvin, L.-M. Duan, and L. Sun, "Quantum error correction and universal gate set operation on a binomial bosonic logical qubit", Nat. Phys. **15**, 503–508 (2019) (cit. on pp. 3, 92).

[32] R. W. Heeres, P. Reinhold, N. Ofek, L. Frunzio, L. Jiang, M. H. Devoret, and R. J. Schoelkopf, "Implementing a universal gate set on a logical qubit encoded in an oscillator", Nat. Commun. **8**, 94 (2017) (cit. on pp. 3, 86).

[33] S. Rosenblum, Y. Y. Gao, P. Reinhold, C. Wang, C. J. Axline, L. Frunzio, S. M. Girvin, L. Jiang, M. Mirrahimi, M. H. Devoret, and R. J. Schoelkopf, "A CNOT gate between multiphoton qubits encoded in two cavities", Nat. Commun. **9**, 652 (2018) (cit. on pp. 3, 20, 102).

[34] Y. Y. Gao, B. J. Lester, Y. Zhang, C. Wang, S. Rosenblum, L. Frunzio, L. Jiang, S. M. Girvin, and R. J. Schoelkopf, "Programmable Interference between Two Microwave Quantum Memories", Phys. Rev. X **8**, 021073 (2018) (cit. on pp. 3, 20, 102, 136).

[35] Y. Y. Gao, B. J. Lester, K. S. Chou, L. Frunzio, M. H. Devoret, L. Jiang, S. M. Girvin, and R. J. Schoelkopf, "Entanglement of bosonic modes through an engineered exchange interaction", Nature **566**, 509–512 (2019) (cit. on pp. 3, 102).

[36] Z. Leghtas, S. Touzard, I. M. Pop, A. Kou, B. Vlastakis, A. Petrenko, K. M. Sliwa, A. Narla, S. Shankar, M. J. Hatridge, M. Reagor, L. Frunzio, R. J. Schoelkopf, M. Mirrahimi, and M. H. Devoret, "Confining the state of light to a quantum manifold by engineered two-photon loss", Science **347**, 853–857 (2015) (cit. on pp. 3, 75–77, 82, 84, 90).

[37] S. Touzard, A. Grimm, Z. Leghtas, S. O. Mundhada, P. Reinhold, C. Axline, M. Reagor, K. Chou, J. Blumoff, K. M. Sliwa, S. Shankar, L. Frunzio, R. J. Schoelkopf, M. Mirrahimi, and M. H. Devoret, "Coherent Oscillations inside a Quantum Manifold Stabilized by Dissipation", Phys. Rev. X **8**, 021005 (2018) (cit. on pp. 3, 76, 78, 85, 86, 90, 132, 134).

[38] M. A. Nielsen and I. L. Chuang, *Quantum Computation and Quantum Information* (Cambridge University Press, Cambridge, 2010) (cit. on p. 7).

[39] J. Koch, T. M. Yu, J. Gambetta, A. A. Houck, D. I. Schuster, J. Majer, A. Blais, M. H. Devoret, S. M. Girvin, and R. J. Schoelkopf, "Charge-insensitive qubit design derived from the Cooper pair box", Phys. Rev. A **76**, 042319 (2007) (cit. on pp. 8, 43).

[40] F. Yan, S. Gustavsson, A. Kamal, J. Birenbaum, A. P. Sears, D. Hover, T. J. Gudmundsen, D. Rosenberg, G. Samach, S. Weber, J. L. Yoder, T. P. Orlando, J. Clarke, A. J. Kerman, and W. D. Oliver, "The flux qubit revisited to enhance coherence and reproducibility", Nat. Commun. **7**, 12964 (2016) (cit. on p. 8).

[41] C. Rigetti, J. M. Gambetta, S. Poletto, B. L. T. Plourde, J. M. Chow, A. D. Córcoles, J. A. Smolin, S. T. Merkel, J. R. Rozen, G. A. Keefe, M. B. Rothwell, M. B. Ketchen, and M. Steffen, "Superconducting qubit in a waveguide cavity with a coherence time approaching 0.1 ms", Phys. Rev. B **86**, 100506 (2012) (cit. on pp. 8, 14, 54).

[42] J. S. Bell, "On the Einstein Podolsky Rosen paradox", Physics Physique Fizika **1**, 195–200 (1964) (cit. on p. 14).

[43] A. Aspect, J. Dalibard, and G. Roger, "Experimental Test of Bell's Inequalities Using Time- Varying Analyzers", Phys. Rev. Lett. **49**, 1804–1807 (1982) (cit. on p. 14).

[44] B. Hensen, H. Bernien, A. E. Dréau, A. Reiserer, N. Kalb, M. S. Blok, J. Ruitenberg, R. F. L. Vermeulen, R. N. Schouten, C. Abellán, W. Amaya, V. Pruneri, M. W. Mitchell, M. Markham, D. J. Twitchen, D. Elkouss, S. Wehner, T. H. Taminiau, and R. Hanson, "Loophole-free Bell inequality violation using electron spins separated by 1.3 kilometres", Nature **526**, 682–686 (2015) (cit. on p. 14).

[45] D. G. Cory, M. D. Price, W. Maas, E. Knill, R. Laflamme, W. H. Zurek, T. F. Havel, and S. S. Somaroo, "Experimental Quantum Error Correction", Phys. Rev. Lett. **81**, 2152–2155 (1998) (cit. on p. 16).

[46] M. D. Reed, L. DiCarlo, S. E. Nigg, L. Sun, L. Frunzio, S. M. Girvin, and R. J. Schoelkopf, "Realization of three-qubit quantum error correction with superconducting circuits", Nature **482**, 382–385 (2012) (cit. on p. 16).

[47] G. Waldherr, Y. Wang, S. Zaiser, M. Jamali, T. Schulte-Herbrüggen, H. Abe, T. Ohshima, J. Isoya, J. F. Du, P. Neumann, and J. Wrachtrup, "Quantum error correction in a solid-state hybrid spin register", Nature **506**, 204–207 (2014) (cit. on pp. 16, 132).

[48] D. Gottesman, "Stabilizer Codes and Quantum Error Correction", (1997), arXiv:9705052 [quant-ph] (cit. on pp. 16, 95).

[49] J. Kelly, R. Barends, A. G. Fowler, A. Megrant, E. Jeffrey, T. C. White, D. Sank, J. Y. Mutus, B. Campbell, Y. Chen, Z. Chen, B. Chiaro, A. Dunsworth, I.-C. Hoi, C. Neill, P. J. J. O'Malley, C. Quintana, P. Roushan, A. Vainsencher, J. Wenner, A. N. Cleland, and J. M. Martinis, "State preservation by repetitive error detection in a superconducting quantum circuit", Nature **519**, 66–69 (2015) (cit. on p. 16).

[50] J. Cramer, N. Kalb, M. A. Rol, B. Hensen, M. S. Blok, M. Markham, D. J. Twitchen, R. Hanson, and T. H. Taminiau, "Repeated quantum error correction on a continuously encoded qubit by real-time feedback", Nat. Commun. **7**, 11526 (2016) (cit. on pp. 16, 132).

[51] E. Knill and R. Laflamme, "Theory of quantum error-correcting codes", Phys. Rev. A **55**, 900–911 (1997) (cit. on p. 17).

[52] D. W. Leung, M. A. Nielsen, I. L. Chuang, and Y. Yamamoto, "Approximate quantum error correction can lead to better codes", Phys. Rev. A **56**, 2567–2573 (1997) (cit. on p. 17).

[53] J. I. Cirac and P. Zoller, "Quantum Computations with Cold Trapped Ions", Phys. Rev. Lett. **74**, 4091–4094 (1995) (cit. on p. 19).

[54] K. Mølmer and A. Sørensen, "Multiparticle Entanglement of Hot Trapped Ions", Phys. Rev. Lett. **82**, 1835–1838 (1999) (cit. on p. 19).

[55] L. DiCarlo, J. M. Chow, J. M. Gambetta, L. S. Bishop, B. R. Johnson, D. I. Schuster, J. Majer, A. Blais, L. Frunzio, S. M. Girvin, and R. J. Schoelkopf, "Demonstration of two-qubit algorithms with a superconducting quantum processor", Nature **460**, 240–244 (2009) (cit. on p. 20).

[56] D. Aharonov and M. Ben-Or, "Fault-tolerant quantum computation with constant error", in Proceedings of the twenty-ninth annual acm symposium on theory of computing (Nov. 1997), pp. 176–188 (cit. on pp. 20, 92).

[57] A. G. Fowler, M. Mariantoni, J. M. Martinis, and A. N. Cleland, "Surface codes: Towards practical large-scale quantum computation", Phys. Rev. A **86**, 032324 (2012) (cit. on pp. 20, 92, 109).

[58] L. G. Lutterbach and L. Davidovich, "Method for Direct Measurement of the Wigner Function in Cavity QED and Ion Traps", Phys. Rev. Lett. **78**, 2547–2550 (1997) (cit. on p. 28).

[59] P. Bertet, A. Auffeves, P. Maioli, S. Osnaghi, T. Meunier, M. Brune, J. M. Raimond, and S. Haroche, "Direct Measurement of the Wigner Function of a One-Photon Fock State in a Cavity", Phys. Rev. Lett. **89**, 200402 (2002) (cit. on p. 28).

[60] S. Puri, S. Boutin, and A. Blais, "Engineering the quantum states of light in a Kerr-nonlinear resonator by two-photon driving", npj Quantum Information **3**, 18 (2017) (cit. on pp. 31, 90).

[61] S. M. Girvin, "Circuit QED: superconducting qubits coupled to microwave photons", in *Quantum mach. meas. control eng. quantum syst.* (Oxford University Press, June 2014), pp. 113–256 (cit. on p. 34).

[62] U. Vool and M. Devoret, "Introduction to quantum electromagnetic circuits", Int. J. Circuit Theory Appl. **45**, 897–934 (2017) (cit. on pp. 34, 35, 37).

[63] V. E. Manucharyan, J. Koch, L. I. Glazman, and M. H. Devoret, "Fluxonium: Single

Cooper-Pair Circuit Free of Charge Offsets", Science **326**, 113–116 (2009) (cit. on p. 35).

[64] M. Reagor, W. Pfaff, C. Axline, R. W. Heeres, N. Ofek, K. Sliwa, E. Holland, C. Wang, J. Blumoff, K. Chou, M. J. Hatridge, L. Frunzio, M. H. Devoret, L. Jiang, and R. J. Schoelkopf, "Quantum memory with millisecond coherence in circuit QED", Phys. Rev. B **94**, 014506 (2016) (cit. on pp. 37, 56, 77, 107).

[65] C. Axline, M. Reagor, R. Heeres, P. Reinhold, C. Wang, K. Shain, W. Pfaff, Y. Chu, L. Frunzio, and R. J. Schoelkopf, "An architecture for integrating planar and 3D cQED devices", Appl. Phys. Lett. **109**, 042601 (2016) (cit. on pp. 37, 77).

[66] D. A. Steck, "Quantum and Atom Optics", available online at http://steck.us/teaching (2007) (cit. on p. 37).

[67] A. A. Clerk, M. H. Devoret, S. M. Girvin, F. Marquardt, and R. J. Schoelkopf, "Introduction to quantum noise, measurement, and amplification", Rev. Mod. Phys. **82**, 1155–1208 (2010) (cit. on pp. 37, 60).

[68] L. Verney, R. Lescanne, M. H. Devoret, Z. Leghtas, and M. Mirrahimi, "Structural Instability of Driven Josephson Circuits Prevented by an Inductive Shunt", Phys. Rev. Appl. **11**, 024003 (2019) (cit. on p. 38).

[69] F. Lecocq, I. M. Pop, Z. Peng, I. Matei, T. Crozes, T. Fournier, C. Naud, W. Guichard, and O. Buisson, "Junction fabrication by shadow evaporation without a suspended bridge", Nanotechnology **22**, 315302 (2011) (cit. on p. 41).

[70] A. A. Houck, J. A. Schreier, B. R. Johnson, J. M. Chow, J. Koch, J. M. Gambetta, D. I. Schuster, L. Frunzio, M. H. Devoret, S. M. Girvin, and R. J. Schoelkopf, "Controlling the Spontaneous Emission of a Superconducting Transmon Qubit", Phys. Rev. Lett. **101**, 080502 (2008) (cit. on pp. 45, 53).

[71] M. D. Reed, B. R. Johnson, A. A. Houck, L. DiCarlo, J. M. Chow, D. I. Schuster, L. Frunzio, and R. J. Schoelkopf, "Fast reset and suppressing spontaneous emission of a superconducting qubit", Appl. Phys. Lett. **96**, 203110 (2010) (cit. on pp. 45, 54).

[72] D. P. DiVincenzo, "The Physical Implementation of Quantum Computation", Fortschritte der Physik **48**, 771–783 (2000) (cit. on p. 52).

[73] A. Blais, R.-S. Huang, A. Wallraff, S. M. Girvin, and R. J. Schoelkopf, "Cavity quantum electrodynamics for superconducting electrical circuits: an architecture for quantum computation", Phys. Rev. A **69**, 062320 (2004) (cit. on p. 52).

[74] A. Wallraff, D. I. Schuster, A. Blais, L. Frunzio, R. S. Huang, J. Majer, S. Kumar, S. M. Girvin, and R. J. Schoelkopf, "Strong coupling of a single photon to a superconducting qubit using circuit quantum electrodynamics", Nature **431**, 162 (2004) (cit. on p. 52).

[75] J. Gambetta, A. Blais, M. Boissonneault, A. A. Houck, D. I. Schuster, and S. M. Girvin, "Quantum trajectory approach to circuit QED: Quantum jumps and the Zeno effect", Phys. Rev. A **77**, 1–20 (2008) (cit. on pp. 52, 59).

[76] M. A. Castellanos-Beltran, K. D. Irwin, G. C. Hilton, L. R. Vale, and K. W. Lehnert, "Amplification and squeezing of quantum noise with a tunable Josephson metamaterial", Nat. Phys **4**, 929–931 (2008) (cit. on p. 55).

[77] N. Bergeal, F. Schackert, M. Metcalfe, R. Vijay, V. E. Manucharyan, L. Frunzio, D. E. Prober, R. J. Schoelkopf, S. M. Girvin, and M. H. Devoret, "Phase-preserving amplification near the quantum limit with a Josephson ring modulator", Nature **465**, 64–68 (2010) (cit. on p. 55).

[78] N. E. Frattini, V. V. Sivak, A. Lingenfelter, S. Shankar, and M. H. Devoret, "Optimizing the nonlinearity and dissipation of a snail parametric amplifier for dynamic range", Phys. Rev. Appl. **10**, 054020 (2018) (cit. on pp. 55, 108).

[79] A. J. Kerman, "Quantum information processing using quasiclassical electromagnetic interactions between qubits and electrical resonators", New J. Phys. **15**, 123011 (2013) (cit. on pp. 55, 56).

[80] P. M. Billangeon, J. S. Tsai, and Y. Nakamura, "Circuit-QED-based scalable architectures for quantum information processing with superconducting qubits", Phys. Rev. B **91**, 094517 (2015) (cit. on p. 55).

[81] D. Vion, A. Aassime, A. Cottet, P. Joyez, H. Pothier, C. Urbina, D. Esteve, and M. H. Devoret, "Manipulating the Quantum State of an Electrical Circuit", Science **296**, 886–889 (2002) (cit. on p. 55).

[82] T. Roy, S. Kundu, M. Chand, S. Hazra, N. Nehra, R. Cosmic, A. Ranadive, M. P. Patankar, K. Damle, and R. Vijay, "Implementation of Pairwise Longitudinal Coupling in a Three-Qubit Superconducting Circuit", Phys. Rev. Appl. 7, 054025 (2017) (cit. on p. 55).

[83] C. Eichler and J. R. Petta, "Realizing a Circuit Analog of an Optomechanical System with Longitudinally Coupled Superconducting Resonators", Phys. Rev. Lett. **120**, 227702 (2018) (cit. on p. 55).

[84] N. Didier, J. Bourassa, and A. Blais, "Fast Quantum Nondemolition Readout by Parametric Modulation of Longitudinal Qubit-Oscillator Interaction", Phys. Rev. Lett. **115**, 203601 (2015) (cit. on pp. 56, 64).

[85] H. Paik, D. I. Schuster, L. S. Bishop, G. Kirchmair, G. Catelani, A. P. Sears, B. R. Johnson, M. J. Reagor, L. Frunzio, L. I. Glazman, S. M. Girvin, M. H. Devoret, and R. J. Schoelkopf, "Observation of High Coherence in Josephson Junction Qubits Measured in a Three-Dimensional Circuit QED Architecture", Phys. Rev. Lett. **107**, 240501 (2011) (cit. on p. 56).

[86] S. Touzard, A. Kou, N. E. Frattini, V. V. Sivak, S. Puri, A. Grimm, L. Frunzio, S. Shankar, and M. H. Devoret, "Gated Conditional Displacement Readout of Superconducting Qubits", Phys. Rev. Lett. **122**, 080502 (2019) (cit. on pp. 57, 64, 102, 106, 133).

[87] J. Gambetta, W. A. Braff, A. Wallraff, S. M. Girvin, and R. J. Schoelkopf, "Protocols for optimal readout of qubits using a continuous quantum nondemolition measurement", Phys. Rev. A **76**, 012325 (2007) (cit. on p. 62).

[88] C. A. Ryan, B. R. Johnson, J. M. Gambetta, J. M. Chow, M. P. da Silva, O. E. Dial, and T. A. Ohki, Phys. Rev. A **91**, 022118 (2015) (cit. on pp. 62, 65).

[89] C. C. Bultink, B. Tarasinski, N. Haandbæk, S. Poletto, N. Haider, D. J. Michalak, A. Bruno, and L. DiCarlo, "General method for extracting the quantum efficiency of dispersive qubit readout in circuit QED", Appl. Phys. Lett. **112**, 092601 (2018) (cit. on p. 63).

[90] T. Picot, A. Lupacscu, S. Saito, C. J. P. M. Harmans, and J. E. Mooij, "Role of relaxation in the quantum measurement of a superconducting qubit using a nonlinear oscillator", Phys. Rev. B **78**, 132508 (2008) (cit. on p. 64).

[91] M. Boissonneault, J. M. Gambetta, and A. Blais, "Dispersive regime of circuit QED: Photon-dependent qubit dephasing and relaxation rates", Phys. Rev. A **79**, 013819 (2009) (cit. on p. 64).

[92] D. H. Slichter, R. Vijay, S. J. Weber, S. Boutin, M. Boissonneault, J. M. Gambetta, A. Blais, and I. Siddiqi, "Measurement-Induced Qubit State Mixing in Circuit QED from Up-Converted Dephasing Noise", Phys. Rev. Lett. **109**, 153601 (2012) (cit. on p. 64).

[93] D. Sank, Z. Chen, M. Khezri, J. Kelly, R. Barends, B. Campbell, Y. Chen, B. Chiaro, A. Dunsworth, A. Fowler, E. Jeffrey, E. Lucero, A. Megrant, J. Mutus, M. Neeley,

C. Neill, P. J. J. O'Malley, C. Quintana, P. Roushan, A. Vainsencher, T. White, J. Wenner, A. N. Korotkov, and J. M. Martinis, "Measurement-Induced State Transitions in a Superconducting Qubit: Beyond the Rotating Wave Approximation", Phys. Rev. Lett. **117**, 190503 (2016) (cit. on p. 64).

[94] A. Eddins, S. Schreppler, D. M. Toyli, L. S. Martin, S. Hacohen-Gourgy, L. C. G. Govia, H. Ribeiro, A. A. Clerk, and I. Siddiqi, "Stroboscopic Qubit Measurement with Squeezed Illumination", Phys. Rev. Lett. **120**, 040505 (2018) (cit. on pp. 65, 103).

[95] H. Krauter, C. A. Muschik, K. Jensen, W. Wasilewski, J. M. Petersen, J. I. Cirac, and E. S. Polzik, "Entanglement Generated by Dissipation and Steady State Entanglement of Two Macroscopic Objects", Phys. Rev. Lett. **107**, 080503 (2011) (cit. on p. 70).

[96] K. W. Murch, U. Vool, D. Zhou, S. J. Weber, S. M. Girvin, and I. Siddiqi, "Cavity-Assisted Quantum Bath Engineering", Phys. Rev. Lett. **109**, 183602 (2012) (cit. on p. 70).

[97] S. Shankar, M. Hatridge, Z. Leghtas, K. M. Sliwa, A. Narla, U. Vool, S. M. Girvin, L. Frunzio, M. Mirrahimi, and M. H. Devoret, "Autonomously stabilized entanglement between two superconducting quantum bits", Nature **504**, 419–422 (2013) (cit. on p. 70).

[98] Y. Lin, J. P. Gaebler, F. Reiter, T. R. Tan, R. Bowler, A. S. Sørensen, D. Leibfried, and D. J. Wineland, "Dissipative production of a maximally entangled steady state of two quantum bits", Nature **504**, 415–418 (2013) (cit. on p. 70).

[99] R. Lescanne, S. Deléglise, E. Albertinale, U. Réglade, T. Capelle, E. Ivanov, T. Jacqmin, Z. Leghtas, and E. Flurin, "Detecting itinerant microwave photons with engineered non-linear dissipation", (2019), arXiv:1902.05102 (cit. on p. 70).

[100] R. Ma, B. Saxberg, C. Owens, N. Leung, Y. Lu, J. Simon, and D. I. Schuster, "A dissipatively stabilized Mott insulator of photons", Nature **566**, 51–57 (2019) (cit. on p. 70).

[101] A. Metelmann and A. A. Clerk, "Nonreciprocal Photon Transmission and Amplification via Reservoir Engineering", Phys. Rev. X **5**, 021025 (2015) (cit. on p. 71).

[102] V. V. Albert, B. Bradlyn, M. Fraas, and L. Jiang, "Geometry and Response of Lindbladians", Phys. Rev. X **6**, 041031 (2016) (cit. on pp. 71, 86).

[103] H. J. Carmichael, *Statistical Methods in Quantum Optics 2*, Theoretical and Mathematical Physics (Springer, Berlin, Heidelberg, 2008) (cit. on p. 75).

[104] L.-A. Wu, H. J. Kimble, J. L. Hall, and H. Wu, "Generation of Squeezed States by Parametric Down Conversion", Phys. Rev. Lett. **57**, 2520–2523 (1986) (cit. on p. 75).

[105] M. Wolinsky and H. J. Carmichael, "Quantum noise in the parametric oscillator: From squeezed states to coherent-state superpositions", Phys. Rev. Lett. **60**, 1836–1839 (1988) (cit. on pp. 75, 77).

[106] B. Misra and E. C. G. Sudarshan, "The Zeno's paradox in quantum theory", J. Math. Phys. **18**, 756–763 (1977) (cit. on p. 86).

[107] W. M. Itano, D. J. Heinzen, J. J. Bollinger, and D. J. Wineland, "Quantum Zeno effect", Phys. Rev. A **41**, 2295–2300 (1990) (cit. on p. 86).

[108] S. R. Wilkinson, C. F. Bharucha, M. C. Fischer, K. W. Madison, P. R. Morrow, Q. Niu, B. Sundaram, and M. G. Raizen, "Experimental evidence for non-exponential decay in quantum tunnelling", Nature **387**, 575–577 (1997) (cit. on p. 86).

[109] P. Facchi, V. Gorini, G. Marmo, S. Pascazio, and E. Sudarshan, "Quantum Zeno dynamics", Phys. Lett. A **275**, 12–19 (2000) (cit. on p. 86).

[110] A. Beige, D. Braun, B. Tregenna, and P. L. Knight, "Quantum Computing Using Dissipation to Remain in a Decoherence-Free Subspace", Phys. Rev. Lett. **85**, 1762–1765 (2000) (cit. on p. 86).

[111] A. Carollo, M. F. Santos, and V. Vedral, "Coherent Quantum Evolution via Reservoir Driven Holonomies", Phys. Rev. Lett. **96**, 020403 (2006) (cit. on p. 86).

[112] O. Oreshkov and J. Calsamiglia, "Adiabatic Markovian Dynamics", Phys. Rev. Lett. **105**, 050503 (2010) (cit. on p. 86).

[113] P. Zanardi and L. Campos Venuti, "Coherent Quantum Dynamics in Steady-State Manifolds of Strongly Dissipative Systems", Phys. Rev. Lett. **113**, 240406 (2014) (cit. on p. 86).

[114] V. V. Albert, S. O. Mundhada, A. Grimm, S. Touzard, M. H. Devoret, and L. Jiang, "Multimode cat codes", arXiv:1801.05897 (2018) (cit. on p. 86).

[115] R. Azouit, F. Chittaro, A. Sarlette, and P. Rouchon, "Towards generic adiabatic elimination for bipartite open quantum systems", Quantum Science and Technology **2**, 044011 (2017) (cit. on p. 86).

[116] Z. Wang, M. Pechal, E. A. Wollack, P. Arrangoiz-Arriola, M. Gao, N. R. Lee, and A. H. Safavi-Naeini, "Quantum dynamics of a few-photon parametric oscillator", (2019), arXiv:1901.09171 (cit. on p. 90).

[117] P. Aliferis and J. Preskill, "Fault-tolerant quantum computation against biased noise", Phys. Rev. A **78**, 052331 (2008) (cit. on pp. 90, 132).

[118] D. K. Tuckett, S. D. Bartlett, and S. T. Flammia, "Ultrahigh Error Threshold for Surface Codes with Biased Noise", Phys. Rev. Lett. **120**, 050505 (2018) (cit. on p. 91).

[119] J. Guillaud and M. Mirrahimi, "Repetition cat-qubits: fault-tolerant quantum computation with highly reduced overhead", (2019), arXiv:1904.09474 (cit. on pp. 91, 132, 133).

[120] S. Puri, L. St-Jean, J. A. Gross, A. Grimm, N. E. Frattini, P. S. Iyer, A. Krishna, S. Touzard, L. Jiang, A. Blais, S. T. Flammia, and S. M. Girvin, "Bias-preserving gates with stabilized cat qubits", (2019), arXiv:1905.00450 (cit. on pp. 91, 133).

[121] S. Puri, A. Grimm, P. Campagne-Ibarcq, A. Eickbusch, K. Noh, G. Roberts, L. Jiang, M. Mirrahimi, M. H. Devoret, and S. M. Girvin, "Stabilized Cat in Driven Nonlinear Cavity: A Fault-Tolerant Error Syndrome Detector", arXiv:1807.09334 (2018) (cit. on pp. 91, 135).

[122] R. Barends, J. Kelly, A. Megrant, A. Veitia, D. Sank, E. Jeffrey, T. C. White, J. Mutus, A. G. Fowler, B. Campbell, Y. Chen, Z. Chen, B. Chiaro, A. Dunsworth, C. Neill, P. O'Malley, P. Roushan, A. Vainsencher, J. Wenner, A. N. Korotkov, A. N. Cleland, and J. M. Martinis, "Superconducting quantum circuits at the surface code threshold for fault tolerance", Nature **508**, 500–503 (2014) (cit. on p. 92).

[123] A. Kitaev, A. Shen, and M. Vyalyi, *Classical and Quantum Computation*, Vol. 47, Graduate Studies in Mathematics (American Mathematical Society, Providence, Rhode Island, May 2002) (cit. on p. 97).

[124] B. M. Terhal and D. Weigand, "Encoding a qubit into a cavity mode in circuit QED using phase estimation", Phys. Rev. A **93**, 012315 (2016) (cit. on pp. 97, 112, 134).

[125] V. V. Albert, K. Noh, K. Duivenvoorden, D. J. Young, R. T. Brierley, P. Reinhold, C. Vuillot, L. Li, C. Shen, S. M. Girvin, B. M. Terhal, and L. Jiang, "Performance and structure of single-mode bosonic codes", Phys. Rev. A **97**, 032346 (2018) (cit. on pp. 98, 126).

[126] L. Viola, S. Lloyd, and E. Knill, "Universal Control of Decoupled Quantum Systems", Phys. Rev. Lett. **83**, 4888–4891 (1999) (cit. on pp. 103, 105).

[127] S. E. Nigg, H. Paik, B. Vlastakis, G. Kirchmair, S. Shankar, L. Frunzio, M. H. Devoret, R. J. Schoelkopf, and S. M. Girvin, "Black-box superconducting circuit quantization", Phys. Rev. Lett. **108**, 1–5 (2012) (cit. on p. 109).

[128] K. Fukui, A. Tomita, A. Okamoto, and K. Fujii, "High-Threshold Fault-Tolerant Quantum Computation with Analog Quantum Error Correction", Phys. Rev. X **8**, 021054 (2018) (cit. on pp. 121, 135).

[129] S. Bravyi and A. Kitaev, "Universal quantum computation with ideal Clifford gates and noisy ancillas", Phys. Rev. A **71**, 022316 (2005) (cit. on p. 124).

[130] E. Knill, R. Laflamme, and L. Viola, "Theory of Quantum Error Correction for General Noise", Phys. Rev. Lett. **84**, 2525–2528 (2000) (cit. on p. 131).

[131] W. Pfaff, C. J. Axline, L. D. Burkhart, U. Vool, P. Reinhold, L. Frunzio, L. Jiang, M. H. Devoret, and R. J. Schoelkopf, "Controlled release of multiphoton quantum states from a microwave cavity memory", Nat. Phys. **13**, 882–887 (2017) (cit. on p. 133).

[132] C. J. Axline, L. D. Burkhart, W. Pfaff, M. Zhang, K. Chou, P. Campagne-Ibarcq, P. Reinhold, L. Frunzio, S. M. Girvin, L. Jiang, M. H. Devoret, and R. J. Schoelkopf, "On-demand quantum state transfer and entanglement between remote microwave cavity memories", Nat. Phys **14**, 705–710 (2018) (cit. on p. 133).

[133] P. Campagne-Ibarcq, E. Zalys-Geller, A. Narla, S. Shankar, P. Reinhold, L. Burkhart, C. Axline, W. Pfaff, L. Frunzio, R. J. Schoelkopf, and M. H. Devoret, "Deterministic Remote Entanglement of Superconducting Circuits through Microwave Two-Photon Transitions", Phys. Rev. Lett. **120**, 200501 (2018) (cit. on p. 133).

[134] C. Vuillot, H. Asasi, Y. Wang, L. P. Pryadko, and B. M. Terhal, "Quantum error correction with the toric Gottesman-Kitaev-Preskill code", Phys. Rev. A **99**, 032344 (2019) (cit. on p. 135).

[135] A. B. Zorin, "Josephson Traveling-Wave Parametric Amplifier with Three-Wave Mixing", Phys. Rev. Appl. **6**, 034006 (2016) (cit. on p. 136).

[136] N. E. Frattini, U. Vool, S. Shankar, A. Narla, K. M. Sliwa, and M. H. Devoret, "3-wave mixing Josephson dipole element", Appl. Phys. Lett. **110**, 222603 (2017) (cit. on p. 136).

[137] K. Noh, S. M. Girvin, and L. Jiang, "Encoding an oscillator into many oscillators", (2019), arXiv:1903.12615 (cit. on p. 136).

Appendices

A

Phase-space representations

A.1 Characteristic function

We want to see how the conditional displacement of a storage cavity conditioned on $\boldsymbol{\sigma}_z$ of an ancilla two-level system leads to a measurement of the characteristic function. For this, we start by expanding the conditional displacement $D\left(\frac{\tilde{\alpha}}{2}\boldsymbol{\sigma}_z\right) = e^{(\tilde{\alpha}\boldsymbol{a}^\dagger - \tilde{\alpha}^*\boldsymbol{a})\boldsymbol{\sigma}_z/2}$ into

$$D\left(\frac{\tilde{\alpha}}{2}\boldsymbol{\sigma}_z\right) = \sum_k \frac{((\tilde{\alpha}\boldsymbol{a}^\dagger - \tilde{\alpha}^*\boldsymbol{a})/2)^k}{k!}\boldsymbol{\sigma}_z^k \tag{A.1}$$

$$= \boldsymbol{\Sigma}\left(\frac{\tilde{\alpha}}{2}\right)\boldsymbol{I} + \boldsymbol{\Delta}\left(\frac{\tilde{\alpha}}{2}\right)\boldsymbol{\sigma}_z, \tag{A.2}$$

where $\boldsymbol{\Sigma}\left(\frac{\tilde{\alpha}}{2}\right) = \frac{1}{2}\left(D\left(\frac{\tilde{\alpha}}{2}\right) + D\left(-\frac{\tilde{\alpha}}{2}\right)\right)$ are the even terms of the expansion, and $\boldsymbol{\Delta}\left(\frac{\tilde{\alpha}}{2}\right) = \frac{1}{2}\left(D\left(\frac{\tilde{\alpha}}{2}\right) - D\left(-\frac{\tilde{\alpha}}{2}\right)\right)$ are the odd terms of the expansions. Note that $\boldsymbol{\Sigma}$ is an even function while $\boldsymbol{\Delta}$ is an odd function. This way, the unitary evolution of the cavity and the ancilla, whose density matrix is $\rho_c\left|+\right\rangle\left\langle+\right|$, is

$$\begin{aligned} D\left(\frac{\tilde{\alpha}}{2}\boldsymbol{\sigma}_z\right)\rho_c\left|+\right\rangle\left\langle+\right|D\left(-\frac{\tilde{\alpha}}{2}\boldsymbol{\sigma}_z\right) = &\boldsymbol{\Sigma}\left(\frac{\tilde{\alpha}}{2}\right)\rho_c\boldsymbol{\Sigma}\left(\frac{\tilde{\alpha}}{2}\right)\left|+\right\rangle\left\langle+\right| \\ &- \boldsymbol{\Delta}\left(\frac{\tilde{\alpha}}{2}\right)\rho_c\boldsymbol{\Delta}\left(\frac{\tilde{\alpha}}{2}\right)\left|-\right\rangle\left\langle-\right| \\ &+ \boldsymbol{\Delta}\left(\frac{\tilde{\alpha}}{2}\right)\rho_c\boldsymbol{\Sigma}\left(\frac{\tilde{\alpha}}{2}\right)\left|-\right\rangle\left\langle+\right| \\ &- \boldsymbol{\Sigma}\left(\frac{\tilde{\alpha}}{2}\right)\rho_c\boldsymbol{\Delta}\left(\frac{\tilde{\alpha}}{2}\right)\left|+\right\rangle\left\langle-\right|. \end{aligned} \tag{A.3}$$

We now expand Σ and Δ, which gives various types of terms. The first terms are $\boldsymbol{D}\left(\frac{\tilde{\alpha}}{2}\right)\rho_c\boldsymbol{D}\left(-\frac{\tilde{\alpha}}{2}\right)$ and Hermitian conjugates. These simply correspond to a displacement of the entire state. Hence, when the storage cavity is traced, these terms are equal to the trace of the density matrix, which is 1. The second terms are $\boldsymbol{D}\left(\frac{\tilde{\alpha}}{2}\right)\rho_c\boldsymbol{D}\left(\frac{\tilde{\alpha}}{2}\right)$ and $\boldsymbol{D}\left(-\frac{\tilde{\alpha}}{2}\right)\rho_c\boldsymbol{D}\left(-\frac{\tilde{\alpha}}{2}\right)$ that are more complicated. Within the trace, the displacements can be reorganized into $\boldsymbol{D}\left(\tilde{\alpha}\right)$. Thus, after taking the trace over the storage cavity, these terms correspond to the characteristic function $C_s(\tilde{\alpha})$ and $C_s(-\tilde{\alpha}) = C_s^*(\tilde{\alpha})$. Overall, we get

$$
\begin{aligned}
\mathrm{Tr}_c\left(\boldsymbol{D}\left(\frac{\tilde{\alpha}}{2}\boldsymbol{\sigma}_z\right)\rho_c\left|+\right\rangle\left\langle+\right|\boldsymbol{D}\left(-\frac{\tilde{\alpha}}{2}\boldsymbol{\sigma}_z\right)\right) &= \frac{1}{2}((1+\mathrm{Re}(C_s(\tilde{\alpha})))\left|+\right\rangle\left\langle+\right| \\
&+ (1-\mathrm{Re}(C_s(\tilde{\alpha})))\left|-\right\rangle\left\langle-\right| + i\mathrm{Im}(C_s(\tilde{\alpha}))(\left|-\right\rangle\left\langle+\right| - \left|+\right\rangle\left\langle-\right|)) \\
&= \frac{1}{2}\left(\boldsymbol{I} + \mathrm{Re}(C_s(\tilde{\alpha}))\boldsymbol{\sigma}_x + \mathrm{Im}(C_s(\tilde{\alpha}))\boldsymbol{\sigma}_y\right).
\end{aligned}
\tag{A.4}
$$

This result corresponds to what was found in the section about harmonic oscillators.

A.2 Wigner function

The Wigner function in α is given by $\langle\boldsymbol{D}(\boldsymbol{\alpha})\boldsymbol{\mathcal{P}}\boldsymbol{D}(-\alpha)\rangle$, where $\boldsymbol{\mathcal{P}} = e^{i\pi a^\dagger a}$ is the parity operator of the cavity. Note that here, we have omitted the normalization of the Wigner function $\frac{2}{\pi}$. In order to measure the Wigner function of a cavity using an ancilla, the cavity is first displaced, such that its density matrix is $\boldsymbol{D}(\alpha)\rho_c\boldsymbol{D}(-\alpha)$. Because parity will have an important part, we expand this density matrix onto the Fock-state basis

$$
\boldsymbol{D}(\alpha)\rho_c\boldsymbol{D}(-\alpha) = \sum_{k,l} c_{k,l}\left|k\right\rangle\left\langle l\right|.
\tag{A.5}
$$

The operator $e^{i\pi a^\dagger a\boldsymbol{\sigma}_z/2}$ is a rotation by an angle π around the z-axis of the ancilla qubit, conditioned on the excitation number of the cavity. When the cavity is displaced and that

the initial state of the ancilla is $|+\rangle \langle+|$, the unitary evolution due to $e^{-i\pi a^\dagger a \sigma_z/2}$ is

$$
\begin{aligned}
e^{-i\pi a^\dagger a \sigma_z/2}(D(\alpha)\rho_c D(-\alpha))\,&|+\rangle \langle+|\, e^{i\pi a^\dagger a \sigma_z/2} \\
&= \sum_{k,l} c_{k,l} e^{-i\pi a^\dagger a \sigma_z/2} |k\rangle \langle l|\,|+\rangle \langle+|\, e^{i\pi a^\dagger a \sigma_z} \\
&= \sum_{k,l} (c_{2k,2l} |2k\rangle \langle 2l|\,|+\rangle \langle+| + c_{2k+1,2l+1} |2k+1\rangle \langle 2l+1|\,|-\rangle \langle-|) \\
&\quad + \text{off-diagonal cavity terms.}
\end{aligned}
\tag{A.6}
$$

The off-diagonal terms will not be relevant when we take the partial trace over the cavity. The probabilities to measure even/odd terms from this density matrix are given by

$$
P_e = \sum_{k,l} c_{2k,2l}
\tag{A.7}
$$

$$
P_o = \sum_{k,l} c_{2k+1,2l+1}.
\tag{A.8}
$$

This way, we have

$$
\begin{aligned}
\mathrm{Tr}_c(e^{-i\pi a^\dagger a \sigma_z/2}(D(\alpha)\rho_c D(-\alpha))\,&|+\rangle \langle+|\, e^{i\pi a^\dagger a \sigma_z/2}) \\
&= P_e\, |+\rangle \langle+| + P_o\, |-\rangle \langle-| \\
&= \frac{(P_e + P_o)I + (P_e - P_o)\sigma_x}{2} \\
&= \frac{I + \langle D(\alpha)\mathcal{P}D(-\alpha)\rangle \sigma_x}{2}.
\end{aligned}
\tag{A.9}
$$

We see that the value of the Wigner function in α is directly the expectation value of σ_x.

B

Wigner functions of GKP states

In this appendix, we schematically represent the Wigner functions of maximally mixed states and all possible basis states of both the square GKP code and the hexagonal GKP code. The red points represent a value of $+\frac{2}{\pi}$ while the blue points represent a value of $-\frac{2}{\pi}$. We also represent the marginal distributions of these Wigner functions, which represent the probability distribution for a quadrature. We note these quadratures Q_θ, where θ is a rotation angle. For example, Q_0 is what we usually refer to as the position while $Q_{\frac{\pi}{2}}$ is what we usually refer to as the momentum.
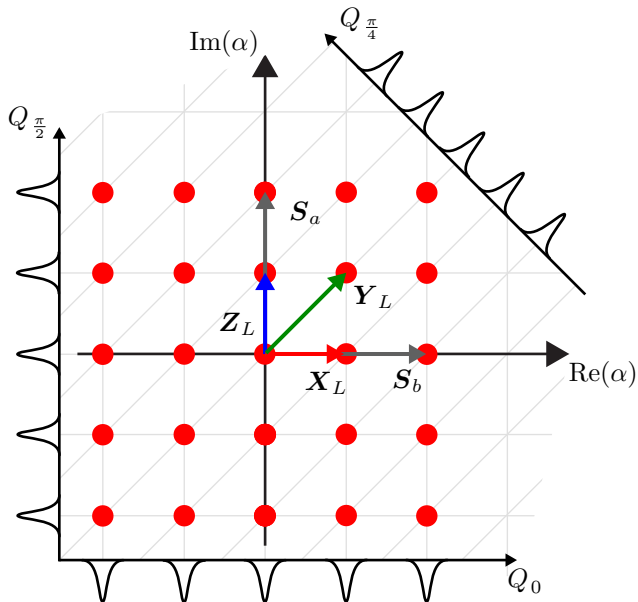
Figure B.1: Square GKP mixed state
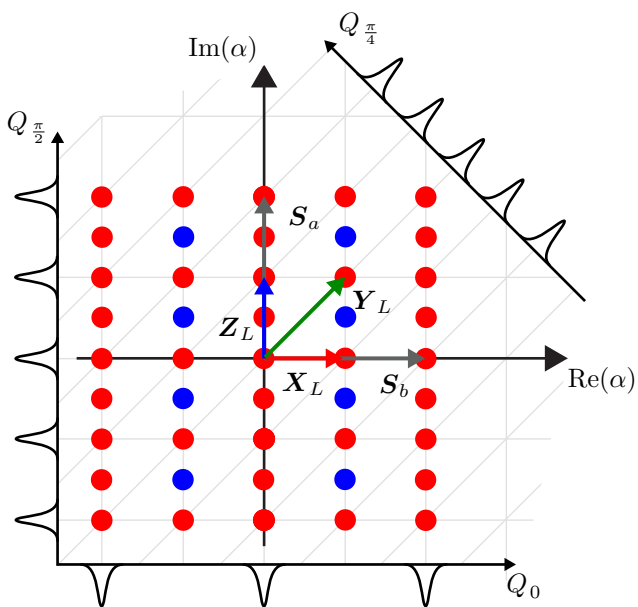
Figure B.2: Square GKP state $|0\rangle_L$
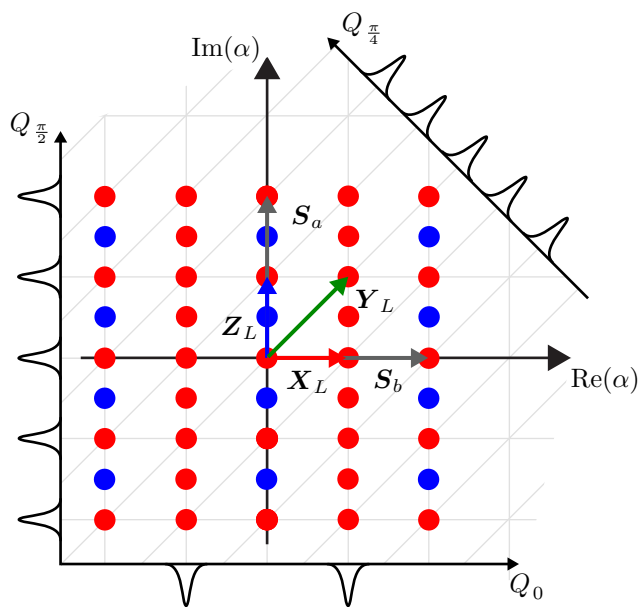
Figure B.3:   Square GKP state $|1\rangle_L$
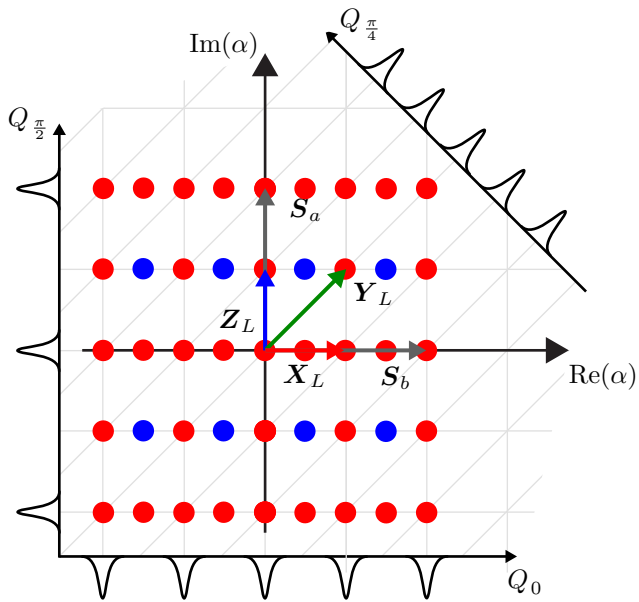
Figure B.4:   Square GKP state $\left|+\right\rangle_L$
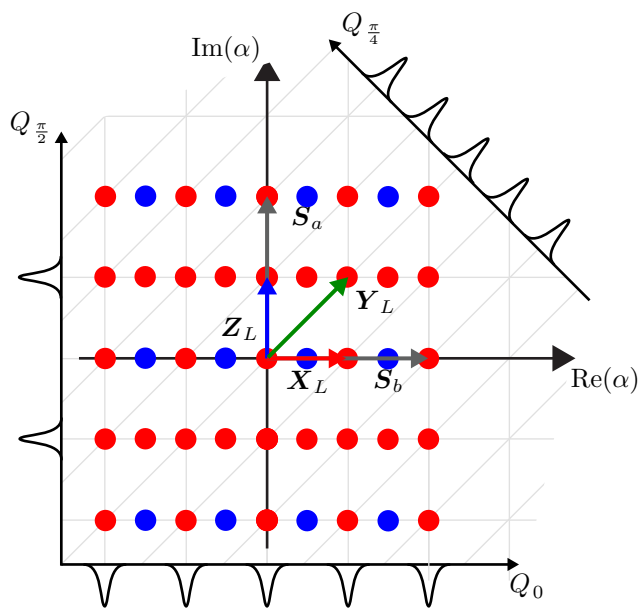
Figure B.5: Square GKP state $\left|-\right\rangle_L$
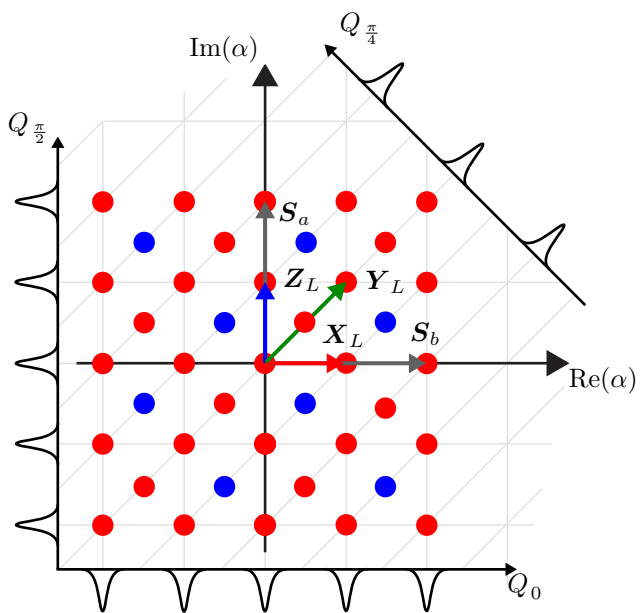
Figure B.6: Square GKP state $|+i\rangle_L$
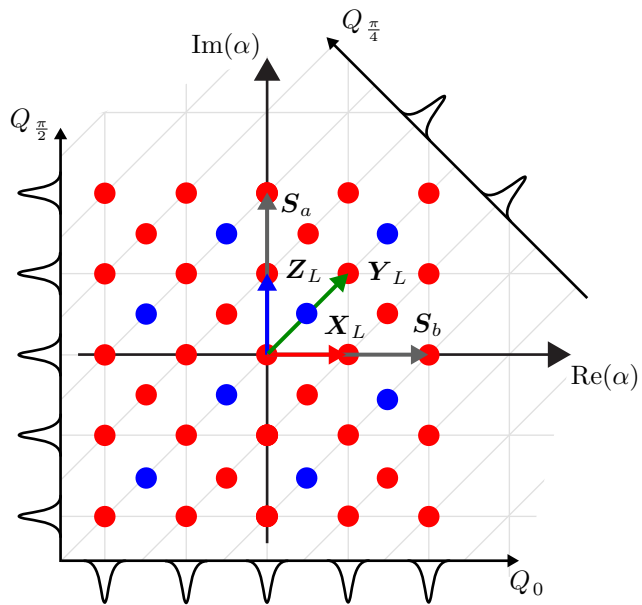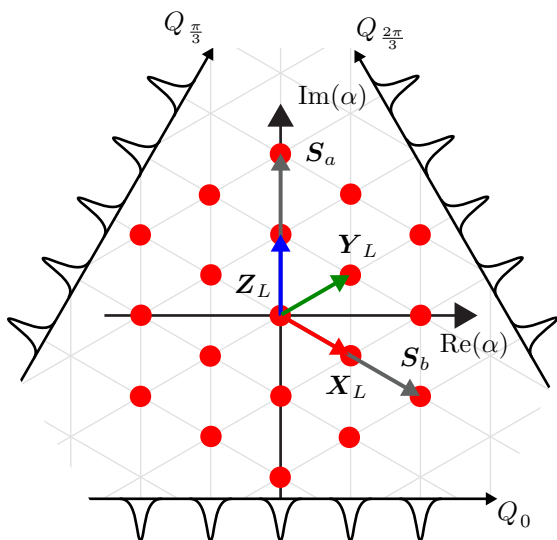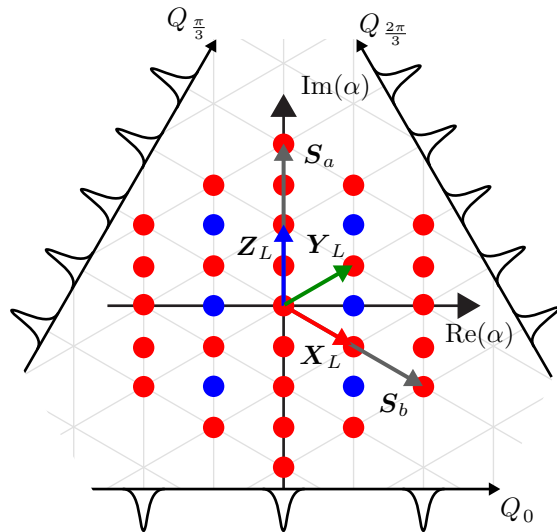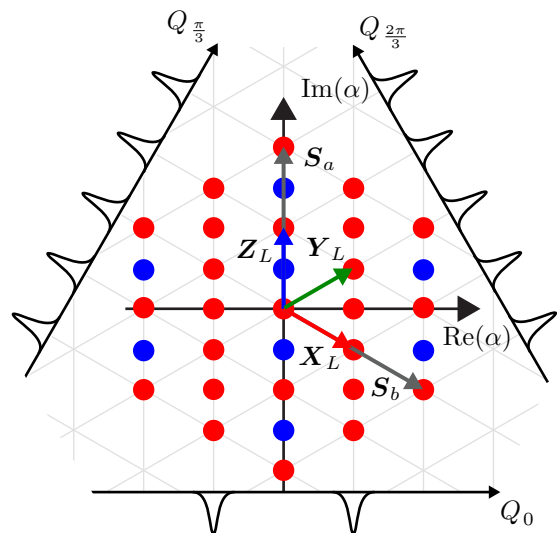
Figure B.7: Square GKP state $|-i\rangle_L$

Figure B.8: Hexagonal GKP mixed state

Figure B.9: Hexagonal GKP state $|0\rangle_L$

Figure B.10: Hexagonal GKP state $|1\rangle_L$
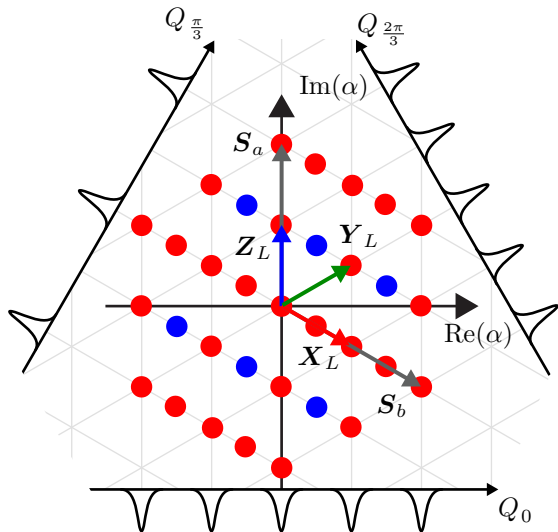
Figure B.11: Hexagonal GKP state $|+\rangle_L$
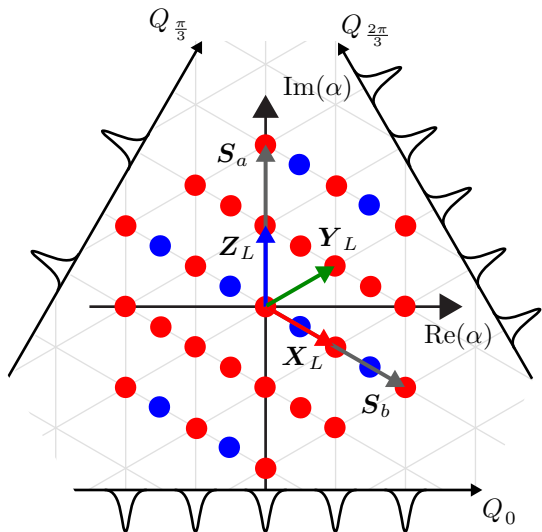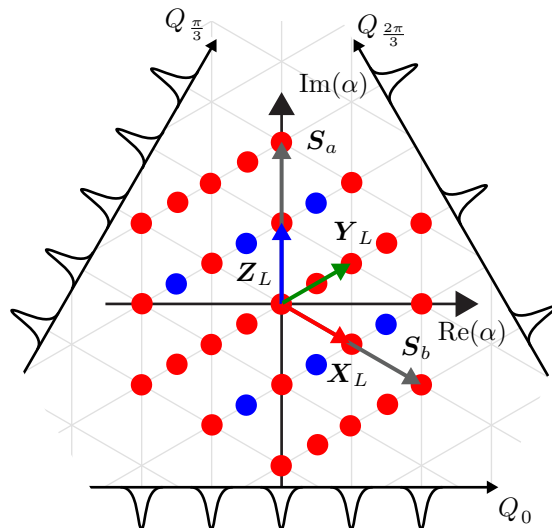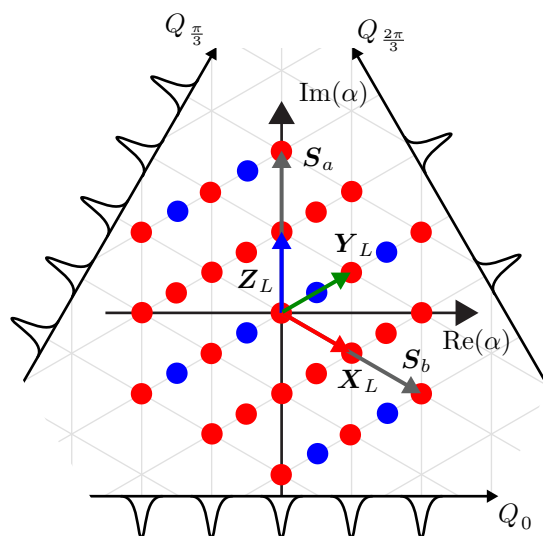
Figure B.12: Hexagonal GKP state $|-\rangle_L$

Figure B.13: Hexagonal GKP state $|{+}i\rangle_L$

Figure B.14: Hexagonal GKP state $|{-}i\rangle_L$